UNIVERSITAT POLITÈCNICA DE CATALUNYA BARCELONATECH

Development, optimization and experimental validation of smart devices for substations and power transmission lines

Yuming Liu

UNIVERSITAT POLITÈCNICA DE CATALUNYA
BARCELONATECH

Development, optimization and experimental validation of smart devices for substations and power transmission lines

by

Yuming Liu (Full-time Researcher)

Dissertation presented as a compendium of publications in partial fulfillment of the requirements for the Ph.D. Degree issued by the Universitat Politècnica de Catalunya in its Electrical Engineering Program.

Supervisors:

Dr. Jordi-Roger Riba Ruiz

Dr. Manuel Moreno Eguílaz

Terrassa, Spain

2023

To my family.

Acknowledgements

I would like to express my heartfelt gratitude to my entire family, especially my beloved parents, who have unconditionally supported me in every step of the way and helped me become who I am today. Despite the pandemic, the geographical distance and the time differences that separate us, you are always with me and give me the best support to keep moving forward. To my love Ilin (김일인), for bringing happiness and smiles to my life even in the most adverse situations.

This thesis would not have been made possible without the financial support of the Generalitat de Catalunya and Spanish Ministry of Economy and Competitiveness, within the framework of the Industrial Doctorates Plan 2020 DI 007.

I wish to express my gratitude to my supervisors, Dr. Jordi Riba and Dr. Manuel Moreno, for their invaluable help and guidance throughout my Ph.D. journey. Jordi, your mentorship, patience, and support over the past three years have been fundamental in shaping my academic research, your enthusiasm for both research and life has motivated me to strive for excellence, both professionally and personally, making you a remarkable role model. Manuel, I extend my appreciation for your dedication and indispensable contributions to this thesis, particularly in the development of experiments.

Special thanks to SBI Connectors España, particularly to Josep and Joan for giving me the opportunity to carry out this thesis within the industrial PhD program. Also, I remain grateful to David for his technical expertise, support, and friendship, which helped me greatly throughout the project.

Next, I would like to convey special thanks to Pau, José and Joaquín for all the good times in Amber. I would like to express special thanks to Pau for his friendship, patience and support, who has been treating me like a brother during this journey. We have shared ups and downs, but in the end, we will make it. Also, I take this opportunity to thank the former members of Amber as Akash, Jimmy, Gabriel, Carlos. You cannot imagine how much you have helped me in the first stage of my PhD journey.

Last but not least, thank you to all the people who gave me their smiles and hugs in the hardest moments.

Abstract

In recent years, there has been a significant increase in the growth of electricity demand. This electricity demand requires retrofitting of lines or exploiting the maximum capacity of existing power lines. In addition, substation connectors are the critical components of power systems since the failure of substation connectors can lead to serve power outages and significantly affect the power transmission efficiency. Therefore, it is vital to have real-time information on key elements of electrical systems, such as connectors and conductors, in order to ensure the reliability and efficiency of power transmission systems. To this end, the *Smartconnector* project aims to combine ICT (Information and Communication Technologies), IoT (Internet of Things) and data-driven technologies to estimate the state of health of substation connectors and take advantage of the maximum capacity of lines. Over the past few years, several research projects have been carried out to develop a smart high voltage connectors prototype, *Smartconnector*, in order to collect and wirelessly transmit information from power connectors in real time. Moreover, a prediction model has been proposed to utilize the collected data to separately predict the remaining useful life of connectors. However, improvements, experimental validation and field application are still needed to verify the reliability and feasibility of the *Smartconnector* prototype. In addition, field application of the IoT device is required for both connectors and conductors.

This thesis is dedicated to the **development**, **improvement**, and **experimental validation** of the IoT prototype and the **extension** of its application to further increase the efficiency of power transmission systems. It is divided into two cores, which include the **optimization** of the *Smartconnector* prototype, and the **extension** of its application. This thesis improves the power management system, which helps to prolong the lifetime of the device. This improvement is based on thermal energy harvesting together with the energy balance strategy. Also, it develops statistical filtering algorithms for data processing. The proposed algorithms are finally implemented on the embedded system of the *Smartconnector* device, ensuring the accuracy of the continuous measurements. This thesis also focuses on the application of the *Smartconnector* for the dynamic monitoring of the line capacity considering weather conditions. In conclusion, this thesis aims to provide improvements and developments for the *Smartconnector*, as well as to open its application to other fields.

Resumen

En los últimos años se ha producido un aumento significativo del crecimiento de la demanda de electricidad. Este crecimiento requiere el reequipamiento de las líneas o el aumento de la capacidad de las líneas eléctricas existentes. Además, los conectores de subestación son componentes críticos, ya que su fallo de los conectores puede provocar cortes de servicio y afectar significativamente a la eficiencia de la transmisión de energía. Por lo tanto, es vital disponer de información en tiempo real sobre elementos clave de los sistemas eléctricos, como conectores y conductores, para garantizar la fiabilidad y eficiencia de los sistemas de transmisión de energía. Con este fin, el proyecto *Smartconnector* pretende combinar las TIC (Tecnologías de la Información y la Comunicación), el IoT (Internet of Things) y las tecnologías basadas en datos para estimar el estado de salud de los conectores de las subestaciones y aprovechar al máximo la capacidad de las líneas. En los últimos años, se han llevado a cabo varios proyectos de investigación para desarrollar un prototipo de conectores inteligentes de alta tensión, *Smartconnector*, con el fin de recopilar y transmitir de forma inalámbrica información de los conectores de potencia en tiempo real. Además, se ha propuesto un modelo de predicción que utiliza los datos recogidos para predecir por separado la vida útil restante de los conectores. Sin embargo, aún son necesarias mejoras, validación experimental y aplicación sobre el terreno para verificar la fiabilidad y viabilidad del prototipo *Smartconnector*. Además, es necesaria la aplicación sobre el terreno del dispositivo IoT tanto para los conectores como para los conductores.

Esta tesis está dedicada al desarrollo, mejora y validación experimental del prototipo IoT y la extensión de su aplicación para aumentar aún más la eficiencia de los sistemas de transmisión de energía. Esta tesis se divide en dos partes, que incluye la optimización del prototipo *Smartconnector* y la extensión de su aplicación. Esta tesis mejora el sistema de gestión de energía, lo que ayuda a prolongar la vida útil del dispositivo. Dicha mejora, se basa en la captación de energía térmica junto con la estrategia de balance energético. Asimismo, esta tesis presenta desarrollos de algoritmos de filtrado estadístico para el procesamiento de datos. Los algoritmos propuestos se implementan finalmente en el sistema integrado del dispositivo *Smartconnector*, asegurando la precisión de las medidas continuas. Esta tesis también se centra en la aplicación del *Smartconnector* para la monitorización dinámica de la capacidad de la línea teniendo en cuenta las condiciones meteorológicas. En conclusión, esta tesis pretende aportar mejoras y desarrollos para el *Smartconnector*, así como abrir su aplicación a otros campos.

Table of contents

List of Figures

1. Introduction

Utilities around the world are facing challenges such as the rising demand for electric energy, aging, etc. To meet these challenges, substations must have sufficient power transmission capacity and robustness to allow the power to flow where and when it is needed.

Dynamic line rating (DLR) offers a promising solution to increase the power transmission capacity. The allowable conductor temperature limits the load or current capacity of the power line, so the operating temperature must be restricted to below the allowable operating temperature to limit the ground clearance of the conductors [1]. DLR can solve this problem because it is a smart and cost-effective solution for utilizing the ampacity or maximum current capacity of transmission lines [2], which differs from Static Line Rating (SLR), the conventional and simple approach, based on conservative criteria that represent severe or worst-case weather conditions [3]. SLR calculates the ampacity of the line using deterministic or probabilistic methods to determine the atmospheric operating conditions, that have a strong influence. SLR often results in a conservative rating because it determines the same ampacity limit throughout the year; it is a static value, regardless of current weather conditions. Conversely, DLR is based on measuring the weather variables, so the maximum allowable current of the line is dynamically calculated to ensure that the line operates within safe operating limits.

Moreover, it is crucial to ensure the stability and reliability of power transmission systems. Substation power connectors are the joints that connect power transmission lines and substation conductors. They are also key elements of an electrical system, as the failure of any connector can result in severe power outages or shutdowns of parts of substations. The electrical contact resistance (ECR) of the connector is a critical indicator to estimate the health status of connectors Thus, to minimize the power outage as well as reduce the cost and time in installation of new connectors, it is fundamental to measure or estimate the contact resistance to monitor the health condition of connectors in real time and prevent the failure in advance.

The Internet of Things (IoT) makes it possible to measure physical variables and collect data in places that were impossible just a few years ago, such as transmission lines and electrical substations. With the widespread development of sensors, communication technologies, control and signal processing algorithms, the IoT under the guideline of smart grid is becoming a promising solution to enhance power supply reliability, reduce power losses, energy achieve energy independence, and integrate renewable energy sources [4]. To this end, the *Smartconnector* project aims to incorporate sensors through wireless links that can transmit information in real time that can be integrated with the prediction model to make a diagnosis of their state of health, etc., to facilitate predictive maintenance.

The *Smartconnector* project can be specified in two main phases: the **initial phase** and the **optimization phase**, as shown in Figure 1-1. In the initial phase, a prototype was developed [5], including,

1. A sensing system (current, voltage and temperature sensors).

2. An energy harvesting system (thermal energy harvesting).

3. Wireless communication capability via Bluetooth Low Energy 5.0.

This prototype can measure some critical parameters using electronic sensors and estimate the electrical contact resistance of connectors. Besides, several prediction models have also been developed to predict the remaining useful life (RUL) and state of health (SoH). However,

improvements and **experimental validation** are still needed to optimize the measurement accuracy, improve the power management system, etc. To enable the *Smartconnector* prototype to monitor or predict the failure of the connectors, it is imperious to integrate the prediction model into the *Smartconnector* prototype. In the past few years, the *Smartconnector* project has made significant progress, and the initial phase has already been fulfilled. Hence, this thesis is focused on the **optimization phase,** which will improve the power management system and develop the data processing algorithm of the IoT device. Besides, this thesis also presents how the developed IoT prototype can be applied to power transmission lines, thus improving the power transmission efficiency of electrical systems.

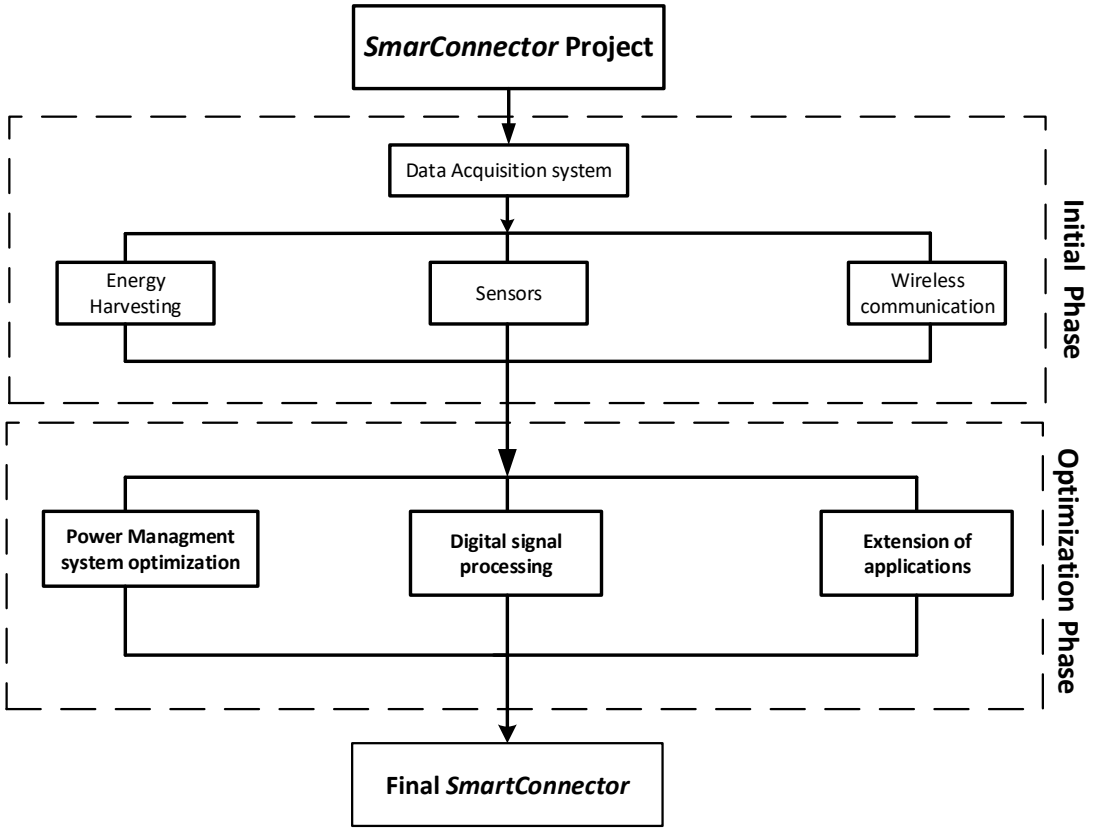

Figure 1-1. *Smartconnectors* project framework.

1.2 Topics and justification

1.2.1 Substation connectors and conductors

Electrical connectors are mechanical and electrical joints for electrical conductors that provide an electrical path for the power transmission system. They are simple components, but possibly the weakest components in the power transmission system. Failure of such components can cause server consequences such as power outages. Therefore, it is a must to ensure the safety of substation connectors. Figure 1-2 displays three types of substation connectors from SBI Connectors España catalogue.

Figure 1-2. Examples of substation connectors from SBI Connectors catalogue.

Meanwhile, with the growing demand of electric vehicles, electric and electronic technologies, there is steady need to increase the current-carrying capacity of power lines. Power line conductors can be of different types, as shown in Figure 1-3. In recent years, various solutions have been proposed, such as reconductoring or increasing the capacity of existing lines by replacing conventional power cables with new ones of larger cross-sectional diameter. Nevertheless, these solutions require more space and are expensive. Dynamic Line Rating is an emerging approach that allows the existing power cables to operate closer to their limit by continuously monitoring key parameters such as weather conditions, wind speed, solar radiation, etc.

This thesis focuses on the development and optimization of a smart device to solve the abovementioned issues.

a) b) c)

Figure 1-3. a) All aluminum stranded conductors b) Aluminum conductor steel-reinforced (ACSR) cables c) A HTLS conductor with carbon-glass epoxy composite core from Sicame Group catalogue.

1.3 Objectives

The main objective of the proposed thesis is " Development and experimental validation of the future generation of smart high voltage connectors and related components for substations, with energy autonomy and wireless data transmission, in order to monitor the connector behavior and diagnose its status".

In order to achieve the proposed overall objective, the *Smartconnector* project has been divided into three specific objectives as described below:

1. **Power management system optimization**

This section presents the development of a power management system for the IoT device, which includes improvements of the thermoelectric modules and DC-DC converters, the analysis of the power consumption of the IoT device and the application of the energy balance for the IoT device.

2. **Digital signal processing**
   This part focuses on the study of digital signal processing techniques to purify the output signal obtained by the electronic sensors. Several digital signal processing algorithms should be studied and implemented to improve measurement accuracy.

3. **Applications extension**

   This objective describes the extension of the IoT concept to other fields such as power transmission lines. It is proven that the use of smart devices for dynamic line rating estimation can significantly increase the capacity of overhead lines.

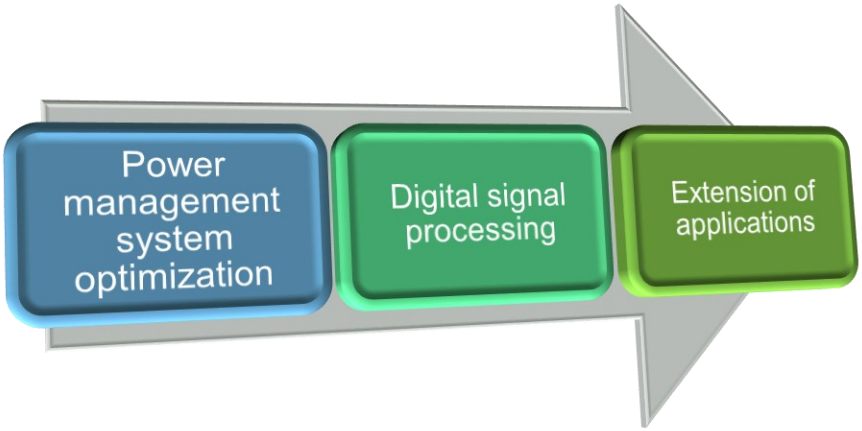

Figure 1-4. Proposed flow of this thesis.

As mentioned above, this research work will be divided into three parts, as shown in Figure 1-4, corresponding to the main objectives of the study, the main tasks of these objectives are specified as follows.

1. Objectives of power management system optimization

1.1 Literature review of energy harvesting technology.

1.2 Selection of thermoelectric modules and DC-DC converters.

1.3 Test the new energy harvesting system in a high-current laboratory.

1.4 Analysis of power consumption of the IoT device in different cases.

1.5 Application of energy balance strategy to the IoT device.

2. Objectives of digital signal processing

2.1 Literature review of digital signal processing algorithms.

2.2 Development of digital signal processing algorithms on a desktop platform to purify signals acquired from sensors.

2.3 Implementation of the DSP algorithms on the embedded system of the IoT device.

2.4 Experimental validation of the signal processing approach.

3. Objectives of extension of applications

3.1 Literature study of dynamic line rating and electrical contact resistance.

3.2 Selection of the electronic system for the application.

3.3 Experimental validation for the proof of applications.

2. Power management system optimization

Power management plays an important role in extending the lifetime of IoT devices. IoT devices, having the ability to sense the fundamental physical variables and transmit the sensed data to a gateway, need a power supply to provide energy for electronic sensors and communication units. *Smartconnector* is a battery-powered IoT device that allows to monitor different physical variables, enabling real-time state of health monitoring methods to be applied. It is known that electrical power connectors are often placed in remote or inaccessible locations, making it a challenging task to frequently replace batteries for *Smartconnector* [5] .

Therefore, to ease predictive maintenance for substation connectors, human intervention has to be minimized due to the existing constraints. For this purpose, *Smartconnector* has been designed with energy autonomy. In [7], it is summarized that there exist different energy harvesting technologies such as thermal, solar photovoltaic, magnetic field/electric field, etc. The most suitable technique for *Smarconnector* application is thermal energy harvesting considering several features such as AC/DC system compatibility, the capability of working both indoors and outdoors, etc.

The thermal energy harvesting system has been proposed as shown in Figure 2-1. The current in an energized tubular bus bar results in a temperature difference due to Joule losses, which can be used by the thermoelectric generator to convert the heat into electrical energy. It is worth noting that in the busbar situation, a low-temperature difference is generated, even with a large current, so the energy harvested is not sufficient to supply the electronic system. Thus, a suitable heat sink and a power converter that can step up the voltage from mV to V were proposed.

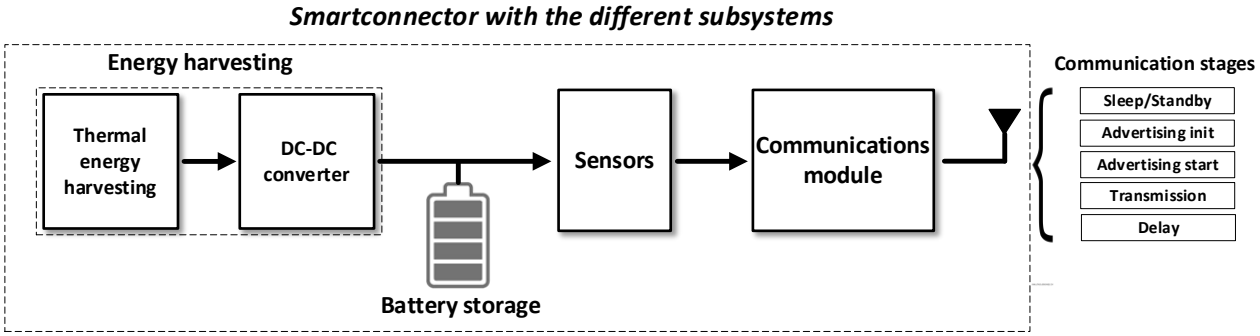

Figure 2-1. Energy flow of the proposed energy harvesting system [8].

Additionally, to ensure the long-term operation of *Smartconnector*, it is important to achieve the energy balance of the entire system which allows to determine the maximum data transfer rate (DTR_{max}).

DTR_{max} is the maximum number of communication cycles (data transfer) permitted without draining the batteries. For this purpose, the energy input and output of the battery must be tested and recorded in a real condition. Therefore, to determine the DTR_{max}, it is necessary to know:

1. Energy input (harvested energy) considering the energy harvesting efficiency.

2. Energy output (energy consumption) taking into account the efficiency of energy storage.

3. Energy balance of the entire system.

This section analyzes the energy harvested, stored and consumed by *Smartconnector*, in order to implement the energy balance strategy, considering the efficiencies of each phase, respectively. *Smartconnector* includes a thermal energy harvesting system, an energy storage unit, a microcontroller, a communication module, and several electronic sensors (temperature, current

and voltage drop) to estimate the electrical contact resistance of power connectors used in high-voltage substations.

2.2 Energy harvesting and its efficiency

Thermoelectric modules (TEMs) or generators (TEGs) offer a reliable solution to achieve the energy autonomy for IoT devices, transferring thermal energy from a temperature gradient directly into electrical energy [9]–[12]. TEG materials must have high electrical conductivity to minimize the Joule effect, a large Seebeck coefficient for maximum conversion of heat into electrical energy, and low thermal conductivity to minimize thermal conduction through the material [13]. When applied to power lines or substation busbars, there is very little temperature gradient between the environment and the busbar, typically a few degrees Celsius. This is a challenging application that has hardly been analyzed in the technical literature since most TEG applications focus on high-temperature gradients [13].

It is known that the existing thermal energy harvesting technique applied in *Smartconnector* can only start to scavenge energy when the temperature difference between the hot side and cold side of the thermoelectric generator is more than 15˚C. In some situations, this temperature difference is difficult to be reached. Thus, the selection of a new thermal energy harvesting system is based on several features, such as ultra-low temperature difference, efficiency, MPPT capability, etc., as shown in Figure 2-2.

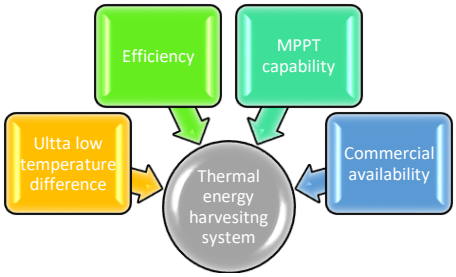

Figure 2-2. Main features for the improvement of thermal energy system.

2.2.1 The Seebeck effect

The Seebeck effect, also known as the thermoelectric effect, is due to the movement of charge carriers, where a temperature difference between two dissimilar conductive materials creates an electrical voltage.

Based on the Seebeck effect, Seebeck generators or TEGs are devices used to convert a temperature difference directly into electrical energy. Semiconductors, ceramics, and polymers are commonly used as materials to fabricate TEGs [14], while semiconductor materials are particularly appropriate for thermoelectric applications due to their high Seebeck coefficient [15].

Figure 2-3 illustrates the basic principle of semiconductor TEGs, which transfer thermal energy into electricity. Due to the temperature gradient between the hot and cold sides of a TEG, the electrons surrounding the metal atoms on the hot side have more kinetic energy, so they diffuse from the hot side to the cold side of the semiconductor. Eventually, the cold side of the TEG becomes negatively charged and the hot side becomes positively charged because the hot electrons move towards the cold end faster than the cold electrons travel towards the hot end. To boost the voltage and current generated, commercial TEGs contain many pairs of n-type and p-type couples

connected in series and/or parallel to generate the desired electrical voltage and current. The couples are typically placed between two parallel ceramic plates that provide a flat surface, structural rigidity, and an insulating layer to prevent short circuits [13].

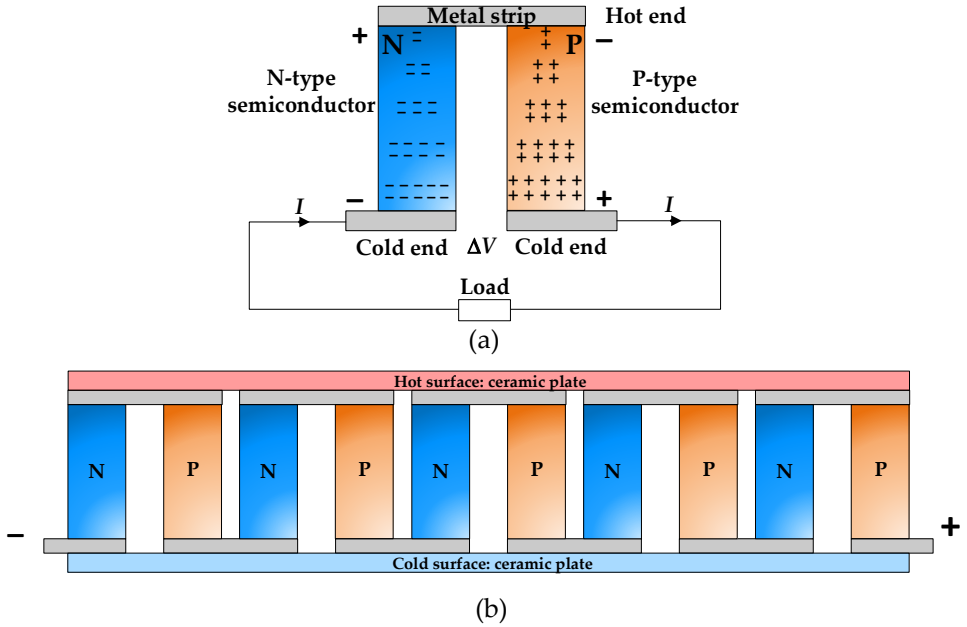

Figure 2-3. (a) Principle of thermoelectric generation, adapted from [16]**. (b) Series connections of different thermoelectric couples, adapted from** [17]**.**

The Seebeck coefficient S is defined from the voltage ΔV produced due to a small temperature gradient ($\Delta T = T_{hot} - T_{cold}$, between the two sides of the TEG) between the two semiconductor materials at the junction under open-circuit conditions [13], [18], [19] as, the Seebeck coefficient is defined as,

$$S = -\Delta V/\Delta T = -(V_{hot} - V_{cold})/(T_{hot} - T_{cold}) \quad (1)$$

The voltage difference ΔV is due to the difference in the electrochemical potentials of the two contacting semiconductor materials [19]. Therefore, the Seebeck coefficient measures the magnitude of the thermoelectric voltage induced due to a temperature difference between the two materials. In general, the Seebeck coefficient depends on the molecular structure of the materials and on the absolute temperature.

2.2.2 The efficiency of energy harvesting

A thermoelectric generator (TEG) is used to capture energy from the thermal gradient existing between a substation busbar and the environment. Substation busbars, typically hollow aluminum tubular conductors, are common connection nodes for multiple circuits. The electrical current injected into a substation busbar causes the generation of heat due to the Joule effect, thus providing a temperature gradient between the busbar and ambient that can be exploited by TEGs to generate electrical energy.

Nonetheless, due to this low-temperature gradient, special care must be taken to select the most suitable TEG. This unfavorable condition forces the TEG to generate a very low voltage, some fractions of a volt, which requires an appropriate DC-DC converter to charge the battery and

power the sensors and the communication module. Therefore, the energy harvesting system consists of a TEG module and a DC-DC converter with a very low input voltage range. Many research works have been carried out on the application of thermal energy harvesting systems [20]–[22]. However, there is a scarcity of works on the implementation of thermal energy harvesting (TEH) systems on substation conductors or power lines, except for [23], which analyzes four different TEG+DC/DC converter settings installed in a tubular busbar found in electrical substations. In this work, the performance and efficiency of thermoelectric harvesting systems are analyzed by determining the input/output power of TEG modules and DC/DC converters. The power produced by a TEG can be expressed as [13],

$$P_{TEG} = P_{transfer} \times \eta_{TEG} \tag{2}$$

Wher e η_{TEG} is the efficiency of the TEGs and $P_{transfer}$ [W] is the rate of heat transfer between the two sides of the TEG.

According to IEEE Std. 605 [24], which describes the design of busbars in air-insulated substations, indoors and under steady state conditions, the heat gain per unit length due to Joule losses must compensate the terms for heat loss per unit length due to convective and radiative cooling as,

$$I_{RMS}^2 R_{ac}(T) = p_c + p_r \quad \text{[W/m]} \tag{3}$$

Where,

I_{RMS} (A) is the current through the busbar,

R_{ac}(T) [Ω/m] is the ac resistance of the conductor per unit length at the operating temperature T,

p_c [W/m] is the cooling term due to natural convection,

p_r [W/m] is the cooling term due to radiation.

The ac resistance per unit length of the conductor, R_{ac} [Ω/m], was measured according to the method described in [25], [26]. This method requires the measurement of the voltage drop ΔV_{1m} [V] between two points on the conductor surface distanced by 1 m, the ac current I [A] flowing through the conductor, the phase shift φ [rad] between the voltage drop and the current, and the conductor temperature T [°C],

$$R_{ac}(T) = \frac{\Delta V_{1\mathrm{m}}}{I} \times \cos\varphi \quad \text{[Ω/m]} \tag{4}$$

To calculate the efficiency of the entire system, including the TEG and the DC/DC converter, $\eta_{TEG+DC/DC}$, the individual efficiencies of the TEG, η_{TEG}, and the DC/DC converter, $\eta_{DC/DC}$, are needed. The efficiency of the TEG η_{TEG} can be calculated as the ratio between the electrical power generated by the TEG, $P_{electric,TEG}$ [W], and the Joule heat generated by the conductor in the area of the TEG, $P_{Joule,TEG\text{-}area}$ [W], as,

$$\eta_{TEG} = \frac{P_{electric,TEG}}{P_{Joule,TEG-area}} \tag{5}$$

$P_{Joule,TEG\text{-}area}$ can be calculated as,

$$P_{Joule,TEG-area} = P_{Joule,conductor} \times \frac{A_{TEG}}{A_{Conductor}} \quad [\mathrm{W}] \tag{6}$$

Where,

A_{TEG} [m^2] is the area of the outer surface of the TEG,

$A_{Conductor}$ [m^2] is the area of the outer surface of the conductor,

$P_{Joule,conductor}$ [W] is the heat generated in the conductor.

Moreover, the efficiency of the DC/DC converter is also needed, which can be expressed as,

$$\eta_{DC/DC} = \frac{V_{out} \times I_{out}}{V_{inp} \times I_{inp}} \quad [-] \tag{7}$$

where V_{out}, I_{out}, V_{inp}, and I_{inp} are, respectively, the output and input voltages and currents of the DC/DC converter.

2.3 The efficiency of energy storage and consumption

Nowadays, rechargeable batteries play a key role in energy storage for IoT applications. Different approaches have been proposed to estimate or predict the lifetime and the health condition of batteries, which can be based on fast impedance measurements [27], or on health indicators such as the internal resistance of batteries, since it is strongly affected by aging [28], or on the battery capacity level [29] among others.

In [30] it is stated that nickel metal hydride (Ni-MH) batteries cannot be fully charged without overcharging owing to side reactions. Ni-MH batteries are applied in many crucial applications such as wearable electronic devices and hybrid vehicles due to their high cycle life and robustness [31], [32]. For *Smartconnector*, a pack of two serially connected Ni-MH batteries is used to store the energy from TEH system and power electronic sensors and a communication module.

Since additional energy is required as a result of energy loss in battery operation, battery energy efficiency is a relevant factor in battery economics and power management. Battery energy efficiency characterizes the utilization rate during energy conversion from chemical energy to electrical energy [33]. In order to minimize the energy losses in the batteries and to evaluate the energy efficiency of the entire thermal energy harvesting system, it is necessary to analyze the efficiency of batteries at a very low current rate, since the analyzed application is characterized by very low current rates.

Since the *Smartconnector* has a very low power consumption, battery efficiency is studied at low current rates. The efficiency has three components, i.e,

1. Charge efficiency η_{Charge}.
2. Discharge efficiency $\eta_{Discharge}$.
3. Overall efficiency $\eta_{Battery}$.

Given the nonlinear characteristics of a rechargeable battery, it is quite challenging to obtain its accurate efficiency. In recent years, several methods have been proposed to estimate the effiency of a battery. In [34], an electrical-thermal model was developed to evaluate the overall efficiency of the battery considering auxiliary losses. In [35], a battery efficiency calculation formula was

proposed based on the internal resistance of a battery, which significantly affects the performance of a battery. Since the difficulty in calculating the battery efficiency is to determine the chemical energy stored in the battery to obtain the net energy, [33],[30] proposed a method to calculate efficiencies based on open-circuit voltage as a function of state of charge (SoC) to compute the net energy under low current rates, which minimizes the dynamics excited in the cells. [30] defined energy storage efficiency under charging conditions as the ratio between the chemical energy gained by the battery during the charging cycle $\Delta E_{Battery\ input}$ [J] and the energy extracted from the power source (the net energy) $\Delta E_{Power\ source}$ [J].

$$\eta_{Charge} = \frac{\Delta E_{Battery\ input}}{\Delta E_{Power\ source}} = \frac{\Delta E_{Battery\ input}}{\Delta E_{Battery\ input} + \Delta E_{Charging\ loss}} \tag{8}$$

Where,

$\Delta E_{Charging\ loss}$ [J] is the energy loss in the battery during the charge or discharge cycles due to Joule heating and the electrochemical reaction process [30], [36].

$\Delta E_{Battery\ input}$ [J] is the chemical energy stored in the battery, i.e., the net energy.

The recharged energy and the net energy are not the same, because the recharged electric energy cannot be completely transformed into chemical energy [33].

The energy extracted from the power source, $\Delta E_{Power\ source}$ [J], can be expressed as [33],

$$\Delta E_{Power\ source} = \int_{t_0}^{t} V_{Charge} I_{Charge} dt = \int_{SoC(t_0)}^{SoC(t)} V_{Charge} C_n dSoC \quad [\mathrm{J}] \tag{9}$$

The net energy gained by the battery during the charge cycle, $\Delta E_{Battery\ input}$, can be expressed as [33],

$$\Delta E_{Batttery\ input} = \int_{SoC(0)}^{SoC(t)} V_{OCV}(SoC) C_n dSoC \quad [\mathrm{J}] \tag{10}$$

Where,

$SoC(t_0)$ [-] is the initial state of charge,

$SoC(t)$ [-] is the final state of charge,

V_{Charge} [V] is the battery voltage,

I_{Charge} [A] is current during the charge process,

V_{OCV} [V] is the open circuit voltage,

C_n [Ah] is the rated capacity of the battery.

The state of charge (SoC) of the battery can be calculated as [33],

$$SoC(t) = SoC(t_0) + \frac{1}{C_n}\int_{t_0}^{t} I_{charge} dt \quad \text{or} \quad SoC(t) = SoC(t_0) - \frac{1}{C_n}\int_{t_0}^{t} I_{discharge} dt \tag{11}$$

According to the IEC 61427-2 standard [37], the **capacity of a battery** expressed in [Ah] is defined as the amount of electric charge that it can deliver under specified discharge conditions and the **state of charge (SOC)** is the energy expressed in [Wh] in a cell related to the rated capacity C_n or energy content expressed as percentage. The rated capacity C_n can be determined according to the IEC 61982 standard [37].

The efficiency of energy consumption or the energy efficiency under discharge conditions [30] is defined as the ratio between the energy consumed by the battery during the discharge ΔE_{Load} [J], and the net energy of the battery $\Delta E_{Battery\ output}$ [J], which can be determined as,

$$\eta_{Discharge} = \frac{\Delta E_{Load}}{\Delta E_{Battery\ output}} = \frac{\Delta E_{Battery\ output} - \Delta E_{Discharging\ loss}}{\Delta E_{Battery\ output}} \quad (12)$$

The energy consumed from the battery during the discharge, $\Delta E_{Load,}$ can be expressed as,

$$\Delta E_{Load} = \int_{t_0}^{t} V_{Discharge} I_{Discharge} dt = \int_{SoC(t_0)}^{SoC(t)} V_{Discharge} C_n dSoC \quad [J] \quad (13)$$

where $V_{Discharge}$ [V] is the voltage of batteries during the discharge process.

Finally, the overall battery efficiency during the charge and discharge cycle [30] is determined as the ratio between ΔE_{Load} and$\Delta\ E_{Power\ source}$,

$$\eta_{Battery} = \frac{\Delta E_{Load}}{\Delta E_{Power\ source}} \quad (14)$$

2.4 Energy balance of the entire system

The energy balance of a device is defined as the energy harvested being equal to the energy consumed over a period of time. In this case, it means that the energy input and output into the battery, $\Delta E_{Battery\ input}$ and $\Delta E_{Battery\ output}$, are equal, which can be expressed as,

$$E_{Battery\ input} = E_{Battery\ output} \quad (15)$$

The equations expressed in the previous section define the battery efficiency if the current rate is constant under charge or discharge conditions. Nevertheless, in practical applications such as the *Smartconnector*, the charge and discharge rates of batteries vary significantly depending on several factors, as shown in Figure 2-4.

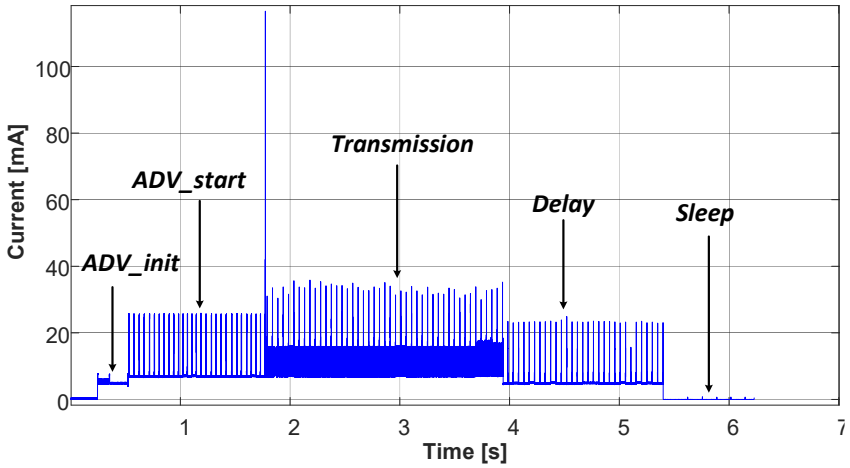

Figure 2-4. Current consumed by the IoT device (*Smartconnector*) during different phases in one communication cycle.

Figure 2-4 shows the different phases during a communication cycle for the *Smartconnector*. In summary, it can be divided into two main modes, that is, data transfer mode (advertisement initialization, advertisement start, transmission, delay) and sleep mode. Each mode has different current rates which makes it difficult to characterize the maximum data transfer rate per hour (DTR_{max}). Thus, there is a need to measure the energy input and output of the battery in a real situation.

In this situation, the energy harvesting unit (thermoelectric generators and DC/DC converter combination) charges the battery to supply the load (sensors and communication module) and the output energy from the battery by the load, so that the energy input and output into the battery can be calculated as,

$$E_{Battery\ input} = E_{out\_DC-DC} \times \eta_{Charge} \quad [J] \tag{16}$$

$$E_{Battery\ output} = \frac{E_{Load}}{\eta_{Discharge}} \quad [J] \tag{17}$$

where, $E_{out\_DC\text{-}DC}$ and E_{load} are the electrical output energy of the DC-DC converter and the energy consumed by the electronic sensors and communication modules of the *Smartconnector*, respectively,

η_{Charge} and $\eta_{Discharge}$ can be determined using equations expressed in (8) and (12), respectively.

Performing the energy balance to the battery for one hour, results in,

$$E_{Battery\ input,1\ h} = E_{Battery\ output,1\ h} = \frac{E_{Load,1\ h}}{\eta_{Discharge}} = \frac{\mathrm{DTR}_{\max}(E_{Load,1\ \text{communication cycle}} + E_{sleep})}{\eta_{Discharge}} \tag{18}$$

Finally, the maximum data transfer rate DTR_{max} is calculated as,

$$\mathrm{DTR}_{\max} = \frac{E_{Battery\ input,1\ h}}{E_{Load,1\ \text{communication cycle}} + E_{sleep}} \eta_{Discharge} = \frac{E_{out\_DC-DC,1\ h}}{E_{Load,1\ \text{communication cycle}} + E_{sleep}} \eta_{Charge} \eta_{Discharge} \tag{19}$$

where $E_{Load,1\ communication\ cycle}$ and E_{sleep} are the energy consumed in data transfer phases (initialization, start, transmission and delay) and energy consumed in sleep mode, which are shown in Figure 2-4.

2.5 Publications

The techniques and methodologies presented in this chapter have been exposed and published in the articles detailed in this section. These articles, therefore, mainly deal with energy harvesting systems, efficiency of different systems and energy balance. They present case studies to evaluate the feasibility of the proposed methodologies for the *Smartconnector*. A complete version of the first and second articles can be found in chapter 5.

> Y. Liu, J. Riba, M. Moreno-Eguilaz, and J. Sanllehí, "Application of Thermoelectric Generators for Low-Temperature-Gradient Energy Harvesting," Appl. Sci. 2023, 13, 2603. https://doi.org/ 10.3390/app13042603..
> This article presents a case study on the application of thermoelectric modules in aluminum substation conductors. As the substation conductors heat up as a result of electrical current passing through due to Joule effect, a small temperature gradient between the conductor and environment is generated, which can be used to convert into

electrical energy. This article assesses the performance of different TEGs designed for low thermal gradient applications.

- Y. Liu, J. Riba, and M. Moreno-Eguilaz, “Energy Balance of Wireless Sensor Nodes Based on Bluetooth Low Energy and Thermoelectric Energy Harvesting,” Sensors 2023, 23, 1480. https://doi.org/10.3390/s23031480.

  This article implements an energy balance strategy to *Smartconnector* prototype, considering the energy harvesting system, the battery, the electronic sensors and a communication module. Also, this article presents a conventional instrumentation to measure the very low energy consumed during the data acquisition and transfer process. The efficiency of the energy harvesting and the effiency of the battery are also taken into consideration to apply an accurate energy balance model of the battery.

2.6 Conclusions

This chapter has presented the thermal energy harvesting system for low temperature gradient application and its efficiency, energy storage efficiency and energy balance strategy. As mentioned in the previous section, to optimize the power management of the *Smartconnector*, case studies have been analyzed and the results have been published in the exposed articles. These case studies have analyzed different energy harvesting systems to characterize each system for high-voltage applications characterized by low thermal gradients. As the tubular busbars heat up due to the Joule effect, a small temperature gradient is generated between the bus bar and the environment, which can be converted into electrical energy by the TEGs to power the *Smartconnector* using a DC/DC converter. The results presented in the articles show that if a temperature gradient of 5 K between the hot and cold sides of the TEGs can drive wireless sensors can be powered by two 40 mm x 40 mm generators.

Besides, the efficiencies of energy storage during both charge and discharge states have been analyzed. The results indicated a significant correlation between the current rate under charge-discharge conditions and the battery charge and discharge efficiencies, η_{Charge} and $\eta_{Discharge}$. The discharge efficiency $\eta_{Discharge}$, for example, can reach 96% at discharge rate of 0.007C and drop to 83% at 0.5C discharge rate. This is due to that the battery pack cannot be fully charged under high charge or discharge rate [33]. The study also illustrates that the overall efficiency of the Ni-MH battery can be as high as 93%, demonstrating its suitability for the *Smartconnector* application.

The power management system of the *Smartconnector* is optimized using a detailed energy balance strategy considering the characterized thermal energy harvesting system and the efficiency of the whole system. This research work demonstrates the possibility of measuring the very low energy consumed by electronic sensors and different modes of a communication module, using conventional instrumentation devices. Finally, the maximum data transfer rate per hour has been estimated based on energy harvesting, consumption, and energy balance of the battery to ensure the long-live operation of the battery that prolongs its lifespan.

3. Digital signal processing

The inherent interference stemming from substation busbars, including electromagnetic interference (EMI) [38], radio frequency interference [39] and harmonic and transients [40], could significantly affect the measurement signals of electronic sensors, ultimately disrupting current and voltage waveforms. As shown in Figure 3-1, the *Smartconnector* includes electronic sensors to measure key parameters such as current, voltage drop between two points of the connector and conductor temperature, as well as a microcontroller and a communication unit. It was designed to monitor the health condition of high-voltage substation connectors by measuring indirectly the electrical contact resistance (ECR). Nevertheless, as the *Smartconnector* needs to be placed on the power connectors, its measurements suffer greatly from the abovementioned interferences, resulting in inaccurate measurements.

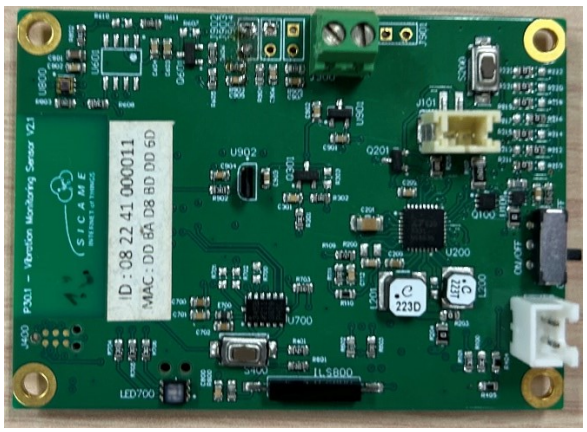

Figure 3-1. Electronic printed circuit board of the *Smartconnector*.

For these reasons, this chapter presents a signal processing approach that is implemented on the microcontroller of the *Smartconnector* to address the abovementioned issues. An overview of the filter-based online ECR measurement approach is presented in Figure 3-2. Initially, electronic sensors are used to measure the key parameters such as voltage and conductor current and temperature. These measurements will pass the prior statistical filter to denoise the original signals. Next, these denoised signals are sent to the nearby gateway to compute the electrical contact resistance. The process to determine the ECR has been presented in section 6.1.

The following sections detail the process of performing online ECR estimation using voltage, conductor current and temperature measurements. Additionally, multiple statistical filtering algorithms have been developed to process the current and voltage waveforms under the high-current environment in order to obtain accurate ECR measurements. In this research work, we implement these algorithms to recover the signals. Our aim is not to provide a filter that outperforms the other filters in just one aspect, but rather to give a comprehensive analysis between several signal processing methods for the high-voltage substations application.

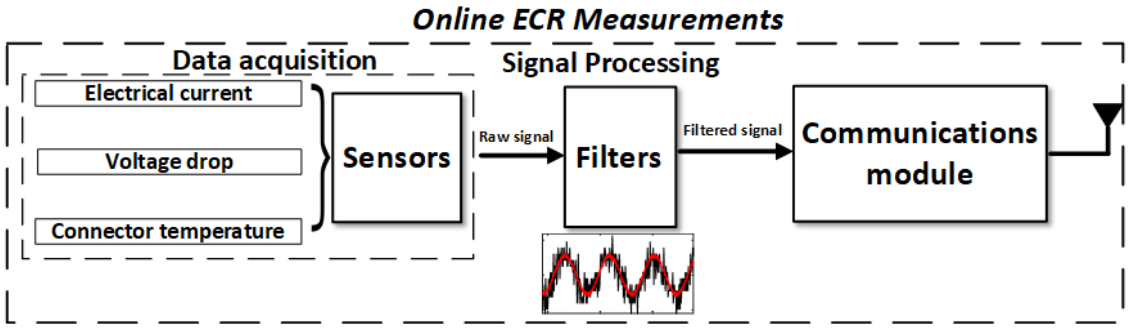

Figure 3-2. Proposed online filter-based ECR measurement method.

3.1 Electrical contact resistance

Electrical power connectors guarantee reliable electrical connections between conductors, serving as the critical components in power transmission systems. Nonetheless, such components may be among the least durable components in power transmission systems, and their failure can trigger severe power outages, with catastrophic consequences [41]. Hence, there is an imperious need to monitor the health condition of these connectors to avoid power network failures.

Contact resistance in electrical connectors, or electrical contact resistance, refers to the resistance to current flow, due to surface conditions and other causes when contacts are touching one another. For most substations, the connectors must be repaired or replaced when the contact resistance exceeds a threshold value. Owing to this fact, the contact resistance is defined as a **reliable indicator** to determine the health condition of high-voltage power connectors [42].

Remaining useful life (RUL) strategies reduce maintenance costs due to unscheduled downtimes, whileavoiding major power system faults [43]. Therefore, in order to apply predictive maintenance plans for power connectors, several RUL and health condition monitoring strategies have been proposed, using electrical contact resistance as health indicator [43]–[46]. In [44], an approach for an on-line diagnosis of the health condition of power connectors has been developed to estimate early failures in the connectors. This approach determines a degradation model of connector resistance by means of the Markov chain Monte Carlo stochastic algorithm. In [43], using the autoregressive integrated moving average (ARIMA) algorithm, an on-line approach to determine the RUL of power connectors was proposed. From the resultsit was shown that by implementing RUL strategies, it is feasible to anticipateincipient failures. In [45], three simple and effective algorithms were tested and compared for the state of health diagnosis of power connectors.

These health condition monitoring strategies are effective and feasible to ease the predictive maintenance of power connectors. To do so, it is a must to acquire the contact resistance data in real time. There are two methods to obtain electrical contact resistance, namely direct measurement and indirect measurement.

The standard Kelvin 4-wire approach is one of the most accepted methods to perform the direct measurement of the ECR[25],[47],[48]. It is based on measuring the voltage $\Delta V_{connector}$ across the connector to calculate the total electrical resistance of the connector $R_{connector}$, while a stabilized DC current I_{DC} is injected [25],

$$R_{connector} = \Delta V_{connector} / I_{DC} \tag{20}$$

Nevertheless, this method can just estimate the contact resistance in DC system since a known DC current I_{DC} is injected into the electrical circuit. Also, in ac systems, the 4-wire method measures the impedance instead of the resistance. Under ac supply, due to the existence of the reactance, the impedance of the connector $Z_{measured}$ is calculated as,

$$Z_{measured} = \Delta V_{connector} / I_{AC} \tag{21}$$

It is seen from equation (21) that when dividing the voltage drop across the connector $\Delta V_{connector}$ by the ac current I_{AC} passing through the loop, the impedance $Z_{measured}$ is obtained. Hence, to acquire the resistance component under ac supply, a suitable approach is still needed to obtain the ECR data in both dc and ac electrical systems.

In [49],[25], an online measurement method was proposed to estimate the contact resistance in real time under both dc and ac supply systems. It is shown that based on the abovementioned

simultaneous current and voltage measurements, the ac resistance of the connector $R_{connector}$ can be estimated from the phase difference φ between the current I_{AC} and the voltage drop across the connector, as,

$$R_{connector} = \frac{\Delta V_{connector}}{I_{AC}} * cos\varphi \quad (22)$$

Finally, the ac resistance of the connector at the standard temperature of 20 ℃ $R_{connector,20℃}$ can be calculated as,

$$R_{connector,20℃} = R_{connector}/[1 + \alpha(T_{connector} - 20)] \quad (23)$$

Where α is the temperature coefficient of the resistance and the $T_{connector}$ is the temperature of the connector.

3.2 Statistical filtering algorithms

Due to high voltage restrictions and the placement of substation connectors in inaccessible areas, human intervention should be restricted. The *Smartconnector* includes an instrumentation amplifier to amplify the weak voltage signal across the connector, a Hall effect sensor to measure the current flowing through the electrical loop, and a temperature sensor to record the bus bars temperature. The electrical contact resistance is also recorded and transmitted wirelessly [5] according to equation (22).

Smartconnector is a novel IoT solution and the accuracy of ECR measurements has been proven experimentally under high-current conditions. However, weak electrical signals can be disrupted by the unwanted electromagnetic (EM) noise caused by bus bars or power transmission lines [50], [51], asshown in Figure 3-3. Moreover, due to the non-linear characteristisc of power electronic devices, the presence of harmonic noise is inevitable [52]. This signal noise leads to inaccurate ECR measurements, making it impossible to apply predictive maintenance strategies in certain circumstances, especially at low current operation.

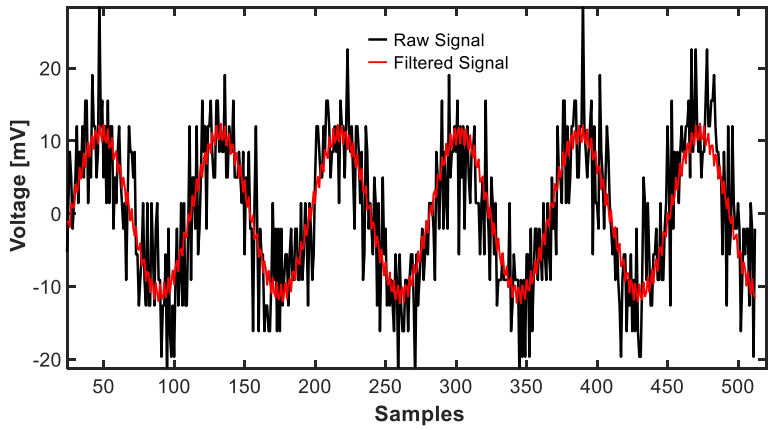

Figure 3-3. Electromagnetic noise in the electrical signal of data acquisition.

Recently, some research groups have intended to develop statistical filtering algorithms to deal with the abovementioned issues. Statistical filtering algorithms have attracted worldwide attention in recent years due to the significant growth in IoT applications. They play an important role in signal processing, providing solutions to filter noisy signals, thus helping to obtain more accurate responses from IoT devices [53].

From the literature review, it is found that many digital filtering algorithms haven been proposed for condition monitoring purposes such as Kalman filter, moving average, harmonic filtering, proportional integral differential (PID), machine learning, autoregressive moving average, etc [54]–[60]. In [59], a detailed review of the techniques implemented in the vibration feature extraction has been concluded. In this review, the signal processing algorithms have been divided into two main streams, namely time-domain techniques and frequency-domain techniques. The advantages and disadvantages of each method are summarized to facilitate the selection of a suitable algorithm. In [54], a discrete Fourier transform filtering algorithm was used to remove the DC component and harmonics of signals obtained. In [55], vibration and current signals are processed to diagnose faults of induction motors. In [60], a Kalman filter framework was proposed to recover the real electrocardiogram signal.

Although many digital filtering algorithms have been developed and tested as mentioned above, they are generally implemented on desktop platforms where there are no computational constraints. However, there is a scarcity of works implementing these filtering algorithms on embedded systems applied in a very high-current environment to improve the electrical contact resistance measurements. To this end, this research work proposed to test and compare several filters on the desktop platform and the most suitable algorithm should be implemented for the embedded system of the *Smartconnector*.

In this chapter, due to the limited computational ability of the microcontrollers of cost-effective IoT devices, three filtering algorithms (Kalman-, Sinusoidal- and Moving average filter), which require relatively low computational cost, were developed and discussed.

3.2.1 Kalman filter

The Kalman filter (KF) is one of the most important and widely accepted filtering algorithms in real-time applications due to its low computational resource requirement, excellent recursive properties, and optimal estimator functionality [61]–[63]. The KF has been applied to topics such as online estimation of state-of-charge for lithium-ion batteries [63]–[66], processing biomedical signals [67], and estimating the velocity and position of 2D-moving objects [68].

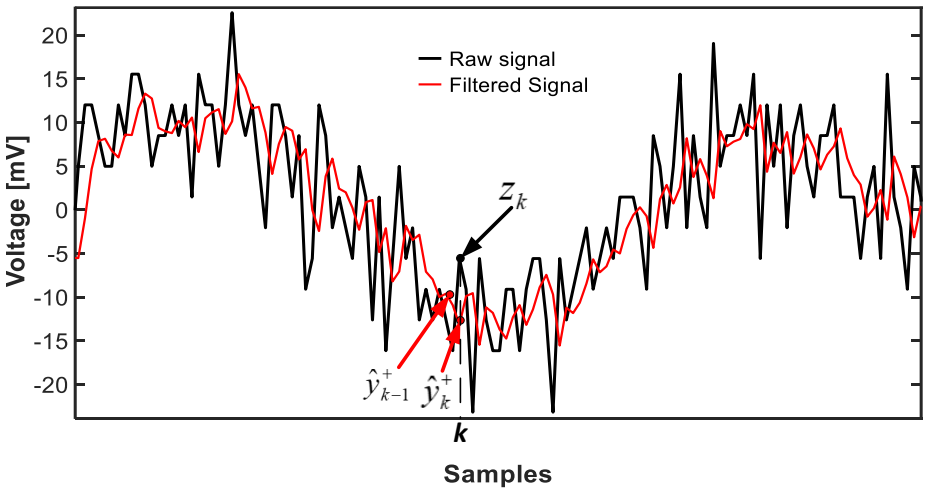

Figure 3-4. An example of the KF implementation on substation signals.

Although the conventional KF is ideal for estimating optimal state for linear Gaussian state space models, many issues found in practical applications are governed by non-linear systems. Hence, several improvements have been achieved during a period of time for non-linear dynamic systems

such as the Extended Kalman filter (EKF) [69],[70], the Robust Kalman filter (RKF) [71],[72], the Unscented Kalman filter (UKF)[73],[74], the Cubature Kalman filter (CKF) [75].

For the *Smartconnector* application, due to its limited computational resources, a simple linear KF is proposed. To model the KF system, there are two important steps:

1. Predict the future state.

2. Update the current state.

The process is illustrated in . Firstly, it is necessary to predict future states $\hat{y}_k^-$ using the current state $\hat{y}_{k-1}^+$ at time-step k – 1, and then update the current state $\hat{y}_k^+$ at time-step k with the experimental measurements z_k.

To achieve the prediction of future states, the first step is to compute the prediction of the estimated covariance $\hat{p}_k^-$ and the covariance of innovation $\hat{s}_k^-$ as [76],

$$\hat{p}_k^- = \hat{p}_{k-1}^+ + Q_k \tag{24}$$

$$\hat{s}_k^- = \hat{p}_k^- + R_k \tag{25}$$

where $\hat{p}_{k-1}^+$ is the covariance of the estimation error at time-step k - 1 in the one-dimensional Kalman filter, whereas the system process noise covariance Q_k and the covariance of measurements noise R are set to be constant, being $Q_k = Q$ and $R_k = R$, respectively.

Next, the Kalman gain G can be obtained using equations (24) and (25),

$$G = \hat{p}_k^- / \hat{s}_k^- \tag{26}$$

The prediction of the future state ($\hat{y}_k^-$) at time-step k is completed by taking the state vector of the previous time-step k-1 [76] as,

$$\hat{y}_k^- = F_k \hat{y}_{k-1}^+ \tag{27}$$

where $\hat{y}_{k-1}^+$ is the current state at time-step k – 1 and F_k is the state-transition model. Finally, the update of current states at time-step k is performed as,

$$\hat{y}_k^+ = G \cdot (z_k - \hat{y}_k^-) + \hat{y}_k^- \tag{28}$$

where z_k is the experimental measurement at time-step k, $\hat{y}_k^+$ is the updated current state at time-step k, $\hat{y}_k^-$ is the prediction of the future state at time-step k , and G is the Kalman gain.

Next, the update of the covariance of the estimation error $\hat{p}_k^+$ is calculated as,

$$\hat{p}_k^+ = \hat{p}_k^- \cdot (1 - G) \tag{29}$$

where $\hat{p}_k^-$ is the prediction of the estimated covariance at time-step k.

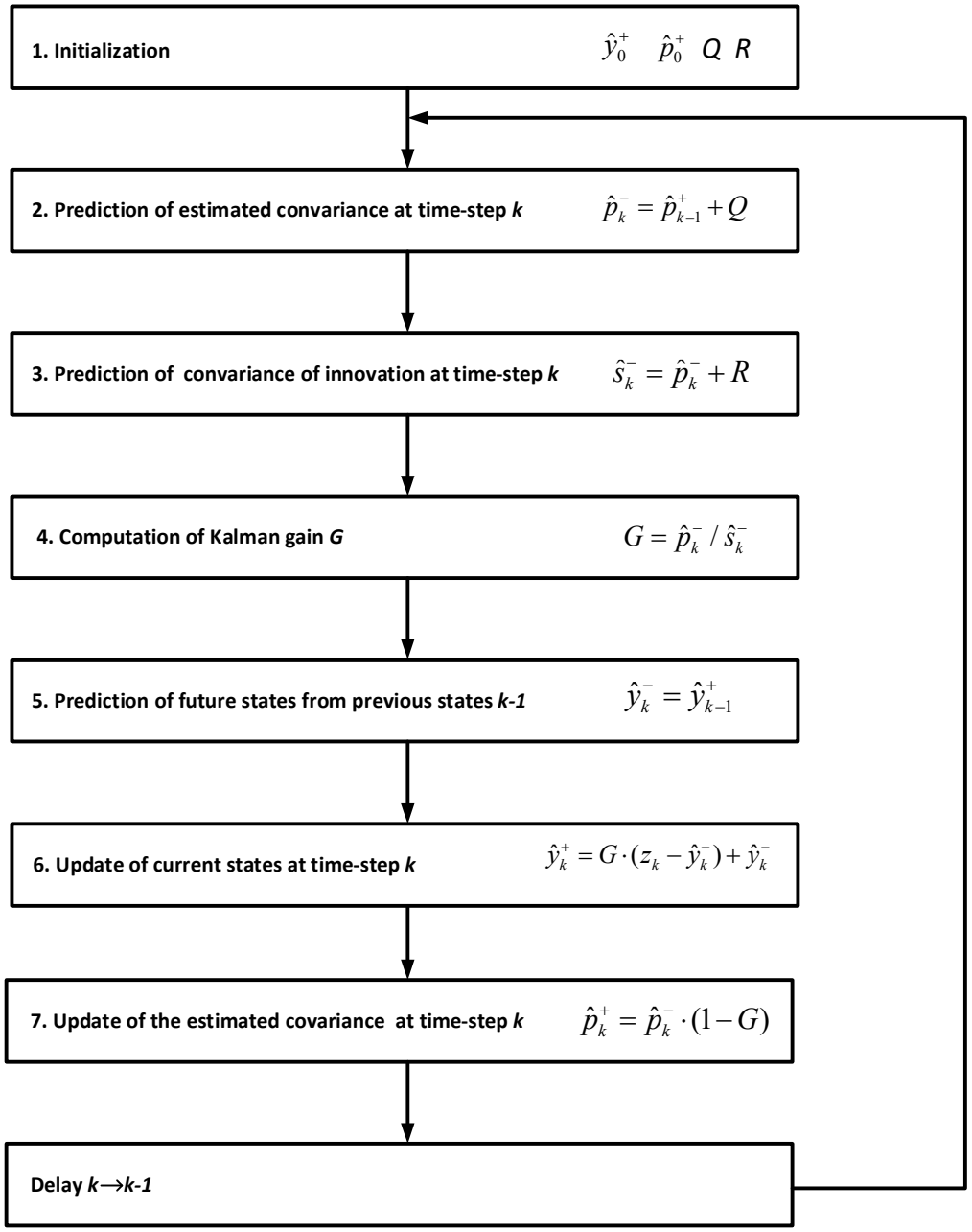

Figure 3-5. Block diagram of proposed Kalman filter modelling process.

It is noted that the initialization of the Kalman filter is indispensable in the modeling the Kalman filter system, so the most suitable seed values of the current state $\hat{y}_0^+$, the estimation of the covariance $\hat{p}_0^+$, the covariance of the system process noise Q_k, and the covariance of the measurement noise R_k are predetermined according to the best knowledge of the author. In this research work, it is assumed that $Q_k = Q$ and $R_k = R$ are constant values. Note that it is necessary to initialize the values for variables $\hat{y}_0^+$, $\hat{p}_0^+$, Q, R according to the best knowledge of the specific application.

In conclusion, the Kalman filter modeling process is detailed in Figure 3-5.

3.2.2 Sum of Sine filter

A discrete cosine transform (DCT) was first developed by Ahmed for signal processing [77]. It is widely accepted in digital filtering applications because of its simplicity, fast convergence speed, and ability to extract the correct information. In [78],[79], the harmonic filtering method was used to correct CoRoT light curves. Meanwhile, [80] employed a sine and cosine form algorithm to process the remaining unevenly spaced data. In [81], a sine filtering formula was used to reduce the impact of residual noise for the power frequency estimation.

Knowing that the *Smartconnector* takes measurements of 6 sinusoidal periods [5], this research work proposed to use a sinusoidal model to approximate the sample signal to a sine function in order to minimize the impact of the noise. According to [57], harmonic filtering is a sum of sine and cosine functions used to describe a periodic signal. The functional form of the sinusoidal filter can be expressed as [80],

$$\hat{y}_k(t_i) = a_0 + \sum_{k=1}^{N} a_k \cos(\frac{\pi t_i k}{D}) + \sum_{k=1}^{N} b_k \sin(\frac{\pi t_i k}{D}) \tag{30}$$

where a_0 is the DC offset in the signal, a_k and b_k are amplitude variables of the model, D is the length of the time series for each calculation cycle, t_i are time stamps of the data under analysis, N is the number of harmonic terms in the series. Since this form does not include phase terms, it is a linear expression to variables a_k, b_k, which facilitates the use of weighted linear minimization to compute the variables [80].

In this research work, a discrete series of sine functions similar to the harmonic filter described in [80] is proposed. It includes phase terms to get a more compact model, although the non-linear method should be used to compute the equation variables. The proposed function is called sum of sine filter (SoSF), since real signal can be considered as the summation of sine waves [82]. Its functional form can be written as,

$$\hat{y}_i = \sum_{k=1}^{N} a_k \sin(b_k x_i + c_k) \tag{31}$$

where k is the order of sine terms, with $k = 1, \ldots N$, N is the total number of sine terms included in the sinusoidal model, x_i is the sample at time-step i, $\hat{y}_i$ is the output estimation at time-step i with $i = 1, \ldots, n$, n being the total number of samples in the signal to be regressed. The amplitude a_k, fundamental frequency b_k and phase shift c_k are determined using the nonlinear least square (NLS) approximation method [83]. For the *Smartconnector* application, based on the author's experience, N is set to 2, which means that two sinusoidal waves are used to fit the regression model.

3.2.3 Moving Average Filter

The moving average algorithm is a promising solution for digital signal processing applications [84][85][86][87]. It is a recursive filter that can be used to smooth out the short-term fluctuations in the data. This technique permits reducing the signal noise with low processing power, making it a suitable approach for embedded systems, since the main concern of these systems is computational resources.

Depending on the application, different types of moving average algorithms have been developed, which can be divided into:

1. **Simple moving average (SMA)**: The simple moving average algorithm is featured as its simplicity and effectiveness to smooth the time-series data. It calculates the average of a fixed moving window of sample points and slides the window through the sensed [85],[87].

2. **Weighted moving average (WMA)**: Weighted moving average algorithms allow assigning different weights to recent sample points, focusing on recent experimental measurements. By regulating the assigned weights, it permits to smooth the fluctuations of signals [88].

3. **Exponential weighted moving average (EWMA)**: Similar to the WMA, the exponential moving average algorithm assigns weights to the last sample points, whereas the decrease of the weighting factors of EWMA is exponential instead of consistent [89].

In [85], a simple moving average technique was used as a low-pass filter to remove the random noise that existed in the raw sampled waveform. Due to the existence of distortion at the endpoints and jumps while the moving average was applied, [86] developed an adaptive moving average filtering (AMA) algorithm to purify experimental signals, the results show that the AMA has better performance and recover the signal with higher signal-to-noise-ratio.

With respect to the application of *Smartconnector*, the SMA was implemented to smooth out the noise generated in sensed signals. This filter requires especially less memory and computational power compared to other filters, making it an appropriate filter for the embedded system of *Smartconnector*. The SMA calculates the average of the last *k* sample as,

$$\hat{y}(t) = \frac{1}{n}\sum_{k=1}^{n} y_k \tag{32}$$

where $\hat{y}(t)$ is the output bias at time *t*, *n* is the total number of points considered in the fixed moving window, and y_k is the sample at point *k*.

Nevertheless, increasing the value of *n* reduces the dynamic response of the system measurement, which rejects the actual system measured response due to disturbances as noise [76]. Hence, careful analysis is required to choose a suitable moving window *k*. In this thesis, to balance the noise reduction and dynamic response, we have applied and analyzed the implementation of SMAF filter with moving window k = 2, 5, 8 on ECR measurements, respectively.

3.3 Publications

This section presents the publications regarding the developments of statistical filtering algorithms for signal processing purposes. The papers include studies of three filtering algorithms and an analysis conducted to compare them in terms of measurement accuracy and computational time required to identify the most suitable algorithm. Moreover, this paper also details the experimental setup implemented to acquire the electrical signals. Chapter 5 includes the full version of this publication.

- Y. Liu, J. Riba, and M. Moreno-Eguilaz, “Denoising of Online Resistance Measurements of Power Connectors for IoT Applications,” *Proc. IECON 2023 - 49th Annu. Conf. IEEE Ind. Electron. Soc*, Singapore, 2023.

This paper presents the developments of three filtering algorithms, namely by the simple moving average filter (SMAF), Kalman filter (KF), and sum of sine filter (SoSF), on the desktop platform. These filters are used to reduce signal noise from an IoT device located in a high-current laboratory. The study compares the three algorithms according to the measurement accuracy and computational time required to select the most suitable filter for this specific IoT application.

3.4 Conclusions

This chapter has addressed the signal noise problem existing in electrical contact resistance measurements under low-current circumstances. Given the limited computer power of common IoT devices, this thesis aims to design a simple but effective filter. So, a careful analysis was conducted to compare these algorithms based on their performance and computational efficiency. In the first experiment, three different filtering methods were proposed and initially tested on a desktop platform with the real signal obtained from a high-current laboratory.

The obtained results indicate that the objective was achieved. By applying these algorithms, the electrical signals obtained from the electronic sensors were filtered, which helps the IoT device to acquire highly accurate ECR data at current levels as low as approximately 150 A_{RMS}. For example, it was found with 312A_{RMS} current injected into the electrical loop, the error of measurement was 12.1% with the raw signal and 1.9%, 3.4%, and 2.1% using SMAF with moving window equal to 8, KF and SoSF, respectively. Furthermore, the SoSF filter exhibits the best performance at the lowest current applied,150 A_{RMS}, providing as low as 3.8% deviation from the standard DAQ reference data. However, this filter also tends to require more computational time than other filters due to its regressing process for each iteration, requiring 0.253 seconds in one data-acquisition process for SoSF calculation and 0.0055 seconds, 0.0054 seconds, 0.0054 seconds, 0.0070 seconds for SMAF with moving window equal to 8 and, respectively. Also, since the SMAF filters demonstrated great performance from 312A_{RMS}, resulting in less than 5% error of measurements, the SMAF was considered to be the most appropriate filter for the *Smartconnector* application.

To evaluate the feasibility of the selected SMAF filtering algorithm, second experiment was conducted. The algorithm was implemented on the built-in system of the *Smartconnector* and tests were carried out under five different current levels (140 A_{RMS}, 310 A_{RMS}, 500 A_{RMS}, 700 A_{RMS} and 900 A_{RMS}) for continuous ECR measurements. The experimental results have proven the accuracy of the *Smartconnector* with the filtering algorithm. Compared to the ECR measurements taken by the IoT device without applying the filter, the proposed filter has significantly increased the accuracy of the measurements, especially at low currents. For instance, when about 150 A_{RMS} were injected, the error with the filter is 4.8%, while the error without the filter is 31%.

The proposed signal filtering framework is useful for the industrial sector, particularly for real-time monitoring applications, enabling them to acquire more accurate key measurements, thereby facilitating predictive maintenance.

4. Extension of applications

Dynamic line rating (DLR) offers a solution to take advantage of the maximum current capacity of power transmission lines [90]. It differs from static line rating (SLR), the conventional and simple approach, which is based on conservative criteria [90] that represent severe or worst-case weather conditions [91].

Various DLR approaches are presented in the technical literature. As stated in [92], DLR methods can be broadly categorized into indirect and direct methods. Indirect methods determine the thermal line rating through weather data collected from weather stations or forecasted data, which serve as the primary input for the approach. These approaches estimate the required thermal rating by solving the heat balance equation of the conductor, as outlined in Cigré [93], IEEE [90], or IEC [91]. In contrast, direct DLR methods involve the direct measurement of physical variables of power lines, including conductor temperature and current, mechanical tension, conductor sag, or ground clearance, as detailed in [3]. Since there is no need to install weather measuring devices on the line and since they offer reliability at relatively low-cost, indirect methods are considered more straightforward and cost-effective compared to direct methods, making them suitable for lightly loaded power lines. In comparison to direct methods, indirect methods are less precise, as the conductor temperature and maximum line capacity are indirectly estimated using theoretical models [94]. Conversely, direct methods rely on field data, allowing for greater accuracy, as they eliminate the need for any relationship between conductor temperature and data obtained from indirect methods [92].

In recent years, rapid advancements in communication systems, sensors, and control algorithms have led to the development of smart grids that integrate distributed energy resources, loads, energy storage, and control systems. They offer substantial benefits, including improved power supply reliability, reduced power losses, energy independence, and the integration of renewable energy sources [4]. In pursuit of these goals, smart grids employ information technology to share power data in real-time for the efficient management of the power demand, thus maximizing power efficiency. As a result, DLR methods play an important role for smart grid development [95]–[101]. Recent research has suggested that IoT solutions can not only boost smart grid reliability but also greatly enhance their capacities [102]–[105].

For these reasons, this chapter presents an extension of the *Smartconnector* application, called *Smartconductor*, which allows real-time estimation of the DLR rating of power lines by integrating the weather data from weather stations and line data recorded by the *Smartconductor*. This approach is a practical application under the guideline of smart grid, as the proposed DLR approach facilitates power lines to operate at their peak capacities by adjusting the rating based on real-time weather conditions.

Given that the DLR rating is significantly influenced by the local wind speed and since the wind speed has an important cooling effect, it plays a much more prominent role than that of ambient temperature and solar radiation in determining the DLR rating [92]. This chapter presents a novel method to estimate the wind speed instead of using anemometers to measure it directly. Moreover, this chapter exposes a method to determine the core losses in ACSR conductors from the alternating current resistance (R_{ac}) measured. The R_{ac} of the conductor is a crucial parameter to accurately estimate the maximum current capacity of power lines [106], and the Joule and core losses represent the main heat source of the conductor and can be determined from the alternating current (ac) resistance R_{ac} [26], [107].

The following sections detail the process of estimating the DLR in real-time by means of the measurements from *Smartconductor* and nearby weather stations and studies of the effect of core losses in determining the DLR of ACSR conductors.

4.1 Core losses determination in ACSR conductors

ACSR conductors comprise several aluminum strands and galvanized steel strands, as illustrated in Figure 4-1. Adjacent aluminum layers are wound in opposite directions around the steel core [108]. While the steel core provides the mechanical strength, the highly conductive aluminum strands provide the current pathway [109]. The flow of electric current tends to spiral along the aluminum strands. The contact resistance between adjacent strands is much higher than the internal resistance of the strands. This results in generating an axial component of the magnetic field. Under ac supply, the axial magnetic flux within the core generates eddy currents and hysteresis losses in the core, modifying the distribution of the current density in the aluminum layers. This redistribution depends greatly on the strength of the magnetic field within the core, so it varies with the intensity of the electric current passing through the strands and the lay length (the distance that the strand needs to complete one revolution around the diameter of the conductor) [110]. As a result, due to the magnetic induction, the steel core increases the ac resistance of the conductor [109].

Due to the opposite winding directions of adjacent aluminum layers, the axial components of the magnetic field produced by the currents in adjacent layers have opposite directions, thereby leading to a reduction in the overall magnetic field. The cancellation of magnetic field is most in conductors comprising two aluminum layers, with this effect being less marked in conductors containing an odd number of layers than in conductors with an even number of aluminum layers [109]–[111]. This means that ACSR conductors with an even number of aluminum layers result in reduced magnetic core losses [108].

Figure 4-1. Cross section of a three-layer ACSR conductor.

The distribution of current density, the internal temperature and the magnetic properties of the steel core affect the ac resistance of conductors. As stated in [112], the ac resistance of ACSR conductors can be expressed as the sum of three terms: the dc resistance, the resistance arising from eddy currents, and the component due to hysteresis losses. This means that core losses, including hysteresis and eddy current losses, as well as any temperature rise, contribute to the increase in the effective ac resistance of the conductor [113]–[115]. Consequently, the combined effects of eddy current, hysteresis losses and the transformer effect increase the ac resistance R_{ac} of the conductor above the dc resistance value, denoted as R_{dc}, at the same temperature. In conclusion, a higher ratio of R_{ac}/R_{dc} increases the energy losses in the conductor [114].

Based on the experimental results obtained in [6], the conductors with an odd number of aluminum layers exhibit higher resistance ratios R_{ac}/R_{dc}, whereas the conductors with an even

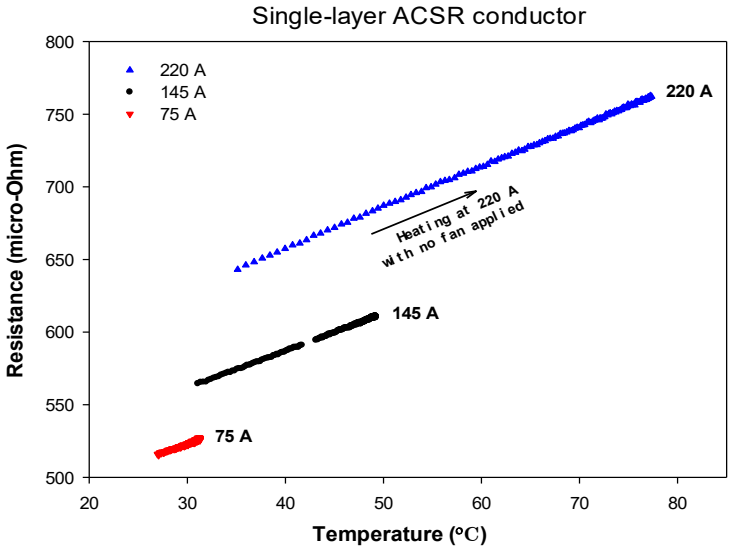

a)

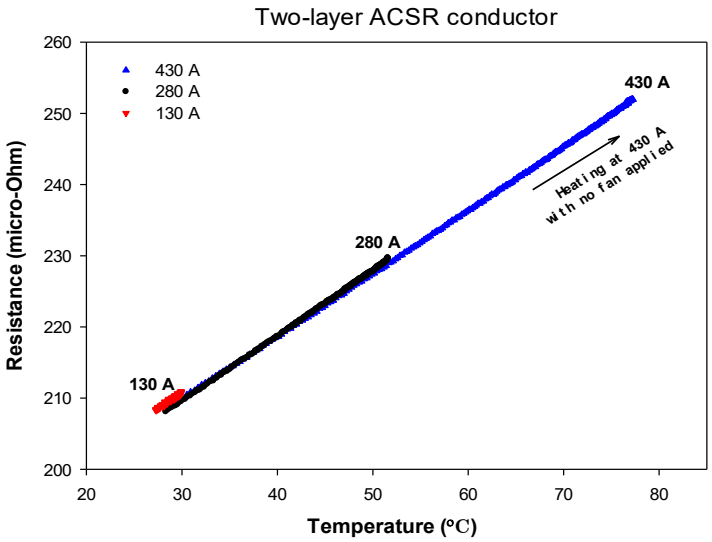

b)

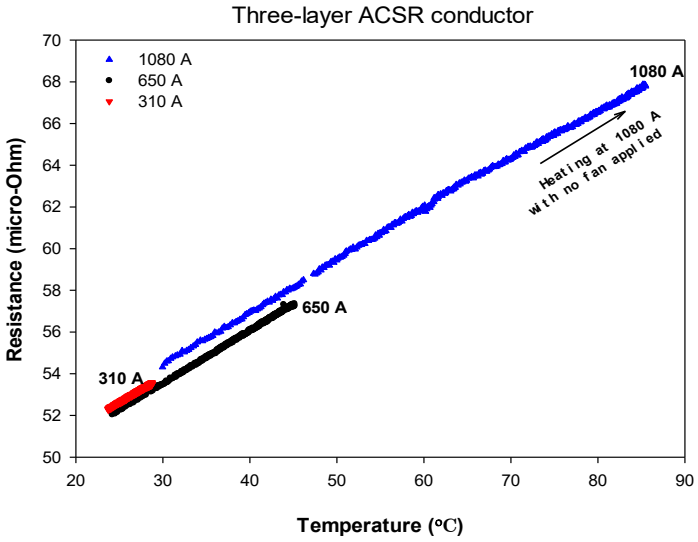

c)

Figure 4-2. R_{ac} versus temperature measured in a high-current laboratory. a) single-layer ACSR conductor b) two-layer ACSR conductor c) three-layer ACSR conductor.

number of aluminum layers exhibit lower resistance ratios, as displayed in . This is due to that the magnetic field cancellation of the axial component has less effect on conductors with an odd number of aluminum layers, resulting in the conductors with one aluminum layer having the highest resistance ratios [113]. Nevertheless, the internal inductance of ACSR conductors increase with electric current up to a maximum level where the steel cores become magnetically saturated [115].Afterwards, any further increase in electric current reduces the internal inductance [113] due to the decrease of the magnetic permeability, thus reducing the resistance ratios.

According to the international standard IEC 60287-1-1 [116], the ac resistance can be expressed as,

$$R_{ac} = R_{dc}(1 + y_s + y_p) \ [\Omega/\mathrm{m}] \tag{33}$$

where y_s and y_p are the skin and proximity effect factors, respectively. The ds resistance considering the effect of temperature can be expressed as,

$$R_{dc} = R_0[1 + \alpha_{20}(T - 20)] \quad [\Omega/\mathrm{m}] \tag{34}$$

where T is the operating conductor temperature, R_0 the dc resistance measured at 20 °C and α_{20} the temperature coefficient at 20 °C.

In the majority of ACSR applications, the skin effect is negligible when compared to the transformer effect. However, in cases requiring low electric currents, large-size conductors or high frequency operation, this difference reduces. Similarly, the proximity effect is negligible when distances between adjacent conductors are greater than ten diameters[114]. While equation (33) is simple to apply, it is exclusively applicable to nonferromagnetic conductors up to 5 kV [116]. Furthermore, it overlooks crucial parameters associated with stranding, including the direction and lay length, as it considers the stranded conductor as a solid conductor [106].

Under dc supply, there is no explicit equation to determine the internal resistance of ACSR conductors, whereas under ac supply, several researchers have proposed formulas, although they are not precise due to the complex behavior of the magnetic flux generated in the steel core. Hence, considering the nonlinearity and complexity of these effects, the most effective way is to determine the ac resistance and the internal reactance of an ACSR conductor through experimental measurements.

In order to determine the per unit length values of the impedance, ac resistance R_{ac} and reactance X of the conductor expressed in Ω/m, according to [26], [110], [113], it is necessary to measure the instantaneous values of the voltage drop per unit length ΔV, the electric current I and the phase shift φ between themas,

$$Z = \frac{\Delta V}{I} \quad [\Omega/\mathrm{m}] \tag{35}$$

$$R_{ac} = \frac{\Delta V}{I} \cdot \cos\varphi \quad [\Omega/\mathrm{m}] \tag{36}$$

$$X = \frac{\Delta V}{I} \cdot \sin\varphi \quad [\Omega/\mathrm{m}] \tag{37}$$

When considering the effect of the temperature, R_{ac} can be described as,

$$R_{ac,T} = R_{ac,0}[1 + \alpha_{ac}(T - T_0)] \quad [\Omega/\mathrm{m}] \tag{38}$$

where $R_{ac,0}$ is the ac component of the resistance at a given temperature T_0, usually 20˚C, and α_{ac} is the temperature coefficient of the ac resistance. It is worth noting that $R_{ac,0}$ is a measured value, that includes the effect of magnetic saturation, as stated in [117].

4.2 Dynamic line rating estimation

Nowadays, dynamic line rating (DLR) is a trending topic due to the fast development of accurate, compact, and low-cost sensors, the widespread use of different communication systems suitable for high-voltage applications, the need to increase power transmission capacity, and the capability of DLR to ensure the maximum current capacity of power lines,.

I. Albizu [107] proposed a new sag-tension ampacity monitoring approach based on direct measurements of key parameters such as current, temperature and mechanical tension of the conductor, as well as weather conditions such as solar radiation and ambient temperatura. Sag-tension methods need accurate state change relations between conductor temperature and sag-tension [118]. A. H. Wijethunga [119] proposed to determine the DLR rating using a cost-effective sensing probe to measure the temperature of conductors and transmit the data through wireless communication. Nevertheless, the current flowing through the line was not acquired in real time, which plays a crucial role in determining the DLR [118]. In [120], an energy-autonomous high-voltage sensor was proposed to measure the conductor temperature, current, voltage, the active and reactive power to estimate the SLR and DLR ratings. This approach also needs environmental measurements such as air pressure or wind speed and direction from nearby weather stations. However, it is known that the average wind speed and direction obtained from local weather stations is often inaccurate, as the wind speed changes with terrain topography. In [121], the wind speed is estimated using a reverse equation together with measurements of line current and temperature, solar radiation and ambient temperature, but this paper does not present a method to estimate DLR ratings.

In this research work, a low-cost, real-time monitoring model to estimate the DLR rating using the *Smartconductor* was proposed. The procedure is detailed in Figure 4-3. The DTLR estimation has been divided into two stages: the wind speed estimation stage and the DTLR calculation stage. Since the constants, B_1 and n depend on surface roughness and Reynolds number, which are not available, the author proposes to set their initial values as $B_1 = 0.641$ and $n = 0.471$, which are taken from [93]. In the first main stage, the *Smartconductor* takes the measurements of line current and temperature, and the Reynolds number is determined for the wind speed estimation. Afterwards, the wind speed is estimated. In the second main stage, the maximum current capacity (ampacity) can be estimated, considering the estimated wind speed.

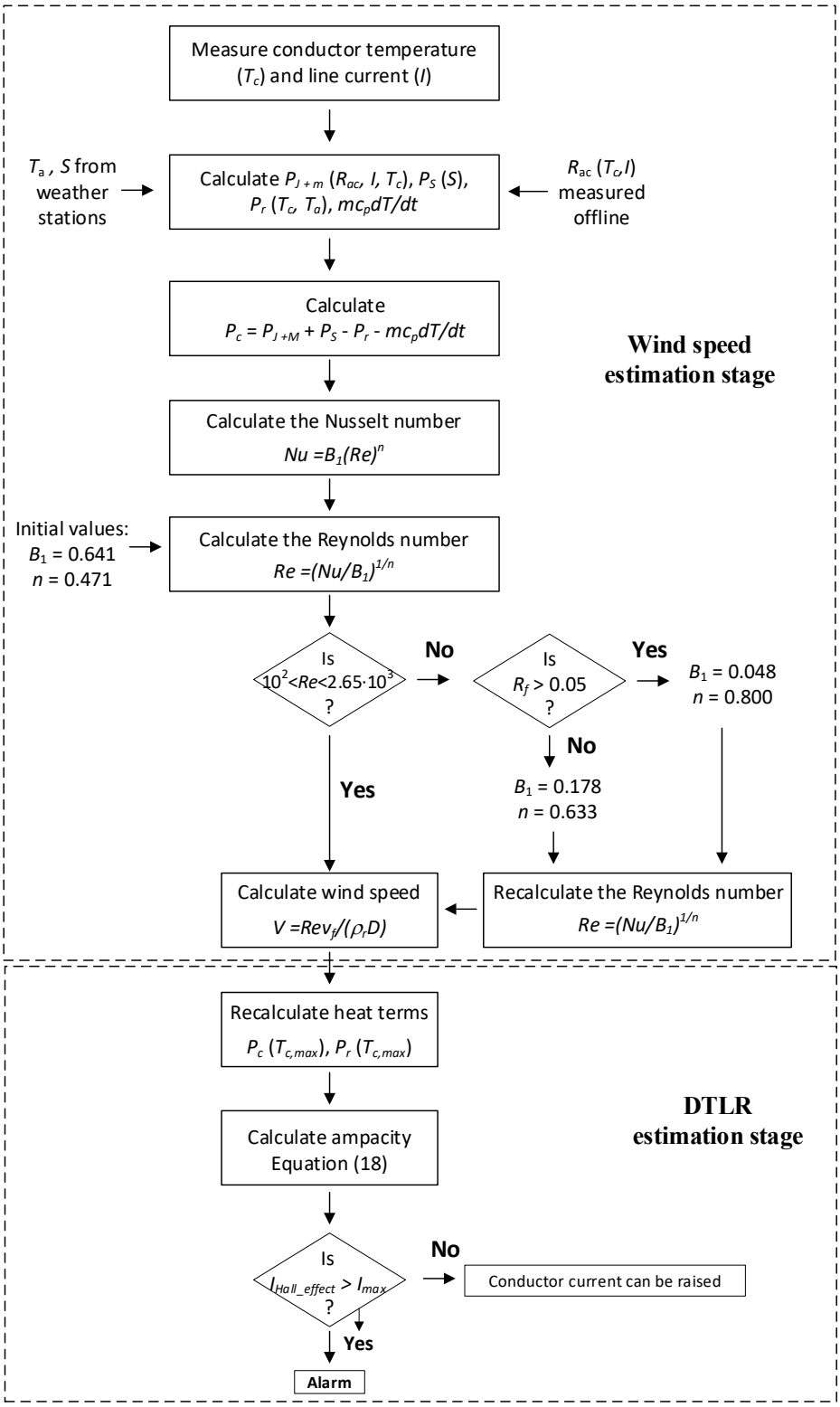

Figure 4-3. A flowchart of the DLR determination approach.

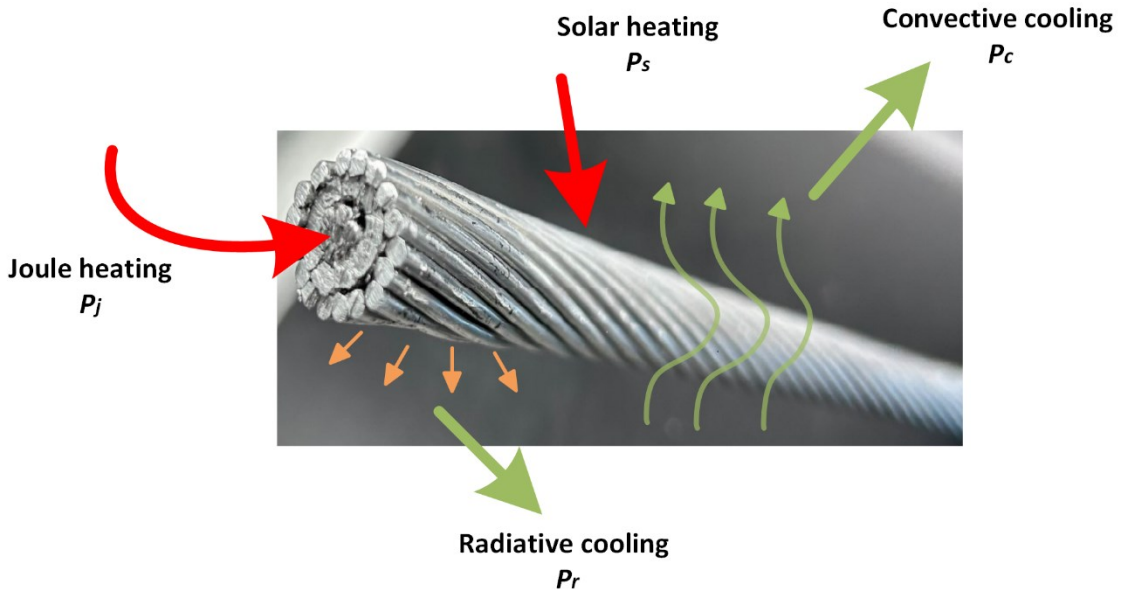

Figure 4-4. Thermal balance in a conductor.

Figure 4-4 shows the diagram of the heating balance within a conductor. According to the CIGRE standard [93], a non-steady-state thermal balance equation can be expressed as,

$$P_J + P_M + P_S = P_c + P_r + mc\frac{dT_c}{dt} \text{ [W/m]} \tag{39}$$

where P_J, P_M, P_S are the heating gain terms through Joule effect, magnetic effect, and solar radiation, respectively; P_c and P_r are the convective and radiative heating loss terms, respectively; m is the mass of the conductor in kg/m, c is the specific heat capacity of the conductor in J/$(kg°C)$, and T_c is the average temperature of the conductor in °C.

The heat capacity c of the ACSR conductor can be calculated as,

$$\begin{cases} mc = m_{Al}c_{Al} + m_s c_{steel} \\ c(T) = c_{20°C}[1 + \beta(T_c - 20)] \end{cases} \tag{40}$$

where m_{Al} and c_{Al} represent the mass per unit length and the specific heat capacity of the aluminum component, respectively, whereas m_{steel} and c_{steel} represent the mass per unit length and specific heat capacity of the steel component, respectively. The values of the temperature coefficient β are 3.8×10^{-4} °C^{-1} for pure Al, 4.5×10^{-4} °C^{-1} for the Al alloy and 1.0×10^{-4} °C^{-1} for steel, according to [93].

As stated in [107], the heating gains due to Joule and magnetic effects can be combined into only one equation, as,

$$P_J + P_M = I^2 R_{ac} \tag{41}$$

where I is the root mean square (RMS) value of the electrical current passing through the conductor, and R_{ac} is the ac resistance of the conductor per unit length at the operating average conductor temperature T_c. The calculation of the ac resistance of the conductor R_{ac} is a challenging task due to the skin, proximity and core loss effects [110]. The author proposes to measure this value according to the procedure described in [115] or in [25].

Therefore, the ac resistance of the conductor R_{ac} (T_c) was measured in the laboratory by measuring the temperature of the conductor, the voltage drop between two points of the conductor surface

spaced by 1 m, and the ac current passing through the conductor. Next by applying (42), the ac resistance was calculated as

$$R_{ac} = \Delta V cos\varphi / I \tag{42}$$

As described in [93], equations (43-48) are used to determine the heat loss due to convective cooling:

$$P_c = \pi \lambda_f (T_c - T_a) N_u \ [\mathrm{W/m}] \tag{43}$$

where λ_f in W/(m °C) is the thermal conductivity of air, T_c is the surface temperature of the conductor, T_a is the ambient temperature.

Equation (43) applies to both natural and forced convective cooling, the difference between both situations is found in the way to allow the calculation of the de Nusselt number N_u.

In the case of forced convection, the Nusselt number is calculated as

$$N_u = B_1 (Re)^n \ [-] \tag{44}$$

where the Reynolds number is calculated as

$$Re = \rho_r V \frac{D}{\nu_f} \ [-] \tag{45}$$

where V (m/s) is the wind speed, ρ_r (−) and ν_f (m^2/s) are the relative density and kinematic viscosity of air, respectively, D (m) is the diameter of the conductor, and B_1 and n are constants depending on the Reynolds number Re and conductor surface roughness, respectively. It is worth noting that the wind speed can be estimated by applying (45), as described in Figure 4-3.

In case of natural cooling, the Nusselt number is obtained from the Grashof (Gr) and Prandtl (Pr) numbers as follows:

$$Nu = A_2 (GrPr)^{m_2} \tag{46}$$

$$Pr = 0.715 - 2.5 \times 10^{-4} T_f \tag{47}$$

$$Gr = D^3 (T_c - T_a) g / (T_f + 273) \nu_f^2 \tag{48}$$

where g = 9.807 m/s^2 and the values of A_2 and m_2 can be found in [93].

Since in this research work, we propose to estimate the wind speed instead of taking direct measurements, the wind speed is not known. Therefore, both forced and natural cooling equations are applied. If the power loss due to forced convection is greater than the power loss due to natural convection, it is assumed that the wind speed is not null, and the Nusselt number Nu is calculated by applying (44); otherwise, it is calculated from (46). Nevertheless, in virtually all situations found in outdoor environments, the Nusselt number should be calculated from (44).

The heat gain due to the solar radiation can be calculated using the global solar radiation S (W/m^2), as seen in [93]:

$$P_s = \alpha_s S D \ [\mathrm{W/m}] \tag{49}$$

where α_s (-) is the solar absorptivity of the conductor surface, and D (m) is the external diameter of the conductor.

Finally, radiative heating losses can be described as [93]:

$$P_r = \pi \varepsilon D \sigma_B [(T_c + 273)^4 - (T_a + 273)^4] \ [\mathrm{W/m}] \tag{50}$$

where ε is the emissivity factor, which depends on the conductor surface, and σ_B = 5.6697×10^{-8} W/(m^{2}K^4) is the Stefan–Boltzmann constant.

Finally, the DLR rating is calculated when the conductor temperature reaches it maximum value under thermal equilibrium, so from (39) and (41), it results in [5,28]:

$$I_{max} = \sqrt{\frac{P_c(T_{c,max}) + P_r(T_{c,max}) - P_s}{R_{ac}(T_{c,max})}} \tag{51}$$

4.3 Publications

This section presents the publications related to the developments exposed in this chapter of the thesis, detailing the methodological framework for the estimation of the dynamic line rating in real time. In these articles, experiments are carried out to evaluate the accuracy of the proposed methodologies and techniques for power transmission lines. Chapter 5 includes the full version of them.

- Y. Liu, J. R. Riba, M. Moreno-Eguilaz, and J. Sanllehí, "Analysis of a smart sensor based solution for smart grids real-time dynamic thermal line rating," *Sensors*, vol. 21, no. 21, pp. 1–17, 2021, doi: 10.3390/s21217388.

  This article proposes a real-time approach to determine the DLR rating of ACSR conductors. The proposed method requires a thermal transient model of the line to determine the real-time values of the solar radiation and the ambient temperature, which can be acquired from weather stations placed near the analyzed conductors as well as the temperature and the current of the conductor, which can be measured directly with a smart device and can be transmitted wirelessly to a nearby gateway. Also, it is known that the wind speed shows important fluctuations, even in nearby areas, and since it plays a crucial role in determining the DLR, it is significant to estimate this parameter accurately at the location where the conductors are placed. This article presents a method to estimate the wind speed and the DLR rating of the analyzed conductor. Experimental tests have been conducted to evaluate the accuracy of the proposed approach based on ACSR conductors.

- Riba, J.-R.; Liu, Y.; Moreno-Eguilaz, M.; Sanllehí, J. On-Line Core Losses Determination in ACSR Conductors for DLR Applications. Materials 2022, 15, 6143. https://doi.org/10.3390/ ma15176143

  Since DLR approaches require determining the ac resistance of the power transmission lines, which is a main parameter that enables it to determine Joule and core losses. This paper presents an approach for an on-line alternating current (ac) resistance estimation of ACSR conductors for the determination of the DLR rating of such conductors from real-time conductor and meteorological parameter measurements. For this purpose, conductors with one, two and three layers of aluminum strands are analyzed in detail. Based on the experimental results presented in this paper, two possible approaches are proposed.

4.4 Conclusions

This chapter presents an extension of the *Smartconnector* to determine the DLR rating in real time for power lines, called the *Smartconductor*. To do so, the real values of the solar radiation and ambient temperature are needed, which can be acquired from a nearby weather station, whereas the line current and temperature can be measured directly by using a *Smartconductor*. Moreover, due to the local fluctuations of the wind speed, this thesis proposes a cost-effective approach to estimate the wind speed accurately. Once the wind speed is estimated, it is possible to estimate the DLR rating of the ACSR conductor based on a thermal transient model. To evaluate the accuracy and the performance of the exposed in this chapter, different case studies have been conducted in the high-current laboratory based on ACSR conductors by controlling and measuring the solar radiation, ambient temperature, line temperature and current. The experimental results exposed in the paper [58] prove that the real-time method presented in this article is able to estimate both the local wind speed and the DLR rating accurately and with low computational cost, so that the estimations can be performed in low-capacity microcontrollers used in low-cost devices that are needed for global deployment of smart grids. Thus, the findings made in this article prove the feasibility of the extension of the *Smartconnector* for the determination of the maximum current capacity of power transmission lines.

The ac resistance determines Joule and core losses, so it is a main parameter to determine the DLR. Therefore, the article [6] proposed two approaches to determine the ac resistance of ACSR conductors. The first and more accurate method is based on the simultaneous measurements of the voltage drop per certain length of the conductor, the current, the phase shift between the voltage drop and the current, as well as the conductor temperature. Several case studies have been conducted for single-, two- and three-layer conductors. Experimental results show that for two-layer and three-layer conductors, the ac resistance is almost independent of the electrical current flowing through the conductors, whereas, for single-layer conductors, the variation of the current level has a great impact on the value of the ac resistance. Based on these experimental observations, the second method was proposed, and it avoids measuring the voltage drop and the phase shift, thus simplifying installation and measurement requirements, although it requires prior laboratory experiments to determine the required parameters $R_{ac,0}$ and α_{ac}.

The methodology exposed in this chapter is useful as it presents a practical way to improve the capacity of overhead lines, thus enhancing the reliability of power transmission systems. The proposed DLR method allows power lines to perform at their peak by adjusting the ratings of power lines based on the weather conditions in real time, making it a smart solution for future smart grids.

5. Compendium of publications

5.1 Energy Balance of Wireless Sensor Nodes Based on Bluetooth Low Energy and Thermoelectric Energy Harvesting

Reference:

Liu, Y.; Riba, J.-R.; Moreno-Eguilaz, M. Energy Balance of Wireless Sensor Nodes Based on Bluetooth Low Energy and Thermoelectric Energy Harvesting. Sensors 2023, 23, 1480. Under a CC BY 4.0 license. https://doi.org/10.3390/s23031480.

Publication framework:

This article shows that using conventional instrumentation, it is feasible to measure the energy consumed in the different phases of a communication cycle of a substation IoT device. It proposed a detailed energy balance of the battery during charge and discharge cycles, as well as communication modes, from which the maximum allowable data transfer rate is calculated. The methodology presented herein can be applied to many other smart grid applications.

Main contributions:

- **Development of conventional instrumentation method to measure the energy involved in different modes of communication cycles of a low-cost IoT device.**
- **Application of thermal energy harvesting system for very low-temperature gradients application.**
- **Development of a detailed energy balance strategy to determine the maximum data transfer rate.**

Key words:

energy harvesting; thermoelectric generator; high voltage; substation connector; battery efficiency; power consumption

sensors

MDPI

Article

Energy Balance of Wireless Sensor Nodes Based on Bluetooth Low Energy and Thermoelectric Energy Harvesting

Yuming Liu [1,2], Jordi-Roger Riba [1,*] and Manuel Moreno-Eguilaz [1]

[1] Electrical and Electronics Engineering Departments, Universitat Politècnica de Catalunya, Rambla Sant Nebridi 22, 08222 Terrassa, Spain
[2] SBI Connectors, Sant Esteve Sesrovires, Albert Einstein, 5, 08635 Sant Esteve Sesrovires, Spain
* Correspondence: jordi.riba-ruiz@upc.edu; Tel.: +34-937-398-365

Abstract: The internet of things (IoT) makes it possible to measure physical variables and acquire data in places that were impossible a few years ago, such as transmission lines and electrical substations. Monitoring and fault diagnosis strategies can then be applied. A battery or an energy harvesting system charging a rechargeable battery typically powers IoT devices. The energy harvesting unit and rechargeable battery supply the sensors and wireless communications modules. Therefore, the energy harvesting unit must be correctly sized to optimize the availability and reliability of IoT devices. This paper applies a power balance of the entire IoT device, including the energy harvesting module that includes two thermoelectric generators and a DC–DC converter, the battery, and the sensors and communication modules. Due to the small currents typical of the different communication phases and their fast-switching nature, it is not trivial to measure the energy in each phase, requiring very specific instrumentation. This work shows that using conventional instrumentation it is possible to measure the energy involved in the different modes of communication. A detailed energy balance of the battery is also carried out during charge and discharge cycles, as well as communication modes, from which the maximum allowable data transfer rate is determined. The approach presented here can be generalized to many other smart grid IoT devices.

Keywords: energy harvesting; thermoelectric generator; high voltage; substation connector; battery efficiency; power consumption

Citation: Liu, Y.; Riba, J.-R.; Moreno-Eguilaz, M. Energy Balance of Wireless Sensor Nodes Based on Bluetooth Low Energy and Thermoelectric Energy Harvesting. *Sensors* **2023**, *23*, 1480. https://doi.org/10.3390/s23031480

Academic Editor: Lorenzo Vangelista

Received: 23 December 2022
Revised: 14 January 2023
Accepted: 27 January 2023
Published: 28 January 2023

1. Introduction

Wireless sensor nodes (WSNs) enable connecting things to the internet through a gateway interfacing the internet and the WSNs. WSNs allow collecting sensed data and send this information to the gateway using a one-way or two-way communication protocol [1]. Internet of things (IoT) devices allow the monitoring of different physical objects [2,3] while enabling real-time health condition approaches to be applied. It is known that electrical connections are among the critical points in power systems, often being placed in remote or inaccessible locations, so they deserve special attention [4]. It is interesting to provide the connections with the ability to measure fundamental physical variables, as well as to communicate, in order to determine their state of health and remaining useful life (RUL) [5,6]. With the development of IoT technology, today this goal is within reach. Devices designed for this purpose must include an energy harvesting unit, specific sensors, and a communication module to acquire the key physical variables and send this information wirelessly to the cloud to be analyzed in real time to apply predictive maintenance approaches [7]. The required energy and communication capabilities are critical factors, which are highly influenced by factors such as data transfer rate and distances to be covered [8]. In any case, the energy harvesting unit plays a key role. The energy harvesting unit converts the energy from the environment into electrical energy [9], being the unit in charge of supplying the required energy to the IoT system at the right time. Energy

harvesters also enable prolonging the life of battery-powered WSNs, as they allow the battery to be recharged [10] and minimize maintenance costs [11].

Transmission systems are a fundamental part of today's electrical grid. To ensure stable and reliable power grid operation, key parameters of transmission systems need to be measured, monitored, and analyzed in real time. They can operate in both direct and alternating current power systems. WSNs have a key role in meeting this need, since they are the devices in charge of measuring basic data and sending this information to the gateway. Based on the analysis of this information, predictive maintenance approaches can be applied to optimize the reliability, availability, and stability of the electrical grid. This strategy also makes it possible to minimize human intervention in the data acquisition process, which is especially important in remote and difficult-to-access areas [4], where human intervention can be very expensive and even unsafe. Therefore, self-powered WSNs can be very useful for monitoring transmission systems [12].

This paper performs an energy balance of the *SmartConnector*, an IoT device that includes a thermoelectric energy harvesting system, an energy storage unit, and different electronic sensors (current, voltage drop and temperature) to estimate the electrical contact resistance of the connector, a microprocessor, and a communications module. There is a shortage of works that perform an energy balance of the full system, so this work contributes to this area. The *SmartConnector* is a challenging project because these electronic modules must be added to aluminum substation connectors, which operate outdoors at voltage levels up to 550 kV. The *SmartConnector* can measure in situ and in real-time different parameters of the high-voltage substation connector, which can be used to determine the state of health or the remaining useful life. The data are transmitted wirelessly to a nearby gateway, which sends the data to the cloud for further visualization and analysis.

Figure 1 schematizes the main modules of an IoT-WSN for substation connectors, here called *SmartConnector*. Due to the limited amount that the energy harvesting unit can generate, WSs usually operate in an intermittent on-off pattern [4,13], so communication protocols typically have different phases. The energy harvesting unit analyzed in this paper is based on a solid-state thermoelectric generator (TEG), which transforms a temperature difference into useful electrical energy.

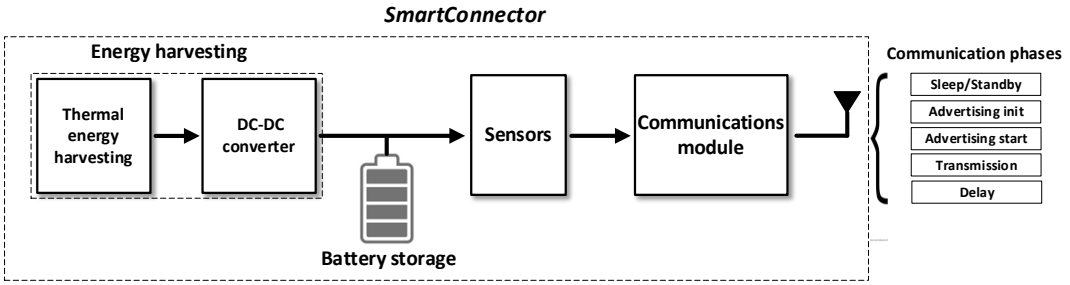

Figure 1. Diagram of the wireless *SmartConnector* device.

This paper applies an energy balance of the entire *SmartConnector* device, including the energy harvesting module, DC–DC converter, battery and sensors, and communication modules. Due to the small currents that intervene in the different phases of the communications and the fast-switching pulses that characterize these currents, special care must be taken when measuring the energy in each phase. Therefore, very specific and expensive instrumentation is required. This paper shows that using conventional instrumentation it is also possible to measure the energy involved in each phase of the communications. Since the *SmartConnector* is installed on large tubular aluminum busbars, there is a small temperature gradient between the ambient and the busbar. This work also focuses on a challenging problem, the thermoelectric energy harvesting under very low temperature gradients, which has been poorly studied in the technical literature. Due to these

unfavorable conditions, thermoelectric generators produce a very low voltage, which requires a suitable DC–DC converter. In addition, a detailed energy balance of the thermoelectric energy harvesting unit and the battery is also carried out during the charge and discharge cycles, as well as during the communication phases, this being a novelty of this work. The energy balance allows determining the maximum data transfer rate (DTR_{max}), that is, the maximum communication cycles per hour the *SmartConnector* can do without draining the batteries. Although the results presented in this paper have been applied to a particular IoT device, the *SmartConnector*, the approach presented here can be generalized to many other smart grid IoT devices incorporating energy harvesting units, such as triboelectric or piezoelectric nanogenerators. These results could potentially contribute to improve the energy management and lifetime of WSNs.

2. System Efficiency

This section describes the system to determine the efficiency of the entire system comprising the energy harvesting system (TEGs + DC–DC converter), the battery, and the sensors and communication modules.

2.1. Energy Harvesting Efficiency

A thermoelectric generator (TEG) is used to capture energy from the thermal gradient existing between a substation busbar and the environment. Substation busbars, usually hollow cylindrical aluminum tubes, are common connection nodes for multiple incoming and outgoing circuits. Due to the low temperature gradient between the busbar and the environment, special care must be taken to select the most appropriate TEG. This unfavorable condition forces the TEG to generate a very low voltage, some fractions of a volt, requiring a suitable DC–DC converter to charge the battery and supply the sensors and the communications module. Therefore, the energy harvesting system consists of a TEG module and a DC–DC converter with a very low input voltage range.

The specific efficiencies of the TEG, η_{TEG}, and of the DC–DC converter, $\eta_{DC/DC}$, must be calculated to determine the efficiency of the entire energy harvesting system (TEG + DC–DC converter), $\eta_{TEG+DC/DC}$.

The steady state heat transfer equation in a busbar can be expressed as [14],

$$I_{RMS}^2 r_{ac}(T) - p_c - p_r = 0 \ \text{[W/m]} \tag{1}$$

I_{RMS} [A] being the electric current flowing in the busbar, $r_{ac}(T)$ [Ω/m] the per unit length ac resistance of the busbar at the operating temperature T [°C], and p_c [W/m] and p_r [W/m] being the cooling terms due to natural convection and radiation, respectively.

The resistance term r_{ac} [Ω/m] can be measured as [5,15]

$$r_{ac}(T) = \frac{\Delta V_{1m}}{I} \cos\varphi \quad [\Omega/\text{m}] \tag{2}$$

where ΔV_{1m} [V] is the voltage drop measured between two points of the busbar separated by 1 m, I [A] is the ac current flowing through the busbar, φ [rad] is the phase shift between the voltage drop and the current, and T [°C] is the temperature of the busbar.

The efficiency of the TEG is calculated as

$$\eta_{TEG} = \frac{P_{out,TEG}}{P_{inp,TEG}} = \frac{P_{electric,TEG}}{P_{Joule,TEG-area}} \tag{3}$$

where $P_{electric,TEG}$ [W] is the electric power generated by the TEG, and $P_{Joule,TEG\text{-}area}$ [W] is the Joule heat generated by the busbar in the area of the TEG (80 mm × 40 mm), which can be calculated as

$$P_{Joule,TEG-area} = P_{Joule,conductor} \frac{A_{TEG}}{A_{Conductor}} \quad [\text{W}] \tag{4}$$

where A_{TEG} [m²] and $A_{Conductor}$ [m²] are, respectively, the area of the outer surfaces of the TEG and conductor, and $P_{Joule,conductor}$ [W] is the power loss in the busbar due to the Joule effect.

Finally, the energy efficiency of the DC–DC converter is calculated as the ratio between the output and input electrical powers as

$$\eta_{DC-DC} = \frac{P_{out\_DC-DC}}{P_{inp\_DC-DC}} = \frac{V_{out} I_{out}}{V_{inp} I_{inp}} \quad [-] \tag{5}$$

V_{out}, I_{out}, V_{inp}, and I_{inp} being the output and input voltages and currents of the DC–DC converter.

2.2. Battery Efficiency

Today, rechargeable batteries play a leading role in energy management for IoT applications. Various methods have been proposed to estimate battery lifetime and the state of health, which can be based on fast impedance measurements [16], or on health indicators based on the internal resistance because it is greatly impacted by ageing [17], or on the capacity level [18] among others.

It is known that, as a result of energy loss in battery operation, additional energy is required, so battery energy efficiency is a relevant factor of battery economy. Battery energy efficiency characterizes the utilization rate during energy conversion from chemical energy to electrical energy [19]. In order to minimize the energy losses in the batteries and to evaluate the energy efficiency of the entire thermal energy harvesting system, this paper analyzes the efficiency of the batteries under a very low current rate, since the analyzed application is characterized by very low current rates.

In [20] it is concluded that for nickel metal hydride (Ni-MH) batteries, full charge cannot be reached without overcharging due to side reactions. Ni-MH batteries are applied in many crucial applications such as wearable electronic devices and hybrid vehicles due to the high cycle life and robustness [10,21]. This paper analyzes a pack of two series connected Ni-MH batteries. It is important to determine the energy loss in the batteries and the input and output energies in the batteries during the charge and discharge cycles to characterize their efficiency and energy behavior.

Since the IoT device analyzed in this paper has a very low power consumption, battery efficiencies under low current rates are studied. These efficiencies have three components, that is, charge efficiency η_{charge}, discharge efficiency $\eta_{discharge}$, and overall efficiency $\eta_{Battery}$.

The energy efficiency under charging conditions [20] is the ratio between the chemical energy gained by the battery during the charge cycle $\Delta E_{Battery\ input}$ [J] and the energy extracted from the power source $\Delta E_{Power\ source}$ [J].

$$\eta_{Charge} = \frac{\Delta E_{Battery\ input}}{\Delta E_{Power\ source}} = \frac{\Delta E_{Battery\ input}}{\Delta E_{Battery\ input} + \Delta E_{Charging\ loss}} \tag{6}$$

where $\Delta E_{Charging\ loss}$ [J] is the energy loss in the battery during the charging cycles due to Joule heating and electrochemical reaction processes [20,22]. $\Delta E_{Battery\ input}$ is the chemical energy stored in the battery, i.e., the net energy. The recharged energy and the net energy are not the same because the recharged electric energy cannot be completely transformed into chemical energy [19].

The energy extracted from the power source, $\Delta E_{Power\ source}$ [J], can be determined as [19]:

$$\Delta E_{Power\ source} = \int_{t_0}^{t} V_{Charge} I_{Charge} dt = \int_{SoC(t_0)}^{SoC(t)} V_{Charge} C_n dSoC \quad [J] \tag{7}$$

The net energy gained by the battery during the charge cycle, $\Delta E_{Battery\ input}$, can be expressed as [19]

$$\Delta E_{Batttery\ input} = \int_{SoC(0)}^{SoC(t)} V_{OCV}(SoC) C_n dSoC \quad [J] \tag{8}$$

where $SoC(t_0)$ [-] is the initial state of charge, $SoC(t)$ [-] is the final state of charge, V_{Charge} [V], and I_{Charge} [A] are the battery voltage and current during the charge process, respectively, V_{OCV} [V] is the open circuit voltage, and C_n [Ah] is the rated capacity of the battery.

The state of charge (SoC) of the battery can be calculated as [19]:

$$SoC(t) = SoC(t_0) + \frac{1}{C_n}\int_{t_0}^{t} I_{charge} dt \quad \text{or} \quad SoC(t) = SoC(t_0) - \frac{1}{C_n}\int_{t_0}^{t} I_{discharge} dt \tag{9}$$

The rated capacity C_n [Ah] of the battery plays a major role in calculating the net energy ΔE_{net} and in determining the SoC. The method for determining C_n is described in Section 4.2.

The energy efficiency under discharge conditions [20] is the ratio between the energy extracted from the battery during the discharge ΔE_{Load} [J] and the net energy of the battery $\Delta E_{Battery\ output}$ [J], which can be expressed as

$$\eta_{Discharge} = \frac{\Delta E_{Load}}{\Delta E_{Battery\ output}} = \frac{\Delta E_{Battery\ output} - \Delta E_{Discharging\ loss}}{\Delta E_{Battery\ output}} \tag{10}$$

where $\Delta E_{Discharging\ loss}$ [J] is the energy loss in the battery during the discharging cycles.

The energy extracted from the battery during the discharge, $\Delta E_{Load,}$ can be determined as

$$\Delta E_{Load} = \int_{t_0}^{t} V_{Discharge} I_{Discharge} dt = \int_{SoC(t_0)}^{SoC(t)} V_{Discharge} C_n dSoC \quad [J] \tag{11}$$

where $V_{Discharge}$ [V] is the battery voltage during the discharge process.

Finally, the overall energy efficiency of the charge and discharge cycle [20] is determined as the ratio between $\Delta E_{Power\ source}$ and ΔE_{Load},

$$\eta_{Battery} = \frac{\Delta E_{Load}}{\Delta E_{Power\ source}} \tag{12}$$

2.3. Proposed Method to Determine the Energy Balance of the Battery

The efficiencies in (6)–(12) are generally determined for constant charge and discharge rates. However, in practical applications, the charge and discharge rates are not constant. To determine the maximum data transfer per hour (DTR_{max}), that is, the number of communication cycles that the IoT device can perform each hour without draining the battery, the energy input and output of the battery must be measured in a real situation. In this case, the energy harvesting unit supplies the load (sensors and communication modules) through the battery, so it must be accomplished

$$E_{Battery\ input} = E_{out\_DC-DC}\eta_{Charge} \quad [J] \tag{13}$$

where E_{out_DC-DC} is the electrical energy at the output of the DC–DC converter, the power source in this case, and η_{Charge} is given by (6).

The output power delivered by the battery can be calculated as

$$E_{Battery\ output} = \frac{E_{Load}}{\eta_{Discharge}} \quad [J] \tag{14}$$

where E_{Load} is the energy consumed by the IoT device (sensors and communication modules), the load of the analyzed circuit, and $\eta_{Discharge}$ is given by (10).

Finally, the energy balance is reached when the energy harvested is equal to the energy consumed by the load

$$E_{Battery\ input} = E_{Battery\ output} \quad (15)$$

Applying the energy balance to the battery for 1 h results in:

$$E_{Battery\ input,1\ h} = E_{Battery\ output,1\ h} = \frac{E_{Load,1\ h}}{\eta_{Discharge}} = \frac{\mathrm{DTR}_{\max}(E_{Load,1\ communication\ cycle} + E_{sleep})}{\eta_{Discharge}} \quad (16)$$

Finally, the maximum data transfer rate DTR_{max} is obtained as

$$\mathrm{DTR}_{\max} = \frac{E_{Battery\ input,1\ h}}{E_{Load,1\ communication\ cycle} + E_{sleep}} \eta_{Discharge} = \frac{E_{out\_DC-DC,1\ h}}{E_{Load,1\ communication\ cycle} + E_{sleep}} \eta_{Charge}\eta_{Discharge} \quad (17)$$

where $E_{Load,1\ communication\ cycle}$ and E_{sleep} are shown in Figure 2.

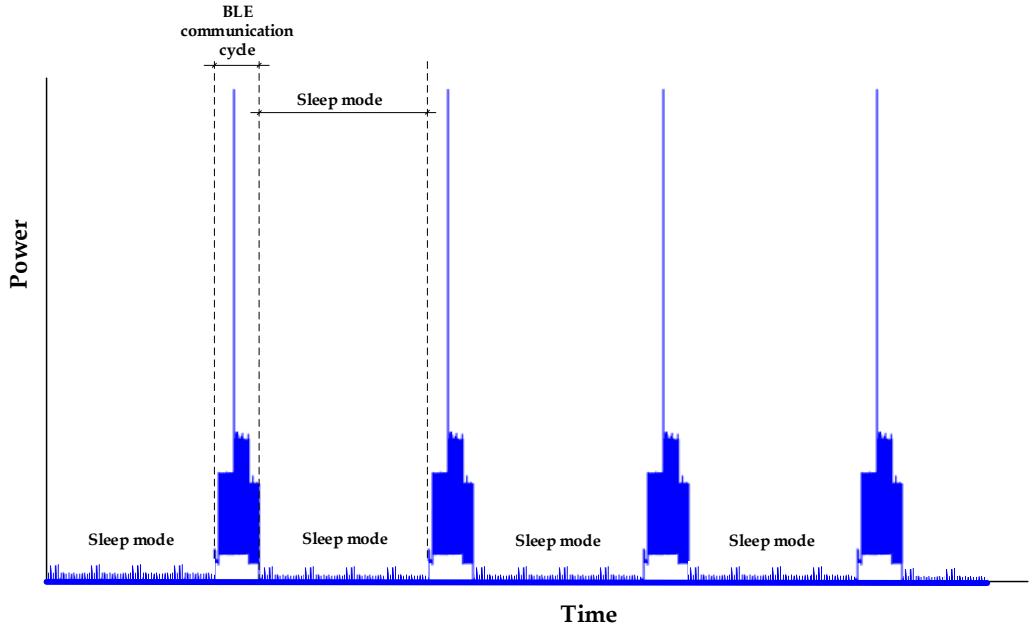

Figure 2. Power consumed by the IoT device (*SmartConnector*) during multiple BLE communication cycles separated by sleep mode periods.

3. Experimental Setup

This section describes the experimental setup required to determine the energy efficiency of the entire IoT device and to determine the DTR_{max}.

3.1. Energy Harvesting System

As explained, in the analyzed application, there is a small temperature gradient between the busbar and the environment, so the selection of the most appropriate TEG is critical. Due to the low temperature difference, the TEG generates a very low voltage of a few fractions of a volt, thus requiring a DC–DC converter with a very low input voltage range.

The GM250-157-14-16 TEG from European Thermodynamics (Kibworth, Leicestershire, United Kingdom) was selected due to its ability to handle small temperature gradients. The dimensions of this TEG are 40 mm × 40 mm × 4.1 mm.

The selected DC–DC converter is the LTC3108 from Analog Devices (Wilmington, Massachusetts, USA), which is linked to an ADEH harvesting board based on maximum power point tracking (MPPT) technology and a high efficiency boost converter with an input voltage range of 50–400 mV and an output voltage output range of 2.35–5.0 V.

Figure 3 shows the experimental setup used to test the energy harvesting test, which is composed of a conductor loop. This loop was exposed to heating and cooling cycles.

The low impedance loop consists of a stainless-steel tubular busbar with an inner diameter of 120 mm and a wall thickness of 0.4 mm, connected to the output of a high current transformer. The energy harvesting unit includes two TEGs (thermoelectric generators) connected in series and a DC–DC converter. A Ni-MH battery pack composed of two cells in series was also used for power management purposes. In order to test the energy harvesting system in a realistic situation, the TEGs and the DC–DC converter were installed on the top of the tubular busbar, which was exposed to the heat cycle tests, as shown in Figure 3.

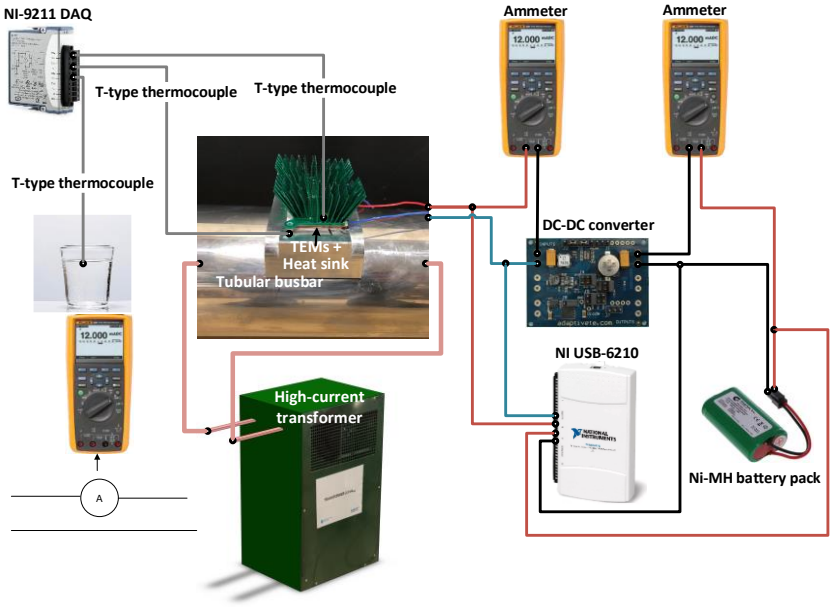

Figure 3. Experimental setup to test the behavior of the energy harvesting system mounted on a tubular busbar.

Regarding the measurement systems, two Fluke 289 data logger multimeters (Fluke, Everett, Washington, DC, USA) were used in ammeter mode to measure the output currents of the TEGs and the DC–DC converter. Simultaneously, a NI USB-6210 data acquisition system (National Instruments, Austin, TX, USA) was used to acquire the output terminal voltages of the TEGs and DC–DC converter. Three T-type thermocouples together with a NI-9211 temperature measurement system (National Instruments, Austin, TX, USA) were used to measure the environment temperature and the temperatures of the hot and cold sides of the TEGs. A Python code programmed by the authors of this work was used to synchronize all measurement systems.

3.2. Energy Storage

Rechargeable Ni-MH batteries are widely used in consumer electronics, such as digital cameras or portable electronic devices [23]. Therefore, we proposed to use a Ni-MH pack of two rechargeable battery cells to store the energy generated by the energy harvesting system (TEG + DC–DC converter) for the IoT device (BM2000C1450AA2S1PATP, GlobTek, Northvale, New Jersey, USA). Table 1 shows the main characteristics of the battery pack analyzed in this work.

Table 1. Main characteristics of the analyzed battery pack of two cells from GlobTek.

Parameters	Values
Rated capacity, C_n	2000 mAh
Nominal voltage	2.4 V (1.2 V per cell)
Cut-off voltage	2.0 V (1.0 V per cell)
Standard charge current	200 mA (0.1 C), 16 h
Trickle charge current *	60 mA–100 mA (0.03 C–0.05 C)
Rapid charge current	1 A (0.5 C)
Internal impedance	<30 mΩ (upon fully charged)

* Trickle charging means charging a fully charged battery cell at a rate equal to its self-discharge rate, enabling the battery to keep fully charged.

As shown in Table 1, the two series connected rechargeable Ni-MH batteries used in this application generate around 2.4 V. Ni-MH batteries were selected because this voltage level is directly compatible with that required by the electronic sensors and the microcontroller that includes an inbuilt BLE module (see Section 3.3), which is between 1.8 V and 3.0 V.

The electronics incorporated in the *SmartConnector* IoT device consume very little power, in the milliwatt range [4]. Therefore, to analyze the behavior of the Ni-MH battery used in this IoT application, the charge and discharge profiles of the batteries analyzed in this paper require very low C rates, the unit to measure the speed at which a battery charges or discharges. For example, a charge cycle at a C rate of n^{-1} C means that the battery is charged from 0% to 100% in n hours.

Figure 4 shows the experimental setup implemented in this work to analyze the behavior of the rechargeable battery pack. The charge and discharge experiments were performed using a bidirectional regenerative power system (IT-M3632, 800 W, 60 V, 30 A, ITECH, New Taipei City, Taiwan) connected to the two terminals of the battery pack. This instrument measures and records voltage and current with an accuracy of ±0.1% and 0.1% + 0.1% FS, respectively. Simultaneously, a battery tester (IT-5101, ITECH, New Taipei City, Taiwan) was used to measure the voltage and internal impedance of the battery with an accuracy of ±(0.01% + 0.01% FS) and ±(0.4% + 0.05% FS), respectively. The measurements of the voltage and impedance of the battery from the tester were synchronized with a computer using a Python code programmed by the authors of this work.

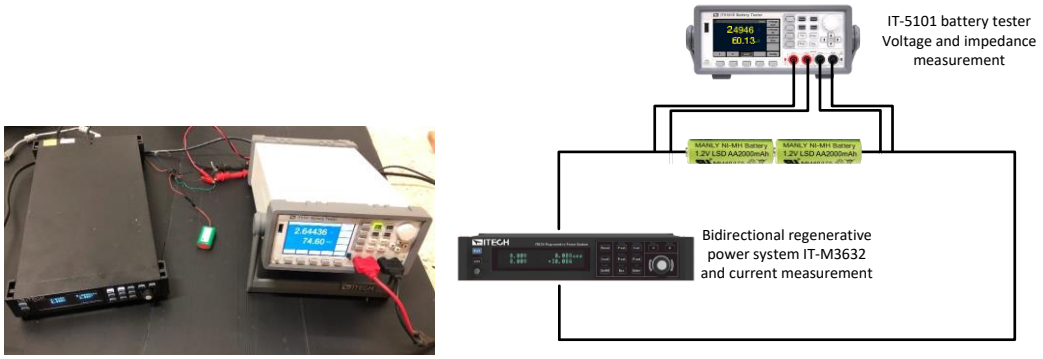

Figure 4. Experimental setup used for battery charge–discharge cycle tests.

3.3. IoT Device

The IoT device analyzed in this work consists of the energy harvesting system described in Section 3.1, the energy storage unit described in Section 3.2, three sensors, temperature (Pt-1000 sensor, PTFC102T1G0, TE Connectivity, Schaffhausen, Switzerland), voltage drop (AD627 instrumentation amplifier from Analog Devices, Wilmington, MA, USA), and current (DVR5053VA Hall effect sensor, Texas Instruments, Dallas, Texas,

USA), as well as a Bluetooth low energy (BLE) communications module (nRF52832 microcontroller from Nordic Semiconductors mounted on Sparkfun breakout board that includes an inbuilt BLE module).

This section presents two systems to measure the very low energy consumption of the analyzed IoT device. Since this device communicates cyclically with a gateway, the energy consumption has a cyclic profile consisting of five modes, advertising parameter initialization, advertising start, transmission, delay, and sleep, as shown in Figure 5.

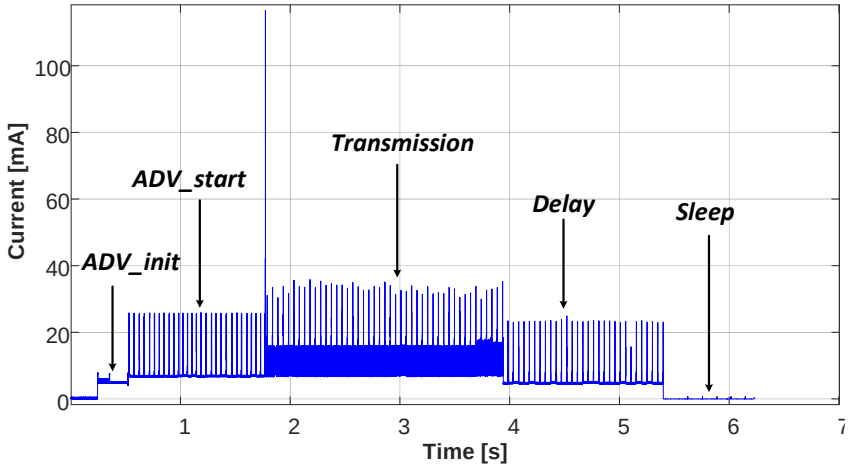

Figure 5. Experimental current versus time profile of the communications cycle.

The *SmartConnector* was programmed to enter low power mode during the sleep phase, drawing a few microamps [4]. However, it is very difficult and expensive to acquire current probes for oscilloscopes compatible with this range, being a challenging task to determine the energy consumption of the IoT device. A lab-design data acquisition system was designed for this purpose and assembled, as shown in Figure 6a. It consists of a precision current sense resistor (SR10, 0.02 Ω, ±1%, 1W, Caddock Electronics, Roseburg, OR, USA) and two instrumentation amplifiers (AD620, Analog Devices, Wilmington, MA, USA) connected in cascade that were used to amplify the output voltage. Simultaneously, a wired DAQ module (NI USB-6210, National Instruments, Austin, TX, USA) was connected to the output terminals of the amplifiers and to the power supply to measure both voltages.

To evaluate the accuracy of the measurements made with the lab-design system, a current waveform analyzer (CX3324A, 1 GSa/s, 14/16-bit, 4 Channels, Keysight Technologies, CA, USA) with two current probes (CX1102A Dual Channel, ±12 V, 100 MHz, 40 nA–1 A, Keysight Technologies, Santa Rosa, CA, USA) and one passive voltage probe (N2843A, Keysight Technologies, Santa Rosa, CA, USA) was also used to measure the energy consumed by the *SmartConnector*, which is shown in Figure 6b.

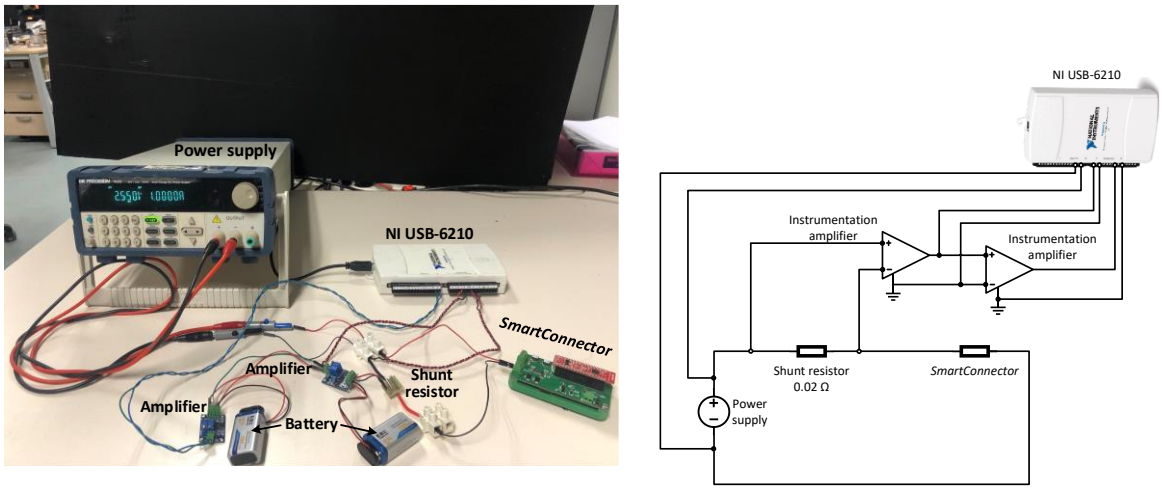

(**a**)

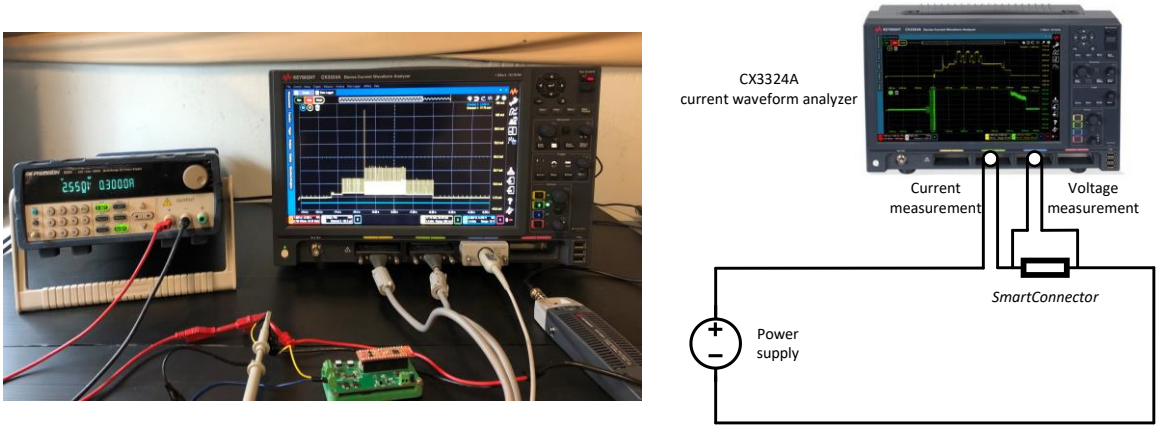

(**b**)

Figure 6. Experimental setup to determine the energy consumption of the IoT device. (**a**) Lab-design system. (**b**) CX3324A current waveform analyzer.

Finally, the energy consumed by the IoT device in one communication cycle, $E_{Load,\ 1\ communication\ cycle,}$ can be calculated as

$$E_{Load,\ 1\ communication\ cycle} = \int_{t=0}^{t=T} V(t)I(t)dt \quad [\mathrm{J}] \tag{18}$$

where $V(t)$ and $I(t)$ are, respectively, the instantaneous value of the voltage and current measured by the lab-design or CX3324A waveform analyzer, and T is the duration of the communication cycle.

4. Experimental Results

4.1. Energy Harvesting System

This section shows the results of the experimental tests carried out indoors at an ambient temperature of 20 °C to determine the energy generated by the energy harvesting system under different operating conditions.

As already explained, the energy harvesting system is installed on top of a tubular busbar. It consists of two TEGs connected in series, which are connected to a DC–DC converter. The busbar was heated until reaching the steady state temperature by applying currents of different intensities, whose values are summarized in Table 2. After reaching the steady state temperature, the system was cooled to room temperature by natural convection. Therefore, different heating tests were carried out. The powers and efficiencies of the different heat cycle tests summarized in Table 2 are based on Equations (1)–(5). It is noted

that $\Delta T_{Hot\text{-}Ambient}$ is the temperature gradient between the hot side of the TEG and the ambient, while $\Delta T_{Hot\text{-}Cold}$ is the temperature gradient between the hot and cold sides of the TEG.

Table 2. Power and efficiency of the TEGs and DC–DC converter when the busbar reaches the steady state temperature.

Current (A_{rms})	$\Delta T_{Hot\text{-}Ambient}$ (°C)	$\Delta T_{Hot\text{-}Cold}$ (°C)	$p_{Joule,conductor}$ (W/m)	$P_{Joule,TEG\text{-}area}$ (W)	$P_{electric,TEG}$ (mW)	$P_{out\_DC\text{–}DC}$ (mW)	η_{TEG} (%)	$\eta_{DC\text{–}DC}$ (%)	$\eta_{TEG+DC/DC}$ (%)
136	20.7	3.35	99.5	0.845	1.24	0.21	0.15	17.0	0.025
169	26.1	3.85	155.6	1.321	2.50	0.34	0.19	13.6	0.026
194	31.7	4.46	207.5	1.76	4.47	0.48	0.25	10.7	0.027
226	37.7	5.05	284.0	2.41	7.34	0.66	0.30	9.0	0.027
254	43.7	5.67	362.7	3.08	11.2	0.84	0.36	7.5	0.027

4.2. Battery Efficiency

4.2.1. Experimental Determination of C_n and V_{OCV}

To determine the efficiency of the battery (charge, discharge and charge-discharge cycles), the rated capacity C_n and the open circuit voltage V_{OCV} are required, as described in Equations (6)–(12). The following paragraphs explain how they were determined from experimental tests.

According to the IEC 61434 standard [24], the reference current of the test is $I_t = C_n/(1\ h)$ [A], and all charge and discharge currents must be expressed as fractions or multiples of I_t. The pack of two rechargeable Ni-MH cells has a rated capacity C_n = 2 Ah (see Table 1), so I_t = 2 A. The end-of-charge voltage per cell was set to 1.75 V, while the end-of-discharge voltage (cut-off voltage) per cell was set to 1.0 V (see Table 1).

The rated capacity C_n [Ah] of the battery pack was calculated according to the procedure described in the IEC 61982 standard [25]. First, the cells were discharged at 25 °C ± 2 °C at a constant current of $0.333I_t$ (corresponding to 0.67 A) down to 2 V, the end-of-discharge voltage of the two cells specified by the manufacturer. After 1 h of rest, the cells were charged at a constant rate of $0.1I_t$ (corresponding to 0.20 A) for 16 h at 25 °C ± 2 °C. After another 1 h rest, the batteries were discharged at a constant rate of $0.333It$ (corresponding to 0.67 A) down to 2 V, the end-of-discharge voltage of the two cells. The rated discharge capacity was found to be C_n = 1.75 Ah, as shown in Figure 7.

As shown in Figure 7, the two cells were discharged at a constant rate of $0.333I_t$, from an initial voltage of around 2.45 V down to 2.0 V. They were then rested for 1 h, and then charged at a constant current rate of $0.1I_t$ for 16 h (the charging time specified by the manufacturer, as shown in Table 1) to around 3 V. After another rest of 1 h, the rated discharged capacity C_n was obtained by discharging the cells at a constant rate of $0.333It$ to reach the end-of-discharge voltage (2 V).

$$C_n = \int_{t=0}^{t_{EoD}} 0.333 I_t dt \ = 1.75 \ [\text{Ah}] \tag{19}$$

where t_{EoD} is the time required to reach the cut-off or end-of-discharge voltage.

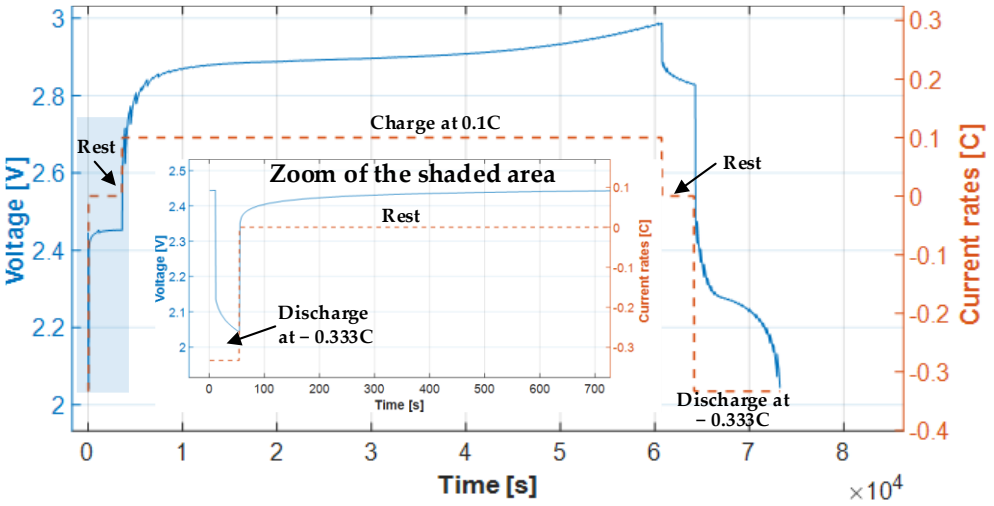

Figure 7. Determination of the rated discharge capacity C_n when the two batteries were discharged at a rate of $0.333I_t$ = 0.67 A from 3 V to 2 V (end-of-discharge voltage).

It is observed that the obtained value of the rated discharge capacity C_n = 1.75 Ah corresponds to 87.5% of the maximum capacity specified by the manufacturer, which is 2.0 Ah. This is because C_n is highly dependent on how the Ni-MH battery is charged, so it cannot reach the maximum capacity of 2.0 Ah without overcharging due to side reactions [26,27]. Therefore, this study considers the rated capacity C_n of the cells instead of the maximum capacity.

The open circuit voltage *Vocv* of each cell can be obtained from measurements, averaging the charge and discharge curves obtained at very low charge and discharge rates as a function of the *SoC*. In this way, the effects of hysteresis and ohmic resistance are minimized [19,28]. The method developed by Plett [28] was applied to obtain the *Vocv* shown in Figure 8. First, the cells were fully charged at 0.05 C. They were then discharged to the end-of-discharge voltage (2 V) at a rate of 0.007 C (0.007 C = 0.007 × 2 A = 0.014 A). Once discharged, they were charged at a rate of 0.007 C until fully charged. Next, the *Vocv* curve was obtained by averaging the charge and discharge curves at a rate of 0.007 C, as shown in Figure 8.

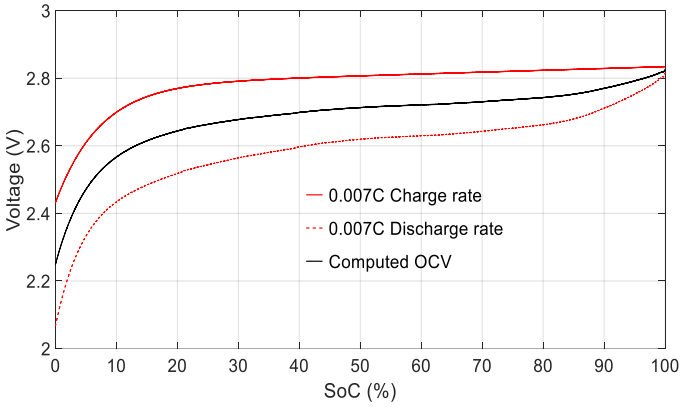

Figure 8. Open circuit voltage *Vocv* versus *SoC* obtained by averaging the terminal battery voltage during an entire charge and discharge cycle at 0.007 C.

The charge and discharge rate was fixed at 0.007 C for two main reasons. First, this discharge rate is similar to the average current consumed by the *SmartConnector*. Second, it is a very low rate, which helps to minimize the influence of hysteresis and Ohmic resistance.

4.2.2. Battery Efficiencies during the Charge, Discharge and Charge-Discharge Cycles

Knowing the rated capacity C_n and the V_{OCV}–SoC curve, it is possible to determine the efficiency of the battery during the charge and discharge cycles, as well as the overall efficiency from (6), (10) and (12), respectively. To acquire the curves shown in Figures 9 and 10, the cells were first fully charged or discharged at a rate of 0.05 C, and then discharged or charged at different *C* rates to obtain the voltage curves as a function of the *SoC*. Figure 9a shows the battery voltage versus *SoC* during the charge cycle, while Figure 9b shows the charge efficiency versus the C rate.

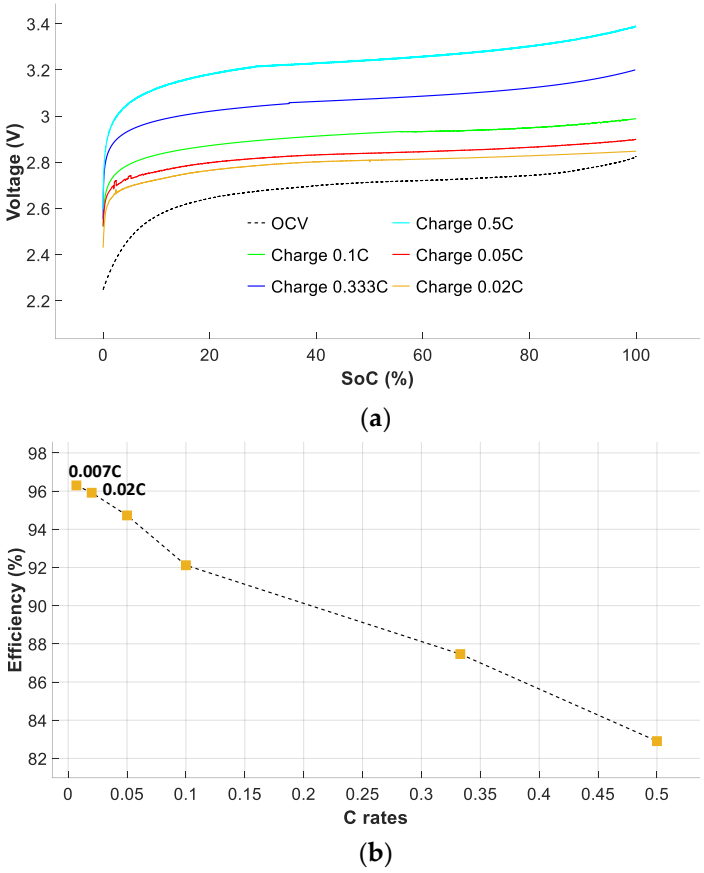

Figure 9. Battery pack performance during the charge cycle. (**a**) Voltage curves as a function of *SoC*. (**b**) Battery charge efficiencies at different current rates.

Figure 9a shows that the terminal voltage behavior of the battery pack is highly dependent on the *SoC* during the charge cycle. At relatively small C rates, such as 0.02 C, 0.05 C, or 0.1 C, the voltage is always below 3 V for *SoC* = 100%. Otherwise, under moderate C rates (0.333 C and 0.5 C), the voltage level rises significantly above 3 V when the cells are fully charged. The charge efficiency η_{Charge} shown in Figure 9b was calculated according to (6).

Figure 10a shows the battery voltage versus *SoC* during the discharge cycle, while Figure 10b shows the discharge efficiency versus the C rate.

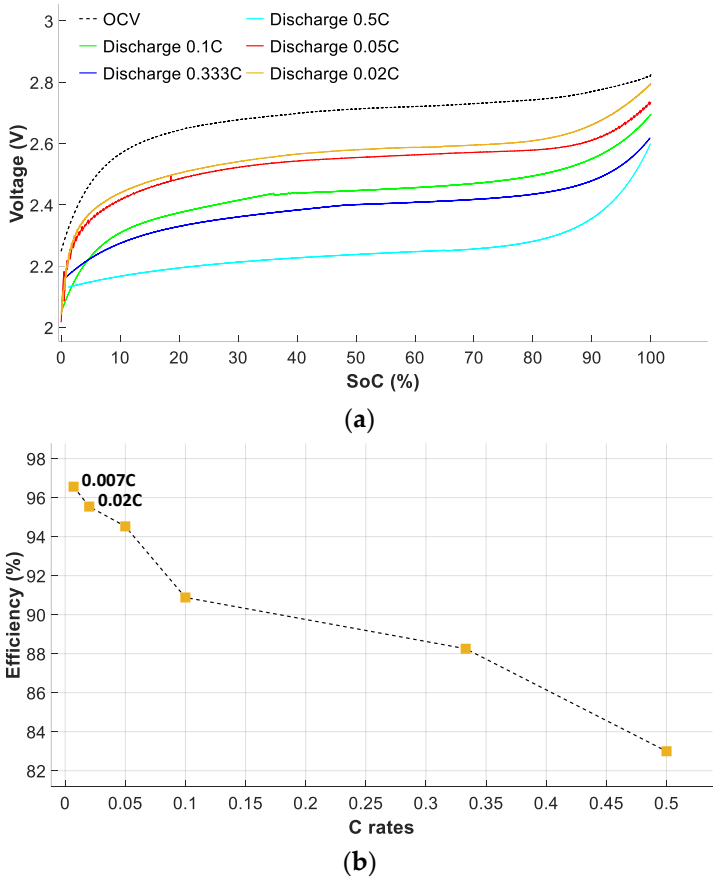

Figure 10. Battery pack performance during the discharge cycle. (**a**) Voltage curves as a function of *SoC*. (**b**) Battery discharge efficiencies at different current rates.

Figure 10a shows that the terminal voltage behavior of the battery pack is highly dependent on the *SoC* during the discharge cycle. According to these results, $\eta_{Discharge}$ obviously decreases at high C rates because the cells cannot fully discharge at higher C rates [19].

Figure 10b shows the discharge efficiency $\eta_{Discharge}$ versus *SoC*. The $\eta_{Discharge}$ characteristic has been calculated according to (19). These results show that $\eta_{Discharge}$ also decreases drastically at higher C rates.

Finally, Figure 11 shows the charge and discharge energy efficiency of the battery pack. It is seen that the overall battery efficiency can be as high as 93% at a rate of 0.007 C, thus decreasing at higher C rates. In this case, the overall efficiency during the charge and discharge cycles has been calculated from (12).

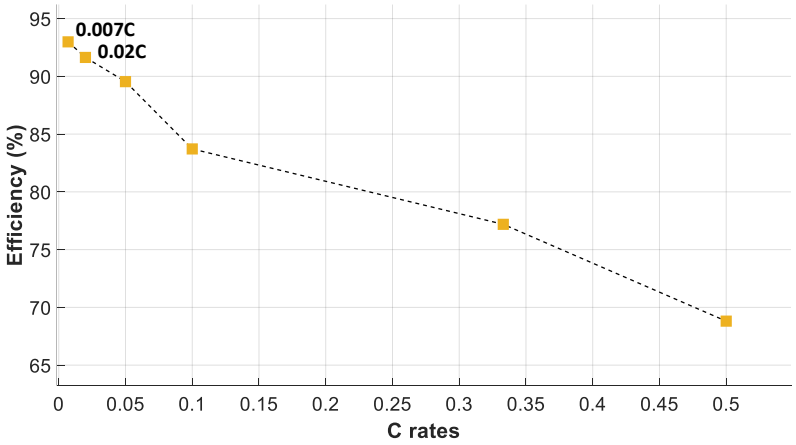

Figure 11. Battery pack efficiency during charge and discharge cycles at different C rates.

The results presented in Figure 11 show that, due to the low level of current generated by the energy harvesting system of the *SmartConnector* and the low current required to supply the sensors and communication modules, the battery will be used efficiently.

4.3. Energy Consumption of the IoT Device (Sensors and Communications Module)

This section measures the power and energy consumed by the *SmartConnector*. To this end, the *Smartconnector* was programmed to send data to a nearby gateway every seven seconds.

Figure 12 shows the current consumed by the *SmartConnector* when supplied with a fixed voltage of 2.55 V. It was measured with the sophisticated CX3324A current waveform analyzer and with the lab-design system.

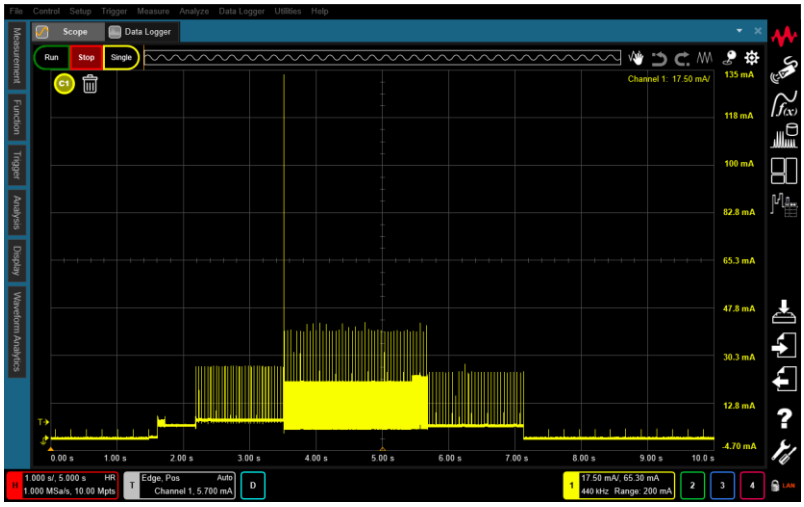

(**a**)

(**b**)

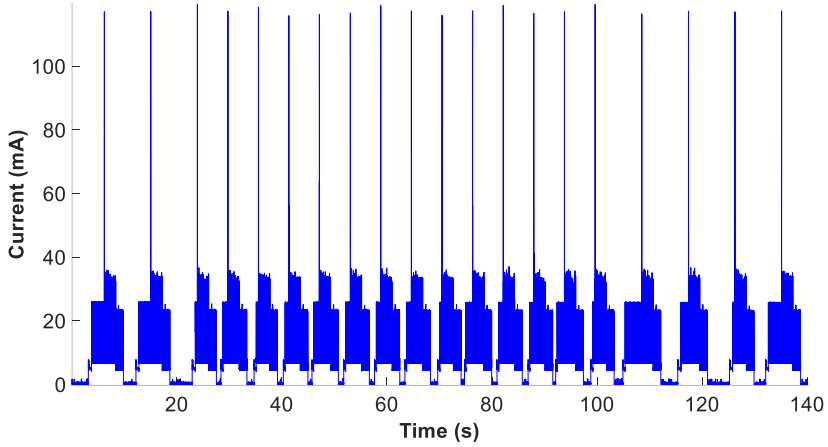

(**c**)

Figure 12. Current consumed by the *SmartConnector*. (**a**) Measured with the CX3324A current waveform analyzer during one entire BLE communication cycle. (**b**) Measured with the CX3324A current waveform analyzer during the sleep mode. (**c**) Measured with the lab-design system during 20 BLE communication and sleep cycles.

Table 3 summarizes the results obtained with the two measuring devices in the different phases of power consumption of the BLE communication cycle. These results show that the differences obtained with the CX3324A current waveform analyzer and the lab-design system are very low in all the consumption modes, always less than 5%, which validates the proposed lab-design system.

Table 3. Current consumption of the IoT device during the different BLE communication modes.

Communication Modes	Supply Voltage [V]	Average Current Measured with the CX3324A Waveform Analyzer [mA]	Average Current Measured with the Lab-Design System [mA]	Difference [%]
Advertising parameters initialization	2.55	5.02	4.97	1.0
Advertising start	2.55	7.44	7.46	0.3
Transmission	2.55	11.42	11.43	0.1
Delay	2.55	4.90	4.89	0.2
Sleep	2.55	0.00510	0.00535	4.9

4.4. Energy Balance of the Entire System

This section calculates the energy balance of the *SmartConnector*, from which the DTR_{max} is obtained by applying (17). For this, the energy outputted by the DC–DC converter in 1 h $E_{out\_DC-DC,1\,h}$, the energy consumed by the IoT device during 1 communication cycle $E_{Load,\,1\,communication\,cycle}$, and the efficiencies of the battery during the charge and discharge cycles, η_{Charge} and $\eta_{Discharge}$, respectively, were determined.

Table 4 summarizes the energy consumption measured with the lab-design system and the CX3324A current waveform analyzer shown in Figure 12 and Table 3. The results presented in Table 4 have been calculated by averaging the energy consumption of 20 BLE communication cycles, resulting in $E_{Load,\,1\,communication\,cycle}$ = 0.110 J for the lab-design system and $E_{Load,\,1\,communication\,cycle}$ = 0.113 J for the high-performance CX3324A current waveform analyzer, the total energy consumption in one communication cycle.

Table 4. Energy consumption of the IoT device in one BLE communication cycle.

Communication Modes	Voltage [V]	Time [s]	Average Current [mA]	Energy Consumption of Each Mode [J]

Lab-design	Advert. param. initialization	2.55	0.41	4.97	0.005
	Advertising start	2.55	1.18	7.46	0.023
	Transmission	2.55	2.17	11.43	0.064
	Delay	2.55	1.45	4.89	0.018
	Total cycle BLE consumption *	2.55	5.21	8.20	0.110
	Sleep	2.55	1.00	$5.35 \cdot \times 10^{-3}$	13.64×10^{-6}
CX3324A	Advert. param. initialization	2.55	0.58	5.02	0.007
	Advertising start	2.55	1.32	7.44	0.025
	Transmission	2.55	2.17	11.42	0.063
	Delay	2.55	1.45	4.90	0.018
	Total cycle BLE consumption *	2.55	5.52	8.10	0.113
	Sleep	2.55	1.00	5.10×10^{-3}	13.01×10^{-6}

* The energy consumed in one BLE communication cycle is the sum of the consumptions in each mode (advertising initialization phase, advertising start phase, transmission phase and delay).

Table 5 shows the data required to determine the DTR_{max} under different operating conditions defined by different temperature gradients between the environment and the busbar. Since the IoT device consumes a few mA (see Table 4), the battery efficiency has been determined at a current rate of 0.007 C, which corresponds to 14 mA. According to the results presented in Figure 11, the charge and discharge energy efficiency of the battery pack is $\eta_{Charge}\eta_{Discharge} = 0.93$ at a rate of 0.007 C. The maximum data transfer rate DTR_{max} has been determined from (17).

Table 5. Determination of the maximum data transfer rate for the IoT device.

	$\Delta T_{Busbar\_ambient}$ [°C]	P_{out_DC-DC} [mW]	$E_{out\_DC-DC,\,1\,h}$ [J]	Baterry Efficiency $\eta_{Charge}\eta_{Discharge}$	DTR_{max} [Communications/h]
Lab-Design	20.7	0.21	0.756	0.93	6 [a]
	26.1	0.34	1.224	0.93	10 [a]
	31.7	0.48	1.728	0.93	14 [a]
	37.7	0.66	2.376	0.93	19 [a]
	43.7	0.84	3.024	0.93	25 [a]
CX3324A	20.7	0.21	0.756	0.93	5 [b]
	26.1	0.34	1.224	0.93	9 [b]
	31.7	0.48	1.728	0.93	13 [b]
	37.7	0.66	2.376	0.93	19 [b]
	43.7	0.84	3.024	0.93	24 [b]

[a] DTR_{max} calculations assume $E_{Load,1\ communication\ cycle} = 0.110$ J and $E_{sleep} = 13.64 \cdot \times 10^{-6}$ J/s. [b] DTR_{max} calculations assume $E_{Load,1\ communication\ cycle} = 0.113$ J and $E_{sleep} = 13.01 \times 10^{-6}$ J/s.

The results presented in Table 5 show a great similitude between the DTR_{max} predicted by the Las-design system and the high performance CX3324A current waveform analyzer. These results also show that even with a temperature difference between the environment and the busbar of only 20 °C, the energy harvesting system allows generating enough energy to sustain a minimum of 5 communications per hour.

5. Conclusions

Due to the great expansion of IoT applications, there is a growing interest in developing wireless devices capable of acquiring and transmitting data in transmission lines and electrical substations. This paper has analyzed the behavior of the energy harvesting system, composed of two thermoelectric generators and a DC–DC converter, a rechargeable battery and the sensors and wireless communications modules. Based on experimental tests, an energy balance of the entire IoT device has been carried out, from which

the maximum data transfer rate per hour has been determined. The fast switching nature and the small values of the currents of the different communication phases make this measurement challenging. This work has shown that using conventional instrumentation makes it possible to measure the energy involved in the different modes of communication. A detailed energy balance of the battery has also been carried out during charge and discharge cycles, from which the maximum permissible data transfer rate has been determined. It has been shown that, even with small temperature gradients between the environment and the cold side of the thermoelectric generator, it is possible to make several communications per hour. The approach presented here can be generalized to many other smart grid IoT devices.

Author Contributions: Conceptualization, Y.L., M.M.-E. and J.-R.R.; methodology, J.-R.R.; software, Y.L.; validation, Y.L.; formal analysis, M.M.-E. and J.-R.R.; investigation, Y.L., M.M.-E. and J.-R.R.; resources, M.M.-E. and J.-R.R.; writing—original draft preparation, Y.L. and J.-R.R.; writing—review and editing, M.M.-E.; supervision, M.M.-E. All authors have read and agreed to the published version of the manuscript.

Funding: This research was funded by Generalitat de Catalunya, grant numbers 2021 SGR 00392 and 2020 DI 007.

Institutional Review Board Statement: Not applicable.

Informed Consent Statement: Not applicable.

Data Availability Statement: Not applicable.

Conflicts of Interest: The authors declare no conflict of interest.

References

1. Khalil, N.; Abid, M.R.; Benhaddou, D.; Gerndt, M. Wireless sensors networks for Internet of Things. In Proceedings of the 2014 IEEE Ninth International Conference on Intelligent Sensors, Sensor Networks and Information Processing (ISSNIP 2014), Singapore, 21–24 April 2014.
2. Bellini, P.; Nesi, P.; Pantaleo, G. IoT-Enabled Smart Cities: A Review of Concepts, Frameworks and Key Technologies. *Appl. Sci.* **2022**, *12*, 1607.
3. Al Mamun, M.A.; Yuce, M.R. Sensors and Systems for Wearable Environmental Monitoring toward IoT-Enabled Applications: A Review. *IEEE Sens. J.* **2019**, *19*, 7771–7788.
4. Kadechkar, A.; Riba, J.R.; Moreno-Eguilaz, M.; Perez, J. SmartConnector: A Self-Powered IoT Solution to Ease Predictive Maintenance in Substations. *IEEE Sens. J.* **2020**, *20*, 11632–11641.
5. Kadechkar, A.; Moreno-Eguilaz, M.; Riba, J.-R.J.-R.; Capelli, F. Low-Cost Online Contact Resistance Measurement of Power Connectors to Ease Predictive Maintenance. *IEEE Trans. Instrum. Meas.* **2019**, *68*, 4825–4833.
6. Martínez, J.; Riba, J.R.; Moreno-Eguilaz, M. State of health prediction of power connectors by analyzing the degradation trajectory of the electrical resistance. *Electronics* **2021**, *10*, 1409.
7. Vitolo, P.; De Vita, A.; Di Benedetto, L.; Pau, D.; Licciardo, G.D. Low-Power Detection and Classification for In-Sensor Predictive Maintenance Based on Vibration Monitoring. *IEEE Sens. J.* **2022**, *22*, 6942–6951.
8. Pereira, F.; Correia, R.; Pinho, P.; Lopes, S.I.; Carvalho, N.B. Challenges in Resource-Constrained IoT Devices: Energy and Communication as Critical Success Factors for Future IoT Deployment. *Sensors* **2020**, *20*, 6420.
9. Eunice Akin-Ponnle, A.; Borges Carvalho, N.; Poniszewska-Maranda, A.; Maranda, W. Energy Harvesting Mechanisms in a Smart City—A Review. *Smart Cities* **2021**, *4*, 476–498.
10. Liu, Y.; Khanbareh, H.; Halim, M.A.; Feeney, A.; Zhang, X.; Heidari, H.; Ghannam, R.; Correspondence, R.; Ghannam, J. Piezoelectric energy harvesting for self-powered wearable upper limb applications. *Nano Sel.* **2021**, *2*, 1459–1479.
11. Verma, G.; Sharma, V. A Novel RF Energy Harvester for Event-Based Environmental Monitoring in Wireless Sensor Networks. *IEEE Internet Things J.* **2022**, *9*, 3189–3203.
12. Chen, X.; Sun, L.; Zhu, H.; Zhen, Y.; Chen, H. Application of internet of things in power-line monitoring. In Proceedings of the 2012 International Conference on Cyber-Enabled Distributed Computing and Knowledge Discovery, CyberC, Sanya, China, 10–12 October 2012; pp. 423–426.
13. Sabovic, A.; Delgado, C.; Subotic, D.; Jooris, B.; De Poorter, E.; Famaey, J. Energy-Aware Sensing on Battery-Less LoRaWAN Devices with Energy Harvesting. *Electronics* **2020**, *9*, 904.
14. *Std 605-2008*; Guide for Bus Design in Air Insulated Substations. IEEE: Piscataway, NJ, USA, 2010; ISBN 9780738158570.
15. Liu, Y.; Riba, J.-R.; Moreno-Eguilaz, M.; Sanllehí, J. Analysis of a Smart Sensor Based Solution for Smart Grids Real-Time Dynamic Thermal Line Rating. *Sensors* **2021**, *21*, 7388.

16. Locorotondo, E.; Cultrera, V.; Pugi, L.; Berzi, L.; Pierini, M.; Lutzemberger, G. Development of a battery real-time state of health diagnosis based on fast impedance measurements. *J. Energy Storage* **2021**, *38*, 102566.
17. Zhu, M.; Hu, W.; Kar, N.C. The SOH estimation of LiFePO4 battery based on internal resistance with Grey Markov Chain. In Proceedings of the 2016 IEEE Transportation Electrification Conference and Expo (ITEC'16), Dearborn, MI, USA, 27–29 June 2016.
18. Noura, N.; Boulon, L.; Jemeï, S. A Review of Battery State of Health Estimation Methods: Hybrid Electric Vehicle Challenges. *World Electr. Veh. J.* **2020**, *11*, 66.
19. Kang, J.; Yan, F.; Zhang, P.; Du, C. A novel way to calculate energy efficiency for rechargeable batteries. *J. Power Sources* **2012**, *206*, 310–314.
20. Kang, J.; Yan, F.; Zhang, P.; Du, C. Comparison of comprehensive properties of Ni-MH (nickel-metal hydride) and Li-ion (lithium-ion) batteries in terms of energy efficiency. *Energy* **2014**, *70*, 618–625.
21. Young, K.H. Research in Nickel/Metal Hydride Batteries 2017. *Batteries* **2018**, *4*, 9.
22. Lee, J.; Kim, J.-M.; Yi, J.; Won, C.-Y.; Averbukh, M.; Rodriguez, N. Battery Management System Algorithm for Energy Storage Systems Considering Battery Efficiency. *Electronics* **2021**, *10*, 1859.
23. Calautit, K.; Nasir, D.S.; Hughes, B.R. Low power energy harvesting systems: State of the art and future challenges. *Renew. Sustain. Energy Rev.* **2021**, *147*, 111230.
24. *IEC 61434:1996*; Secondary Cells and Batteries Containing Alkaline or Other Non-Acid Electrolytes—Guide to Designation of Current in Alkaline Secondary Cell and Battery Standards. IEC: London, UK, 1996; pp. 1–7.
25. *IEC 61982:2012*; Secondary Batteries (Except Lithium) for the Propulsion of Electric Road Vehicles—Performance and Endurance Tests. IEC: Geneva, Switzerland, 2012.
26. Albertus, P.; Christensen, J.; Newman, J. Modeling Side Reactions and Nonisothermal Effects in Nickel Metal-Hydride Batteries. *J. Electrochem. Soc.* **2008**, *155*, A48.
27. Yang, X.-G.; Liaw, B.Y. Numerical Simulation on Fast Charging Nickel Metal Hydride Traction Batteries. *J. Electrochem. Soc.* **2004**, *151*, A265.
28. Plett, G.L. Extended Kalman filtering for battery management systems of LiPB-based HEV battery packs: Part 2. Modeling and identification. *J. Power Sources* **2004**, *134*, 262–276.

5.2 Application of Thermoelectric Generators for Low-Temperature-Gradient Energy Harvesting

Reference:

Liu, Y.; Riba, J.-R.; Moreno-Eguilaz, M.; Sanllehí, J. Application of Thermoelectric Generators for Low-Temperature- Gradient Energy Harvesting. Appl. Sci. 2023, 13, 2603. Under a CC BY 4.0 license. https://doi.org/ 10.3390/app13042603.

Publication framework:

This article presents an analysis of the performance of state-of-the-art thermoelectric generators (TEGs) designed for low-temperature gradient applications, which are implemented on IoT systems for health condition monitoring for high-voltage alternating and direct current applications. This article evaluates the behavior of different thermoelectric generators for this application, where very low-temperature gradients are expected.

Main contributions:

- **Experimental study of the generated power and the efficiency of thermoelectric devices installed in tubular conductors.**
- **Analysis of four different commercially available combinations of TEG-DC/DC converters, which are tested and evaluated under realistic operating conditions.**
- **Analysis of efficiencies of several combinations of TEG-DC/DC converters.**

Key words:

energy harvesting; power systems; solid-state thermoelectric generator; wireless sensors

applied sciences

MDPI

Article

Application of Thermoelectric Generators for Low-Temperature-Gradient Energy Harvesting

Yuming Liu [1,2], Jordi-Roger Riba [1,*], Manuel Moreno-Eguilaz [1] and Josep Sanllehí [2]

[1] Electrical and Electronics Engineering Departments, Universitat Politècnica de Catalunya, Rambla Sant Nebridi 22, 08222 Terrassa, Spain
[2] SBI Connectors, Sant Esteve Sesrovires, Albert Einstein, 5, 08635 Sant Esteve Sesrovires, Spain
* Correspondence: jordi.riba-ruiz@upc.edu; Tel.: +34-937398365

Abstract: Thermoelectric generators (TEGs) convert a temperature difference into useful direct current (DC) power. TEGs are solid-state semiconductor devices that are generating a lot of interest for energy harvesting purposes in Internet of Things (IoT) applications. This paper analyzes the behavior of state-of-the-art TEGs designed for low temperature gradient operation, with special emphasis on IoT systems for health monitoring for high-voltage alternating current (AC) and DC applications. In such applications, the energy harvesting unit plays a leading role in supplying wireless sensors (WSs). An application example is also presented with the aim to monitor the health condition of devices installed in the tubular busbars found in electrical substations. Since substation busbars heat up due to the Joule effect, there is a small thermal gradient between the busbar and the ambient, so the TEG can convert this heat flow into useful DC energy to supply low-power WSs. This paper assesses the performance of different TEG devices for this application, where very low temperature gradients are expected. The results presented show that with temperature gradients as low as 5 °C it is possible to supply WSs.

Keywords: energy harvesting; power systems; solid-state thermoelectric generator; wireless sensors

Citation: Liu, Y.; Riba, J.-R.; Moreno-Eguilaz, M.; Sanllehí, J. Application of Thermoelectric Generators for Low-Temperature-Gradient Energy Harvesting. *Appl. Sci.* **2023**, *13*, 2603. https://doi.org/10.3390/app13042603

Academic Editor: Yoshiyasu Takefuji

Received: 14 December 2022
Revised: 15 February 2023
Accepted: 16 February 2023
Published: 17 February 2023

1. Introduction

Transmission and distribution lines are the highways of today's electrical systems, so it is vital to maximize their reliability, efficiency, and stability, due to the enormous economic and social impacts they have. Transmission lines are found in semi-urban areas but also in remote regions, where regular inspections can be expensive and complex. These inspections are necessary to minimize the risk of transmission line failures due to the impact of different environmental factors such as ice, rain, wind or extreme temperatures on their operational performance. Therefore, self-powered wireless sensors can be of great help for real-time monitoring of transmission lines [1]. To supply these sensors, an energy harvesting unit is required, that is, a device for converting energy from the environment or other sources into electrical energy [2]. Energy harvesters allow extending the lifetime of battery-powered sensors because in many applications they minimize or avoid battery replacement and maximize the duration of their use [3]. In some cases, such as in battery-less autonomous systems, energy harvesters allow battery usage to be eliminated [4]. Therefore, energy harvesters minimize or eliminate battery replacement and associated maintenance costs [5].

In the case of overhead power lines, the temperature gradient between the ambient and conductor is limited, because overhead line conductors (OHLC) rating is typically 75 °C for conventional aluminum-conductor steel-reinforced conductors [6], while the maximum allowable temperature is about 90 °C [7]. The operating temperature and thus thermal stress of OHLCs are restricted to limit vertical sag clearance, elongation and creep, tensile loss, and maximize conductors' lifespan [6]. Instead of conductors, the substations

use aluminum tubular busbars, whose maximum operating temperature is lower than that of OHLCs [8,9]. Therefore, temperature gradients in the conductors and busbars of transmission systems are reduced.

IoT devices allow us to monitor different devices [10,11], thus facilitating the determination of their health condition. Today, there is an urgent need to have a better control of high-voltage transmission and distribution systems. It is accepted that by introducing low-cost wireless sensors (WSs) in this field, we can increase their stability, availability and reliability while allowing predictive maintenance strategies to be applied. Furthermore, transmission systems are found in remote areas [12], where human intervention is very difficult and expensive, so IoT-based solutions can be very useful. Thus, there is an increasing demand to monitor the health condition of such systems [13]. WSs found in IoT solutions typically include an energy harvesting unit, dedicated sensors and a communication module. It makes it possible to acquire the key parameters and send the information wirelessly to the cloud, where it can be monitored and analyzed in real time to facilitate the application of predictive maintenance plans [14]. A key element in WSs for IoT applications is the energy harvesting unit, which allows reduction of the carbon footprint by minimizing battery replacement and enabling the deployment of electronic sensors in inaccessible or hostile places [15]. Due to the lack of a time-varying magnetic or electric field, the development of energy harvesting systems for DC systems is more challenging, making the use of TEGs a necessity.

Due to the ohmic resistance, conductors are heated by the action of an electric current, which generates a temperature difference between the conductor and the environment [16]. This temperature gradient produces a heat flow that allows energy to be harvested [17]. When applied to power conductors or substation busbars, TEGs convert the temperature gradient between the environment and the conductor into electric energy, which can be used to supply autonomous sensors [18]. It is a recognized fact that due to the lack of a time-varying magnetic or electric field, in direct current (DC) systems it is more difficult to develop energy harvesting systems. However, due to their nature, TEGs allow us to bypass this difficulty, since heat is generated by the Joule effect in both DC and AC systems. Therefore, TEGs allow the design of energy harvesting units compatible with both DC and AC systems. Most commercial transmission line products are supplied by batteries and/or electromagnetic energy harvesters, so there are several works using TEGs for such applications. In [16], the possibility of using a TEG wrapped around the conductor to harvest the energy of the heat flux between the conductor and the environment is described. However, a heat exchanger connected to the cold side of the TEG is required to maximize the temperature gradient between the hot and cold ends. A similar approach was applied in [12] to power a wireless system mounted on a substation cylindrical busbar, which was composed of different sensors (voltage drop, current and temperature).

When applied to power lines, the intensity of the current has a profound impact on the temperature of the conductor. As in the case of other energy harvesting approaches, i.e., solar or wind, thermoelectric energy harvesting depends on environmental variables. Therefore, it is difficult to generate a stable supply of electrical power [19], as it is necessary to apply specific energy management strategies to ensure a stable and reliable generation of electrical energy [20].

This paper presents an experimental study of the generated power and the efficiency of TEG devices installed in tubular busbars, which are characteristic of electrical substations. Due to their large diameters, there is very little temperature gradient between the ambient and the busbar, generally a few degrees Celsius. This is a challenging application that has hardly been analyzed in the technical literature, since most TEG applications are focused on high temperature gradients [21]. Under such unfavorable conditions, the TEGs generate very low voltage, so a suitable DC/DC converter is required to supply the sensors and communications module. This work analyzes four different combinations of TEG–DC/DC converters, which are tested under realistic operating conditions and their efficiencies are analyzed.

This article is organized as follows. Section 2 reviews the basic principles of thermoelectric generators including aspects such as efficiency or their use in energy harvesting systems for transmission lines. Section 3 selects the most suitable TEG + DC/DC converter combination for this application from among four candidate options. Section 4 analyzes in depth the experimental behavior of the most appropriate TEG + DC/DC combination. Finally, Section 5 develops the conclusions of this work.

2. Basic Principles of Thermoelectric Generators

Thermoelectric energy harvesting is typically based on thermoelectric generators (TEGs), which, based on the Seebeck effect, directly convert a temperature gradient between their hot and cold ends into electrical energy [4,22]. As will be detailed in the next subsection, due to the inherent limitations of the thermoelectric conversion process, the efficiency of TEGs is always low, usually below 8–9%, and much less for small temperature gradients, since the efficiency is governed by the Carnot cycle [17].

2.1. The Seebeck Effect

Seebeck generators or thermoelectric generators (TEGs) are semiconductor devices designed to convert heat flow or a temperature gradient directly into DC electrical energy through the Seebeck effect. The Seebeck effect, which is due to the motion of charge carriers within semiconductors, produces an electromotive force (emf) across two points of a conductive material when there is a temperature gradient between these points.

Semiconductors are particularly appropriate for thermoelectric applications because the concentration of charge carriers can be changed by doping the material. In an n-type doped semiconductor, the charge carriers are mostly free electrons, while in a p-type doped semiconductor, the charge carriers are free holes, i.e., missing electrons in the valence band. The thermocouple (consisting of a p-type and an n-type semiconductor connected in series by a metal strip) is the basic building block of a TEG. Due to the temperature gradient, the charge carriers of the hot side have higher kinetic energy, so they diffuse from the hot to the cold side of the semiconductor. Eventually, the cold end of the TEG becomes positively (p-type semiconductor) or negatively (n-type semiconductor) charged, and the hot end negatively (p-type semiconductor) or positively (n-type semiconductor) charged [23]. Charges build-up at the cold end, creating an electromotive force (ΔV or Seebeck voltage) [24] between the n-type and p-type hot ends of the semiconductors that is directly proportional to the temperature difference $\Delta T = T_{hot} - T_{cold}$ between the hot and cold ends of the semiconductors, as shown in Figure 1. To boost the voltage and current generated, commercial TEGs include many pairs of n-type and p-type couples [21] connected in series and/or parallel to generate the desired electrical voltage and current. The couples are typically placed between two parallel ceramic plates, which provide a flat surface, structural rigidity, and an insulating layer to prevent short circuits.

TEGs offer several advantages, including reliability and quiet operation, since they are solid-state devices with no moving parts, are compact, do not emit greenhouse gases, can be mounted in any orientation, are scalable from μW to kW, and directly convert heat into electrical energy.

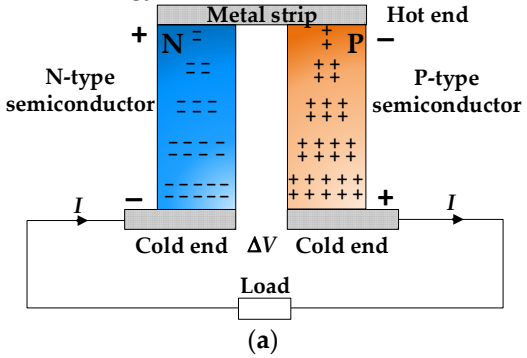

(**a**)

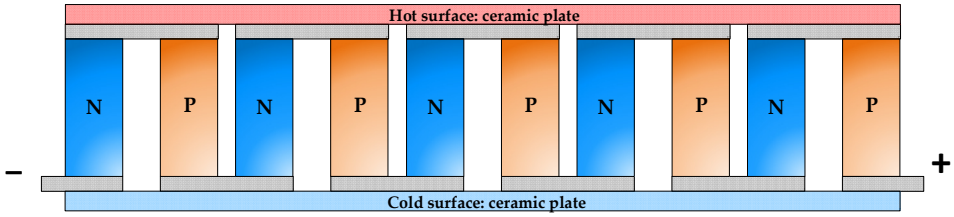

(**b**)

Figure 1. (**a**) Schematics of a thermoelectric generator indicating the charge carriers, adapted from [25]. (**b**) Series connections of different thermoelectric couples, adapted from [26].

2.2. The Seebeck Coefficient

The Seebeck coefficient S is defined from the voltage ΔV produced due to a small temperature gradient ($\Delta T = T_{hot} - T_{cold,}$ between the two sides of the TEG) between the two semiconductor materials at the junction under open circuit conditions [21,27,28] as,

$$S = -\Delta V/\Delta T = -(V_{hot} - V_{cold})/(T_{hot} - T_{cold}) \quad (1)$$

The voltage difference ΔV is due to the difference in the electrochemical potentials of the two semiconductor materials in contact [28]. Therefore, the Seebeck coefficient measures the magnitude of the thermoelectric voltage induced due to a temperature difference between the two materials. In general, the Seebeck coefficient depends on the molecular structure of the materials and on the absolute temperature.

For most semiconductor materials, the voltage ΔV generated due to the Seebeck effect is very low, on the order of a few tens or hundreds of μV/K. For example, for the commonly used Bi_2Te_3 semiconductor, the Seebeck coefficient S is 160 μV/K for p-type material and −170 μV/K for n-type material [29].

TEG materials must have high electrical conductivity to minimize the Joule effect, a large Seebeck coefficient for maximum conversion of heat to electrical energy, and low thermal conductivity to minimize thermal conduction through the material [21]. These properties are combined into a z-metric, the figure of merit, which quantifies the overall output of the TEG, and is defined as [30],

$$z = S^2\rho^{-1}\kappa^{-1}\ [K^{-1}] \quad (2)$$

where ρ is the electrical resistivity and κ the thermal conductivity. The Seebeck coefficient S is typically determined over a 5–10 K range, so the figure of merit z is valid only for a small temperature difference [31]. The dimensionless figure of merit z_T is commonly used to characterize TEG's behavior [30],

$$z_T = S^2\rho^{-1}\kappa^{-1}T\ [-] \quad (3)$$

where $T = (T_{hot} + T_{cold})/2$ is the average temperature.

When assuming a one-dimensional steady state heat transfer process and no heat loss through the heat exchanger wall [32], uniform temperature distribution across each surface of the material [31], a rough estimation of the maximum thermo-electrical conversion efficiency of the TEG is determined by [30,31,33–35],

$$\eta_{\mathrm{TEG,max}} = \frac{T_{hot} - T_{cold}}{T_{hot}} \times \frac{\left(1 + z_T\right)^{1/2} - 1}{\left(1 + z_T\right)^{1/2} + \frac{T_{cold}}{T_{hot}}} \quad (4)$$

where the term $(T_{hot} - T_{cold})/T_{hot}$ is the Carnot efficiency.

According to (4), the efficiency of a TEG depends on the hot and cold junction temperatures and on the thermoelectric properties of the material through the merit factor z_T. However, (4) only predicts η_{max} accurately for small temperature differences $\Delta T = T_{hot} - T_{cold}$, or for materials with z_T almost constant over a wide temperature range [36]. In practical scenarios, the efficiency of a TEG can be more complex when considering the thermal

and electrical resistances, heat leakage, Thompson effect, and the temperature gradient in the heat sinks at the hot and cold ends of the TEG [37].

From (3) and (4), it is evident that the efficiency of TEGs depends on the properties of the internal semiconductor materials through the figure of merit and the temperature, so to improve the efficiency, materials with a high figure of merit are required. TEGs are mostly based on three semiconductor materials, i.e., Bi_2Te_3, PbTe and SiGe. The election of the material depends on the heat source characteristics, cold sink and TEG design. According to [38], the z_T of most currently available thermoelectric materials is at most 1, although the bulk alloy of bismuth–antimony–telluride yields a p-type z_T = 1.4 at 100 °C [31]. For example, in the case of Bi_2Te_3, the most used thermoelectric material, z_T is in the range of 0.5–0.8. According to (3), the efficiency at ΔT = 300 K is 6.6–9.4%, for z_T = 0.5 and z_T = 0.8, respectively, whereas at ΔT = 10 K, the efficiency reduces to 0.34–0.49%, respectively, as shown in Figure 2. It should be noted that both tellurium and bismuth are relatively plentiful in the Earth's crust [39]. Different solid-state thermoelectric materials are still being investigated to increase TEG efficiency, but have not been commercialized.

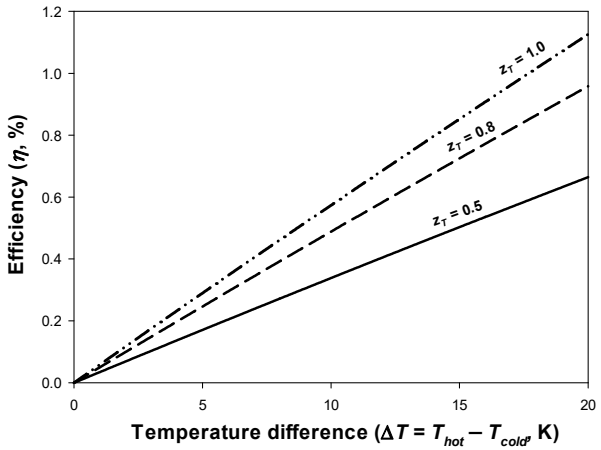

Figure 2. Efficiencies calculated from (4) for different figures of merit z_T versus the temperature difference between the hot and cold sides of the TEG, assuming T_{cold} = 20 °C and $T_{hot} = T_{cold} + \Delta T$.

The power generated by the TEG can be calculated as [21],

$$P_{TEG} = P_{transfer} \times \eta_{TEG} \tag{5}$$

where $P_{transfer}$ [W] is the rate of heat transfer between the two sides of the TEG, which can be expressed as [35],

$$P_{transfer} = \frac{T_{hot} - T_{cold}}{R_{TEG}} \tag{6}$$

where R_{TEG} [°C/W] is the thermal resistance of the TEG.

According to [35], the maximum power that the TEG can generate corresponds to the point with half the short circuit current I_{sc} and half the open circuit voltage V_{oc}, thus resulting in,

$$P_{TEG,max} = \frac{V_{oc}}{2} \times \frac{I_{sc}}{2} \tag{7}$$

Equation (7) is demonstrated in Figure 6.

3. Selection of the Best TEG + DC/DC Converter Combination

As explained, TEGs generate very low voltage under small temperature gradients, so a suitable DC/DC converter is required to supply the sensors and communications module in WSs. This section analyzes two TEGs specially designed for low temperature gradients and two DC/DC converters designed for very low input voltage. The performance of the four possible combinations between the selected TEGs and the DC/DC converters summarized in Table 1 under very low temperature gradients is also studied. The results obtained will allow selection of the most appropriate combination to supply the low power WSs electronics.

Table 1. Combinations of TEGs and DC/DC converters.

Combination	Devices Involved
1	TEG #1 + DC/DC converter #1
2	TEG #1 + DC/DC converter #2
3	TEG #2 + DC/DC converter #1
4	TEG #2 + DC/DC converter #2

3.1. Experimental Setup

After a careful literature review, two commercial low-temperature TEGs and two commercial DC/DC converters were selected, which are compared in this paper. As the output voltage generated by the TEGs is in the range of some mV, two DC/DC converters with extreme low startup voltage were selected to amplify the voltage from the millivolt range to the volt range to supply WSs.

Tables 2 and 3 present the main characteristics of the TEGs and DC/DC converters.

Table 2. Analyzed TEG modules.

TEG Modules	TEG #1	TEG #2
Model	GM250-157-14-16	TG12-8
Manufacturer	European Thermodynamics	Marlow Industries
Dimensions (mm)	40 × 40	40 × 40
Thickness (mm)	4.1	3.6
Matched load resistance (Ω)	3.65	3.46
Hot side temperature (°C)	250	230
Cold side temperature (°C)	30	50
Optimum output voltage (V)	5.05	5.25
Optimum output power (W)	6.99	7.95

Table 3. Analyzed DC/DC converters.

DC/DC Converters	DC/DC #1	DC/DC #2
Model	LTC3108	LTC3109
Manufacturer	Analog devices	Analog devices
Harvesting board	Adaptive ADEH	Demo circuit 1664 A
Input voltage range	50–400 mV	30–500 mV
Voltage regulation	2.35–5.00 V	2.30–5.10 V
MPPT technology *	Yes	No

* MPPT stands for maximum power point tracking.

To compare the behavior of the different TEGs, they were placed on the top of a flat aluminum busbar, which was exposed to heat cycle tests. To this end, six resistances (HS50 1R F from ARCOL,1 Ω, 50 W) connected in series to a BK9205 power supply (BK Electronics, Southend On Sea, England) were used, jointly with two TEGs connected in series, as

shown in Figure 3. A rechargeable BM2000C1450AA2S1PATP Nickel battery from GlobTek (GlobalTek, Miami, FL, USA) was also used to store the energy generated by the TEGs and converted by the DC/DC converter.

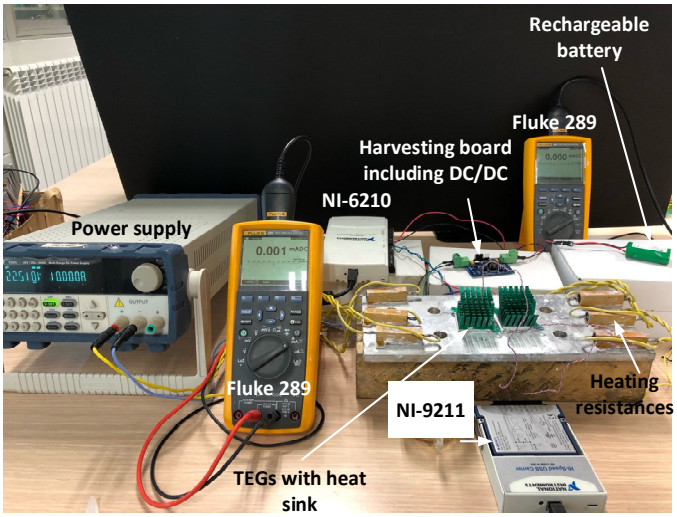

Figure 3. Experimental setup to compare the performance of TEGs and DC/DC converters.

To study the performance and efficiency of thermoelectric energy harvesting systems, it is necessary to determine the input/output power of TEG modules and DC/DC converters. Two Fluke 289 data-logger multimeters (Fluke, Everett, WA, USA) were used in ammeter mode to measure the value of the small currents generated by the TEGs (microamp to milliamp range) due to the low temperature gradients analyzed. An NI USB-6210 data acquisition system (National Instruments, Austin, TX, USA) was used to acquire the voltages from the output terminals of the TEG module and the DC/DC converter. Three T-type thermocouples together with an NI-9211 thermocouple acquisition module (National Instruments, Austin, TX, USA) were used to measure the ambient temperature and the temperatures of the hot and cold sides of the TEGs. To ensure a simultaneous acquisition, the Fluke multimeters, the NI USB-6210 and NI-9211 modules were synchronized using a Python code programmed by the authors of this work.

A thermal joint compound (120-SA, Wakefield-Vette, NH, USA) was used to ensure good thermal contact between the heat source, TEG and heat sink. This compound fills the tiny air gap between mating surfaces with a grease-like paste containing zinc oxide in a silicone oil carrier. It is used for several reasons such as its ability to fill the air gap between different surfaces, its high thermal conductivity and its adhesive ability.

3.2. Experimental Tests

The tests were carried out indoors at an ambient temperature of about 20 °C. The TEGs were mounted on a flat rectangular aluminum busbar that was heated from room temperature to approximately 50 °C using a power supply and heating resistors, as shown in Figure 3. Next, to determine the performance of the devices during the cooling phase, the power supply was disconnected, whereby the aluminum bar cooled by natural convection. The electrical output power of the TEGs and DC/DC converters was determined by multiplying the respective voltages and currents.

Figure 4 shows the performance of TEG #1 combined with DC/DC converter #1. According to Figure 4b,c, with the same temperature difference between the busbar and the ambient, more power is generated during the heating cycle than during the cooling cycle. This hysteresis response is mainly due to the delayed thermal diffusion from the ceramic plate to the hot junction of the TEGs [40].

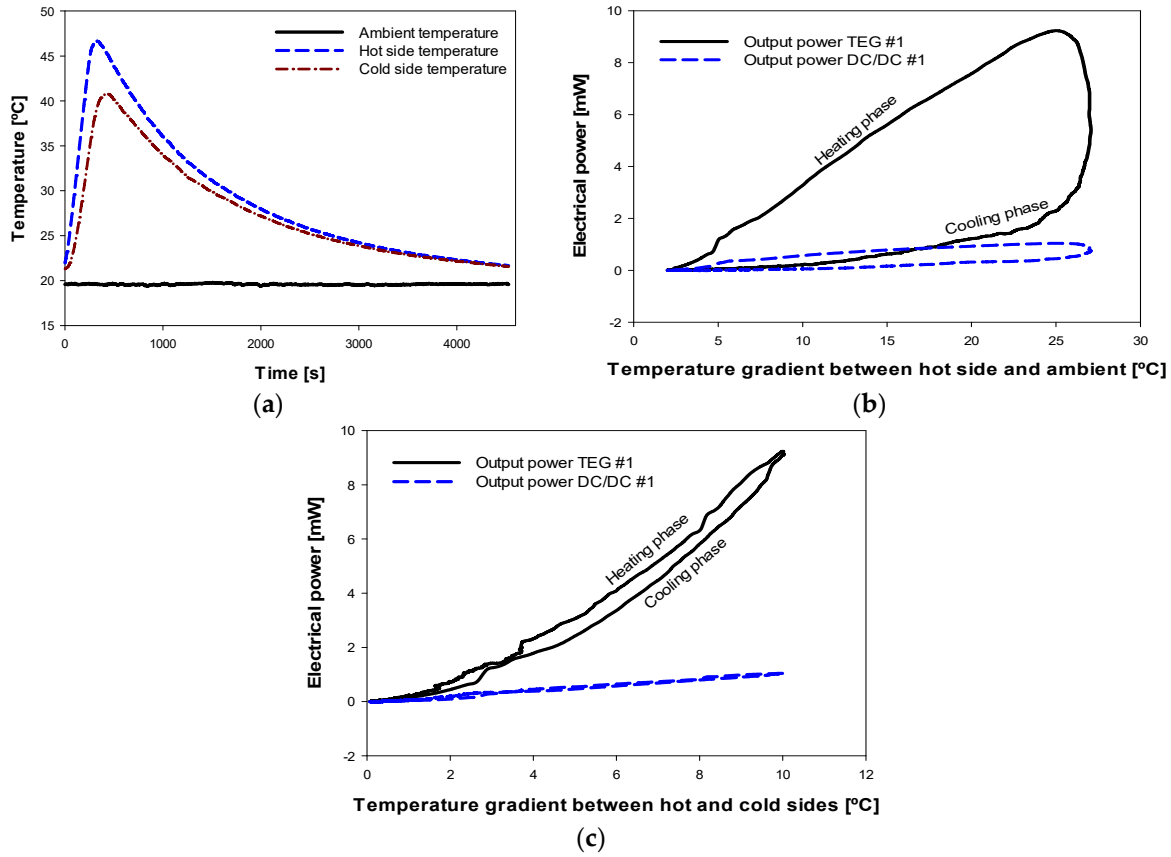

Figure 4. TEG #1 combined with DC/DC converter #1. (**a**) Ambient, hot and cold side temperatures measured by T-type thermocouples. (**b**) Output power of TEG #1 and DC/DC converter #1 versus the temperature difference between the hot and cold sides of TEG #1. (**c**) Output power of the analyzed TEGs and DC/DC converter versus the temperature difference between the hot and cold sides of the TEG #1.

Figure 5 shows the experimental performance of each TEG, DC/DC converter and the different combinations of TEG + DC/DC converter. It is noted that the TEG #1 + DC/DC converter #1 combination has a better performance than the others, this being the most suitable combination for applications with very low temperature gradients. Therefore, the next sections take a closer look at the TEG #1 + DC/DC converter #1 combination.

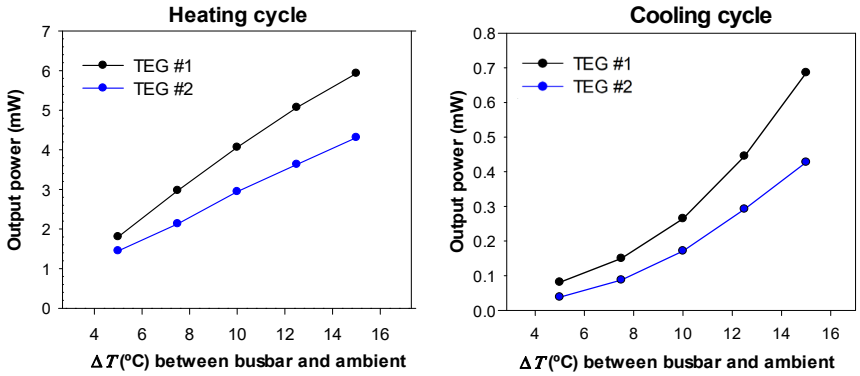

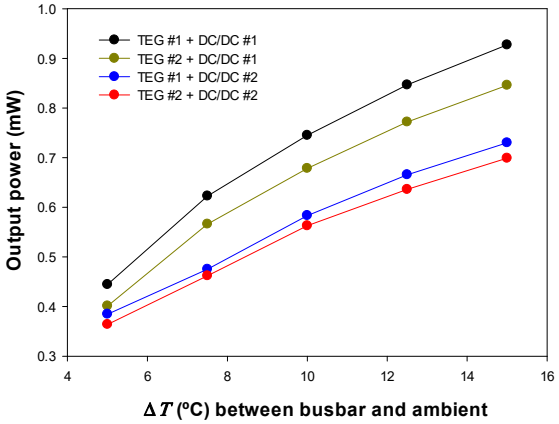

(**b**)

Figure 5. Combined performance of TEGs #1 and #2 combined with DC/DC converters #1 and #2. (**a**) Power generated by the analyzed TEG modules versus the temperature difference between the busbar and the ambient during the heating and cooling cycles. (**b**) Output power of the different combinations of TEG + DC/DC converter versus the temperature difference between the busbar and the ambient during the heating cycle.

3.3. Characterization of TEG #1

First, the characteristic voltage—current and power—current curves of TEG #1 were obtained by heating the busbar. The hot and cold side temperatures of the TEG were 67.7 °C and 57.8 °C, respectively, with an ambient temperature of 21.5 °C. This corresponds to a temperature gradient $\Delta T = T_{hot} - T_{cold} \approx 10$ °C between the hot and cold sides of the TEG. During the tests, a variable resistor was connected between the terminals of TEG #1, and the voltage V and current I flowing through its terminals were measured. These values are shown in Figure 6 together with the $P - I$ fit, where $P = V \cdot I$.

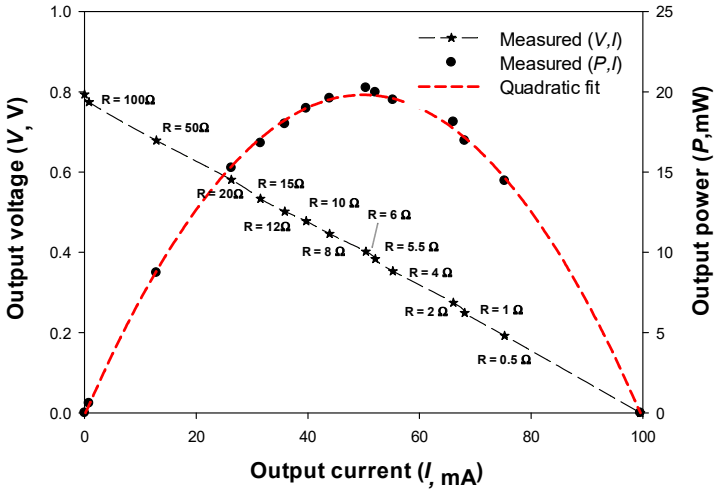

Figure 6. Characteristic TEG curves, $V - I$ and $P - I$. The quadratic fit obtained is P (mW) = $-0.008014 \cdot I^2 + 0.7995 \cdot I - 0.1176$. The parameters related to goodness of fit are $R^2 = 0.9992$, SSE = 0.676, and RMSE = 0.2373.

Table 4 summarizes the main parameters of the test performed to determine the $V - I$ and $P - I$ characteristics of TEG #1.

Table 4. Parameters of the analyzed TEG module.

Parameters	Measured Values

Ambient temperature (°C)	21.5
Cold side temperature (°C)	57.8
Hot side temperature (°C)	67.7
Open circuit voltage (V)	0.79
Short-circuit current (mA)	99.56
Maximum power point voltage (V)	0.40
Maximum power point current (mA)	50.39
Resistance at the maximum power point (Ω)	6.00
Maximum power (mW)	20.25

The results presented in Figure 6 and Table 4 show that the power that can be drawn from the TEG is highly dependent on the resistance of the load, so the use of a DC/DC converter that includes a maximum power point tracker (MPPT) could be beneficial.

4. Efficiency Determination of the Best Combination of TEG + DC/DC Converter

This section discusses in detail the efficiency of the best combination of TEG + DC/DC converter, that is, TEG #1 + DC/DC converter #1. For this, the assembly shown in Figure 7 is analyzed, which corresponds to a realistic situation. The TEG #1 + DC/DC converter #1 combination is mounted on a stainless steel tubular hollow conductor with an inner diameter of 120 mm and a wall thickness of 0.4 mm. Using this configuration, the steady-state performance of TEG #1 + DC/DC converter # 1 is studied.

To calculate the efficiency of the entire TEG #1 + DC/DC converter #1 system $\eta_{TEG+DC/DC}$, the individual efficiencies of the TEG η_{TEG} and the DC/DC converter $\eta_{DC/DC}$ are required. According to IEEE Std. 605 [41] describing the design of busbars in air insulated substations, indoors and under steady state conditions, the heat gain per unit length due to Joule losses must compensate the terms of heat loss per unit length due to convective and radiative cooling as,

$$I_{RMS}^2 r_{ac}(T) = p_c + p_r \quad [\text{W/m}] \tag{8}$$

where I_{RMS} (A) is the current through the busbar, $r_{ac}(T)$ [Ω/m] is the ac resistance of the conductor per unit length at the operating temperature T, and p_c [W/m] and p_r [W/m] are, respectively, the losses due to natural convection and radiation.

The ac resistance per unit length of the conductor, r_{ac} [Ω/m], was measured according to the method described in [7,13]. This method requires measuring the voltage drop ΔV_{1m} [V] between two points of the conductor surface separated by 1 m, the ac current I [A] flowing through the conductor, the phase shift φ [rad] between the voltage drop and the current, and the conductor temperature T [°C],

$$r_{ac}(T) = \frac{\Delta V_{1m}}{I} \times \cos\varphi \quad [\Omega/\text{m}] \tag{9}$$

To calculate the efficiency of entire system, including the TEG and the DC/DC converter, $\eta_{TEG+DC/DC}$, the individual efficiencies of the TEG, η_{TEG}, and the DC/DC converter, $\eta_{DC/DC}$, are needed. The efficiency of the TEG η_{TEG} can be calculated as the ratio between the electrical power generated by the TEG, $P_{electric,TEG}$ [W], and the Joule heat generated by the conductor in the area of the TEG (80 mm × 40 mm), $P_{Joule,TEG\text{-}area}$ [W], as,

$$\eta_{TEG} = \frac{P_{electric,TEG}}{P_{Joule,TEG-area}} \tag{10}$$

$P_{Joule,TEG\text{-}area}$ can be calculated as,

$$P_{Joule,TEG-area} = P_{Joule,conductor} \times \frac{A_{TEG}}{A_{Conductor}} \quad [\text{W}] \tag{11}$$

where A_{TEG} [m²] and $A_{Conductor}$ [m²] are the area of the outer surfaces of the TEG and conductor, respectively, while $P_{Joule,conductor}$ [W] is the heat generated in the conductor.

The efficiency of the DC/DC converter can be calculated as,

$$\eta_{DC/DC} = \frac{V_{out} \times I_{out}}{V_{inp} \times I_{inp}} \quad [-] \tag{12}$$

where V_{out}, I_{out}, V_{inp}, and I_{inp} are, respectively, the output and input voltages and currents of the DC/DC converter.

Figure 7. Experimental setup to characterize the performance of TEG #1 + DC/DC converter #1 mounted on a tubular conductor.

Figure 7 also shows the heat sinks (height = 25 mm, base length = 38 mm, top fin field length = 65 mm, and width = 40 mm) attached to each TEG.

4.1. Steady State Performance of TEG #1

Using the setup shown in Figure 7, a second experiment was carried out on the 120 mm diameter tubular conductor to characterize the steady state performance of TEG #1. Five levels of current (136 A, 169 A, 194 A, 226 A and 254 A) were injected to heat the tubular conductor to steady state.

Figure 8a shows the evolution of the temperature with time of the hot side and the cold sides of TEG #1, while Figure 8b shows the evolution with time of the output electrical power of TEG # 1 and DC/DC converter #1.

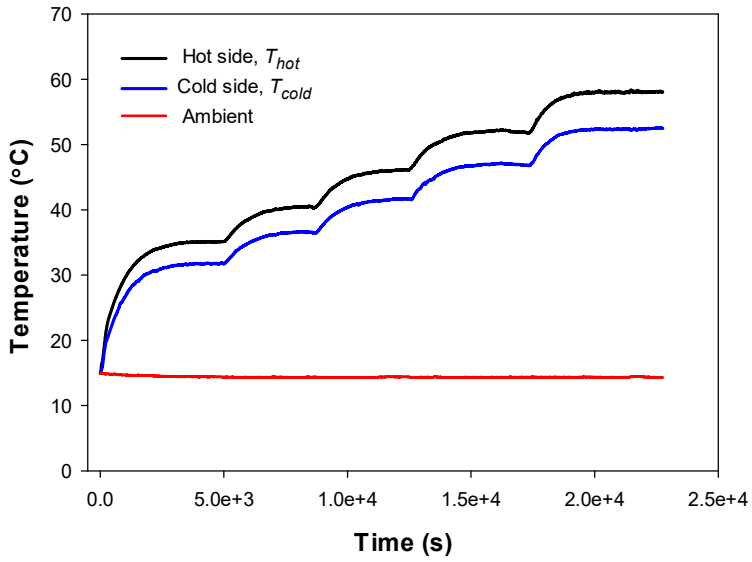

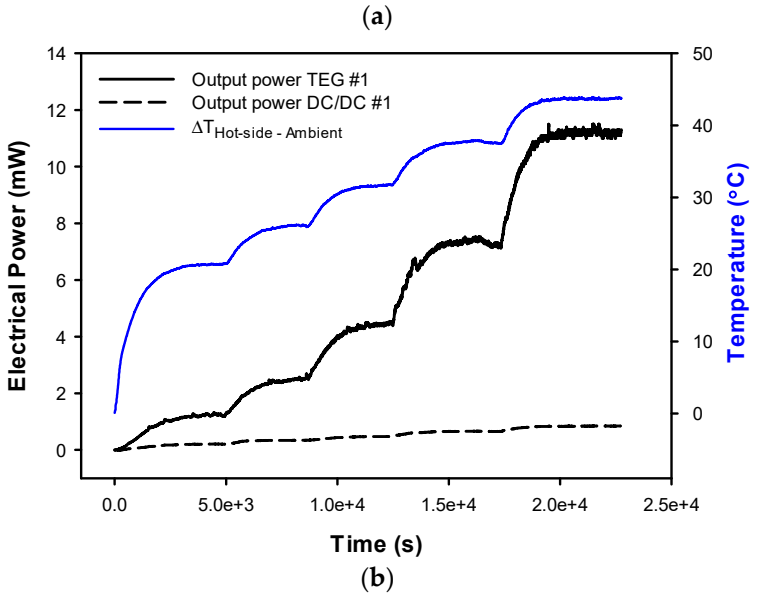

Figure 8. (**a**) Hot side, heat sink and ambient temperatures measured by T-type thermocouples. (**b**) Electrical output power of TEG and DC/DC converter, and temperature difference between hot side and ambient.

To determine the $I_{RMS}^2 r_{ac}(T)$ Joule heating in (8), r_{ac} as a function of temperature is required. For this purpose, an offline experiment was carried out, measuring the voltage drop, the current flowing throng the tubular conductor, the conductor temperature and cosφ. The results obtained are summarized in Table 5.

Table 5. Dependence of r_{ac} with the temperature of the tubular conductor.

T (°C)	ΔV_{1m} (V_{RMS})	Current (A_{RMS})	cosφ	r_{ac} (μΩ/m)
25	1.4735	280	0.9997	5267
30	1.4845	279	0.9997	5319
35	1.4913	277	0.9997	5378
40	1.5085	277	0.9997	5441
45	1.5148	275	0.9997	5501
50	1.5200	274	0.9997	5545
55	1.5290	273	0.9997	5591
60	1.5313	271	0.9997	5635
65	1.5353	271	0.9997	5657

Table 6 summarizes the results obtained with the entire system, including the tubular bus bar, TEG #1 and DC/DC converter #1. It shows that when current applied is, for example, I = 254 A_{rms}, the steady state temperature difference between the hot side of TEG #1 and the ambient is $\Delta T_{Hot\text{-}Ambient}$ = 43.7 °C, while the temperature difference between the hot and cold sides of TEG #1 is $\Delta T_{Hot\text{-}Cold}$ = 5.67 °C. In this steady-state condition, the output power of TEG #1 and DC/DC converter#1 are, respectively, $P_{electric,TEG}$ = 11.2 mW and $P_{DC/DC}$= 0.84 mW. They correspond to efficiencies of TEG #1, η_{TEG}, and TEG#1 + DC/DC #1, $\eta_{TEG+DC/DC}$, of 0.36% and 0.027%, respectively. Although the overall efficiency is quite low, the output power of the whole system, which is in the order of 0.84 mW for $\Delta T_{Hot\text{-}Cold}$ = 5.67 °C, is enough to supply low power WSs. According to a previous study [12], and supposing a communication cycle of 5 s using a Bluetooth low energy module and three sensors (temperature, current and voltage), on average, each communication cycle consumes an energy of 0.16 J. Therefore, according to Table 6, when ΔT = 5.05 °C, $P_{DC/DC}$ = 0.66 mW, so in 1 h, about 2.4 J are harvested, so, this energy is enough for 10–15 communication cycles per hour. This is not a problem in many applications, because WSs typically operate in an intermittent on–off pattern [42].

Table 6. Steady-state performance results of the entire system.

Current (A_{rms})	r_{ac} (μΩ/m)	$\Delta T_{Hot\text{-}Ambient}$ (°C)	$\Delta T_{Hot\text{-}Cold}$ (°C)	$p_{Joule,conductor}$ (W/m)	$P_{Joule,TEG\text{-}area}$ (W)	$P_{electric,TEG}$ (mW)	$P_{DC/DC}$ (mW)	R_{TEG} (°C/W)	η_{TEG} (%)	$\eta_{TEG+DC/DC}$ (%)
136	5380	20.7	3.4	99.5	0.85	1.24	0.21	3.964	0.15	0.025
169	5448	26.1	3.9	155.6	1.32	2.50	0.34	2.914	0.19	0.026
194	5512	31.7	4.5	207.5	1.76	4.47	0.48	2.534	0.25	0.027
226	5560	37.7	5.1	284.0	2.41	7.34	0.66	2.095	0.30	0.027
254	5622	43.7	5.7	362.7	3.08	11.2	0.84	1.841	0.36	0.027

4.2. Cold Starting

Conventional circuits are based on active circuits that require some level of energy to operate. In the cold start scenario, there is not enough stored energy to supply the circuit components, so the system cannot harvest energy and is stuck in a shutdown state. Circuits with cold starting capability allow scavenging energy in these critical situations, when the storage element is completely depleted. Cold start situations can occur after manufacturing, when the circuit has never been powered on, or when the storage element is completely depleted after prolonged periods of power shortage.

This paper also analyzes the cold start capability of the proposed energy harvesting solution by charging a battery pack with two NiMH cells in series (BM2000C1450AA2S1PATP nickel battery, GlobTek) that were discharged during a previous experiment. The initial voltage between the terminals of the two cells was 1.85 V, or 0.925 V per cell, which corresponds to a discharged condition, since NiMH batteries are

considered discharged below 1 V per cell [43]. Figure 9 shows the output voltage generated by TEG #1 and the battery voltage during a cold start situation, where it can be seen that the system is capable of charging the batteries.

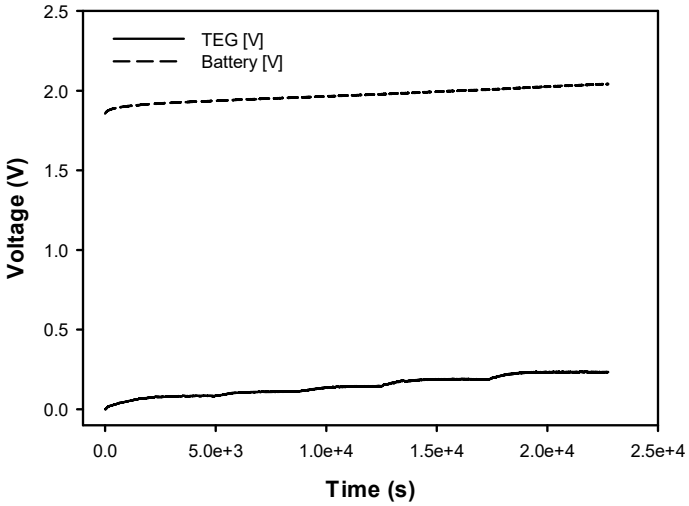

Figure 9. Voltage generated by TEG #1 and the voltage across the battery during a cold start situation using the TEG #1 + DC/DC converter #1 combination.

5. Conclusions

IoT devices with data acquisition and processing capabilities offer solutions for health condition monitoring, which require on-line data monitoring. However, in high-voltage substations applications, as they are often in remote locations and due to harsh environments, the application of these smart devices remains a challenging task. Therefore, a proper and maintenance-free energy harvesting system is required. Thermal energy harvesting has become a hot topic due to the minimal maintenance required, compactness, and solid-state nature. This research work has analyzed different thermal energy harvesting systems and has conducted several experiments to characterize the behavior of each system for high-voltage transmission applications characterized by very low temperature gradients. This work has analyzed the performance of state-of-the-art of TEGs designed to operate with low temperature gradients intended for IoT systems to be applied in AC and DC tubular busbars found in high-voltage substations. Since the tubular busbars are heated by the Joule effect, there is a small temperature difference between the busbar and the ambient, so the TEG converts this heat flow into useful energy, which is used to supply low-power WSs by means of a DC/DC converter. The results presented in this paper have shown that if a temperature difference of around 5 K can be maintained between the hot and cold sides of the thermoelectric power generation modules, it will drive WSs using two 40 mm × 40 mm modules.

Author Contributions: Conceptualization, Y.L., M.M.-E. and J.-R.R.; methodology, J.-R.R.; software, Y.L.; validation, Y.L. and J.S.; formal analysis, M.M.-E. and J.-R.R.; investigation, Y.L., M.M.-E. and J.-R.R.; resources, J.S., M.M.-E. and J.-R.R.; writing—original draft preparation, Y.L. and J.-R.R.; writing—review and editing, M.M.-E.; supervision, J.S. and M.M.-E.; All authors have read and agreed to the published version of the manuscript.

Funding: This research was funded by Generalitat de Catalunya, grant numbers 2021 SGR 00392 and 2020 DI 007.

Institutional Review Board Statement: Not applicable.

Informed Consent Statement: Not applicable.

Data Availability Statement: Not applicable.

Conflicts of Interest: The authors declare no conflict of interest.

References

1. Chen, X.; Sun, L.; Zhu, H.; Zhen, Y.; Chen, H. Application of Internet of Things in Power-Line Monitoring. In Proceedings of the 2012 International Conference on Cyber-Enabled Distributed Computing and Knowledge Discovery, Sanya, China, 10–12 October 2012; pp. 423–426. https://doi.org/10.1109/cyberc.2012.77.
2. Eunice Akin-Ponnle, A.; Borges Carvalho, N.; Poniszewska-Maranda, A.; Maranda, W. Energy Harvesting Mechanisms in a Smart City—A Review. *Smart Cities* **2021**, *4*, 476–498. https://doi.org/10.3390/smartcities4020025.
3. Liu, Y.; Khanbareh, H.; Halim, M.A.; Feeney, A.; Zhang, X.; Heidari, H.; Ghannam, R.; Correspondence, R.; Ghannam, J. Piezoelectric energy harvesting for self-powered wearable upper limb applications. *Nano Sel.* **2021**, *2*, 1459–1479. https://doi.org/10.1002/nano.202000242.
4. Prajwal, K.T.; Manickavasagam, K.; Suresh, R. A review on vibration energy harvesting technologies: Analysis and technologies. *Eur. Phys. J. Spéc. Top.* **2022**, *231*, 1359–1371. https://doi.org/10.1140/epjs/s11734-022-00490-0.
5. Verma, G.; Sharma, V. A Novel RF Energy Harvester for Event-Based Environmental Monitoring in Wireless Sensor Networks. *IEEE Internet Things J.* **2022**, *9*, 3189–3203. https://doi.org/10.1109/jiot.2021.3097629.
6. Mohd Zainuddin, N.; Abd Rahman, M.S.; Ab Kadir, M.Z.A.; Nik Ali, N.H.; Ali, Z.; Osman, M.; Mansor, M.; Mohd Ariffin, A.; Syahmi, M.; Nor, S.F.M.; et al. Review of Thermal Stress and Condition Monitoring Technologies for Overhead Transmission Lines: Issues and Challenges. *IEEE Access* **2020**, *8*, 120053–120081. https://doi.org/10.1109/access.2020.3004578.
7. Liu, Y.; Riba, J.-R.; Moreno-Eguilaz, M.; Sanllehí, J. Analysis of a Smart Sensor Based Solution for Smart Grids Real-Time Dynamic Thermal Line Rating. *Sensors* **2021**, *21*, 7388. https://doi.org/10.3390/s21217388.
8. Risdiyanto, A.; Arifin, M.; Khayam, U.; Suwarno Study on temperature distribution at busbar connection based on contact resistance of different plating contact surface. In Proceedings of the 2013 Joint International Conference on Rural Information & Communication Technology and Electric-Vehicle Technology (rICT & ICeV-T), Bandung, Indonesia, 26–28 November 2013. https://doi.org/10.1109/rict-icevt.2013.6741537.
9. Kadechkar, A.; Capelli, F.; Riba, J.-R.; Moreno-Eguilaz, M. Feasibility Study on Thermal Energy Harvesting for Low Powered Electronics in High-Voltage Substations. In Proceedings of the IECON 2018—44th Annual Conference of the IEEE Industrial Electronics Society, Washington, DC, USA, 21–23 October 2018; pp. 4224–4229. https://doi.org/10.1109/iecon.2018.8591532.
10. Bellini, P.; Nesi, P.; Pantaleo, G. IoT-Enabled Smart Cities: A Review of Concepts, Frameworks and Key Technologies. *Appl. Sci.* **2022**, *12*, 1607. https://doi.org/10.3390/app12031607.
11. Al Mamun, A.; Yuce, M.R. Sensors and Systems for Wearable Environmental Monitoring Toward IoT-Enabled Applications: A Review. *IEEE Sens. J.* **2019**, *19*, 7771–7788. https://doi.org/10.1109/jsen.2019.2919352.
12. Kadechkar, A.; Riba, J.-R.; Moreno-Eguilaz, M.; Perez, J. *SmartConnector*: A Self-Powered IoT Solution to Ease Predictive Maintenance in Substations. *IEEE Sens. J.* **2020**, *20*, 11632–11641. https://doi.org/10.1109/jsen.2020.2998157.
13. Kadechkar, A.; Moreno-Eguilaz, M.; Riba, J.-R.; Capelli, F. Low-Cost Online Contact Resistance Measurement of Power Connectors to Ease Predictive Maintenance. *IEEE Trans. Instrum. Meas.* **2019**, *68*, 4825–4833. https://doi.org/10.1109/tim.2019.2899481.
14. Vitolo, P.; De Vita, A.; Di Benedetto, L.; Pau, D.; Licciardo, G.D. Low-Power Detection and Classification for In-Sensor Predictive Maintenance Based on Vibration Monitoring. *IEEE Sens. J.* **2022**, *22*, 6942–6951. https://doi.org/10.1109/jsen.2022.3154479.
15. Riba, J.-R.; Moreno-Eguilaz, M.; Bogarra, S. Energy Harvesting Methods for Transmission Lines: A Comprehensive Review. *Appl. Sci.* **2022**, *12*, 10699. https://doi.org/10.3390/app122110699.
16. Schlechter, T. Energy Harvesting Approaches for Wireless Sensor Nodes In High Voltage Direct Current Systems. In Proceedings of the 2019 IEEE 5th World Forum on Internet of Things (WF-IoT), Limerick, Ireland, 15–18 April 2019; pp. 243–246. https://doi.org/10.1109/wf-iot.2019.8767253.
17. Moghe, R.; Yang, Y.; Lambert, F.; Divan, D. A scoping study of electric and magnetic field energy harvesting for wireless sensor networks in power system applications. In Proceedings of the 2009 IEEE Energy Conversion Congress and Exposition, San Jose, CA, USA, 20–24 September 2009; pp. 3550–3557.
18. Sudevalayam, S.; Kulkarni, P. Energy Harvesting Sensor Nodes: Survey and Implications. *IEEE Commun. Surv. Tutorials* **2011**, *13*, 443–461. https://doi.org/10.1109/surv.2011.060710.00094.
19. Cetinkaya, O.; Akan, O.B. Electric-Field Energy Harvesting in Wireless Networks. *IEEE Wirel. Commun.* **2017**, *24*, 34–41. https://doi.org/10.1109/mwc.2017.1600215.
20. Guo, F.; Hayat, H.; Wang, J. Energy harvesting devices for high voltage transmission line monitoring. In Proceedings of the 2011 IEEE Power and Energy Society General Meeting, Detroit, MI, USA, 24–28 July 2011; Volume 43210, pp. 1–8. https://doi.org/10.1109/pes.2011.6039037.
21. Jouhara, H.; Żabnieńska-Góra, A.; Khordehgah, N.; Doraghi, Q.; Ahmad, L.; Norman, L.; Axcell, B.; Wrobel, L.; Dai, S. Thermoelectric generator (TEG) technologies and applications. *Int. J. Thermofluids* **2021**, *9*, 100063. https://doi.org/10.1016/j.ijft.2021.100063.

22. Becker, T.; Kluge, M.; Schalk, J.; Otterpohl, T.; Hilleringmann, U. Power management for thermal energy harvesting in aircrafts. In Proceedings of the IEEE Sensors Conference, IEEE, Lecce, IT, USA, 26–29 October 2008; pp. 681–684. https://doi.org/10.1109/ICSENS.2008.4716533.
23. Jouhara, H.; Khordehgah, N.; Almahmoud, S.; Delpech, B.; Chauhan, A.; Tassou, S.A. Waste heat recovery technologies and applications. *Therm. Sci. Eng. Prog.* **2018**, *6*, 268–289. https://doi.org/10.1016/j.tsep.2018.04.017.
24. Moultif, N.; Divay, A.; Joubert, E.; Latry, O. Reliability Study of High-Power Mechatronic Components by Spectral Photoemission Microscopy. *Reliab. High-Power Mechatron. Syst. 2 Aerosp. Automot. Appl. Issues Test. Anal.* **2017**, 241–271. https://doi.org/10.1016/b978-1-78548-261-8.50008-5.
25. How Thermoelectric Generators Work—Applied Thermoelectric Solutions LLC. Available online: https://thermoelectricsolutions.com/how-thermoelectric-generators-work/ (accessed on 5 October 2022).
26. Thermoelectricity Using Semiconductor Thermocouples. Available online: https://www.mpoweruk.com/thermoelectricity.htm (accessed on 5 October 2022).
27. Di Stefano, V.; Muscato, O. Seebeck Effect in Silicon Semiconductors. *Acta Appl. Math.* **2012**, *122*, 225–238. https://doi.org/10.1007/s10440-012-9739-6.
28. Cai, J.; Mahan, G.D. Effective Seebeck coefficient for semiconductors. *Phys. Rev. B—Condens. Matter Mater. Phys.* **2006**, *74*, 075201. https://doi.org/10.1103/physrevb.74.075201.
29. Goldsmid, H.J. Bismuth Telluride and Its Alloys as Materials for Thermoelectric Generation. *Materials* **2014**, *7*, 2577–2592. https://doi.org/10.3390/ma7042577.
30. Kim, H.S.; Liu, W.; Chen, G.; Chu, C.-W.; Ren, Z. Relationship between thermoelectric figure of merit and energy conversion efficiency. *Proc. Natl. Acad. Sci. USA* **2015**, *112*, 8205–8210. https://doi.org/10.1073/pnas.1510231112.
31. Stobart, R.; Milner, D. The Potential for Thermo-Electric Regeneration of Energy in Vehicles. *SAE Tech. Pap.* **2009**,*14* https://doi.org/10.4271/2009-01-1333.
32. Remeli, M.F.; Date, A.; Orr, B.; Ding, L.C.; Singh, B.; Affandi, N.D.N.; Akbarzadeh, A. Experimental investigation of combined heat recovery and power generation using a heat pipe assisted thermoelectric generator system. *Energy Convers. Manag.* **2016**, *111*, 147–157. https://doi.org/10.1016/j.enconman.2015.12.032.
33. Angrist, S.W. *Direct Energy Conversion*; Allyn and Bacon: Boston, MA, USA, 1982; ISBN 0205077587.
34. Orr, B.; Singh, B.; Tan, L.; Akbarzadeh, A. Electricity generation from an exhaust heat recovery system utilising thermoelectric cells and heat pipes. *Appl. Therm. Eng.* **2014**, *73*, 588–597. https://doi.org/10.1016/j.applthermaleng.2014.07.056.
35. Orr, B.; Taglieri, J.; Ding, L.C.; Akbarzadeh, A. Validating an alternative method to predict thermoelectric generator performance. *Energy Convers. Manag.* **2016**, *116*, 134–141. https://doi.org/10.1016/j.enconman.2016.02.074.
36. Shuai, J.; Kim, H.S.; Lan, Y.; Chen, S.; Liu, Y.; Zhao, H.; Sui, J.; Ren, Z. Study on thermoelectric performance by Na doping in nanostructured Mg1-Na Ag0.97Sb0.99. *Nano Energy* **2015**, *11*, 640–646. https://doi.org/10.1016/j.nanoen.2014.11.027.
37. Wu, Y.; Zuo, L.; Chen, J.; Klein, J.A. A model to analyze the device level performance of thermoelectric generator. *Energy* **2016**, *115*, 591–603. https://doi.org/10.1016/j.energy.2016.09.044.
38. Champier, D. Thermoelectric generators: A review of applications. *Energy Convers. Manag.* **2017**, *140*, 167–181. https://doi.org/10.1016/j.enconman.2017.02.070.
39. Rare Earth Elements—Critical Resources for High Technology|USGS Fact Sheet 087-02. Available online: https://pubs.usgs.gov/fs/2002/fs087-02/ (accessed on 5 October 2022).
40. Meng, J.-H.; Zhang, X.-X.; Wang, X.-D. Dynamic response characteristics of thermoelectric generator predicted by a three-dimensional heat-electricity coupled model. *J. Power Sources* **2014**, *245*, 262–269. https://doi.org/10.1016/j.jpowsour.2013.06.127.
41. IEEE. *IEEE Std 605-2008 Guide for Bus Design in Air Insulated Substations*; IEEE: Piscataway, NJ, USA, 2010; ISBN 9780738158570.
42. Sabovic, A.; Delgado, C.; Subotic, D.; Jooris, B.; De Poorter, E.; Famaey, J. Energy-Aware Sensing on Battery-Less LoRaWAN Devices with Energy Harvesting. *Electronics* **2020**, *9*, 904. https://doi.org/10.3390/electronics9060904.
43. Kang, J.; Yan, F.; Zhang, P.; Du, C. Comparison of comprehensive properties of Ni-MH (nickel-metal hydride) and Li-ion (lithium-ion) batteries in terms of energy efficiency. *Energy* **2014**, *70*, 618–625. https://doi.org/10.1016/j.energy.2014.04.038.

5.3 Denoising of Online Resistance Measurements of Power Connectors for IoT Applications

Reference:

 Y. Liu, J. Riba, and M. Moreno-Eguilaz, "Denoising of Online Resistance Measurements of Power Connectors for IoT Applications," *Proc. IECON 2023 - 49th Annu. Conf. IEEE Ind. Electron. Soc*, Singapore, 2023. DOI: 10.1109/IECON51785.2023.10311806

Publication framework:

This article implements the simple moving average filter (SMAF), the Kalman filter (KF), and the sum of sine filter (SoSF) on the desktop platform and conducts an analysis using these three filtering algorithms to reduce signal noise existing in an IoT device mounted in a high-current laboratory. Next, the most appropriate algorithm is chosen and implemented in the IoT device to ease the real-time signal processing task and obtain accurate ECR measurements.

Main contributions:

- **Review of statistical filtering algorithms for real-time monitoring applications.**
- **Development and implementation of filtering algorithms on the desktop platform.**
- **Selection and implementation of the most suitable algorithm on the embedded system of an IoT device.**

Key words:

filter, power connector, electrical contact resistance

Denoising of Online Resistance Measurements of Power Connectors for IoT Applications

Yuming Liu[1,2], Jordi-Roger Riba[1,] Manuel Moreno-Eguilaz[1], Josep Sanllehí[2]

[1]Dept. of Electrical Engineering, Universitat Politècnica de Catalunya, 08222 Terrassa (Barcelona Spain)

[2]Engineering Department, SBI Connectors, Sant Esteve Sesrovires (Barcelona Spain)

Corresponding author: jordi.riba-ruiz@upc.edu

ORCID number of the corresponding author: 0000-0001-8774-2389

***Abstract*— The increasing development of the Internet of Things (IoT) allows the acquisition of key parameters to develop health monitoring strategies for power transmission systems. These IoT devices need to incorporate sensors for data acquisition. However, noise is often present in the signals, especially in AC systems, making it a challenging task to obtain an accurate response from the deployed sensors. This paper develops simple moving average filter (SMAF), kalman filter (KF), and sum of sine filter (SoSF) on desktop platform, and analyzes these three filtering algorithms used to reduce signal noise from an IoT device mounted in a high-current laboratory. The IoT device can estimate the electrical contact resistance (ECR) in real time using smart sensors. Then, the most suitable algorithm is selected and implemented in the IoT device to facilitate the real-time signal processing task and obtain accurate ECR measurements. The experimental results have proven the feasibility and suitability of the proposed approach as it allows to extract useful information from the signals, thus facilitating the predictive maintenance task. The experimental results show that with the help of filtering algorithms, the error of raw signal is significantly reduced. For instance, when 312Arms is injected into the electrical loop, measurement error is 12.1% with raw signal and 1.9%, 3.4%, 2.1% using SMAF with moving window equal to 8, KF and SoSF, respectively. Furthermore, it is shown that with the approriate application of the filter, the IoT device is able to obtain highly accurate ECR measurements even at relatively low current.**

Keywords—filter, power connector, electrical contact resistance

I. INTRODUCTION

There is an increasing demand for stability and reliability in power systems. Therefore, minimizing power outages or potential power system failures is critical. Power connectors are perhaps the weakest components in power transmission systems, and failure of these elements can lead to severe power outages with costly and catastrophic consequences [1]. Therefore, there is an increasing need to monitor the health of thses connectors in order to apply a predictive maintenance plan to avoid network failures.

Electrical contact resistance (ECR) is considered to be the health indicator of substation connectors [2]. Hence, the real-time acquisition of ECR data is a reliable solution for predictive maintenance. However, it is a challenging task to directly measure this parameter because it is in the order of a few micro-ohms. In [3], a novel method was proposed to obtain ECR in real time by measuring the main parameters. However, since the power connectors are usually located in remote places and due to high voltage limitations, human intervention should be minimized. Thus, a low-cost IoT solution was developed to perform the data acquisition of ECR wirelessly. It is a promising solution that provides experimentally proven accuracy of ECR measurements to enable predictive maintenance. However, the unwanted electromagnetic (EM) noise from power transmission lines or busbars can interfere with the weak electrical signal obtained from the line [4], [5]. In addition, since power electronic devices are non-linear, the presence of harmonic noise is inevitable [6]. This signal noise leads to inaccurate ECR measurements, making it impossible to apply the predictive maintenance in extreme conditions.

However, some research groups have attempted to address the above issues by using signal filtering methods. With the increasing development of IoT applications, digital filtering algorithms have attracted worldwide attention in recent years. They play a key role in signal processing, providing solutions to extract useful information from noisy signals, thus helping to achieve more accurate responses from IoT devices [7]. Although many filtering algorithms have been developed for condition monitoring purposes, such as Kalman filter, moving average, harmonic filtering, proportional integral differential (PID), etc [8]–[10], they are usually implemented on desktop platforms where computational resources are not an issue. Nevertheless, there is a lack of work implementing these filters on the embedded system in a very specific high-current environment to optimize ECR measurements.

Motivated by the above limitations, this paper proposes to investigate a simple but effective and easily implemented filtering algorithm to perform online ECR measurements. To this end, three different filtering algorithms were first tested on a desktop platform to clean or denoise the acquired noisy signal. Their performance was compared and analyzed in terms of computational time (CT) and accuracy of ECR measurements. Next, the most suitable filter was selected to be implemented on the embedded system of the IoT device to validate the feasibility for real-time online ECR measurements.

Fig. 1 shows the main components of the filter-based online ECR measurement method proposed in this paper, which includes several sensors to determine the main parameters,

filters implemented on the embedded system for signal processing, and a communication module to transmit the filtered data to the cloud for further processing.

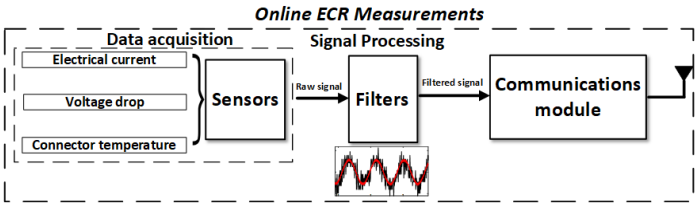

Fig. 1. Proposed online filter-based ECR measurement method.

II. Online Resistance Measurements

ECR is the main health indicator of the substation connector [11]. However, since the ECR is in the order of micro-ohms, it is a challenging task to measure the ECR of the power connectors online for real-time health monitoring. In [12], a novel method was proposed to obtain the ECR under AC supply by simultaneously measuring the voltage across the connector and the current flowing through the busbar [13],

$$R_{20°C} = \frac{\Delta V_{connector} \cdot \cos\varphi}{I_{busbar}} / [1 + \alpha(T_{connector} - 20)] \quad (1)$$

where $R_{20°C}$ is the electrical contact resistance at a standard temperature of 20 °C, $\Delta V_{connector}$ is the voltage drop across the two terminals of the substation connector, I_{busbar} is the current flowing through the busbar, α is the temperature coefficient of the resistance and $T_{connector}$ is the temperature of the connector and φ is the phase angle between the current (I_{busbar}) and voltage drop ($\Delta V_{connector}$) signals, which can be estimated as [13],

$$\varphi = \arccos\left(\frac{\sum_{i=1}^{N} \Delta V_{connector\_ac}[i-1] \cdot V_{current\_ac}[i-1]}{\sqrt{\sum_{i=1}^{N-1} \left|\Delta V_{connector\_ac}[i-1]\right|^2 \cdot \sum_{i=1}^{N-1} \left|V_{current\_ac}[i-1]\right|^2}} \right) \quad (2)$$

where $\Delta V_{connector\_ac}$ and $V_{current\_ac}$ are the AC output components of the voltage drop and current sensors, respectively.

For the current measurement, a non-contact Hall effect sensor was used in the IoT device. According to the Biot-Savart law, the Hall effect sensor detects the magnetic field generated by the AC current injected into the busbar and converts it into a proportional output voltage of the sensor which is linearly related to the current flowing in the busbar [12]. Thus, when a relatively small current is injected into the busbar, the small magnetic field generated results in a large amount of signal noise from the sensor.

For the voltage measurement, an instrumentation amplifier was used to amplify and measure the voltage drop across the connector, as the expected voltage is in the order of mV. Similar to the Hall effect sensor, although the instrumentation amplifier connector can reduce the common mode noise, there is still residual noise due to the low level of voltage being measured, which can significantly affect the accuracy of the voltage measurement. In addition, according to equation (2), the phase shift (φ) estimation is based on the electrical signals from the current and voltage sensors, so the signal noise could lead to an inaccurate phase angle estimation.

III. Filtering Algorithms

A. Simple Moving Average Filter

The simple moving average filter (SMAF) is a linear recursive filter that can be used to smooth out the short-term fluctuations in the data. This filter requires significantly less memory and computational resources than other filtering methods, which is the main concern for the embedded system applications. It calculates the average of the last k samples as,

$$\hat{y}(t) = \frac{1}{n} \sum_{k=1}^{n} y_k \quad (3)$$

where $\hat{y}(t)$ is the output bias at time t, n is the number of points considered in the moving window, and y_k is the sample at point k.

However, increasing the number of n reduces the dynamic response of the system measurement, which rejects the actual system measured response due to disturbances as noise [14]. Therefore, careful analysis is required to select the suitable moving window k. In this research work, to balance the noise reduction and dynamic response, we have applied and analyzed the SMAF filter with moving window k = 2, 5, 8 on ECR measurements, respectively.

B. Kalman Filter

The Kalman filter (KF) is one of the most important and widely used filtering algorithms in real-time applications due to its small memory requirement, excellent recursive properties, and optimal estimator functionality [15], [16]. Therefore, due to the limited computational resources of IoT devices, a linear KF is proposed in this paper. To implement the KF, it is necessary to model the system, predict future states $\hat{y}_k^-$ using the current state $\hat{y}_{k-1}^+$ at time-step $k-1$ and update the current state $\hat{y}_k^+$ at time-step k with the experimental measurements z_k. The process is ilustrated in Fig. 2.

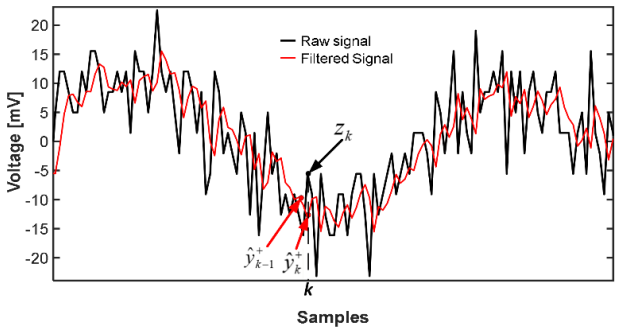

Fig. 2. Kalman filtering implementation.

The design of KF includes two steps, i.e., prediction of future states and updating of current states.

The first step is to compute the prediction of the estimated covariance $\hat{p}_k^-$ and the covariance of innovation $\hat{s}_k^-$ as [14],

$$\hat{p}_k^- = \hat{p}_{k-1}^+ + Q_k \quad (4)$$

$$\hat{s}_k^- = \hat{p}_k^- + R_k \quad (5)$$

where $\hat{p}_{k-1}^+$ is the covariance of the estimation error at time step k - 1 in the one-dimensional Kalman filter, while the system process noise covariance Q_k and the covariance of measurements noise R are set to be constant, being $Q_k = Q$ and $R_k = R$, respectively.

Next, the Kalman gain G can be calculated as using equations (4) and (5),

$$G = \hat{p}_k^- / \hat{s}_k^- \quad (6)$$

The prediction of the future state ($\hat{y}_k^-$) is done by taking the state vector of the previous time step (k-1) [14] as,

$$\hat{y}_k^- = F_k \hat{y}_{k-1}^+ \quad (7)$$

where $\hat{y}_{k-1}^+$ is the current state at time step $k - 1$ and F_k is the state-transition model. Next, the system update is performed as,

$$\hat{y}_k^+ = G \cdot (z_k - \hat{y}_k^-) + \hat{y}_k^- \quad (8)$$

where z_k is the experimental measurement at time-step k, $\hat{y}_k^+$ is the updated current state at time-step k, $\hat{y}_k^-$ is the prediction of the future state at time-step k , and G is the Kalman gain.

Next, the update of the covariance of the estimation error $\hat{p}_k^+$ is calculated as,

$$\hat{p}_k^+ = \hat{p}_k^- \cdot (1 - G) \quad (9)$$

where $\hat{p}_k^-$ is the prediction of the estimated covariance at time-step k.

It is worth noting that the initialization of the Kalman filter plays a key role in the modelling of the Kalman filter, so the most appropriate seed values of the current state $\hat{y}_0^+$, the estimation of the covariance $\hat{p}_0^+$, the covariance of the system process noise Q_k, and the covariance of the measurement noise R_k are predetermined according to the best experience of the author. In this paper it is assumed that $Q_k = Q$ and $R_k = R$ are constant values. The initial value of the state vector $\hat{y}_0^+$ is chosen to be 0.02, in the order of magnitude of the waveform to be filtered (see Fig. 2), while a higher initial value is given to $\hat{p}_0^+ = 1$, since it represents the covariance of the estimation error. Finally, the system process noise covariance Q is set to 0.001 and the measurement noise covariance R is set to 0.003. Finally, the state-transition model F_k is set to 1. Note that Q and R are set to 0.001 and 0.003 respectively to the best knowledge of the author.

Thus, the final algorithm is as follows,

1.- Initialization of $\hat{y}_0^+ = 0.02$, $\hat{p}_0^+ = 1$, $Q = 0.001$ and $R = 0.003$.

2.- $\hat{p}_k^- = \hat{p}_{k-1}^+ + Q$

3.- $\hat{s}_k^- = \hat{p}_k^- + R$

4.- $G = \hat{p}_k^- / \hat{s}_k^-$

5.- $\hat{y}_k^- = \hat{y}_{k-1}^+$

6.- $\hat{y}_k^+ = G \cdot (z_k - \hat{y}_k^-) + \hat{y}_k^-$

C. Sum of Sine Filter

Harmonic filtering has been widely used in digital filtering applications because of its simplicity, low computational cost, and ability to extract the correct information. It is a sum of sine and cosine functions used to describe a periodic signal. The functional form of the harmonic filter can be written as [10],

$$\hat{y}_k(t_i) = a_0 + \sum_{k=1}^{N} a_k \cos(\frac{\pi t_i k}{D}) + \sum_{k=1}^{N} b_k \sin(\frac{\pi t_i k}{D}) \quad (10)$$

where a_0 is the DC offset in the signal, a_k and b_k are variables of the model, D is the length of the time series for each calculation cycle, t_i are time stamps of the data under analysis, N is the number of harmonic terms in the series. The variables are computed by means of weighted linear minimization.

However, in (10) a phase term is missing, which could increase the compactness of the filtering algorithm. Therefore, in this article, a discrete series of harmonic sine functions similar to the harmonic filter form proposed in [10] is proposed, which is called sum of sine filter (SoSF), since real signals can be considered as summation of sine waves [17]. Its functional form can be described as,

$$\hat{y}_i = \sum_{k=1}^{N} a_k \sin(b_k x_i + c_k) \quad (11)$$

where k is the number of sine terms considered with $k = 1, \ldots N$, where N is the number of sine terms. x_i is the sample at time-step i, $\hat{y}_i$ is the output estimation at time-step i with $i = 1, \ldots, n$, n being the total number of samples in the signal to be filtered. The amplitude a_k, fundamental frequency b_k and phase shift c_k are determined using the nonlinear least square (NLS) approximation method [18]. In this paper, based on the author's experience, N is set to 2, which means that two sinusoidal waves are used to fit the regression model.

IV. Experimental Setup

To evaluate and validate the feasibility and performance of the proposed filters, several experiments were performed in a high current laboratory. First, the filters were implemented on a desktop platform with the instantaneous measurements of the IoT device to select the most suitable filter for this application. Next, the selected filter algorithm was implemented in the embedded system of the IoT device to perform the online measurements of the contact resistance.

The experimental setup is shown in Fig. 3. To perform the tests in the high-current laboratory, two cylindrical busbars (Al alloy 6063-T5, length = 2000 mm, thickness = 6 mm) electrically connected by the analyzed substation straight connector (A356.0 alloy, length = 230 mm, inner diameter = 120 mm) were used to form an electrical loop.

Since the contact resistance of the substation connector is in the order of micro-ohms, it is a challenging task to perform on-line measurements of such a low value. As described in Section II, it is necessary to measure the current, the voltage across the connector, and the temperature of the connector to perform the on-line contact resistance measurements For this purpose, the IoT device includes a contactless current sensor (DRA5053 analog bipolar Hall effect sensor, Texas Instruments, Dallas,

TX, USA), an instrumentation amplifier (AD627) to amplify the voltage drop signal across the connector, a PT1000 temperature sensor (PTFC102T1G0, Schaffhausen, Switzerland) with an accuracy of ±0.1 °C to obtain the temperature measurements.

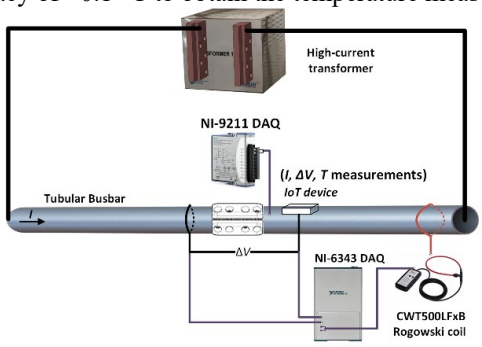

Fig. 3. Experimental setup in high current laboratory.

In addition, a low-power nRF52832 microcontroller unit (Nordic Semiconductor, Trondheim, Norway) with a built-in BLE module and ADC converter was used. This microchip allows the implementation of the filtering algorithm and the built-in BLE module allows the transmission of the data collected from the sensors to the nearby gateway Raspberry Pi.

To evaluate the accuracy of the online measurements provided by the filter-based IoT device, a wired DAS (data acquisition system) was used, including a data acquisition module (NI USB-6343 DAQ, National Instruments, Dallas, TX, USA) and a thermocouple module (NI-9211, National Instruments, Dallas, TX, USA). The data acquisition module is connected to the two end terminals of the connector and a Rogowski coil (CWT500LFxB from PEM, Nottingham, UK) with a sensitivity of 0.06mV/A is used to obtain the voltage drop and current measurements, respectively. At the same time, a T-type thermocouple is connected to the thermocouple module to measure the busbar temperature.

V. Experimental Results

The experiment consists of two stages to validate the effectiveness of the proposed methodology. The first stage involves filtering the real signals from the smart sensor with different algorithms. In the second stage, the most appropriate filtering algorithm is used for the continuous online ECR measurements.

A. Performance evaluation

This section evaluates the performance and efficiency of the different filtering algorithms used to process the electrical signals obtained in the high-current laboratory with the IoT device. The IoT device was set to debug mode to acquire instantaneous samples from the sensors.

For simplicity, the analysis is performed on a desktop platform using a 2.10 GHz Xeon(r) CPU E5-2620 with 64Mb RAM memory, 64-bit WIN10 operating system, and MATLAB 2021b. The measurements of DAS are used to evaluate the filtering accuracy, and the filtering efficiency is evaluated according to the computational time (CT).

As shown in Fig. 4, when the current flowing through the busbar is as low as 150 A_{RMS}, the output signals from the current and voltage sensors suffer significantly from noise. This is due to the very low output values generated by the sensors. Therefore, a suitable filtering algorithm is required. Filters are used to purify the signal. This helps to extract the true signals from the sensors, thereby increasing the accuracy of the measurements.

On the other hand, the signal noise almost disappears in the high current application (around 900 A_{RMS}), as shown in Fig. 5. In this case, the filtering algorithms may not play a dominant role since the IoT device can already provide raw measurements with an average error as low as 3.7%, as shown in Table I.

Table I summarizes the results of the comparison between different filters at five power levels. It can be seen that without the implementation of filters, the IoT device tends to provide very inaccurate raw ECR measurements, with 37.1% and 12.1% at around 150 A_{RMS} and 310 A_{RMS}, respectively. In particular, when 150 A_{RMS} is injected into the loop, a large amount of noise remains in the signal even with SMAF 2, SMAF 5, and KF, while SMAF 8 and SoSF can successfully help the IoT device keep an error of ECR measurements below 5% at all five current levels. In conclusion, the SMAF provides more accuracte measurements than SoSF and KF in most cases. This is due to the fact that the SoSF and KF are highly dependent on the knowledge of the raw measurements, for instance, it is important to know the system process noise and measurement noise beforehand to build KF model.

TABLE I
Comparison Between Filtering Accuracy and Efficiency

Current	154A	312A	480A	684A	920A
ECR (DAS)	**8.48** μΩ	**8.45** μΩ	**8.45** μΩ	**8.43** μΩ	**8.43** μΩ
ECR (RAW)	5.33 μΩ	7.43 μΩ	8.10 μΩ	8.23 μΩ	8.74 μΩ
ECR (SMAF 2)	6.51 μΩ	7.93 μΩ	8.12 μΩ	8.14 μΩ	8.58 μΩ
ECR (SMAF 5)	7.64 μΩ	8.17 μΩ	8.65 μΩ	8.21 μΩ	8.61 μΩ
ECR (SMAF 8)	8.12 μΩ	8.61 μΩ	8.34 μΩ	8.31 μΩ	8.56 μΩ
ECR (KF)	7.11 μΩ	8.18 μΩ	8.23 μΩ	8.20 μΩ	8.62 μΩ
ECR (SoSF)	8.16 μΩ	8.63 μΩ	8.25 μΩ	8.27 μΩ	8.67 μΩ
Error (RAW)	37.1 %	12.1 %	4.1 %	2.4 %	3.7 %
Error (SMAF 2)	23.2 %	6.2 %	3.9 %	3.4 %	1.8 %
Error (SMAF 5)	9.9 %	3.3 %	2.4 %	2.6 %	2.1 %
Error (SMAF 8)	4.2 %	**1.9** %	**1.5 %**	**1.4 %**	**1.5 %**
Error (KF)	16.2 %	3.2 %	2.6 %	2.7 %	2.3 %
Error (SoSF)	**3.8 %**	2.1**%**	2.4 %	1.9%	2.8 %
CT (SMAF 2)	0.0055 s	**0.0048 s**	0.0055 s	0.0053 s	0.0053 s
CT (SMAF 5)	0.0054 s	0.0049 s	**0.0054 s**	0.0051 s	0.0056 s
CT (SMAF 8)	**0.0054 s**	0.0049 s	0.0058 s	**0.0051 s**	**0.0053 s**
CT (KF)	0.0070 s	0.0064 s	0.0065 s	0.0063 s	0.0065 s
CT (SoSF)	0.2532 s	0.2719 s	0.1836 s	0.1543 s	0.3113 s

* SMAF 2, 5 and 8 means that the moving window is equal to 2, 5 and 8, respectively.

In terms of filtering efficiency, the SoSF has a CT that is significantly higher than the CT of other methods, which means that the SoSF algorithm requires complex computational resources. This is due to the complex Fourier series calculation for each iteration required by the SoSF method. As the both SMAF and KF are recursive algorithms, they are relatively simpler and require less computational resources. Moreover, as shown in Table I, the CT of SMAF method has almost the same computational time due to its simplicity.

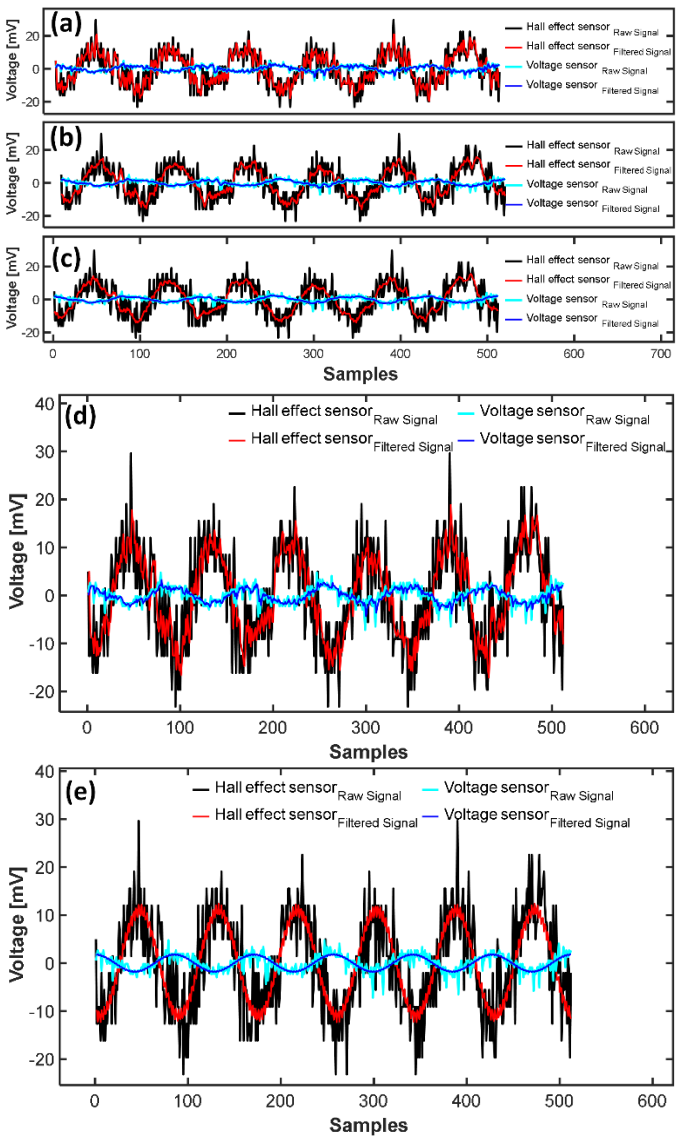

Fig. 4. Raw and filtered signals with a current of 150 A_{RMS}. (a), (b) and (c) Signals processed using SMAF with moving window = 2, 5 and 8, respectively. (d) Signals processed with the KF algorithm. (e) Signals processed with the SoSF algorithm.

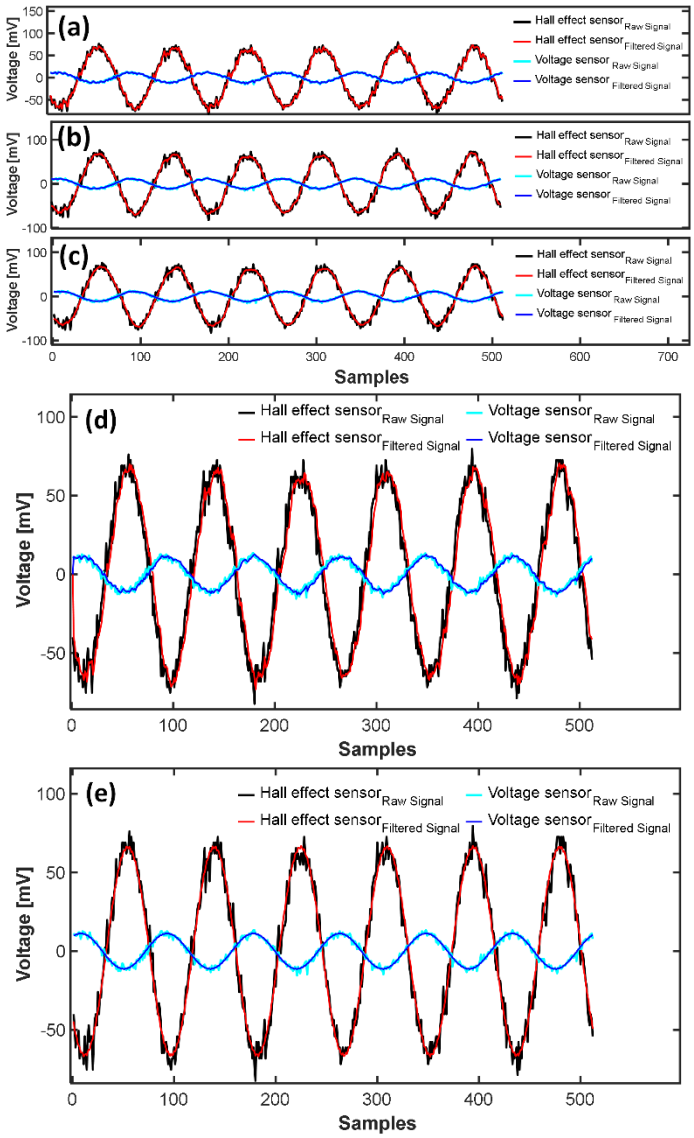

Fig. 5. Raw and filtered signals with a current of 920 A_{RMS}. (a), (b) and (c) Signals processed using SMAF with moving window = 2, 5 and 8, respectively. (d) Signals processed with the KF algorithm. (e) Signals processed with the SoSF algorithm.

B. Online contact resistance measurements

To verify the feasibility of the proposed filtering algorithm, the IoT device with the filtering algorithm implemented on the built-in system was tested under five different current levels (140 A_{RMS}, 310 A_{RMS}, 500 A_{RMS}, 700 A_{RMS} and 900 A_{RMS}) for continuous ECR measurements.

Prior to applying electric current to the loop, the DC contact resistance was measured as a reference value using the 4-wire method [12] with a calibrated micro-ohmmeter.

Next, the DAS and the IoT device with and without the filtering algorithm were used to take the continuous ECR measurements simultaneously.

Fig. 6 shows the results of the continuous measurements. It can be seen that the IoT device with and without the filter provides fluctuating ECR measurements at low current levels (140 A_{RMS}, 310 A_{RMS}), while this fluctuation decreases as the increase of current injected. Nevertheless, the IoT device without filter can only provide high accuracy measurements above 500 A_{RMS}, while after implementing the filter, high accuracy measurements above 140 A_{RMS} can be obtained.

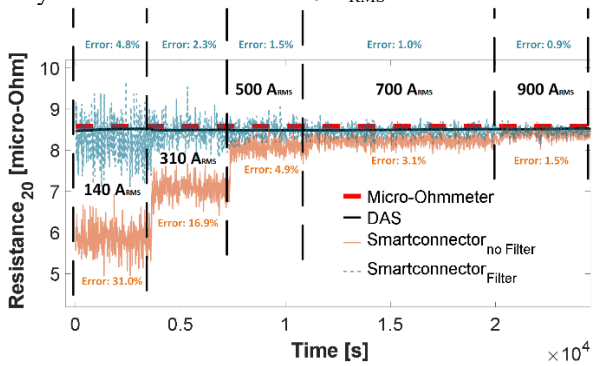

Fig. 6. Continuous electrical contact resistance measurements using the DC Micro-Ohmmeter, DAS and the IoT device.

VI. Conclusion

Three different filtering algorithms were proposed and initially tested on the desktop platform with the data obtained from the high current laboratory. By using these algorithms, the electrical signals from the sensors were purified and the IoT device can obtain highly accurate ECR measurements at the current level as low as approximatelt 150 A_{RMS}.

Due to the limited computational resources of common IoT devices, the design goal of this paper is simplicity. Therefore, after carefully comparing these three algorithms in terms of performance and computational efficiency, the SMAF was considered to be the most suitable filter for this application. Next, this filter was implemented on the embedded system of the IoT device for continuous online ECR measurements to validate its effectiveness. The results obtained show that the objective was achieved. Compared to the ECR measurements taken by the IoT device without applying the filter, the proposed filter has significantly increased the accuracy of the measurements, especially at low currents. For example, when about 150 A_{RMS} were injected, the error with the filter is 4.8%, while the error without the filter is 31%. It is worth noting that the proposed filtering algorithms can also be applied to many other signal processing applications affected by noisy acquired signals.

Acknowledgment

This research was funded by Generalitat de Catalunya, grant numbers 2021 SGR 00392 and 2020 DI 007.

References

[1] F. Capelli, J.-R. Riba, and J. Sanllehí, “Finite element analysis to predict temperature rise tests in high-capacity substation connectors,” *IET Gener. Transm. Distrib.*, vol. 11, no. 9, pp. 2283–2291, Jun. 2017.

[2] International Electrotechnical Commission, “IEC TS 61586:2017 Estimation of the reliability of electrical connectors.” IEC, pp. 1–55, 2017.

[3] A. Kadechkar, J. R. Riba, M. Moreno-Eguilaz, F. Capelli, and D. Gonzalez, “On-line Resistance Measurement of Substation Connectors Focused on Predictive Maintenance,” *Proc. - 2018 IEEE 18th Int. Conf. Power Electron. Motion Control. PEMC 2018*, no. 1, pp. 846–851, 2018.

[4] M. Yamaguchi, K. H. Kim, T. Kuribara, and K. I. Arai, “Thin-film RF noise suppressor integrated in a transmission line,” *IEEE Trans. Magn.*, vol. 38, no. 5 I, pp. 3183–3185, 2002.

[5] S. Jinno, S. Kitora, H. Toki, and M. Abe, “Mechanism of Common-mode Noise Generation in Multi-conductor Transmission Lines,” *Sci. Reports 2019 91*, vol. 9, no. 1, pp. 1–8, Oct. 2019.

[6] J. Gong, D. Li, T. Wang, W. Pan, and X. Ding, “A comprehensive review of improving power quality using active power filters,” *Electr. Power Syst. Res.*, vol. 199, p. 107389, Oct. 2021.

[7] C. Morales-Perez, J. Rangel-Magdaleno, H. Peregrina-Barreto, J. Cerezo-Sanchez, and A. Leon-Bonilla, “Selective Signal Extraction based on OMP algorithm and DCT and DST Dictionaries,” *2022 IEEE Int. Autumn Meet. Power, Electron. Comput. ROPEC 2022*, 2022.

[8] P. Gangsar and R. Tiwari, “Signal based condition monitoring techniques for fault detection and diagnosis of induction motors: A state-of-the-art review,” *Mech. Syst. Signal Process.*, vol. 144, p. 106908, Oct. 2020.

[9] F. Khan, A. Ghaffar, N. Khan, and S. H. Cho, “An Overview of Signal Processing Techniques for Remote Health Monitoring Using Impulse Radio UWB Transceiver” *Sensors 2020, Vol. 20, Page 2479*, vol. 20, no. 9, p. 2479, Apr. 2020.

[10] D. M. Kipping *et al.*, “THE HUNT for EXOMOONS with KEPLER (HEK). V. A SURVEY of 41 PLANETARY CANDIDATES for EXOMOONS,” *Astrophys. J.*, vol. 813, no. 1, Nov. 2015.

[11] J. Martinez, A. Gomez-Pau, J.-R. Riba, and M. Moreno-Eguilaz, “On-Line Health Condition Monitoring of Power Connectors Focused on Predictive Maintenance,” *IEEE Trans. Power Deliv.*, pp. 1–1, Dec. 2020.

[12] A. Kadechkar, M. Moreno-Eguilaz, J.-R. J.-R. Riba, and F. Capelli, “Low-Cost Online Contact Resistance Measurement of Power Connectors to Ease Predictive Maintenance,” *IEEE Trans. Instrum. Meas.*, vol. 68, no. 12, pp. 4825–4833, 2019.

[13] A. Kadechkar, J. R. Riba, M. Moreno-Eguilaz, and J. Perez, “SmartConnector: A Self-Powered IoT Solution to Ease Predictive Maintenance in Substations,” *IEEE Sens. J.*, vol. 20, no. 19, pp. 11632–11641, Oct. 2020.

[14] W. Dyason, T. I. Van Niekerk, R. Phillips, and R. Stopforth, “Performance evaluation and comparison of filters for real time embedded system applications,” *2017 Pattern Recognit. Assoc. South Africa Robot. Mechatronics Int. Conf. PRASA-RobMech 2017*, vol. 2018-January, pp. 242–248, Jul. 2017.

[15] M. Khodarahmi and V. Maihami, “A Review on Kalman Filter Models,” *Arch. Comput. Methods Eng.*, vol. 30, no. 1, pp. 727–747, Jan. 2023.

[16] M. Hossain, M. E. Haque, and M. T. Arif, “Kalman filtering techniques for the online model parameters and state of charge estimation of the Li-ion batteries: A comparative analysis,” *J. Energy Storage*, vol. 51, p. 104174, Jul. 2022.

[17] L. Tuta, M. Nicolaescu, G. Rosu, A. Grivei, and B. Barbulescu, “A Robust Adaptive Filtering Method based on Independent Component Analysis (ICA),” *2020 13th Int. Conf. Commun. COMM 2020 - Proc.*, pp. 59–64, Jun. 2020.

[18] S. K. S. Fan, Y. J. Chang, and N. Aidara, “Nonlinear Profile Monitoring of Reflow Process Data Based on the Sum of Sine Functions,” *Qual. Reliab. Eng. Int.*, vol. 29, no. 5, pp. 743–758, Jul. 2013.

5.4 Analysis of a Smart Sensor Based Solution for Smart Grids Real-Time Dynamic Thermal Line Rating

Reference:

Liu, Y.; Riba, J.-R.; Moreno-Eguilaz, M.; Sanllehí, J. Analysis of a Smart Sensor Based Solution for Smart Grids Real-Time Dynamic Thermal Line Rating. *Sensors* 2021, *21*, 7388. Under a CC BY 4.0 license. https://doi.org/10.3390/s21217388.

Publication framework:

This article presents a novel approach to determining the dynamic thermal line rating of aluminum conductor steel-reinforced conductors. The proposed method needs a thermal model of the power line that requires the real-time values of the solar radiation and the environment temperature, which can be acquired from nearby weather stations as well as the temperature and the current of the conductor, which can be measured directly with a *Smartconductor* device and can be transmitted wirelessly to a nearby gateway. Also, this paper proposed a method to estimate the wind speed and the DLR rating of the studied conductor. Experimental tests have been carried out to evaluate the accuracy of the proposed method for ACSR conductors.

Main contributions:

- **Development of *Smartconductor* device for the measurement of temperature and current of the conductor in real time.**
- **Estimation of the wind speed based on a thermal model of the conductor to avoid using a wind speed sensor.**
- **Estimation of Joule and magnetic losses of the analyzed conductor from the measured ac resistance of the conductor.**

Key words:

wind speed; dynamic thermal line rating; ACSR conductor; real-time monitoring; wireless communications

sensors

MDPI

Article

Analysis of a Smart Sensor Based Solution for Smart Grids Real-Time Dynamic Thermal Line Rating

Yuming Liu [1,2], Jordi-Roger Riba [1,*], Manuel Moreno-Eguilaz [1] and Josep Sanllehí [2]

[1] Campus Terrassa, Universitat Politècnica de Catalunya, Rambla Sant Nebridi 22, 08222 Terrassa, Spain; yuming.liu@upc.edu (Y.L.); manuel.moreno.eguilaz@upc.edu (M.M.-E.)
[2] SBI Connectors, Albert Einstein 5, 08635 Sant Esteve Sesrovires, Spain; josep.sanllehi@sbiconnect.es
* Correspondence: jordi.riba-ruiz@upc.edu; Tel.: +34-937398365

Abstract: Dynamic thermal line rating (DTLR) allows us to take advantage of the maximum transmission capacity of power lines, which is an imperious need for future smart grids. This paper proposes a real-time method to determine the DTLR rating of aluminum conductor steel-reinforced (ACSR) conductors. The proposed approach requires a thermal model of the line to determine the real-time values of the solar radiation and the ambient temperature, which can be obtained from weather stations placed near the analyzed conductors as well as the temperature and the current of the conductor, which can be measured directly with a *Smartconductor* and can be transmitted wirelessly to a nearby gateway. Real-time weather and overhead line data monitoring and the calculation of DTLR ratings based on models of the power line is a practical smart grid application. Since it is known that the wind speed exhibits important fluctuations, even in nearby areas, and since it plays a key role in determining the DTLR, it is essential to accurately estimate this parameter at the conductor's location. This paper presents a method to estimate the wind speed and the DTLR rating of the analyzed conductor. Experimental tests have been conducted to validate the accuracy of the proposed approach using ACSR conductors.

Keywords: wind speed; dynamic thermal line rating; ACSR conductor; real-time monitoring; wireless communications

Citation: Liu, Y.; Riba, J.-R.; Moreno-Eguilaz, M.; Sanllehí, J. Analysis of a Smart Sensor Based Solution for Smart Grids Real-Time Dynamic Thermal Line Rating. *Sensors* **2021**, *21*, 7388. https://doi.org/10.3390/s21217388

Academic Editor: Fco Javier Rodríguez

Received: 15 October 2021
Accepted: 2 November 2021
Published: 6 November 2021

1. Introduction

With the widespread deployment of heat pumps, electric vehicles, and different electric and electronic technologies, the consumption of electrical power is increasing steadily, so there is a need to increase the capacity of existing power lines. However, any increase of the transmission capacity must not compromise safe operation, supply security, and reliability [1].

High-voltage overhead transmission lines typically use aluminum conductor steel-reinforced (ACSR) cables [2]. It is known that due to the steel core, ACSR conductors have a larger ac/dc resistance ratio compared to all-aluminum conductors due to the magnetic induction in the steel core. This magnetic induction causes power losses due to the induced eddy currents and the hysteresis effect and redistributes the current in the aluminum wires layers [3].

The allowable conductor temperature limits the load or current capacity of the power line, so the operating temperature must be restricted to below the allowable operating temperature to limit the ground clearance of the conductors [4]. Dynamic thermal line rating (DTLR) offers a solution to this problem because it is a smart and cost-effective solution for utilizing the maximum ampacity or ampere capacity of transmission lines [5], which differs from static line rating (SLR), the conventional and simple approach, which is based on conservative criteria [5] that represent severe or worst case weather conditions

[6]. SLR calculates the ampacity of the line from deterministic or probabilistic methods to determine the atmospheric operating conditions, which have a heavy influence. SLR often results in a conservative rating because it determines the same ampacity limit for the whole year; it is a static value, regardless of current weather conditions. Conversely, DTLR is based on measuring the weather variables, so the maximum allowable current of the line is dynamically calculated to ensure that the line operates within safe operation limits. Therefore, DTLR requires the current and temperature of the line and the weather variables in the vicinity of the power line to be monitored online using specific sensors and weather stations [1]. By applying a DTLR approach, the maximum rating or ampacity can be calculated from the mathematical line models that can be found in [7,8], with the results being greatly influenced by the current weather conditions. The current carrying capacity or ampacity of overhead power conductors can be affected by many factors such as wind speed, wind direction, solar radiation, and ambient temperature. Among these factors, wind speed is significant in terms of ampacity calculation [9,10].

Different DTLR approaches can be found in the technical literature. According to [9], DTLR methods can be roughly classified into indirect and direct methods. Indirect methods estimate the thermal line rating from the weather data gathered from weather stations or that have been forecasted, representing the main inputs of the method. These methods determine the required thermal rating based on solving the conductor heat balance equation, as detailed in Cigré [7], IEEE [8], or IEC [11]. Direct methods for dynamic line rating directly measure physical power line variables, including conductor temperature or/and current, line mechanical tension, conductor sag, or ground clearance, as described in [6]. Since there is no need to install weather measuring devices on the line and since they are reliable and not very expensive, indirect methods are simpler and present lower costs compared to direct methods, so indirect methods are indicated for power lines that are relatively light load. Compared to direct methods, indirect methods are less accurate because the conductor temperature and line ampacity are estimated indirectly using theoretical models [12]. Conversely, direct methods rely on field data; thus, they can be more accurate since no relationship between conductor temperature and the measured data from indirect methods is needed [9].

The fast progress made in the development of communication systems, sensors, and control algorithms has led to the development of smart grids, which integrate distributed energy resources, loads, energy storage, and control systems. They present substantial advantages, such as enhanced power supply reliability, reduced power losses, energy independence, and the integration of renewable energy sources [13]. To this end, smart grids integrate information technology to share power data in real-time for the efficient management of the power demand to maximize power efficiency, so DTLR methods represent a key element for smart grid development [14–20]. Recent studies have suggested that IoT solutions allow smart grid reliability to be enhanced while also remarkably improving their capacity of [21–24].

Nowadays, DTLR is a hot topic because of the widespread use of accurate, reduced-size, and cost-effective sensors; the development of several communication systems that are compatible with high-voltage applications; the need to expand power transmission capability; and the fact that DTLR allows the ampacity of overhead power lines to be improved through the measurement of the line and weather variables.

In [25], wind speed and DTLR ampacity are estimated by measuring different parameters such as the conductor current, temperature, and mechanical tension; ambient temperature; and solar radiation and by applying the sag-tension method. Sag-tension monitoring methods require precise state change equations to relate the conductor temperature to the sag-tension [26]. In [27],the DTLR rating of a distribution line was calculated using a low cost sensing probe to measure the conductor temperature and to transmit the data wirelessly. However, the line current was not measured in real-time, which is an important parameter in this application [26]. In [28], a self-powered high-voltage sensor is presented that measures line temperature, voltage, current, and the active and

reactive power to determine the SLR and DTLR ratings. It also requires environmental data such as average wind speed and direction or air pressure from local weather stations. Nevertheless, the average wind speed taken from nearby weather stations is often not accurate, as wind speed changes with terrain topography and vegetation. In [29], a reverse calculation is presented to estimate the wind speed from an online conductor current and temperature, solar radiation, and ambient temperature measurements, but the paper does not present estimates of the DTLR rating.

This paper presents an approach to estimate the DTLR rating of power lines based on ACSR conductors, combining the real-time monitoring of weather and line data. It is a practical smart grid application since the proposed DTLR approach allows the power lines to operate at their maximum capacity by adapting the rating according to the current real-time weather conditions. Solar radiation and ambient temperature are important variables that can be used to determine the maximum allowable power transmission conductor current. Nevertheless, in this paper, they are not directly measured. Instead, such variables are obtained from a nearby weather station. The principal reason for this is because of the similarities between the ambient temperature and the solar radiation measured by the weather station and the local values at the conductor's surface. Secondly, there is a need to simplify the system with the purpose of reducing the power consumption and the cost of the sensors installed in the high-voltage conductors. Finally, wind speed plays a much more significant role than that of ambient temperature and solar radiation in terms of DTLR calculation [9]. The proposed method presents several novelties and contributions. First, it develops the *Smartconductor* prototype, which measures the current and temperature of the conductor in real-time. Second, it requires reduced computational resources and presents a low computational burden to minimize the hardware requirements for compatibility, only requiring inexpensive devices global smart grid deployment. Third, the proposed method estimates the wind speed; thus, there is no need to use a wind speed sensor. Since the DTLR rating depends heavily on the local wind speed and since the wind speed has an important cooling effect, it is estimated based on a reverse calculation by applying a thermal model of the ACSR conductor. Once the wind speed has been estimated, the DTLR rating is calculated from the thermal model. Fourth, the proposed method estimates the joule and magnetic losses of the ACSR conductor from the measured ac resistance of the conductor, this being another contribution of the paper. The proposed approach has been validated under different operating conditions by means of experimental tests by considering different controlled wind speeds.

The experimental results prove that the real-time approach presented in this paper can predict both the value of the local wind speed and the DTLR rating with accuracy and with a reduced computational burden, so the calculations can be implemented in the low-power microprocessors that are used in inexpensive devices that are required for global smart grid deployment. Therefore, the developments made in this paper contribute the research area focusing on smart grids. The proposed DTLR approach allows us to take advantage of the maximum transmission capacity of power lines by adapting the rating of the line according to the current weather conditions in real-time, making it a smart solution of paramount importance in future smart grids.

Section 2 describes the *Smartconductor* device, including its sensors and wireless communications. Section 3 details the equations required to estimate the wind speed and the dynamic thermal line rating. Section 4 outlines the strategy applied to estimate the wind speed and the dynamic thermal line rating and includes a flow chart detailing the full process. Section 5 describes the experimental setup, including the power source, conductors, sensors, and measuring devices. Section 6 presents and explains the results that were attained, and finally, Section 7 concludes the study.

2. *Smartconductor*. Sensors and Wireless Communications

This section describes the sensors used in the *Smartconductor* device as well as the wireless communications approach that is applied.

2.1. Current Sensor

Different sensor technologies can be applied to measure the current flowing through a conductor, such as giant magneto resistive, Rogowski coils, current transformers, or Hall effect sensors [30]. The Hall effect sensor was selected for the *Smartconductor* because this technology offers miniaturization, low power consumption, high linearity, and the possibility of sensing high magnetic fields. This sensor measures the magnetic flux density B that is generated by the conductor and generates an output voltage V_{Hall} that is proportional to the measured magnetic flux density as described in (1):

$$V_{Hall} = kB \text{ [V]} \quad (1)$$

where k [V/T] is the sensitivity constant.

According to the Biot–Savart law[31], the magnetic flux density detected by a sensor placed on the top of a cylindrical conductor can be expressed as

$$B = \frac{\mu_0 I}{2\pi(r+h)} \text{ [T]} \quad (2)$$

where $\mu_0 = 4\pi 10^{-7}$ H/m is the permeability of air, I (A) is the current in the conductor, r (m) is the radius of the conductor, and h (m) is the radial distance between the outer surface of the conductor and the sensor.

Hence, when placing the sensor on the surface of the conductor, the position $r + h$ (m) is known as well as the magnetic flux density B in Equation (1), so the current I (A) through the conductor can be obtained as

$$I = \frac{V_{Hall}(r+h)}{k \times 2 \times 10^{-7}} \text{ [A]} \quad (3)$$

2.2. Temperature Sensor

Since the conductor temperature is considered to be an essential parameter in determining the dynamic thermal line rating [32], it is of paramount importance to use a suitable temperature sensor. It should be considered that the maximum allowable temperature of the tested ACSR conductor for continuous operation is 90 °C [33]. Therefore, the temperature sensor should reach this range. When focusing on the expected linearity and accuracy and by taking the high current application into account, a positive temperature coefficient (PTC) resistor is a suitable choice, so a Pt1000 sensor was selected. When dealing with Pt1000 platinum sensors, each temperature value corresponds to exactly one resistance value, the correspondences can be tabulated in the EN 60,751 standard [34] as follows

$$R_T = R_0(1 + aT + bT^2) \text{ for T } > 0 \text{ °C} \quad (4)$$

$$R_T = R_0(1 + aT + bT^2 + c(T - 100)T^3) \text{ for } T < 0 \text{ °C} \quad (5)$$

where $a = 3.9083 \times 10^{-3}$ °C^{-1}, $b = -4.183 \times 10^{-7}$ °C^{-1}, $c = -4.183 \times 10^{-12}$ °C^{-1}, $R_0 = 10^3$ Ω, and R_T is the resistance of the temperature sensor at the measured temperature in ohms.

2.3. Wireless Communications

The wireless communication of the proposed system is based on the Bluetooth SoC (System on Chip) nRF52832 from Nordic Semiconductors (Trondheim, Norway). This chip was selected since it contains an inbuilt BLE (Bluetooth Low Energy) module, inbuilt ADC converters, and low power consumption modes, and it is also inexpensive.

With respect to the gateway, after considering several features, such as cost and size, the Raspberry Pi 4 module was selected. It is worth noting that a Huawei e3372 LTE 4G Wi-Fi dongle was mounted in Raspberry Pi because 4G technology allows it to remotely control the Raspberry Pi and send data to the cloud.

Figure 1 shows the applied strategy to estimate the ampacity. To this end, the solar radiation and ambient temperature values are obtained from a nearby weather station, whereas the *Smartconductor* measures the conductor current and temperature. These values are sent wirelessly via BLE to the local gateway, which, in turn, sends the data to the cloud, where it is stored. The *Smartconductor* was programmed to connect to the gateway and to send the measured line current and conductor temperature values in a packet every 7 s via Bluetooth. Once the gateway receives the data by means of a python script implemented in the Raspberry Pi, the data that are received are decoded, and the ampacity is calculated. The proposed DTLR model takes the ambient temperature and solar radiation data from a nearby weather station, whereas the line current and the temperature of the conductor are directly measured by the *Smartconductor*. From these data, in the first stage, the wind speed is estimated, and in the second stage, the dynamic ampacity is estimated in real-time. Once the calculation is complete, the results are sent to a cloud server via 4G communication.

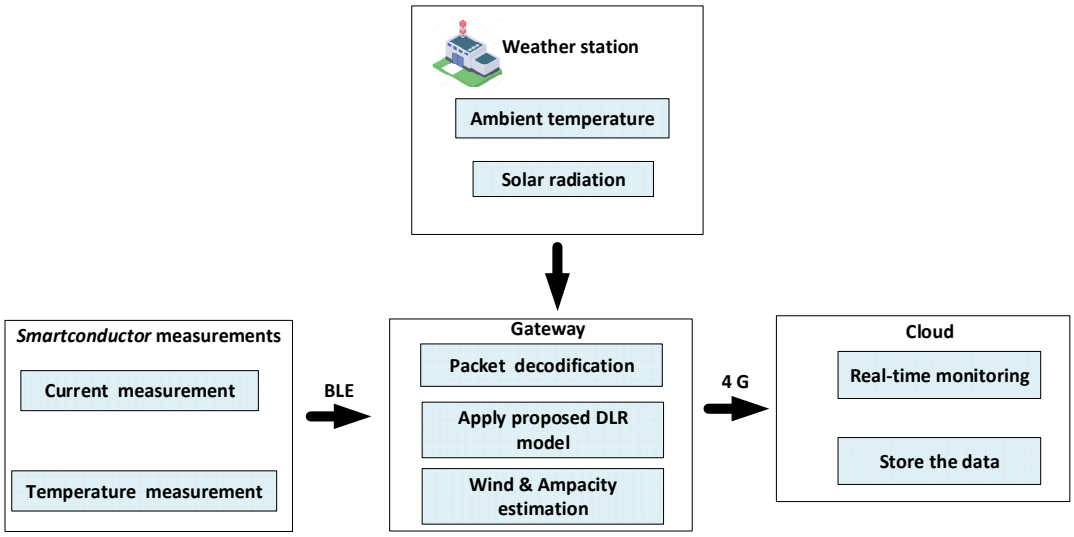

(**a**)

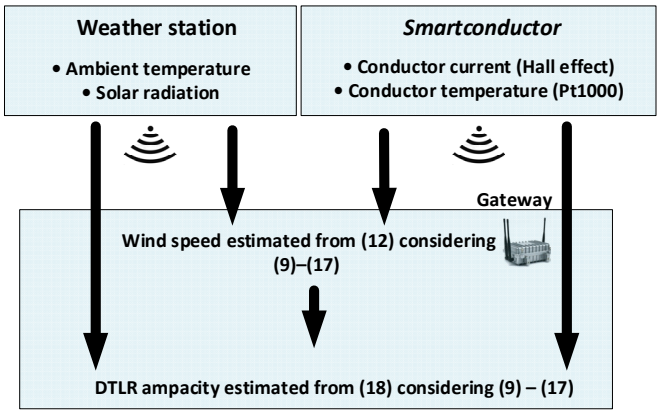

(**b**)

Figure 1. Proposed strategy to estimate the ampacity. (**a**) Global strategy. (**b**) Block diagram of the strategy to determine the DTLR rating.

According to Figure 1b, in the first stage, the wind speed is determined from four readings (ambient temperature, solar radiation, conductor current and conductor temperature), and in the second stage, the DTLR rating is determined.

3. Dynamic Thermal Line Rating Estimation Method

The CIGRE standard [7] describes a non-steady-state equation using the following transient thermal balance equation based, which is expressed as

$$P_J + P_M + P_S = P_c + P_r + mc\frac{dT_c}{dt} \text{ [W/m]} \quad (6)$$

where P_J, P_M, P_S are the heat gain terms due to joule, magnetic, and solar heating effects, respectively; P_c and P_r are the heat loss terms due to convection and radiation, respectively; m is the mass of the conductor in kg/m, c is the specific heat capacity of the conductor in J/$(kg°C)$, and T_c is the average conductor temperature in °C.

The heat capacity c of the ACSR conductor is calculated as follows:

$$\begin{cases} mc = m_{Al}c_{Al} + m_s c_{steel} \\ c(T) = c_{20°C}[1 + \beta(T_c - 20)] \end{cases} \quad (7)$$

where m_{Al} and c_{Al} refer to the mass per unit length and the specific heat capacity of the aluminum part, respectively, whereas m_{steel} and c_{steel} refer to the mass per unit length and specific heat capacity of the steel part, respectively. The values of the temperature coefficient β are 3.8×10^{-4} °C^{-1} for pure Al, 4.5×10^{-4} °C^{-1} for the Al alloy and 1.0×10^{-4} °C^{-1} for steel [7].

According to [25], the joule and magnetic heat gains can be combined in only one equation, which appears as follows:

$$P_J + P_M = I^2 R_{ac} \quad (8)$$

where I is the root mean square (RMS) value of the current, amd R_{ac} is the ac resistance of the conductor per unit length at the operating mean conductor temperature T_c. The ac resistance of the conductor R_{ac} includes the skin and proximity effects as well as the core losses, which can be calculated according to the method detailed in the Cigré Technical Brochure [35], or it can be measured. Measurements can be conducted according to the procedure described in [36] or in [31], with the last method being applied in this paper, a decision that is based on the previous experience of the authors.

As the ac resistance R_{ac} is required during the process to determine the joule and magnetic heat gains, the conductor characteristic $R_{ac}(T_c)$ was measured in the laboratory by measuring the temperature of the conductor, the voltage drop between two points of the conductor surface distanced by 1 m, and the ac current flowing through the conductor. Next by applying (9), the ac resistance was calculated as

$$R_{ac} = \Delta V cos\varphi / I \quad (9)$$

where φ is the phase shift between the voltage drop ΔV and the current I [31].

According to [7], Equations (10–15) are used to determine the heat loss due to convective cooling:

$$P_c = \pi\lambda_f(T_c - T_a)N_u \text{ [W/m]} \quad (10)$$

where λ_f = 2.42×10^{-2} + 7.2×10^{-5}·T_f in W/(m °C) is the thermal conductivity of air, T_c is the conductor surface temperature, T_a is the ambient temperature, and T_f is the film temperature defined as $T_f = 0.5(T_a + T_c)$.

Equation (9) applies for both natural and forced convective cooling, the difference between both situations is found in the way to allow the calculation of the de Nusselt number N_u.

In case of forced convection, the Nusselt number is calculated as

$$N_u = B_1(Re)^n \text{ [−]} \quad (11)$$

where the Reynolds number is calculated as

$$Re = \rho_r V\frac{D}{\nu_f} \text{ [−]} \quad (12)$$

where V (m/s) is the wind speed, ρ_r (−) and ν_f (m²/s) are the relative density and kinematic viscosity of air, respectively, D (m) is the diameter of the conductor, and B_1 and n are constants depending on the Reynolds number Re and conductor surface roughness, respectively. It is worth noting that the wind speed can be estimated by applying (12), as detailed in Figure 2.

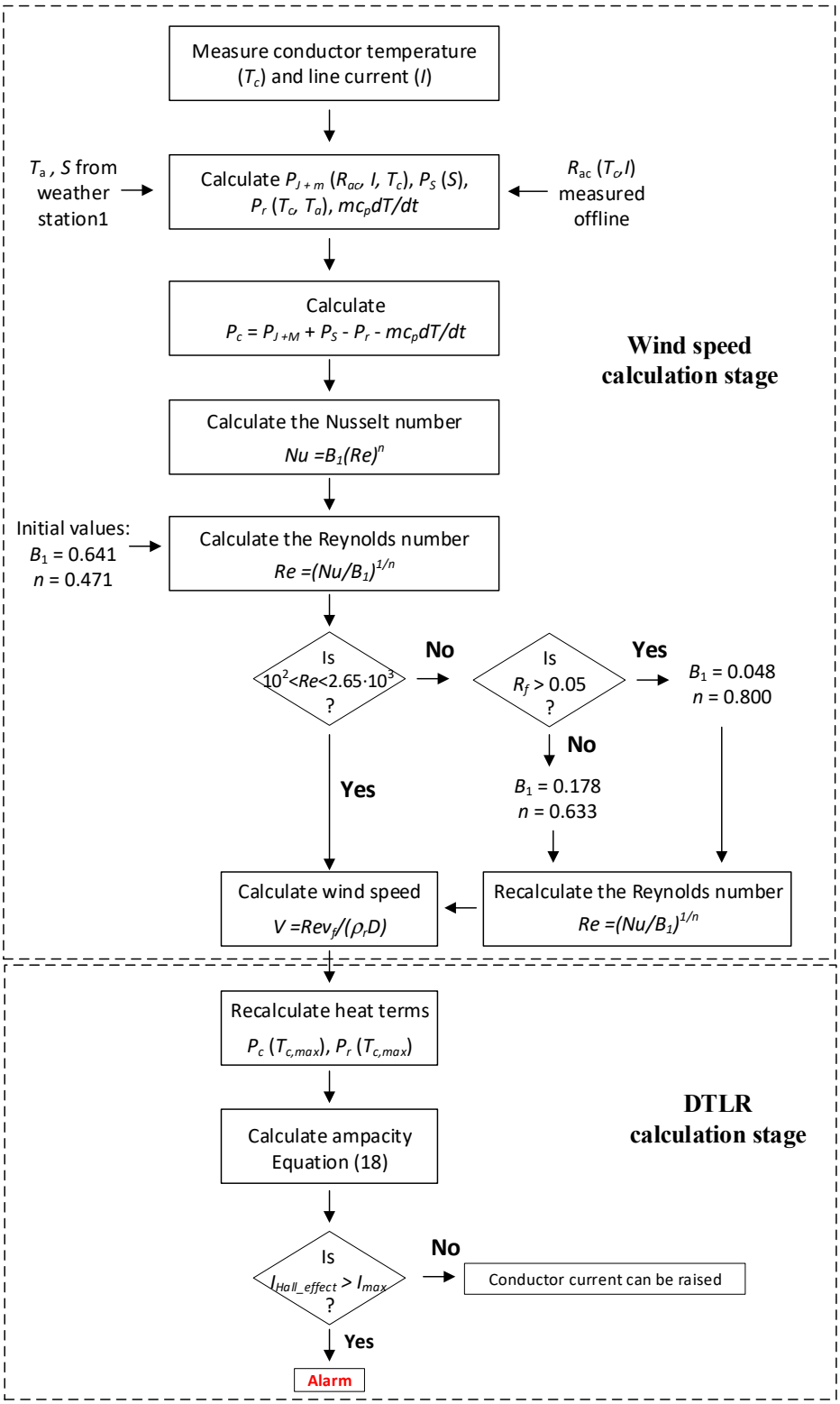

Figure 2. Proposed DTLR calculation method.

Table 1 provides the values of the coefficients n and B_1, which depend on the Reynolds number and the surface roughness defined as $R_f = d/[2(D - d)]$, where d (m) is the diameter of the strands.

Table 1. Values of constants n and B_1 [7].

Surface Type	*Re*	*n*	B_1
All surfaces stranded	100–2650	0.471	0.641
Stranded $R_f \leq 0.05$	2650–50,000	0.633	0.178
Stranded $R_f \geq 0.05$	2650–50,000	0.800	0.048

In case of natural cooling, the Nusselt number is obtained from the Grashof (Gr) and Prandtl (Pr) numbers as follows:

$$Nu = A_2(GrPr)^{m_2} \quad (13)$$

$$Pr = 0.715 - 2.5 \times 10^{-4} T_f \quad (14)$$

$$Gr = D^3(T_c - T_a)g/(T_f + 273)v_f^2 \quad (15)$$

where $g = 9.807$ m/s^2 and the values of A_2 and m_2 are found in Table 2.

Table 2. Values of the product $Gr \cdot Pr$ [7].

$Gr \cdot Pr$	A_2	m_2
10^2–10^4	0.850	0.188
10^4–10^6	0.480	0.250

The procedure described in this paper estimates the wind speed value. Thus, since the wind speed is not known, both forced and natural cooling equations are applied. If the power loss due to forced cooling is greater than the power loss due to natural cooling, it is assumed that the wind speed is not zero, and the Nusselt number Nu is calculated by applying (11); otherwise, it is calculated from (13). However, in virtually all situations found in outdoor environments, the Nusselt number must be calculated from (11).

The heat gain due to the solar radiation can be calculated using the global solar radiation S (W/m^2), as seen in [7]:

$$P_s = \alpha_s S D \text{ [W/m]} \quad (16)$$

where α_s (-) is the solar absorptivity of the conductor surface whose value is assumed to be 0.5 [37], and D (m) is the external diameter of the conductor.

Finally, radiation heat losses can be described as [7]:

$$P_r = \pi \varepsilon D \sigma_B [(T_c + 273)^4 - (T_a + 273)^4] \text{ [W/m]} \quad (17)$$

where ε is the emissivity factor, which depends on the conductor surface, and it is assumed to be 0.5 [4,37], and where $\sigma_B = 5.6697 \times 10^{-8}$ W/(m^{2}K^4) is the Stefan–Boltzmann constant.

Finally, the DTLR rating is determined when the conductor temperature reaches it maximum value under thermal equilibrium, so from (6) and (8), it results in [5,28]:

$$I_{max} = \sqrt{\frac{P_c(T_{c,max}) + P_r(T_{c,max}) - P_s}{R_{ac}(T_{c,max})}} \quad (18)$$

4. Proposed Real-Time Method to Determine the Thermal Line Rating

The dynamic thermal line rating can not only be calculated by obtaining real-time weather data and load, but it can also be estimated several ways [26]. In this paper, a cost-effective, real-time monitoring model to calculate the DTLR rating using the *Smartconductor* is presented, the steps of which are described in Figure 2. This procedure has two main

stages, i.e., the wind speed calculation stage and the DTLR calculation stage. The calculations associated with both stages are performed by the gateway. As constants B_1 and n depend on surface roughness and Reynolds number, which are not available, this paper proposes setting their values to $B_1 = 0.641$ and $n = 0.471$ in the initial stage, which are taken from [7] and are summarized in Table 1. In the first stage, the Reynolds number is corrected in order to estimate the wind speed. Next, the wind speed can be estimated, and if the maximum allowable conductor temperature is known (90 °C in this paper), then the ampacity can be predicted.

Finally, the predicted value of the ampacity (I_{max}) provided by (18) is compared to the measured current by the Hall effect sensor ($I_{HallSensor}$). In the case where $I_{max} < I_{HallSensor}$, the current flowing through the line can be increased. Conversely, an alarm signal will be activated if $I_{max} > I_{HallSensor}$.

5. Experimental Setup

This section develops the experimental part of this paper to evaluate the accuracy and performance of the proposed approach for predicting the thermal line rating of power transmission lines.

The tests were performed in a high-current laboratory (AMBER laboratory from the Universitat Politècnica de Catalunya).

The analyzed ACSR conductor (550-AL1/71-ST1A, HAASE Gesellschaft mbh, Graaz, Austria) was supported by wood trestles and was connected to the output of the high-current transformer, forming a low-impedance loop.

Figure 3 shows the geometry of the 550-AL1/71-ST1A ACSR conductor that was used, including the 7 steel strands and the 54 aluminum strands, whereas Table 3 shows its main properties.

Figure 3 details the geometry of the 550-AL1/71-ST1A ACSR conductor.

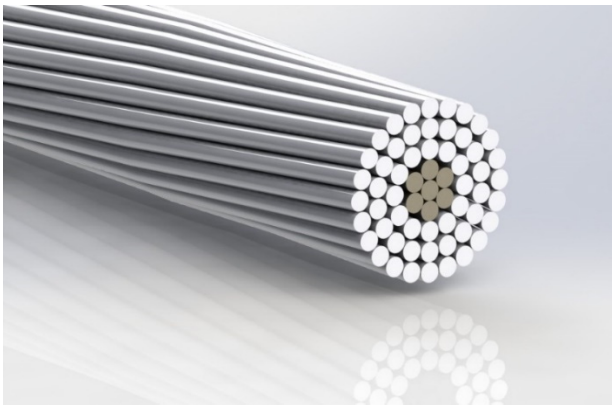

Figure 3. Cross section of the tested conductor.

Table 3. Parameters of the tested ACSR conductor 550-AL1/71-ST1A.

Symbol	Description	Value	Unit
A_{Al}	Area of aluminum	549.7	mm^2
A_{steel}	Area of steel	71.3	mm^2
N_{Al}	Number of aluminum wires	54	-
N_{Steel}	Number of steel wires	7	-
D_{Al}, D_{steel}	Aluminum and steel wire diameter	3.6	mm
D	Diameter of conductor	32.4	mm
m_{AL}	Mass per unit length of aluminum	1.5183	Kg/m
m_{steel}	Mass per unit length of steel	0.5583	Kg/m
$Cp_{aluminum}$	Specific heat of aluminum	897	J/(Kg°C)
Cp_{steel}	Specific heat of steel	481	J/(Kg°C)

$R_{20°C}$	DC resistance of the conductor	0.0526	Ω/km
I_{max}	Current carrying capacity	1020	A

As explained in Section 3, in order to determine the heat gain due to the joule and magnetic heating, it is necessary to determine the evolution of the R_{ac} resistance as a function of the conductor temperature. To this end, an experiment was performed off-line by measuring the voltage drop, temperature, cosφ, and current through 1 m of the analyzed conductor (550-AL1/71-ST1A ACSR conductor). The results that were obtained are summarized in Table 4. These values are required to evaluate (8).

Table 4. Dependence of R_{ac} with the temperature of the conductor.

T (°C)	Voltage Drop (V_{RMS})	Current (A_{RMS})	cosφ	R_{ac} (μΩ/m)
30	0.10	1025	0.59	57.7
40	0.10	1022	0.60	60.2
50	0.10	1023	0.62	62.4
60	0.10	1022	0.63	64.8
70	0.10	1026	0.64	67.2
80	0.11	1028	0.65	69.4
90	0.11	1023	0.67	71.6
100	0.14	1305	0.68	74.3

The R_{dc} resistance at 30°C is 56.7 μΩ/m.

Since the experiment was conducted indoors, two variable speed fans (V-6020 ROVEX, 50 W, 65 m^3/min) and two dimmable linear led lamps (36 inch, 234 W, AUXTINGS, Foshan, China) were used to simulate the effect of wind and solar radiation, respectively.

The current and temperature of the cable were measured by the *Smartconductor* by means of the Hall effect sensor and the Pt1000 sensor, as described in Sections 2.1 and 2.2, respectively.

Regarding the Hall effect sensor, considering several parameters such the possibility of being integrated with microelectronics, performance efficiency, accuracy, cost, and size, the DRA5053 analog-bipolar Hall effect sensor from Texas Instruments (Dallas, TX, USA) [38] was selected for this application [39–41].

Regarding the Pt1000 sensor, the PTFC102T1G0 sensor from TE connectivity (Schaffhausen, Switzerland) is a suitable choice [42] because it has a rated resistance of 1000 Ω to provide typical accuracies of ±0.1 °C with a temperature range between −30 °C to 200 °C.

To measure the wind speed, an anemometer (RH Anemometer Pen 850021, Sper Scientific, Scottsdale, AZ, USA) with a measuring range of 0.4–30 m/s with a resolution of 0.1m/s and an accuracy of 3% full scale when the wind speed is below 20 m/s was used.

Finally, to measure the solar radiation, a solar power meter (PCE-SPM1, Professional Calibrated Equipments, PCE, Tobarra, Spain) was used. It had a measuring range between 0–2000 W/m^2, a resolution of 0.1 W/m^2, and an accuracy of ± 10 W/m^2.

To validate and check the accuracy of the results provided by the *Smartconductor*, the temperature and the current of the conductor were measured using a T-type thermocouple connected to a thermocouple input module (NI-9211, National Instruments, Dallas, TX, USA) and a Rogowski coil (500LFxB from PEM, Nottingham, UK with sensitivity 0.06mV/A) connected to a data acquisition system (NI USB-6356 DAQ, National Instruments, Dallas, TX, USA, with eight differential inputs). For simultaneous acquisition, the NI-9211 thermocouple input module and the NI USB-6356 DAQ were synchronized by means of a Python code. The data from the two DAQs were synchronized with the data from the *Smartconductor* by means of a MATLAB® code.

Figure 4 shows the experimental setup, including the conductor loop, the high-current transformer, and the sensors used to validate the method proposed in this paper to determine the wind speed and the DTLR rating.

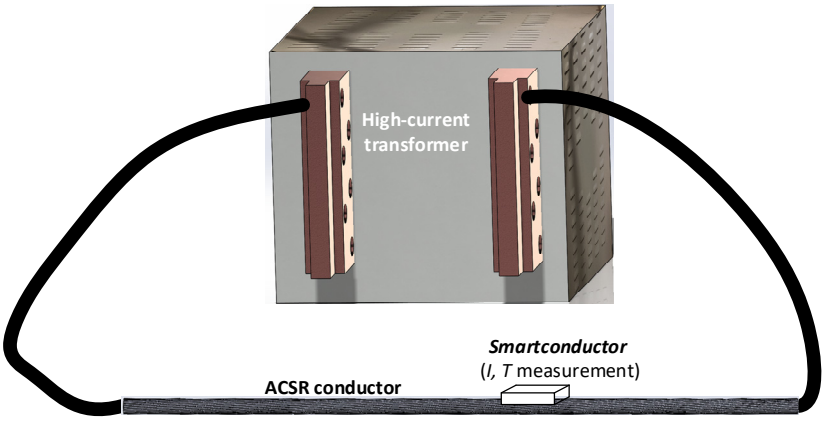

(**a**)

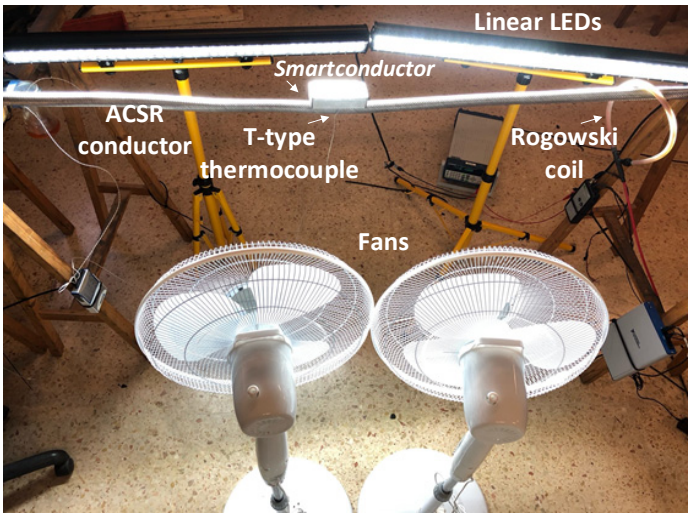

(**b**)

Figure 4. (**a**) Sketch of the experimental setup; (**b**) detail of the ACSR conductor and the sensors.

6. Experimental Results

6.1. First Experiment. Wind Speed and DTLR Estimation

A first experiment that was conducted to determine the accuracy of the proposed method in estimating the wind speed and DTLR of the studied conductor is shown in Figure 5. To this end, a current change (from around 600 A to around 1100 A) was applied to the loop shown in Figure 4, and four wind speeds were applied (0 m/s, 2m/s, 2.5 m/s and 3 m/s) as shown in Figure 5a. During these tests, the solar radiation was set to a constant value of 800 W/m^2.

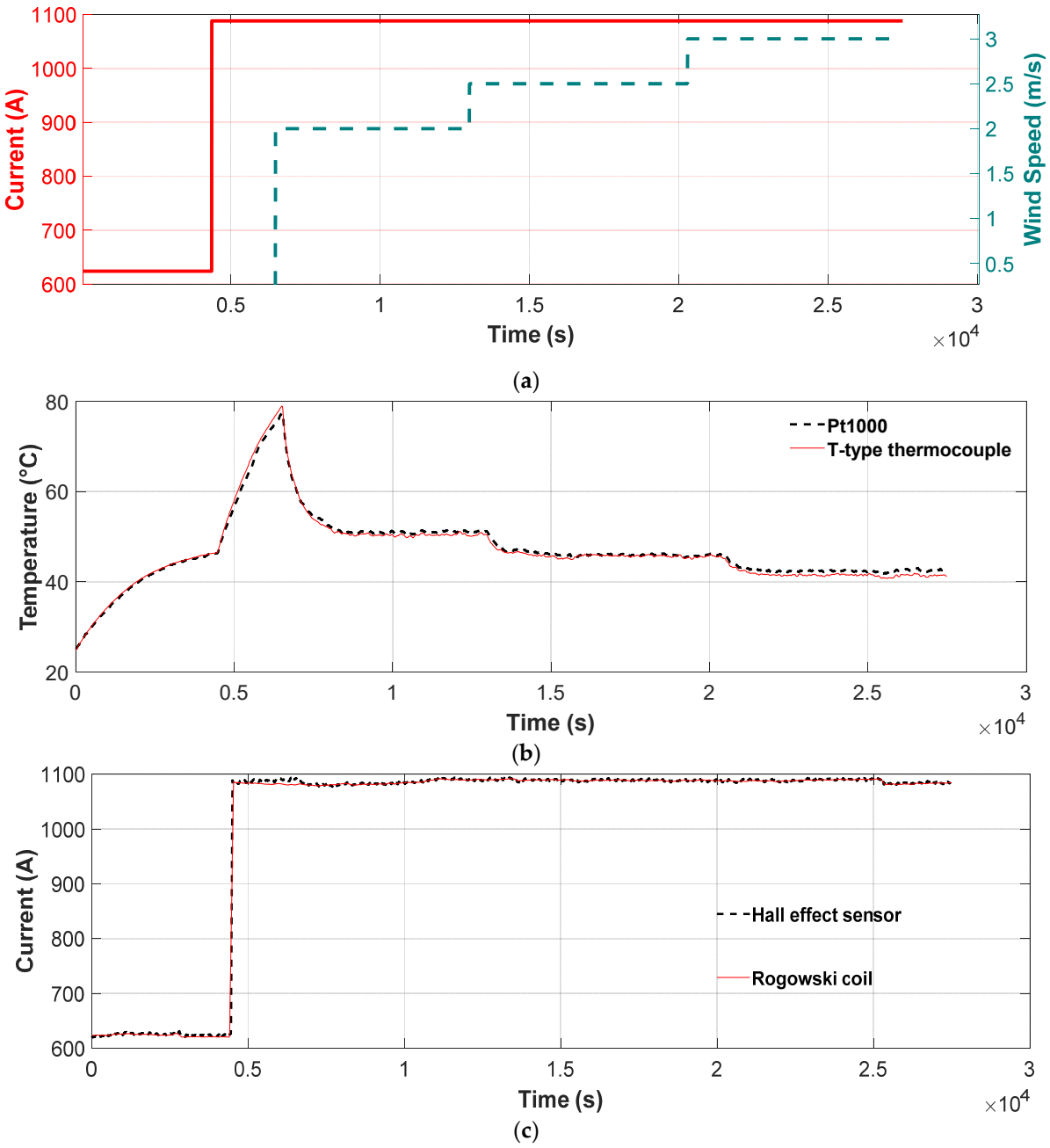

Figure 5. (**a**) Planned current intensity and perpendicular wind speed profiles during the test. (**b**) Conductor temperature measured by the Pt1000 sensor (*Smartconductor*) and the T-type thermocouple. (**c**) Currents measured by the Hall effect sensor (*Smartconductor*) and the Rogowski coil.

Figure 5b shows the temperature measured by the PTC1000 incorporated in the *Smartconductor* and by the laboratory sensor (T-type thermocouple), whereas Figure 5c shows the current measured by the Hall effect sensor and the Rogowki coil under the conditions established in Figure 5a. These results show that the temperature and current measurements made with the *Smartconnector* sensors and the laboratory measurements are very similar, thus validating the accuracy of the *Smartconductor* measurements.

The average difference of the temperature measured by the Pt1000 sensor included in the *Smartconductor* compared to the measurement of the laboratory device (T-type thermocouple) is 1.34%, whereas the maximum difference is 3.48%. The average difference of the current measured by the Hall effect sensor compared to the measurements of the laboratory device (Rogowski coil) is 0.23%, whereas the maximum difference is 1.92%; thus, the *Smartconductor* shows reliable and accurate results.

Figure 6 compares the wind speed and the DTLR estimates provided by the *Smartconductor* and the laboratory measurements with the theoretical values. These estimates are based on the conditions shown in Figure 5. The results presented in Figure 6 show very similar results, thus validating the proposed methodology.

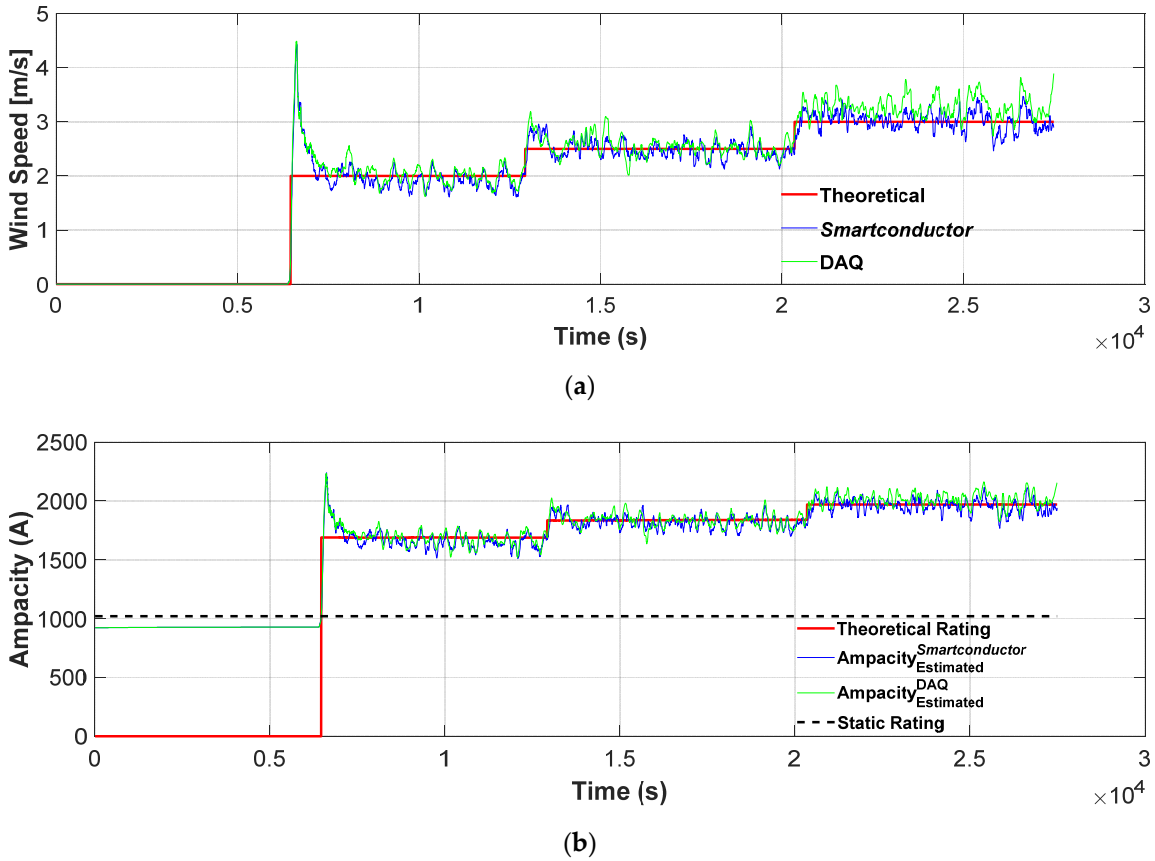

Figure 6. (**a**) Theoretical and estimated wind speeds with the *Smartconductor* (using the Pt1000 and Hall effect sensor) and the DAQ (using T-type thermocouple and Rogowski coil); (**b**) static and theoretical and estimated ampacity values with the *Smartconductor* (using the Pt1000 and Hall effect sensor) and the DAQ (using T-type thermocouple and Rogowski coil).

It is worth noting that the theoretical rating I_{max} (red line in Figure 6b) was obtained from (18) by taking into account the measured values (real values) of the wind speed.

Table 5 summarizes the results that were attained. It shows that the estimated wind speeds are very close to the applied ones and that the estimated ampacities at the different wind speeds are very close to the theoretical values, which were calculated by applying (18) and considering the measured values of the wind speed instead of the ones that were estimated by the method proposed in this work since the differences are below 2.3%.

Table 5. Results of estimated wind speed and ampacity predicted by the proposed approach.

Current (A) (%Static Rating)	Theoretical Wind Speed (m/s)	Theoretical Line Rating (A)	Average Estimated Wind Speed (m/s)by *Smartconductor*	Average Estimated Wind Speed (m/s)By DAQ System	Average Estimated Ampacity(A) by *Smartconductor*	Average Estimated Ampacity (A) by DAQ	Error of Line Rating Calculation by *Smartconductor* (%)	Error of Line Rating Calculation by DAQ System (%)
624 (55%)	0	927	0	0	927	927	0.0	0.0
1088 (97%)	2	1688	1.90	1.99	1648	1670	2.3	1.0
1088 (97%)	2.5	1833	2.48	2.53	1813	1830	1.0	0.2
1088 (97%)	3	1969	3.03	3.28	1961	2016	0.2	2.3

The static rating of the conductor is 1020A.

6.2. Second Experiment. Validation of the Accuracy of the Proposed Method to Estimate the DTLR

A second experiment was conducted to validate the accuracy of the DTLR estimation method proposed in this paper. To this end, the current and wind speed profiles shown in Figure 7a were applied to the analyzed conductor. The values of the applied currents were selected so that the equilibrium conductor temperature was 90 °C under the four wind conditions (0 m/s, 2 m/s, 2.5 m/s and 3 m/s), i.e., the maximum allowable temperature of the tested ACSR conductor for continuous operation. Thus, the same laboratory setup as the one used in the previous tests was used, and four current levels were injected (956 A, 1680 A, 1830 A, and 1980 A, which correspond to the four wind speeds 0 m/s, 2 m/s, 2.5 m/s and 3 m/s, respectively) to heat the ACSR conductor up to 90 °C. The results that were attained are shown in Figure 7.

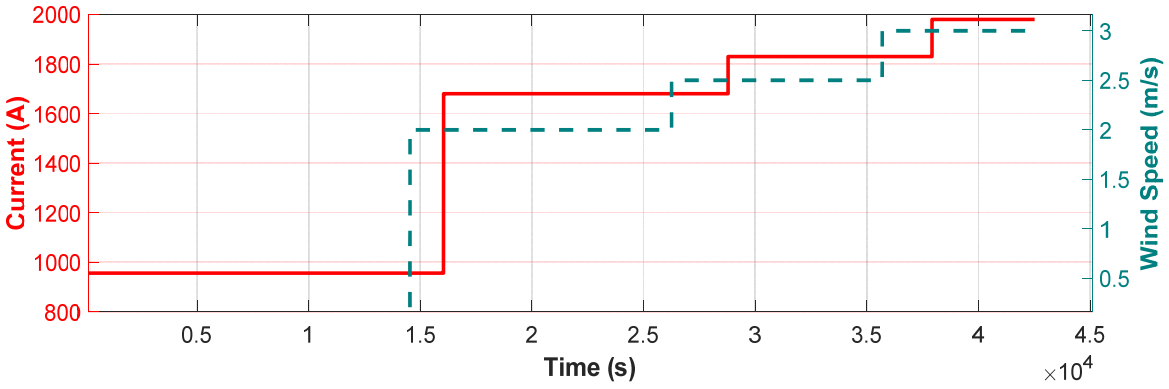

(**a**)

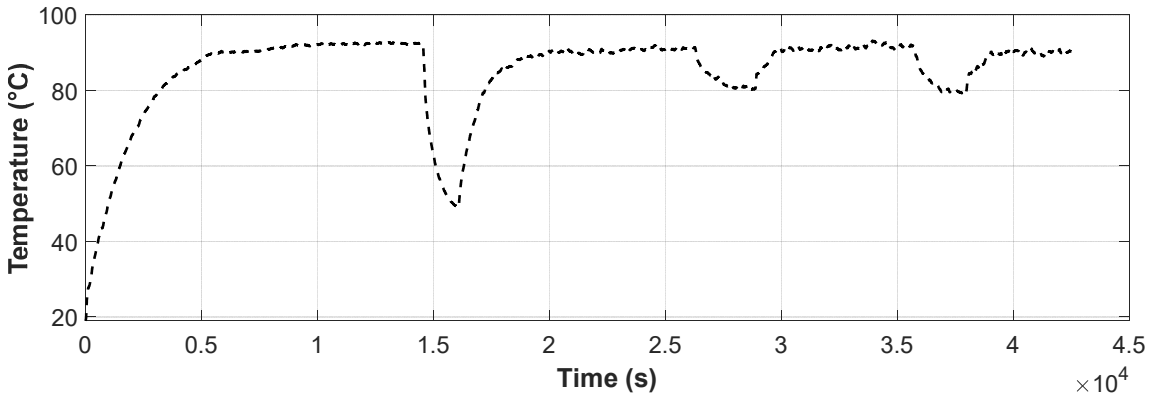

(**b**)

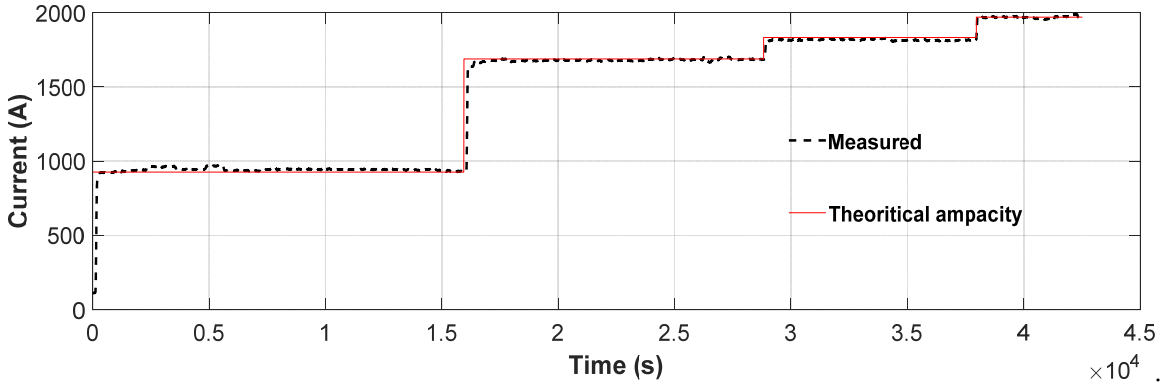

(**c**)

Figure 7. (**a**) Current and wind speed profiles during the test. (**b**) Conductor temperature measured by the T-type thermocouple and the Pt1000 sensor; (**c**) Applied and theoretical current values.

Table 6 summarizes the numerical values corresponding to Figure 7. These results show that the difference between the real and estimated currents needed to bring the conductor to the maximum allowable temperature is low and are always below 3.0%, thus validating the method proposed in this paper.

Table 6. Results of steady-state temperature with different currents and wind speeds.

Currents			Wind Speed(m/s)	Steady-State Conductor Temperature (°C)
Applied (A)	Estimated (A)	Difference (%)		
956	927	3.0	0.0	Around 90
1680	1688	0.5	2.0	Around 89
1830	1833	0.2	2.5	Around 90
1980	1969	0.6	3.0	Around 89

Regarding the computational requirements of the proposed approach, the estimation of the wind speed requires 0.05 ms and the estimation of the DTLR requires 0.07 ms when using a Intel(R) Xeon(R) CPU E5-2620 v4 processor with 64 Gb RAM memory

7. Conclusions

This paper has presented a real-time monitoring system to determine the ampacity of ACSR conductors, called a *Smartconductor*. To this end, the actual values of the ambient temperature and solar radiation are required and can be obtained from a nearby weather station, whereas the *Smartconductor* measures the current and temperature of the conductor. Since the wind speed at the conductor surface greatly depends on its exact location and since it has an important cooling effect, it is essential to have an accurate estimation of the local wind speed at the conductor. Therefore, a method that accurately estimates the wind speed has also been presented. Once this parameter is known, the approach presented in this paper allows the calculation of the DTLR rating of the analyzed conductor based on a thermal model. To validate the accuracy and performance of the approach presented in this paper, different situations have been tested in the laboratory using ACSR conductors by controlling and measuring the solar radiation, wind speed, local temperature, conductor temperature, and line current. The proposed approach also includes a method to estimate the combined joule and magnetic losses of the ACSR conductor from the ac resistance.

The experimental results presented in this paper prove that the real-time approach presented in this paper can predict both the value of the local wind speed and the DTLR with accuracy while requiring a reduced computational burden, so the calculations can be implemented in low-power microprocessors used in inexpensive devices that are required for a global deployment of smart grids. Therefore, the findings in this paper contribute to research concerning smart grids. The proposed DTLR approach allows us to take advantage of the maximum transmission capacity of power lines by adapting the rating of the line according to the current weather conditions in real-time, making it a smart solution that is of paramount importance for future smart grids.

Author Contributions: Conceptualization, Y.L., M.M.-E., and J.-R.R.; methodology, J.-R.R.; software, Y.L.; validation, Y.L. and J.S.; formal analysis, M.M.-E. and J.-R.R.; investigation, Y.L., M.M.-E., and J.-R.R.; resources, J.S., M.M.-E., and J.-R.R.; writing—original draft preparation, Y.L., and J.-R.R.; writing—review and editing, M.M.-E.; supervision, J.S. and M.M.-E.; All authors have read and agreed to the published version of the manuscript.

Funding: This research was funded by Generalitat de Catalunya, grant numbers 2017 SGR 967 and 2020 DI 007, and the Ministerio de Ciencia, Innovación y Universidades de España, grant number RTC-2017-6297-3.

Institutional Review Board Statement: Not applicable

Informed Consent Statement: Not applicable

Conflicts of Interest: The authors declare no conflicts of interest.

References

1. Rácz, L.; Németh, B. Dynamic Line Rating—An Effective Method to Increase the Safety of Power Lines. *Appl. Sci.* **2021**, *11*, 492.
2. Lv, F.; Zhang, P.; Tang, Z.; Yue, Y.; Yang, K. A Guided Wave Transducer with Sprayed Magnetostrictive Powder Coating for Monitoring of Aluminum Conductor Steel-Reinforced Cables. *Sensors* **2019**, *19*, 1550.
3. Morgan, V.T.; Zhang, B.; Findlay, R.D. Effect of magnetic induction in a steel-cored conductor on current distribution, resistance and power loss. *IEEE Trans. Power Deliv.* **1997**, *12*, 1299–1306.
4. Beňa, Ľ.; Gáll, V.; Kanálik, M.; Kolcun, M.; Margitová, A.; Mészáros, A.; Urbanský, J. Calculation of the overhead transmission line conductor temperature in real operating conditions. *Electr. Eng.* **2021**, *103*, 769–780.
5. Alvarez, D.L.; da Silva, F.F.; Mombello, E.E.; Bak, C.L.; Rosero, J.A. Conductor temperature estimation and prediction at thermal transient state in dynamic line rating application. *IEEE Trans. Power Deliv.* **2018**, *33*, 2236–2245.
6. Black, C.R.; Chisholm, W.A. Key Considerations for the Selection of Dynamic Thermal Line Rating Systems. *IEEE Trans. Power Deliv.* **2015**, *30*, 2154–2162.
7. Cigré Working Group 22.12. *Thermal Behaviour of Overhead Conductors*; Cigré: Paris, France, 2002.
8. IEEE Std 738-2012. *IEEE Standard for Calculating the Current-Temperature of Bare Overhead Conductors*; New York, NY, USA, 2012.
9. Karimi, S.; Musilek, P.; Knight, A.M. Dynamic thermal rating of transmission lines: A review. *Renew. Sustain. Energy Rev.* **2018**, *91*, 600–612.
10. Minguez, R.; Martinez, R.; Manana, M.; Cuasante, D.; Garañeda, R. Application of Digital Elevation Models to wind estimation for dynamic line rating. *Int. J. Electr. Power Energy Syst.* **2022**, *134*, 107338.
11. International Electrotechnical Commission and IEC. *IEC TR 61597:2021 Overhead Electrical Conductors—Calculation Methods for Stranded Bare Conductors*; IEC: Geneva, Switzerland, 2021.
12. Hydro Tasmania Consulting. *Dynamic Transmission Line Rating Technology Review*; Cambridge, TAS, Australia, 2009; pp. 1–39.
13. Ho, H.N.; Bui, T.; Do, H.; Rojas, E.; Ojeda, O.; Tran, H.; Hoang, T.; Hernandez, E.; Nguyen, L.; Le, H. Design and Simulation of an Autonomous Smart Microgrid for Energy Independence. *WSEAS Trans. Environ. Dev.* **2021**, *17*, 911–928.
14. Park, K.J. A Novel Way to Select the Optimal Electrical Power Demand Management Provider for Robust Smart Grid. *Int. J. Circuits Syst. Signal. Process.* **2021**, *14*, 511–519.
15. Wallnerstrom, C.J.; Huang, Y.; Soder, L. Impact from dynamic line rating on wind power integration. *IEEE Trans. Smart Grid* **2015**, *6*, 343–350.
16. Hasan, M.K.; Ahmed, M.M.; Musa, S.S. Measurement and Modeling of DTCR Software Parameters Based on Intranet Wide Area Measurement System for Smart Grid Applications. *Adv. Intell. Syst. Comput.* **2021**, *1166*, 1139–1150.
17. Numan, M.; Feng, D.; Abbas, F.; Habib, S.; Hao, S. Coordinated operation of reconfigurable networks with dynamic line rating for optimal utilization of renewable generation. *Int. J. Electr. Power Energy Syst.* **2021**, *125*, 106473.
18. Teh, J.; Lai, C.-M. Reliability Impacts of the Dynamic Thermal Rating System on Smart Grids Considering Wireless Communications. *IEEE Access* **2019**, *7*, 41625–41635.
19. L-Azab, M.E.; Omran, W.A.; Mekhamer, S.F.; Talaat, H.E.A. Congestion management of power systems by optimizing grid topology and using dynamic thermal rating. *Electr. Power Syst. Res.* **2021**, *199*, 107433.
20. Kopsidas, K.; Cruzat, C.; Ni, M. Cyber-physical reliability of dynamic line rating ICT failures in OHL networks. *IET Gener. Transm. Distrib.* **2021**, *15*, 371–382.
21. Pal, R.; Chavhan, S.; Gupta, D.; Khanna, A.; Padmanaban, S.; Khan, B.; Rodrigues, J.J.P.C. A comprehensive review on IoT-based infrastructure for smart grid applications. *IET Renew. Power Gener.* **2021**, *8*, https://doi.org/10.1049/rpg2.12272.
22. Bera, B.; Saha, S.; Das, A.K.; Vasilakos, A.V. Designing blockchain-based access control protocol in iot-enabled smart-grid system. *IEEE Internet Things J.* **2021**, *8*, 5744–5761.
23. Mehmood, M.Y.; Oad, A.; Abrar, M.; Munir, H.M.; Hasan, S.F.; Muqeet, H.; Golilarz, N.A. Edge Computing for IoT-Enabled Smart Grid. *Secur. Commun. Netw.* **2021**, *2021*, 5524025, https://doi.org/10.1155/2021/5524025.
24. Zhang, Y.Z.; Xiong, R.; He, H.W.; Pecht, M. Validation and verification of a hybrid method for remaining useful life prediction of lithium-ion batteries. *J. Clean. Prod.* **2019**, *212*, 240–249.
25. Albizu, I.; Fernandez, E.; Eguia, P.; Torres, E.; Mazon, A.J. Tension and ampacity monitoring system for overhead lines. *IEEE Trans. Power Deliv.* **2013**, *28*, 3–10.
26. Douglass, D.; Chisholm, W.; Davidson, G.; Grant, I.; Lindsey, K.; Lancaster, M.; Lawry, D.; McCarthy, T.; Nascimento, C.; Pasha, M.; et al. Real-Time Overhead Transmission-Line Monitoring for Dynamic Rating. *IEEE Trans. Power Deliv.* **2016**, *31*, 921–927.
27. Wijethunga, A.H.; Wijayakulasooriya, J.V.; Ekanayake, J.B.; de Silva, N. Conductor temperature based low cost solution for dynamic line rating calculation of power distribution lines. In Proceedings of the 2015 IEEE 10th International Conference on Industrial and Information Systems (ICIIS), Peradeniya, Sri Lanka, 18–20 December 2015; pp. 128–133.
28. Singh, C.; Singh, A.; Pandey, P.; Singh, H. Power Donuts in Overhead Lines for Dynamic Thermal Rating Measurement, Prediction and Electric Power Line Monitoring. *Int. J. Adv. Res. Electr. Electron. Instrum. Eng.* **2014**, *3*, 9394–9400.

29. Ding, Y.Q.; Gao, M.; Li, Y.; Wang, T.-L.; Ni, H.-L.; Liu, X.-D.; Chen, Z.; Zhan, Q.-H.; Hu, C. The effect of calculated wind speed on the capacity of dynamic line rating. In Proceedings of the 2016 IEEE International Conference on High Voltage Engineering and Application (ICHVE), Chengdu, China, 19–22 September 2016; pp. 13–16.
30. Xiao, C.; Zhao, L.; Asada, T.; Odendaal, W.G.; Van Wyk, J.D. An Overview of Integratable Current Sensor Technologies. In Proceedings of the 38th IAS Annual Meeting on Conference Record of the Industry Applications Conference, 2003, Salt Lake City, UT, USA, 12–16 October 2003; Volume 2, pp. 1251–1258.
31. Kadechkar, A.; Moreno-Eguilaz, M.; Riba, J.-R.; Capelli, F. Low-Cost Online Contact Resistance Measurement of Power Connectors to Ease Predictive Maintenance. *IEEE Trans. Instrum. Meas.* **2019**, *68*, 4825–4833.
32. Foss, S.D.; Fernandes, R.A. Dynamic thermal line ratings Part I dynamic ampacity rating algorithm. *IEEE Trans. Power Appar. Syst.* **1983**, *PAS-102*, 1858–1864.
33. Miyazaki, H.; Kitamura, S. Temperature distribution within an ACSR conductor during large current flow. *Electr. Eng. Jpn.* **2002**, *140*, 38–45.
34. IEC. *IEC 60751:2008 Industrial Platinum Resistance Thermometers and Platinum Temperature Sensors*; IEC: Geneve, Switzerland, 2007; pp. 1–41.
35. Morgan, V.T. The Current Distribution, Resistance and Internal Inductance of Linear Power System Conductors—A Review of Explicit Equations. *IEEE Trans. Power Deliv.* **2013**, *28*, 1252–1262.
36. Morgan, V.T. Electrical characteristics of steel-cored aluminium conductors. *Proc. Inst. Electr. Eng.* **1965**, *112*, 325.
37. Hong, S.S.; Yang, Y.-C.; Hsu, T.-S.; Tseng, K.-S.; Hsu, Y.-F.; Wu, Y.-R.; Jiang, J.-A. Internet of Things-Based Monitoring for HV Transmission Lines: Dynamic Thermal Rating Analysis with Microclimate Variables. In Proceedings of the 2020 8th International Electrical Engineering Congress (iEECON), Chiang Mai, Thailand, 4–6 March 2020.
38. Texas Instruments. *DRV5053 Analog-Bipolar Hall Effect Sensor*; Texas Instruments: Dallas, TX, USA, 2014; pp. 1–20.
39. Popovic, R.S.; Randjelovic, Z.; Manic, D. Integrated Hall-effect magnetic sensors. *Sens. Actuators A Phys.* **2001**, *91*, 46–50.
40. Dewi, S.D.T.; Panatarani, C.; Joni, I.M. Design and development of DC high current sensor using Hall-Effect method. *AIP Conf. Proc.* **2016**, *1712*, 030006.
41. Khawaja, A.H.; Huang, Q.; Khan, Z.H. Monitoring of Overhead Transmission Lines: A Review from the Perspective of Contactless Technologies. *Sens. Imaging* **2017**, *18*, 24.
42. Kadechkar, A.; Riba, J.R.; Moreno-Eguilaz, M.; Perez, J. SmartConnector: A Self-Powered IoT Solution to Ease Predictive Maintenance in Substations. *IEEE Sens. J.* **2020**, *20*, 11632–11641.

5.5 On-Line Core Losses Determination in ACSR Conductors for DLR Applications

Reference:

Riba, J.-R.; Liu, Y.; Moreno-Eguilaz, M.; Sanllehí, J. On-Line Core Losses Determination in ACSR Conductors for DLR Applications. Materials 2022, 15, 6143. Under a CC BY 4.0 license. https://doi.org/10.3390/ ma15176143.

Publication framework:

This article proposed a method to determine the ac resistance of aluminum steel-reinforced conductors online, in order to estimate the dynamic line rating of such conductors by using real-time conductor and meteorological parameter measurements. To do so, this article analyzed conductors with one, two and three layers of stranded aluminum conductors in detail. Two possible methods are proposed to obtain the ac resistance based on the experimental results obtained.

Main contributions:

- **Online estimation of ac resistance of ACSR conductors to determine dynamic line rating.**
- **Determination of Joule and core losses from the online estimation of ac resistance for ACSR conductors.**
- **Implementation of two approaches to measure the ac resistance of ACSR conductors.**

Key words:

core losses; aluminum conductors steel-reinforced; ac resistance; dynamic line rating

materials

MDPI

Article

On-Line Core Losses Determination in ACSR Conductors for DLR Applications

Jordi-Roger Riba [1,*], Yuming Liu [1,2], Manuel Moreno-Eguilaz [1] and Josep Sanllehí [2]

[1] Electrical Engineering Department, Universitat Politècnica de Catalunya, Rambla Sant Nebridi 22, 08222 Terrassa, Spain
[2] SBI Connectors, Albert Einstein, 5, 08635 Sant Esteve Sesrovires, Spain
* Correspondence: jordi.riba-ruiz@upc.edu; Tel.: +34-937398365

Abstract: Dynamic line rating (DLR) is a method that focuses on dynamically determining the maximum allowable current of power lines, while ensuring they operate within safe limits. DLR needs to monitor the temperature and current of the line in real-time, as well as the weather variables in the surroundings of the power line. DLR approaches also require determining the AC resistance of the power line conductors, which is a key parameter that enables it to determine Joule and core losses. This paper presents an approach for an on-line alternating current (AC) resistance estimation of aluminum conductor steel-reinforced (ACSR) conductors to determine the DLR capability of such conductors from real-time conductor and meteorological parameter measurements. For this purpose, conductors with one, two and three layers of aluminum strands are analyzed in detail. Based on the experimental results presented in this paper, two possible approaches are proposed.

Keywords: core losses; aluminum conductor steel-reinforced; ac resistance; dynamic line rating

Citation: Riba, J.-R.; Liu, Y.; Moreno-Eguilaz, M.; Sanllehí, J. On-Line Core Losses Determination in ACSR Conductors for DLR Applications. *Materials* **2022**, *15*, 6143. https://doi.org/10.3390/ma15176143

Academic Editor: Federico Mazzucato

Received: 17 July 2022
Accepted: 2 September 2022
Published: 4 September 2022

1. Introduction

Today, renewable power generation sources are reinforcing distribution networks. The growing demand for electricity is forcing system operators to take full advantage of the maximum capacity of existing power lines [1]. However, the maximum allowable temperature of the conductor must not be exceeded, as it defines the current carrying capacity of the conductor [2]. The ampacity or maximum allowable loading current is established by the maximum permissible temperature of the conductor [3]. Temperature has a great influence on the mechanical sag of overhead transmission lines [4,5], which is a key parameter for power system operation [6]. Overhead power transmission lines are generally operated below their static line rating (SLR). The SLR is calculated when the conductor operates at the maximum allowable temperature in conservative weather conditions. Contrarily, dynamic line rating (DLR) determines the actual ampacity when conductors are operating at the maximum allowable temperature under actual weather conditions [7]. DLR can be useful for the integration of intermittent renewable energy sources into existing power networks [8]. Intermittent renewable energy sources (IRES) cannot provide constant additional power, making it difficult for system operators to justify the investment required to expand current transmission lines [9]. Dynamic line rating (DLR) allows for the maximum utilization of the conductor, that is, to operate at the maximum ampacity or current that it can withstand without exceeding the upper allowed temperature of the conductor [10]. Although there are different approaches to DLR, the most common approach is to measure weather variables, line current and temperature using dedicated sensors [11]. These measured variables are used to feed mathematical models of conductors, such as the Cigré TB207 [12] and IEEE [13] models, from which the maximum conductor rating is dynamically obtained. Results obtained are significantly dependent on weather conditions, including ambient temperature, wind speed and direction, or solar radiation, although wind speed significantly affects the resulting ampacity [14,15].

The alternating current resistance (R_{ac}) of the conductor is a key parameter which allows the ampacity or maximum current capacity of power conductors to be accurately estimated. This can increase their effective capability [16], since Joule and core losses represent the main heat source of the conductor, and can be determined from the alternating current (AC) resistance R_{ac} [17,18]. Line current, along with ac resistance, are used in some DLR approaches to estimate the effective wind speed [18]. Therefore, DLR enables the development of more accurate power flow analysis approaches if the ac resistance, which changes with temperature, is measured in real time [19].

Stranded aluminum conductor steel-reinforced (ACSR) conductors have been applied for over 100 years in overhead power lines to transmit electrical power at high voltage [20]. ACSR conductors have multiple layers of aluminum [21] and galvanized steel strands. The aluminum wires are wound helically around the core formed by the galvanized steel strands. Adjacent aluminum layers are wound in opposite directions around the steel core [22]. Whereas the steel core provides the mechanical strength, high-conductivity aluminum strands provide the current path [23], carrying approximately 98% of the electric current [24]. Electric current tends to spiral along the aluminum strands because the contact resistance between adjacent strands is much greater than the internal resistance of the strands, producing an axial component of the magnetic field. The axial AC magnetic flux causes eddy currents and hysteresis losses in the core, and forces the current density in the aluminum layers to redistribute to a greater or lesser extent, depending on the strength of the magnetic field in the core, and thus, on the intensity of the electric current and the lay length of the aluminum layers [25]. The lay length is the distance the wire requires to make a complete revolution around the diameter of the conductor, as shown in Figure 1. Therefore, due to magnetic induction, the steel core increases the AC resistance of the conductor [23].

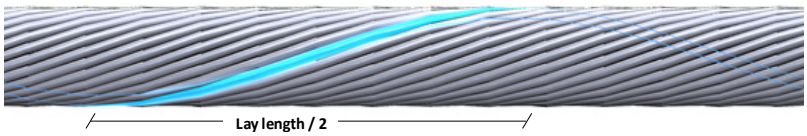

Figure 1. Stranded conductor and lay length.

Due to the opposite stranding directions of adjacent aluminum layers, the axial components of the magnetic field generated by the currents from adjacent layers are in opposite directions, which reduces the total magnetic field. The greatest cancellation of the magnetic field occurs in conductors with two aluminum layers, this effect being less marked in conductors with an odd number of aluminum layers than in conductors with an even number of layers [23,25,26]. Therefore, ACSR conductors with an even number of aluminum layers have lower magnetic core losses [22]. Under AC supply, the axial component of the magnetic field generates eddy currents and hysteresis losses, and modifies the current distribution between the layers. This effect, due to the magnetic coupling of the current in the aluminum layers through the steel core [3], is known as the transformer effect. The magnitude of the axial magnetic flux largely determines the intensity of the transformer effect, so it varies with the intensity of the electric current and the magnetic permeability of the steel core, which in turn depends on the tensile stress of the core and the temperature [27].

The non-uniformity of the current density in the different layers of aluminum due to the transformer effect is greatest for three-layer ACSR conductors [3]. Experimental results performed on a three-layer ACSR conductor show that the current density in the central layer is higher than in the other layers, resulting in a higher R_{ac}/R_{dc} ratio [28], R_{dc} being the direct current (DC) resistance. This is mainly due to the transformer effect [26,27] or current redistribution among the aluminum layers, and only partially due (to a lesser extent) to the eddy currents and hysteresis losses that occur in the steel core [28].

This paper presents an approach for an on-line estimation of the AC resistance of ACSR conductors to determine their DLR capacity from real-time conductor measurements

and weather parameters, thus presenting several novel findings and making unique contributions in this area. Joule and core losses are determined from an on-line measurement of the AC resistance, which, due to its low value, makes its on-line measurement under AC supply a challenging task. The approach proposed here to estimate the AC resistance can be applied to ACSR conductors with any number of aluminum layers, while considering its dependence on the line current. This is a novelty in this work, since most of the current DLR approaches do not take into account the change in the AC resistance of ACSR conductors with the current level, so they can lead to inaccurate estimates of the AC resistance, and thus of the DLR ampacity. To this end, two new methods are proposed to determine the AC resistance. The first one, which is more accurate, is based on measuring temperature, current, voltage drop and the phase shift between voltage drop and current over a short length of conductor. The second method only requires measuring the temperature and current through the conductor, thus avoiding measuring the voltage drop and simplifying installation and measurement requirements. The proposal presented here is in line with the current trend of operating power lines at their maximum instantaneous capacity, since it allows the current rating to be adapted to existing weather conditions in real-time. In addition, it is simple to apply, requires a low computational burden, and is compatible with the Internet of Things (IoT), one of the crucial technologies that improves smartness in many industrial, power line and smart grid applications [29–31], whose basic function is to connect objects [32], including intercommunicating sensors [33], actuators and other smart technologies [34].

The experimental results presented in this paper show that the two proposed approaches are suitable for an on-line determination of the AC resistance of ACSR conductors to apply DLR strategies, so that it is possible to take advantage of the full transmission capacity of ACSR-based power lines. The accuracy of the proposed approaches has been evaluated by analyzing different ACSR conductors, including single-, two- and three-layer conductors in different working conditions, covering a wide range of operations in different weather conditions.

This paper is structured as follows: Section 2 describes the theoretical background, including how to experimentally determine the AC resistance of ACSR conductors, the equations required to estimate power losses in ACSR conductors, the transient thermal balance equation for ACSR conductors and the calculation of the DLR ampacity; Section 3 describes the experimental setup used in this paper, including the electrical loop, the analyzed conductors, the high-current power transformer, the sensors used and the measuring devices; Section 4 shows the experimental results obtained with the different conductors and discusses the results attained; and finally, Section 5 concludes the paper.

2. Theoretical Background

2.1. AC Resistance and Reactance of ACSR Conductors

The AC resistance of a conductor is affected by the current density distribution, the internal temperature and the magnetic properties of the steel core, with the two last parameters being affected by the intensity of the electric current. According to [35], the AC resistance of ACSR conductors can be expressed as the sum of three terms, i.e., the DC resistance, the resistance term due to eddy currents, and the term due to hysteresis losses. Core losses (hysteresis and eddy current losses) as well as any temperature rises also increase the effective AC resistance of the conductor [3,20,36]. The combined action of eddy currents, hysteresis and the transformer effect raises the AC resistance R_{ac} of the conductor above the DC value R_{dc} at the same temperature. Higher values of the R_{ac}/R_{dc} ratio increase the energy losses in the conductor [20].

Since the cancellation of the axial component of the magnetic field is less effective in conductors with an odd number of aluminum layers, these conductors will exhibit higher resistance ratios R_{ac}/R_{dc}. The highest resistance ratio is expected in conductors with a single layer of aluminum, whereas the lowest corresponds to conductors with two layers [3]. The internal inductance of ACSR conductors increases with current up to a maximum value,

where the steel core becomes magnetically saturated [36], and then any further increase in current reduces the internal inductance [3] due to the decrease of the magnetic permeability.

According to the international standard IEC 60287-1-1 [37], the AC resistance can be obtained from the DC resistance as:

$$R_{ac} = R_{dc}(1 + y_s + y_p) \ [\Omega/\mathrm{m}] \tag{1}$$

where y_s and y_p are, respectively, the skin and proximity effect factors. The effect of temperature is considered as:

$$R_{dc} = R_0[1 + \alpha_{20}(T - 20)] \ [\Omega/\mathrm{m}] \tag{2}$$

where T is the operating conductor temperature, R_0 the DC resistance measured at 20 °C and α_{20} is the temperature coefficient at 20 °C.

In most ACSR applications, the skin effect is negligible compared to the transformer effect, but in applications requiring low currents, large diameter conductors or high frequencies, this difference is reduced. The proximity effect is also negligible when distances between adjacent conductors greater than ten diameters are assumed [20]. Although (1) is simple to apply, it only applies to nonferromagnetic conductors up to 5 kV [37], and it does not consider important parameters such as those related to the stranding, including the direction and lay length, as it considers the stranded conductor to be a solid conductor [16,38].

The DC resistance of the conductor only depends on the temperature of the conductor, but the AC resistance also depends on the current [3]. According to [25], the AC resistance of an isothermal ACSR conductor increases with current following a sigmoidal change due to the change in magnetic field strength and the consequent increase in core losses.

There is no explicit equation to determine the internal inductance of an ACSR conductor under DC supply. Several authors have proposed formulas for AC supply, although they are not exact, since it is difficult to model the complex behavior of the magnetic flux in the steel core. It is known that the per-unit length of the internal AC inductance of ACSR conductors also increases with current following a sigmoidal curve up to a maximum value corresponding to the magnetic saturation of the steel core, and then, any further current increases reduce the inductance [25]. The goodness of the electrical contacts between aluminum wires in the same layer and between wires in adjacent layers changes with the tension and degree of oxidation in the conductor. Also, conductors are not isothermal because they exhibit both radial and sometimes axial temperature gradients [3]. Therefore, due to the nonlinearity and complexity of these effects, the most effective way to determine the AC resistance and the internal reactance or inductance of stranded ACSR conductors is from experimental measurements.

By measuring the instantaneous values of the voltage drop per unit length ΔV, the electric current I and the phase shift φ between them, it is possible to determine the per unit length values of the impedance [39], AC resistance R_{ac} and reactance X of the conductor expressed in Ω/m as [3,40]:

$$Z = \frac{\Delta V}{I} \ [\Omega/\mathrm{m}] \tag{3}$$

$$R_{ac} = \frac{\Delta V}{I} \cdot \cos\varphi \ [\Omega/\mathrm{m}] \tag{4}$$

$$X = \frac{\Delta V}{I} \cdot \sin\varphi \ [\Omega/\mathrm{m}] \tag{5}$$

The next equation describes the dependence of R_{ac} with temperature:

$$R_{ac,T} = R_{ac,0}[1 + \alpha_{ac}(T - T_0)] \ [\Omega/\mathrm{m}] \tag{6}$$

where $R_{ac,0}$ is the AC value of the resistance at a given temperature T_0, usually 20 °C, and α_{ac} is the temperature coefficient of the AC resistance. Note that $R_{ac,0}$ is a measured value, which already includes the saturation effect, as proved in [19].

2.2. Power Losses in ACSR Conductors

Core losses take into account the effect of eddy currents and hysteresis in the steel core [3]. These losses, along with current redistribution and the effect of temperature, are key factors determining the AC resistance of ACSR conductors [41]. Eddy current and hysteresis losses increase with the square of the strength of the magnetic flux density and with increasing values of temperature for a constant strength of the magnetic field H. However, they tend to decrease as the resistivity of the steel core material increases, and thus, as the temperature rises [20].

According to [17,18,42], the losses due to Joule (P_J), core (P_M) and redistribution (P_{redis}, transformer effect) effects can be expressed as follows:

$$P_J + P_M + P_{redis} = I^2 R_{ac} \tag{7}$$

Note that (7) is in agreement with the method for measuring power losses detailed in IEEE Std. 2772 [43] to measure the power loss of overhead conductors under real simulated laboratory conditions:

$$P_{loss} = P_J + P_M + P_{redis} = \Delta V I \cos\varphi \tag{8}$$

2.3. Transient Thermal Balance Equation for DLR Calculation

The heat balance equation, which must always be satisfied, is the basis for implementing DLR approaches for ACSR conductors [18]. It states that the sum of the ohmic ($P_J + P_M + P_{redis}$) and solar heat gain must equal the heat loss by convection and radiation [44].

According to [12], the unsteady-state equation that describes the transient thermal balance of an ACSR conductor can be expressed as:

$$P_J + P_M + P_{redis} + P_S - P_C - P_R = mc\frac{dT}{dt}\ [\mathrm{W/m}] \tag{9}$$

P_J, P_M, P_{redis} and P_S being the per unit length heat gain terms of the conductor (Joule, magnetic/core, transformer effect and solar heating terms, respectively, in W/m). P_C and P_R are the per unit length heat loss terms (convective and radiative loss terms, respectively, in W/m), m is the per unit length mass of the conductor in kg/m, c is the specific heat capacity of the conductor expressed in J/(kg °C), T is the average conductor temperature expressed in °C, and t is the time in s. The heat capacity c of the ACSR conductor is calculated as the weighted average of the iron strands in the core and the aluminum strands, and can be expressed as:

$$c(T) = \frac{m_{Al}c_{Al,20^\circ\mathrm{C}}[1+\beta_{Al}(T-20)] + m_{steel}c_{steel,20^\circ\mathrm{C}}[1+\beta_{steel}(T-20)]}{m_{Al,20^\circ\mathrm{C}} + m_{steel,20^\circ\mathrm{C}}}\ [\mathrm{J/(kg^\circ C)}] \tag{10}$$

where c_x is the specific heat capacity of element x (Al = aluminum or steel), m_x is its mass per unit length, and β is the temperature coefficient of the heat capacity, whose values can be found in [10].

According to [10,18], convective heat losses are calculated as:

$$P_C = \pi[0.042 + 3.6{\cdot}10^{-5}(T_a + T)](T - T_a)Nu\ [\mathrm{W/m}] \tag{11}$$

where Nu is the Nusselt number, which can be calculated as detailed in [18] once the conductor diameter, surface roughness, local wind speed, local temperature, relative density and kinematic viscosity of the air are known.

The heat gain by solar radiation is obtained from the global solar radiation S (W/m^2) as [12]:

$$P_S = \alpha_s S D \text{ [W/m]} \quad (12)$$

where D [m] is the outer conductor diameter and α_s is the dimensionless solar absorptivity of the conductor surface, where its value is often assumed to be 0.5 [45].

Heat losses due to radiation are calculated as [12]:

$$P_R = \pi \varepsilon D \sigma_B [(T + 273)^4 - (T_a + 273)^4] \text{ [W/m]} \quad (13)$$

where ε is the emissivity factor of the surface of the conductor (its value is often assumed to be 0.5 [2,45]) and σ_B is the Stefan-Boltzmann constant.

The DLR ampacity I_{max} is calculated at the maximum allowable temperature of the conductor, assuming that the temperature of the conductor is in thermal equilibrium, resulting in [10,46]:

$$I_{\max} = \left(\frac{P_C(T_{\max}) + P_R(T_{\max}) - P_S}{R_{ac}(T_{\max})} \right)^{1/2} \text{ [A]} \quad (14)$$

From (14), it is seen that the AC resistance plays a key role in determining the DLR ampacity, so an accurate estimate is required for this purpose.

3. Experimental Setup

This section describes the experimental devices and materials used in the laboratory experiments, including the ACSR conductors, sensors and measuring devices required to determine the AC resistance of the studied conductors.

3.1. The Analyzed Single-, Two- and Three-Layer ACSR Conductors

As explained in the introduction, ACSR conductors with one, two or three layers have different behaviors due to the interaction of the axial magnetic flux generated by the different layers of aluminum strands with the steel core, thus increasing the AC resistance of the conductor. Since the adjacent aluminum layers are stranded in opposite directions, the axial component of the resulting magnetic field is reduced. Therefore, this cancellation effect is greatest in two-layer ACSR conductors, while it is the least impactful in three-layer conductors, and not present at all in single-layer conductors. Due to the effect of the steel core, the AC resistance of the conductor is expected to depend not only on the temperature of the conductor but also on the intensity of the current flowing through the conductor. However, due to the partial cancellation of the axial component of the magnetic flux generated by layers of aluminum strands wound in opposite directions, the AC resistance of two-layer ACSR conductors should be almost independent of current intensity, while in the case of three-layer ACSR conductors, this dependency should be very low. It should be at the maximum in single-layer ACSR conductors.

This work analyzes the behavior of the three-layer 550-AL1/71-ST1A ACSR conductor (HAASE Gesellschaft mbh, Graaz, Austria), and the two-layer 135-AL1/22-ST1A conductor (EMTA Kablo, Istanbul, Turkey), whose main parameters are summarized in Table 1.

Next, a single-layer ACSR conductor was made from the 135-AL1/22-ST1A two-layer conductor by carefully removing the outer layer of aluminum strands.

The three-layer conductor includes 7 steel strands that form the core, and three successive layers with 12, 18 and 24 aluminum strands, respectively, thus being 7/54.

The two-layer conductor includes 7 steel strands in the core and two layers with 10 and 16 aluminum strands, respectively, being 7/26. The single-layer conductor is 7/10.

Figure 2 shows the geometry of the analyzed three-, two- and single-layer ACSR conductors.

Table 1. Main parameters of the three-layer 550-AL1/71-ST1A ACSR conductor from HAASE Gesellschaft and the two-layer 135-AL1/22-ST1A ACSR conductor from EMTA Kablo.

Symbol	Description	Three-Layer	Two-Layer	Unit
A_{Al}	Area of aluminum	549.7	134.9	mm^2
A_{steel}	Area of steel	71.3	22	mm^2
N_{Al}	Number of aluminum wires	54 (12/18/24)	26 (10/16)	-
N_{Steel}	Number of steel wires	7	7	-
D_{Al}	Aluminum wire diameter	3.6	2.57	mm
D_{steel}	Steel wire diameter	3.6	2.0	mm
D	Conductor diameter	32.4	16.3	mm
m_{AL}	Mass per unit length of aluminum	1.5183	-	kg/m
m_{steel}	Mass per unit length of steel	0.5583	-	kg/m
$R_{20°C}$	DC resistance of the conductor	0.0526	0.2038	Ω/km
I_{max}	Current carrying capacity	1020	430	A

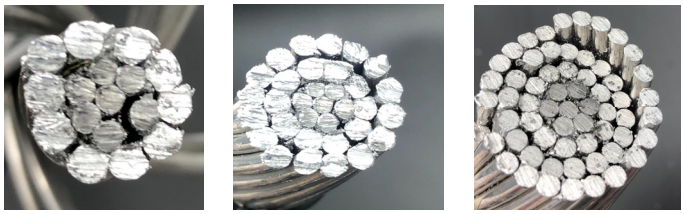

(**a**) (**b**) (**c**)

Figure 2. Cross section of the analyzed ACSR conductors. (**a**) Single-layer 7/10 conductor. (**b**) Two-layers 7/26 conductor. (**c**) Three-layer 7/54 conductor.

3.2. The High-Current Transformer Used to Test the Conductors

To determine the AC resistance of the conductors, they were tested in the laboratory under different operating conditions. For this end, a variable high-current transformer (10 kVA, 380 V/4 V, output current 0–2.5 kA, Transcir, Montcada i Reixac, Spain) was used to generate the current required to test the conductors. The analyzed ACSR conductors were connected to the high-current transformer forming a low impedance circular loop, as shown in Figure 3. To meet the requirements of the Cigré TB345 [3], the length of the conductor was 5.5 m.

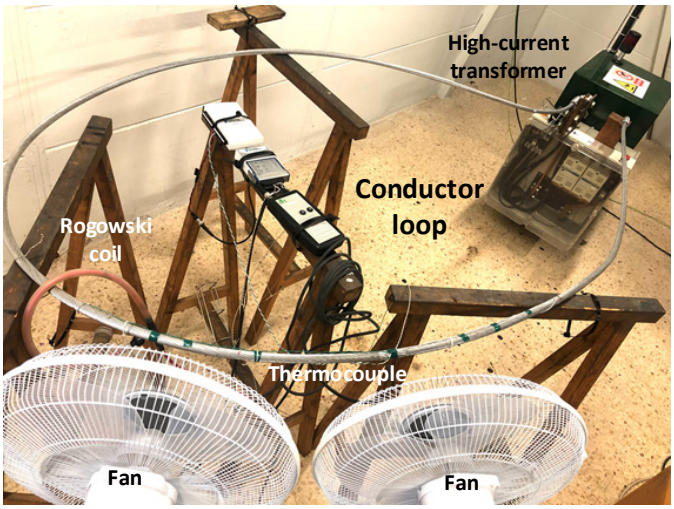

Figure 3. Experimental loop for testing the different ACSR conductors.

It is known that wind speed has a stronger impact in terms of DLR rating than ambient temperature or solar radiation [9], so the effect of wind speed was studied in this paper. As shown in Figure 3, two SF 0147 fans (variable speed, 50 W, Orbegozo, Murcia, Spain) were used to simulate variable wind speed conditions. It should be noted that in the

experiments, a constant wind flow of 5 m/s was applied, which was measured with a Pen 850021 anemometer (0.4–30 m/s measuring range, resolution of 0.1 m/s, accuracy of 3% full scale, Sper Scientific, Scottsdale, AZ, USA) during the entirety of the experiment under wind conditions.

3.3. Measuring Devices

In experimental tests involving the loops of ACSR conductors, the current flowing in the loop, the voltage drop over one meter length of the conductor and the phase shift between the voltage drop and current was measured.

The current flowing through the test loop was measured by means of a CWT500LFxB Rogowski coil (sensitivity = 0.06 mV/A, PEM, Nottingham, UK), which was connected to an NI USB-6210 data acquisition system (National Instruments, Dallas, TX, USA), with a current accuracy of ±1%.

A T-type thermocouple was used to measure the surface temperature of the conductor. It was connected to a NI-9211 thermocouple input module (±1 °C, National Instruments, Dallas, TX, USA).

Acquisitions made with the NI-9211 thermocouple input module and the NI USB-6210 data acquisition system were synchronized using Python code programmed by the authors of this work.

An 850021 RH Pen anemometer was used to measure the wind speed (measuring range 0.4–30 m/s, 0.1 m/s resolution, 3% full scale accuracy, Sper Scientific, Scottsdale, AZ, USA).

4. Experimental Results

This section presents the experimental tests carried out with the three ACSR conductors described in Section 3, which were performed in the AMBER high-current laboratory facilities of the of the Universitat Politècnica de Catalunya.

4.1. Results Obtained with a Single-Layer ACSR Conductor

The first test was conducted with a single-layer conductor, whose rated current was about 220 A. The conductor was heated from room temperature by applying the rated current until reaching the equilibrium temperature, which was about 77 °C. Conventional ACSR conductors usually operate below 90 °C [24] except when operating under emergency contingency conditions [19].

Then, by forcing it to pass the same amount of current, the conductor was cooled with the help of fans. During both parts of this cycle, the temperature of the conductor, the voltage drop and the current through the conductor were measured. From these measurements, the phase shift between the voltage drop and the current was calculated, and the AC resistance was obtained from (4). This test was repeated with currents of 145 A and 75 A. Figure 4 shows the results of the AC resistance as a function of the conductor temperature.

Results presented in Figure 4 clearly show the effect of the core on the AC resistance of the single-layer ACSR conductor. These results proved that the AC resistance of a single-layer ACSR conductor depended not only on temperature but also on the current flowing through the conductor. Results in Figure 4 also show that, in the case of strong wind, the measured surface temperature differs more from that of the interior. Therefore, for a given conductor surface temperature, the apparent AC resistance measured in strong wind is higher than when measured in no wind because of the higher temperature difference between the interior and the surface of the conductor in strong wind conditions (increased radial temperature gradient). However, this difference is always below 5%.

4.2. Results Obtained with a Two-Layer ACSR Conductor

The second test was carried out with a two-layer conductor, whose rated current was about 430 A. Due to the opposite stranding directions of the two layers, the axial

component of the magnetic flux is almost cancelled. Therefore, the AC resistance must be almost independent of the current intensity because the ferrous core is almost unaffected by the magnetic flux generated by the aluminum layers.

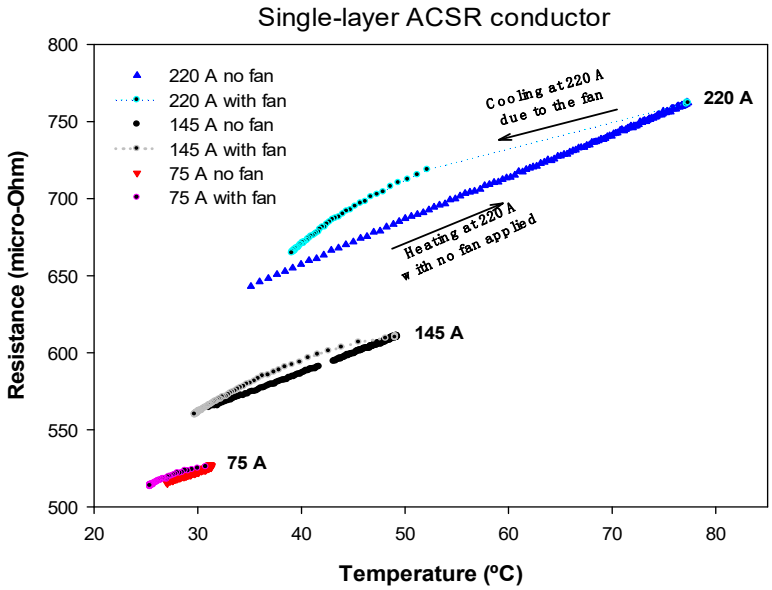

Figure 4. Single-layer ACSR conductor. R_{ac} versus temperature measured for heating-cooling cycles at 220 A, 145 A and 75 A.

As in the previous case, the conductor was heated by applying the rated current until reaching the equilibrium temperature, which was about 77 °C. Then, once again, by forcing it to pass the same amount of current, the conductor was cooled using fans. During the course of the experiment, the conductor temperature, voltage drop and current were measured, so that the AC resistance was calculated from (4). This test was repeated with currents of 280 A and 130 A, where the results of the AC resistance versus the temperature of the conductor are displayed in Figure 5.

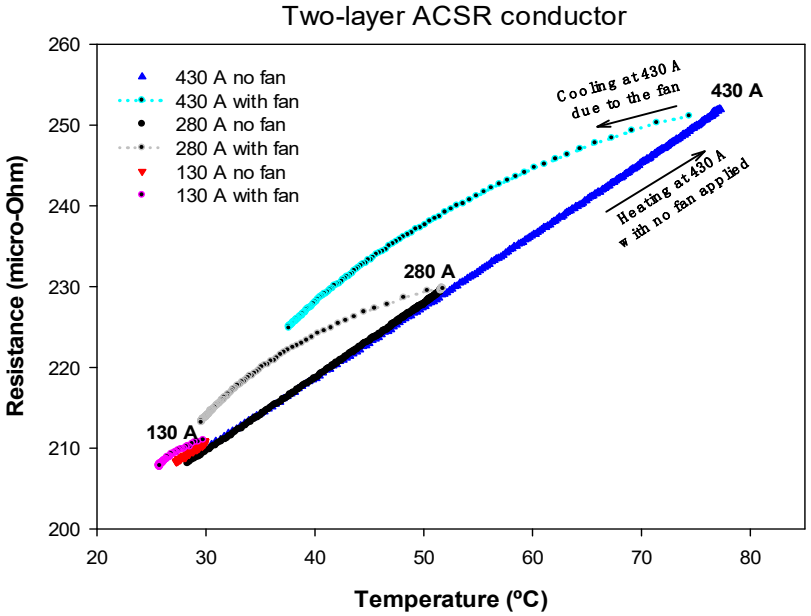

Figure 5. Two-layer ACSR conductor. R_{ac} versus temperature measured for heating-cooling cycles at 430 A, 280 A and 130 A.

From Figure 5, it can be seen that, as expected, the AC resistance of the two-layer ACSR conductor depended on its temperature, but it was almost independent of the current level. The effect of a strong wind increased the R_{ac} value below 5%.

4.3. Results Obtained with a Three-Layer ACSR Conductor

The third test was carried out with a three-layer conductor, whose rated current was around 1080 A. Due to the odd number of layers, the axial component of the magnetic flux does not completely cancel. Therefore, the AC resistance must depend slightly on the current intensity because the iron core is somewhat influenced by the axial component of the magnetic flux generated by the aluminum layers.

The three-layer ACSR conductor was heated by applying the rated current until the equilibrium temperature was reached, which was about 85 °C. Next, by forcing the flow of the same amount of current, the conductor was cooled using fans. During the experiment, the temperature of the conductor, the voltage drop and the current were measured, so that the AC resistance was obtained from (4). The test was repeated twice with current intensities of 650 A and 310 A, respectively. Figure 6 shows the results of the AC resistance versus conductor temperature.

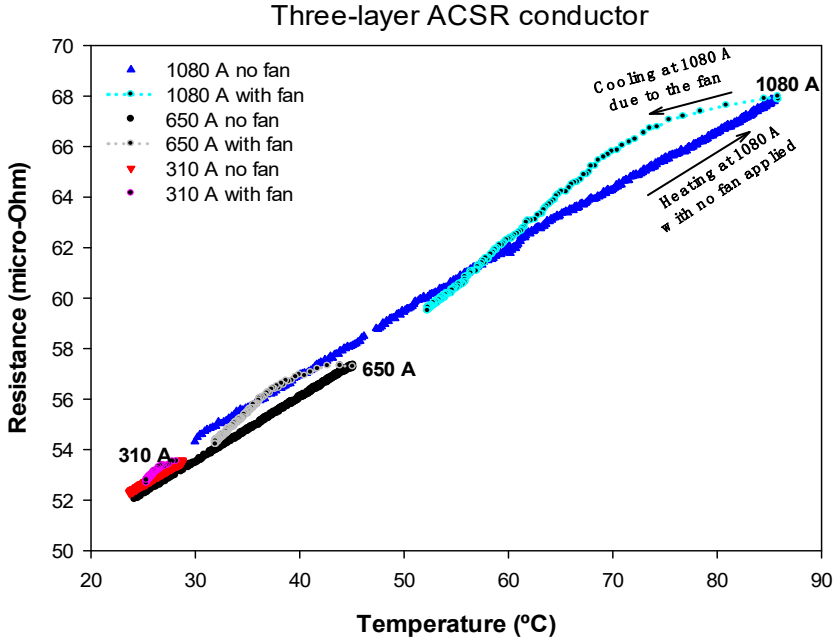

Figure 6. Three-layer ACSR conductor. R_{ac} versus temperature measured for heating-cooling cycles at 1080 A, 650 A and 310 A.

Results in Figure 6 show that the AC resistance of the three-layer ACSR conductor was almost independent of the current level due to the partial cancellation of the axial component of the magnetic flux due to the three layers of aluminum. The effect of a strong wind increased the AC resistance below 2.5%.

4.4. Results Summary

Table 2 shows the $R_{ac,0}$ and α parameters obtained from a linear fit of the experimental data shown in Figures 4–6 according to Equation (6), where R^2 is the coefficient of determination of the linear regression.

Results presented in Table 2 clearly show that, in the case of the single-layer conductor, there was a step change in the AC resistance values $R_{ac,0}$ measured at 20 °C for the three analyzed current levels. This was due to the effect of the axial component of the magnetic flux. However, for two- and three-layer conductors, $R_{ac,0}$ was almost independent of the

current level. Results presented in Table 2 also prove that the temperature coefficient of the resistance was almost independent of the current level and the topology of the conductor.

Table 2. Regression coefficients of (6).

Cable Type	Current	$R_{ac,0}$	α_{ac}	R^2
Single-layer	220 A	602.4 μΩ	0.0046 °C^{-1}	0.9997
	145 A	535.2 μΩ	0.0048 °C^{-1}	0.9991
	75 A	498.5 μΩ	0.0049 °C^{-1}	0.9827
Two-layer	430 A	200.8 μΩ	0.0044 °C^{-1}	0.9999
	280 A	200.2 μΩ	0.0046 °C^{-1}	0.9996
	130 A	201.9 μΩ	0.0044 °C^{-1}	0.9747
Three-layer	1080 A	52.3 μΩ	0.0046 °C^{-1}	0.9987
	650 A	51.0 μΩ	0.0049 °C^{-1}	0.9990
	310 A	51.4 μΩ	0.0047 °C^{-1}	0.9843

From the experimental results summarized in Table 2, and in the previous subsections, the following conclusions can be drawn:

- The AC resistance of two- and three-layer ACSR conductors was nearly independent of the current level, but this simplification cannot be applied to single-layer ACSR conductors. Therefore, for two- and three-layer ACSR conductors, it can be assumed that $R_{ac} = R_{ac}(T)$, so that the heat gain due to the conductor losses P_{loss} only depends on the conductor temperature, but not on the current level, i.e., $P_{loss} = P_{loss}(T)$. In contrast, for single-layer conductors, R_{ac} depends on both conductor temperature and current level, i.e., $R_{ac} = R_{ac}(T,I)$, and hence $P_{loss} = P_{loss}(T,I)$.
- In DLR applications, the conductor surface temperature is often measured, although it differs from the temperature of the internal strands. In strong wind conditions, the temperature difference between the surface of the conductor and the internal parts is typically greater. Therefore, in this study, for a given conductor surface temperature, the apparent AC resistance R_{ac} measured in strong winds was larger than when measured without wind due to the increased radial temperature gradient under strong wind conditions. However, this difference was always below 5%, so it would not have a significant effect on the calculation of the DLR rating.

Therefore, based on the results obtained, two possible approaches are proposed below:

- Approach 1, which is valid for ACSR conductors with any number of layers. The current, conductor temperature, voltage drop and the phase shift between the voltage drop and the current must be measured, so that, by applying (4), the actual value of the AC resistance can be determined.
- Approach 2: Two- and three-layer ACSR conductors. For these conductors, the AC resistance R_{ac} and thus, the heat gain due to conductor losses P_{loss}, are almost independent of current level. Therefore, if the parameters $R_{ac,0}$ and α_{ac} are known, it is possible to measure only the current and the temperature of the conductor, thus avoiding the need to measure the voltage drop and the phase shift between the voltage drop and the current. This is advantageous because the voltage drop measurement has some drawbacks related to the addition of wires placed on the surface of the high-voltage ACSR conductors, with the consequent problems related to outdoor environments. Since R_{ac} cannot be measured without measuring the voltage drop, if $R_{ac,0}$ and α_{ac} are known, R_{ac} can be obtained by applying $R_{ac,T} = R_{ac,0}[1 + \alpha_{ac}(T - T_0)]$. According to this equation, the temperature of the conductor, the parameters $R_{ac,0}$ and α_{ac} can be measured in the laboratory for a sample of the conductor, in a similar way as has been done in this paper.
- Approach 2: Single-layer conductor. In single-layer conductors, both the AC resistance R_{ac} and the heat gain due to conductor losses P_{loss}, depend on the current level and the temperature of the conductor. In this case it is also possible to avoid measuring

the voltage drop. According to the values presented in Table 2, α_{ac} can be considered as a constant value, so the current level determines $R_{ac,0}$. Then, R_{ac} can be obtained by applying $R_{ac,T} = R_{ac,0}[1 + \alpha_{ac}(T - T_0)]$. Once the values of the parameters $R_{ac,0}$ and α_{ac} summarized in Table 2 are known, they can be interpolated for any current level.

Figure 7 summarizes the two proposed strategies to measure the AC resistance of the conductor as a function of temperature and current level.

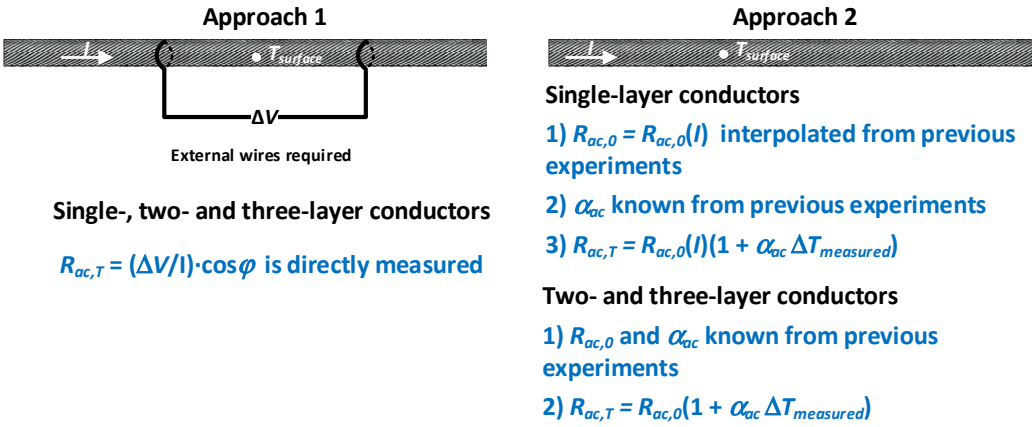

Figure 7. Proposed strategies to measure the AC resistance of the conductor as a function of the temperature and current level.

5. Conclusions

This paper has proposed two methods for the on-line determination of the AC resistance of aluminum conductor steel-reinforced (ACSR) conductors. The AC resistance is a key factor when applying dynamic line rating (DLR) approaches, as it determines Joule and core losses. This paper has analyzed the dependence of the AC resistance of ACSR with the line current, this being a novelty of this work, since most of the current DLR approaches do not consider this dependency, so they can lead to inaccurate estimates of the AC resistance, and thus of the DLR ampacity. To this end, single-layer, two-layer and three-layer conductors have been analyzed. Experimental results showed that while for two- and three-layer conductors the AC resistance is almost independent of the level of current passing through the conductors, for single-layer conductors, the AC resistance is influenced by the current level.

The first and more accurate method is based on a simultaneous measurement of the voltage drop along a certain length of the conductor, the current, the phase-shift between the voltage drop and the current, as well as the temperature of the conductor. However, this method has the disadvantage of requiring operators to install wires to measure the voltage drop. The second method avoids measuring the voltage drop and the phase shift, thus simplifying installation and measurement requirements, although it requires prior laboratory experiments to determine the required parameters $R_{ac,0}$ and α_{ac}.

The approaches presented in this paper are in line with the current need to operate power lines at their maximum instantaneous capacity by adapting in real-time the current rating to the existing weather conditions. These approaches are easy to implement, require low computational load and are compatible with IoT applications.

Author Contributions: Conceptualization, Y.L., M.M.-E. and J.-R.R.; methodology, J.-R.R.; software, Y.L.; validation, Y.L. and J.S.; formal analysis, M.M.-E. and J.-R.R.; investigation, Y.L., M.M.-E. and J.-R.R.; resources, J.S., M.M.-E. and J.-R.R.; writing—original draft preparation, Y.L. and J.-R.R.; writing—review and editing, M.M.-E.; supervision, J.S. and M.M.-E. All authors have read and agreed to the published version of the manuscript.

Funding: This research was funded by Generalitat de Catalunya, grant numbers 2017 SGR 967 and 2020 DI 007.

Institutional Review Board Statement: Not applicable.

Informed Consent Statement: Not applicable.

Data Availability Statement: Not applicable.

Conflicts of Interest: The authors declare no conflict of interest.

References

1. Singh, R.S.; Cobben, S.; Cuk, V. PMU-Based Cable Temperature Monitoring and Thermal Assessment for Dynamic Line Rating. *IEEE Trans. Power Deliv.* **2021**, *36*, 1859–1868. [CrossRef]
2. Beňa, Ľ.; Gáll, V.; Kanálik, M.; Kolcun, M.; Margitová, A.; Mészáros, A.; Urbanský, J. Calculation of the overhead transmission line conductor temperature in real operating conditions. *Electr. Eng.* **2021**, *103*, 769–780. [CrossRef]
3. Cigré 345. *Alternating Current (AC) Resistance of Helically Stranded Conductors*; Cigré Technical Brochure 345: Paris, France, 2008; pp. 1–59.
4. Abboud, A.W.; Gentle, J.P.; McJunkin, T.R.; Lehmer, J.P. Using Computational Fluid Dynamics of Wind Simulations Coupled with Weather Data to Calculate Dynamic Line Ratings. *IEEE Trans. Power Deliv.* **2020**, *35*, 745–753. [CrossRef]
5. Castro, P.; Lecuna, R.; Manana, M.; Martin, M.J.; Del Campo, D. Infrared Temperature Measurement Sensors of Overhead Power Conductors. *Sensors* **2020**, *20*, 7126. [CrossRef] [PubMed]
6. Kumar, P.; Singh, A.K. Optimal mechanical sag estimator for leveled span overhead transmission line conductor. *Measurement* **2019**, *137*, 691–699. [CrossRef]
7. Cheng, Y.; Liu, P.; Zhang, Z.; Dai, Y. Real-Time Dynamic Line Rating of Transmission Lines Using Live Simulation Model and Tabu Search. *IEEE Trans. Power Deliv.* **2021**, *36*, 1785–1794. [CrossRef]
8. Madadi, S.; Mohammadi-Ivatloo, B.; Tohidi, S. Probabilistic Real-Time Dynamic Line Rating Forecasting Based on Dynamic Stochastic General Equilibrium with Stochastic Volatility. *IEEE Trans. Power Deliv.* **2021**, *36*, 1631–1639. [CrossRef]
9. Madadi, S.; Mohammadi-Ivatloo, B.; Tohidi, S. Dynamic Line Rating Forecasting Based on Integrated Factorized Ornstein-Uhlenbeck Processes. *IEEE Trans. Power Deliv.* **2020**, *35*, 851–860. [CrossRef]
10. Alvarez, D.L.; Da Silva, F.F.; Mombello, E.E.; Bak, C.L.; Rosero, J.A. Conductor temperature estimation and prediction at thermal transient state in dynamic line rating application. *IEEE Trans. Power Deliv.* **2018**, *33*, 2236–2245. [CrossRef]
11. Rácz, L.; Németh, B. Dynamic Line Rating—An Effective Method to Increase the Safety of Power Lines. *Appl. Sci.* **2021**, *11*, 492. [CrossRef]
12. Cigré Working Group. *Thermal Behaviour of Overhead Conductors*; CIGRE: Paris, France, 2002.
13. *IEEE Std 738-2012*; IEEE Standard for Calculating the Current-Temperature of Bare Overhead Conductors. IEEE: New York, NY, USA, 2012.
14. Karimi, S.; Musilek, P.; Knight, A.M. Dynamic thermal rating of transmission lines: A review. *Renew. Sustain. Energy Rev.* **2018**, *91*, 600–612. [CrossRef]
15. Minguez, R.; Martinez, R.; Manana, M.; Cuasante, D.; Garañeda, R. Application of Digital Elevation Models to wind estimation for dynamic line rating. *Int. J. Electr. Power Energy Syst.* **2022**, *134*, 107338. [CrossRef]
16. Dai, D.; Zhang, X.; Wang, J. Calculation of AC Resistance for Stranded Single-Core Power Cable Conductors. *IEEE Trans. Magn.* **2014**, *50*, 1–4. [CrossRef]
17. Albizu, I.; Fernandez, E.; Eguia, P.; Torres, E.; Mazon, A.J. Tension and ampacity monitoring system for overhead lines. *IEEE Trans. Power Deliv.* **2013**, *28*, 3–10. [CrossRef]
18. Liu, Y.; Riba, J.-R.; Moreno-Eguilaz, M.; Sanllehí, J. Analysis of a Smart Sensor Based Solution for Smart Grids Real-Time Dynamic Thermal Line Rating. *Sensors* **2021**, *21*, 7388. [CrossRef] [PubMed]
19. Fu, J.; Morrow, D.J.; Abdelkader, S.; Fox, B. Impact of Dynamic Line Rating on Power Systems. In Proceedings of the 2011 46th International Universities' Power Engineering Conference (UPEC), Soest, Germany, 5–8 September 2011; pp. 1–5.
20. Morgan, V.T.; Findlay, R.D. The effect of frequency on the resistance and internal inductance of bare acsr conductors. *IEEE Trans. Power Deliv.* **1991**, *6*, 1319–1326. [CrossRef]
21. Knych, T.; Mamala, A.; Kwaśniewski, P.; Kiesiewicz, G.; Smyrak, B.; Gniełczyk, M.; Kawecki, A.; Korzeń, K.; Sieja-Smaga, E. New Graphene Composites for Power Engineering. *Materials* **2022**, *15*, 715. [CrossRef]
22. Howington, B.S. AC Resistance of ACSR—Magnetic and Temperature Effects: Prepared by a Task Force of the Working Group on Calculation of Bare Overhead Conductor Temperatures. *IEEE Power Eng. Rev.* **1985**, *PER-5*, 67–68. [CrossRef]
23. Morgan, V.T.; Zhang, B.; Findlay, R.D. Effect of magnetic induction in a steel-cored conductor on current distribution, resistance and power loss. *IEEE Trans. Power Deliv.* **1997**, *12*, 1299–1306. [CrossRef]
24. Absi Salas, F.M.; Orlande, H.R.; Domingues, L.A.; Barbosa, C.R. Sequential Estimation of the Radial Temperature Variation in Overhead Power Cables. *Heat Transf. Eng.* **2022**, *43*. [CrossRef]
25. Morgan, V.T. The Current Distribution, Resistance and Internal Inductance of Linear Power System Conductors—A Review of Explicit Equations. *IEEE Trans. Power Deliv.* **2013**, *28*, 1252–1262. [CrossRef]

26. Meyberg, R.A.; Absi Salas, F.M.; Domingues, L.A.M.; Sens, M.A.; Correia de Barros, M.T.; Lima, A.C. Magnetic properties of an ACSR conductor steel core at temperatures up to 230 °C and their impact on the transformer effect. *IET Sci. Meas. Technol.* **2021**, *15*, 143–153. [CrossRef]
27. Meyberg, R.A.; Salas, F.M.A.; Domingues, L.A.M.; de Barros, M.T.C.; Lima, A.C. Experimental study on the transformer effect in an ACSR cable. *Int. J. Electr. Power Energy Syst.* **2020**, *119*, 105861. [CrossRef]
28. Howington, B.S.; Rathbun, L.S.; Douglass, D.A.; Kirkpatrick, L.A. AC resistance of ACSR—Magnetic and temperature effects. *IEEE Trans. Power Appar. Syst.* **1985**, *PAS-104*, 1578–1584.
29. Ferreira Dias, C.; de Oliveira, J.R.; de Mendonça, L.D.; de Almeida, L.M.; de Lima, E.R.; Wanner, L. An IoT-Based System for Monitoring the Health of Guyed Towers in Overhead Power Lines. *Sensors* **2021**, *21*, 6173. [CrossRef]
30. Mendes, A.S.; Ferreira, J.V.; Meirelles, P.S.; de Oliveira Nóbrega, E.G.; de Lima, E.R.; de Almeida, L.M. Evaluation of Multivariable Modeling Methods for Monitoring the Health of Guyed Towers in Overhead Power Lines. *Sensors* **2021**, *21*, 6144. [CrossRef]
31. Rodríguez, F.; Sánchez-Guardamino, I.; Martín, F.; Fontán, L. Non-intrusive, self-supplying and wireless sensor for monitoring grounding cable in smart grids. *Sens. Actuators A Phys.* **2020**, *316*, 112417. [CrossRef]
32. Xiao, N.; Yu, W.; Han, X. Wearable heart rate monitoring intelligent sports bracelet based on Internet of things. *Measurement* **2020**, *164*, 108102. [CrossRef]
33. Narducci, D.; Giulio, F. Recent Advances on Thermoelectric Silicon for Low-Temperature Applications. *Materials* **2022**, *15*, 1214. [CrossRef]
34. Malar, A.J.G.; Kumar, C.A.; Saravanan, A.G. Iot based sustainable wind green energy for smart cites using fuzzy logic based fractional order darwinian particle swarm optimization. *Measurement* **2020**, *166*, 108208.
35. Zhang, D.; Dang, P. Study on AC Resistance of Overhead Conductors by Numerical Simulation. In Proceedings of the 2020 IEEE International Conference on High Voltage Engineering and Application (ICHVE), Beijing, China, 6–10 September 2020.
36. Morgan, V.T. Electrical characteristics of steel-cored aluminium conductors. *Proc. Inst. Electr. Eng.* **1965**, *112*, 325–334. [CrossRef]
37. *IEC 60287-1-1:2006*; Electric Cables-Calculation of the Current Rating-Part 1-1: Current Rating Equations (100% Load Factor) and Calculation of Losses-GENERAL. International Electrotechnical Commission (IEC): Geneva, Switzerland, 2006; pp. 1–136.
38. Riba, J.-R. Analysis of formulas to calculate the AC resistance of different conductors' configurations. *Electr. Power Syst. Res.* **2015**, *127*, 93–100. [CrossRef]
39. Inomata, N.; van Toan, N.; Ono, T. Temperature-dependence of the electrical impedance properties of sodium hydroxide-contained polyethylene oxide as an ionic liquid. *Sens. Actuators A Phys.* **2020**, *316*, 112369. [CrossRef]
40. Riba, J.R.; Martínez, J.; Moreno-Eguilaz, M.; Capelli, F. Characterizing the temperature dependence of the contact resistance in substation connectors. *Sens. Actuators A Phys.* **2021**, *327*, 112732. [CrossRef]
41. Barrett, J.S.; Nigol, O.; Fehervari, C.J.; Findlay, R.D. A new model of AC resistance in acsr conductors. *IEEE Trans. Power Deliv.* **1986**, *1*, 198–208. [CrossRef]
42. Kadechkar, A.; Moreno-Eguilaz, M.; Riba, J.R.; Capelli, F. Low-Cost Online Contact Resistance Measurement of Power Connectors to Ease Predictive Maintenance. *IEEE Trans. Instrum. Meas.* **2019**, *68*, 4825–4833. [CrossRef]
43. *IEEE 2772:2021*; IEEE Standard for Test Method for Energy Loss of Overhead Conductor. Institute of Electrical and Electronics Engineers (IEEE): New York, NY, USA, 2021; pp. 1–29.
44. Engelhardt, J.S.; Basu, S.P. Design, installation, and field experience with an overhead transmission dynamic line rating system. In Proceedings of the 1996 Transmission and Distribution Conference and Exposition, Los Angeles, CA, USA, 15–20 September 1996; pp. 366–370.
45. Hong, S.S.; Yang, Y.C.; Hsu, T.S.; Tseng, K.S.; Hsu, Y.F.; Wu, Y.R.; Jiang, J.A. Internet of Things-Based Monitoring for HV Transmission Lines: Dynamic Thermal Rating Analysis with Microclimate Variables. In Proceedings of the 2020 8th International Electrical Engineering Congress (iEECON), Chiang Mai, Thailand, 4–6 March 2020.
46. Singh, C.; Singh, A.; Pandey, P.; Singh, H. Power Donuts in Overhead Lines for Dynamic Thermal Rating Measurement, Prediction and Electric Power Line Monitoring. *Int. J. Adv. Res. Electr. Electron. Instrum. Eng.* **2014**, *3*, 9394–9400.

6. Conclusions and future work

6.1 General conclusions

The objective of this thesis is to develop and optimize an IoT device, designed to monitor or estimate the health condition of substation connectors, and to extend the application of the developed IoT device to improve the efficiency of power transmission systems. To make this progress, various fields of research areas have been identified, studied, and implemented in this thesis to achieve the objective of the project.

Chapter 1conducts an analysis of various components of power transmission systems. The crucial parameters required to be measured for monitoring the health condition of the high-voltage substation connectors, as well as the approach that allows power lines to operate closer to their limit, were identified. This chapter offered a comprehensive description of the thesis objectives.

Chapter 2 describes in detail the optimization process for the power management system for *Smartconnector* prototype. Several thermal energy harvesting systems were tested and compared to select the most suitable system for the *Smartconnector*. Next, the energy consumption of the *Smartconnector* was measured. Based on the energy harvested and the measured energy consumption, the maximum data transfer rate in an hour can be obtained to reach the energy balance of the energy storage of the *Smartconnector* prototype. The equations required to determine the efficiencies of the energy harvesting unit and the battery storage under different charging/discharging rates were analyzed. Results show that by applying the energy harvesting system, the small temperature difference between the conductor and ambient temperature due to Joule effect can be used to produce electrical power. Moreover, the energy balance strategy helps extending the lifetime of the energy storage system.

Chapter 3 stuides diverse signal processing strategies to denoise the signals acquired by the *Smartconnector*. Owing to the inherent characteristics of high-voltage substations, there exist different kinds of noise in the signals, which may result in inaccurate measurements. Therefore, there is a need to develop an appropriate approach to denoise such signals. From the literature review, three filtering algorithms were selected, developed and tested on the desktop platform. Next, according to the computational time and the accuracy of the electrical contact resistance measurements, the most suitable one was selected to be implemented on the microcontroller of the *Smartconnector* prototype. Experiments concluded that the *Smartconnector* with the filter exhibited better performance than the *Smartconnector* prototype without the filter, proving the feasibility of the filter application.

Chapter 4 explores an extension of the *Smartconnector*, called the *Smartconductor,* to improve the current-carrying capacity of power lines. The *Smartconductor* was developed based on the *Smartconnector* prototype, and it was used to estimate the dynamic line rating (DLR) of power transmission lines. Additionally, the magnetic effect on the determination of DLR was also studied. Based on experimental results, two approaches were proposed to determine the ac resistance of the line. Experimental results also show that the *Smartconductor* prototype can estimate both the wind speed and DLR rating accurately, proving the feasibility of *Smartconductor* applications for power lines.

Chapter 5 presents the compendium of publications. In total, the full version of four journal papers and one conference article are presented. Moreover, the framework and main contributions of each article are outlined.

These developments have resulted in the following main contributions, directly related to the hypothesis of this thesis:

- Selection and validation of suitable thermal energy harvesting systems for high-voltage substation applications.
- Optimization of the power management system of the *Smartconnector* considering the efficiencies of the energy harvesting system, the battery storage at different charge/discharge rates and the measured energy consumption using conventional instrumentations. Based on these, an energy balance strategy was applied to the power management system, which prolongs the lifetime of *Smartconnector* prototype.
- Development and validation of different signal processing algorithms for the signals acquired from high-voltage substations based on online data acquisition. These algorithms are in line with the development of smart grids, being compatible with the *Smartconnector* requirements.
- Estimation of dynamic line ratings of power lines with low- cost electronic devices and low-computational effort. This method also proposes to estimate the wind speed, avoiding the installation of wind speed sensors and reducing the cost.
- Implementation of an in-depth study of the core losses of ACSR conductors, in order to accurately estimate the dynamic line rating.

6.2 Future work

This section exposes future research topics that can be built based on the developments fulfilled in this thesis and that can complement it to enhance the availability and reliability of power systems.

- This thesis provides improvements to *Smartconnector* prototype for real-time data acquisition from substation connectors. Nowadays, there are initiatives in data-driven methods to utilize the collected data to not only predict the remaining useful life (RUL) but also to perform the fault diagnosis for components, which would enhance even more the reliability of power systems.
  Therefore, it would be interesting to develop a suitable algorithm to process the received data from the *Smartconnector* prototype and to perform necessary predictions. To avoid human intervention and ensure data security, the developed algorithm needs to be implemented in the gateway or in the microcontroller.

- This thesis addresses the issue of inaccurate data acquisition by implementing filtering algorithms. Nonetheless, more accurate and cost-effective electronic sensors also deserve to be studied to face more challenging situations. This area could be explored more in-depth to improve the initial measurements of electrical contact resistance.

- The effect of the emissivity on the temperature variation of the power lines also can be explored since the temperature is a key parameter in determining the dynamic line rating. This would foster the thermal model built to estimate the dynamic line rating.

7. References

[1] Ľ. Beňa *et al.*, "Calculation of the overhead transmission line conductor temperature in real operating conditions," *Electr. Eng.*, pp. 769–780, 2020, doi: 10.1007/s00202-020-01107-2.

[2] D. L. Alvarez, F. F. Da Silva, E. E. Mombello, C. L. Bak, and J. A. Rosero, "Conductor temperature estimation and prediction at thermal transient state in dynamic line rating application," *IEEE Trans. Power Deliv.*, vol. 33, no. 5, pp. 2236–2245, 2018, doi: 10.1109/TPWRD.2018.2831080.

[3] C. R. Black and W. A. Chisholm, "Key Considerations for the Selection of Dynamic Thermal Line Rating Systems," *IEEE Trans. Power Deliv.*, vol. 30, no. 5, pp. 2154–2162, Oct. 2015, doi: 10.1109/TPWRD.2014.2376275.

[4] H. N. Ho *et al.*, "Design and Simulation of an Autonomous Smart Microgrid for Energy Independence," *WSEAS Trans. Env.*, vol. 17, pp. 911–928, Aug. 2021, doi: 10.37394/232015.2021.17.85.

[5] A. Kadechkar, J. R. Riba, M. Moreno-Eguilaz, and J. Perez, "SmartConnector: A Self-Powered IoT Solution to Ease Predictive Maintenance in Substations," *IEEE Sens. J.*, vol. 20, no. 19, pp. 11632–11641, 2020, doi: 10.1109/JSEN.2020.2998157.

[6] J. R. Riba, Y. Liu, M. Moreno-Eguilaz, and J. Sanllehí, "On-Line Core Losses Determination in ACSR Conductors for DLR Applications," *Materials (Basel).*, vol. 15, no. 17, 2022, doi: 10.3390/ma15176143.

[7] A. Kadechkar, "Development of the future generation of smart high voltage connectors and related components for substations, with energy autonomy and wireless data transmission …," 2020, [Online]. Available: https://upcommons.upc.edu/handle/2117/335417.

[8] Y. Liu, J. Riba, and M. Moreno-eguilaz, "Energy Balance of Wireless Sensor Nodes Based on Bluetooth Low Energy and Thermoelectric Energy Harvesting," pp. 1–19, 2023.

[9] F. Tohidi, S. Ghazanfari Holagh, and A. Chitsaz, "Thermoelectric Generators: A comprehensive review of characteristics and applications," *Appl. Therm. Eng.*, vol. 201, p. 117793, Jan. 2022, doi: 10.1016/J.APPLTHERMALENG.2021.117793.

[10] Y. Zhao, Y. Fan, W. Li, Y. Li, M. Ge, and L. Xie, "Experimental investigation of heat pipe thermoelectric generator," *Energy Convers. Manag.*, vol. 252, p. 115123, Jan. 2022, doi: 10.1016/J.ENCONMAN.2021.115123.

[11] A. G. Olabi *et al.*, "Potential applications of thermoelectric generators (TEGs) in various waste heat recovery systems," *Int. J. Thermofluids*, vol. 16, p. 100249, Nov. 2022, doi: 10.1016/J.IJFT.2022.100249.

[12] S. Masoumi, S. O'Shaughnessy, and A. Pakdel, "Organic-based flexible thermoelectric generators: From materials to devices," *Nano Energy*, vol. 92, p. 106774, Feb. 2022, doi: 10.1016/J.NANOEN.2021.106774.

[13] H. Jouhara *et al.*, "Thermoelectric generator (TEG) technologies and applications," *Int. J. Thermofluids*, vol. 9, p. 100063, Feb. 2021, doi: 10.1016/J.IJFT.2021.100063.

[14] M. Hamid Elsheikh *et al.*, "A review on thermoelectric renewable energy: Principle parameters that affect their performance," *Renew. Sustain. Energy Rev.*, vol. 30, pp. 337–355, Feb. 2014, doi: 10.1016/J.RSER.2013.10.027.

[15] S. M. Pourkiaei *et al.*, "Thermoelectric cooler and thermoelectric generator devices: A

review of present and potential applications, modeling and materials," *Energy*, vol. 186, p. 115849, Nov. 2019, doi: 10.1016/J.ENERGY.2019.07.179.

[16] "How Thermoelectric Generators Work - Applied Thermoelectric Solutions LLC." .

[17] "Thermoelectricity using Semiconductor Thermocouples." .

[18] V. Di Stefano and O. Muscato, "Seebeck Effect in Silicon Semiconductors," *Acta Appl. Math. 2012 1221*, vol. 122, no. 1, pp. 225–238, May 2012, doi: 10.1007/S10440-012-9739-6.

[19] J. Cai and G. D. Mahan, "Effective Seebeck coefficient for semiconductors," *Phys. Rev. B - Condens. Matter Mater. Phys.*, vol. 74, no. 7, p. 075201, Aug. 2006, doi: 10.1103/PHYSREVB.74.075201/FIGURES/1/MEDIUM.

[20] I. Ahmad, L. M. Hee, A. M. Abdelrhman, S. A. Imam, and M. S. Leong, "Scopes, challenges and approaches of energy harvesting for wireless sensor nodes in machine condition monitoring systems: A review," *Meas. J. Int. Meas. Confed.*, vol. 183, no. April, p. 109856, 2021, doi: 10.1016/j.measurement.2021.109856.

[21] B. Hernández, "Experimental study of the potential for thermal energy recovery with thermoelectric devices in low displacement diesel engines.," *HELIYON*, p. e08273, 2021, doi: 10.1016/j.heliyon.2021.e08273.

[22] S. C. Order and S. Committee, "A Fully Featured Thermal Energy Harvesting Tracker for Wildlife," *Energies*, vol. 14, no. 19, 2021.

[23] Y. Liu, J. Riba, M. Moreno-eguilaz, and J. Sanllehí, "Application of Thermoelectric Generators for Low-Temperature-Gradient Energy Harvesting," pp. 1–16, 2023.

[24] IEEE, *IEEE Std 605-2008 Guide for Bus Design in Air Insulated Substations.* IEEE, 2010.

[25] A. Kadechkar, M. Moreno-Eguilaz, J. R. Riba, and F. Capelli, "Low-Cost Online Contact Resistance Measurement of Power Connectors to Ease Predictive Maintenance," *IEEE Trans. Instrum. Meas.*, vol. 68, no. 12, pp. 4825–4833, 2019, doi: 10.1109/TIM.2019.2899481.

[26] Y. Liu, J. R. Riba, M. Moreno-Eguilaz, and J. Sanllehí, "Analysis of a smart sensor based solution for smart grids real-time dynamic thermal line rating," *Sensors*, vol. 21, no. 21, pp. 1–17, 2021, doi: 10.3390/s21217388.

[27] E. Locorotondo, V. Cultrera, L. Pugi, L. Berzi, M. Pierini, and G. Lutzemberger, "Development of a battery real-time state of health diagnosis based on fast impedance measurements," *J. Energy Storage*, vol. 38, no. August 2020, p. 102566, 2021, doi: 10.1016/j.est.2021.102566.

[28] M. Zhu, W. Hu, and N. C. Kar, "The SOH estimation of LiFePO4 battery based on internal resistance with Grey Markov Chain," *2016 IEEE Transp. Electrif. Conf. Expo, ITEC 2016*, pp. 16–21, 2016, doi: 10.1109/ITEC.2016.7520192.

[29] N. Noura, L. Boulon, and S. Jemeï, "A review of battery state of health estimation methods: Hybrid electric vehicle challenges," *World Electr. Veh. J.*, vol. 11, no. 4, pp. 1–20, 2020, doi: 10.3390/wevj11040066.

[30] J. Kang, F. Yan, P. Zhang, and C. Du, "Comparison of comprehensive properties of Ni-MH (nickel-metal hydride) and Li-ion (lithium-ion) batteries in terms of energy efficiency," *Energy*, vol. 70, pp. 618–625, 2014, doi: 10.1016/j.energy.2014.04.038.

[31] Y. Liu *et al.*, "Piezoelectric energy harvesting for self-powered wearable upper limb applications," *Nano Sel.*, vol. 2, no. 8, pp. 1459–1479, Aug. 2021, doi: 10.1002/NANO.202000242.

[32] K. H. Young, “Research in nickel/metal hydride batteries 2017,” *Batteries*, vol. 4, no. 1, pp. 2–6, 2018, doi: 10.3390/batteries4010009.

[33] J. Kang, F. Yan, P. Zhang, and C. Du, “A novel way to calculate energy efficiency for rechargeable batteries,” *J. Power Sources*, vol. 206, pp. 310–314, 2012, doi: 10.1016/j.jpowsour.2012.01.105.

[34] F. M. Gatta, A. Geri, S. Lauria, M. Maccioni, and F. Palone, “Battery energy storage efficiency calculation including auxiliary losses: Technology comparison and operating strategies,” *2015 IEEE Eindhoven PowerTech, PowerTech 2015*, 2015, doi: 10.1109/PTC.2015.7232464.

[35] J. Lee, J. Kim, J. Yi, and C. Won, “Battery Management System Algorithm for Energy Storage Systems Considering Battery Efficiency,” pp. 1–19, 2021.

[36] J. Lee *et al.*, “Battery Management System Algorithm for Energy Storage Systems Considering Battery Efficiency,” *Electron. 2021, Vol. 10, Page 1859*, vol. 10, no. 15, p. 1859, Aug. 2021, doi: 10.3390/ELECTRONICS10151859.

[37] ISO 7267, “International Standard International Standard,” *61010-1 © Iec2001*, vol. 2003, p. 13, 2003.

[38] C. M. Wiggins, D. E. Thomas, F. S. Nickel, T. M. Salas, and S. E. Wright, “Transient electromagnetic interference in substations,” *IEEE Trans. Power Deliv.*, vol. 9, no. 4, pp. 1869–1884, 1994, doi: 10.1109/61.329520.

[39] F. Sacuto, B. L. Agba, F. Gagnon, and F. Labeau, “Evolution of the RF characteristics of the impulsive noise in high voltage environment,” *2012 IEEE 3rd Int. Conf. Smart Grid Commun. SmartGridComm 2012*, pp. 686–691, 2012, doi: 10.1109/SMARTGRIDCOMM.2012.6486066.

[40] G. A. Franklin, “A practical guide to harmonic frequency interference affecting high-voltage power-line carrier coupling systems,” *IEEE Trans. Power Deliv.*, vol. 24, no. 2, pp. 630–641, 2009, doi: 10.1109/TPWRD.2008.2002700.

[41] F. Capelli, J. R. Riba, and J. Sanllehí, “Finite element analysis to predict temperature rise tests in high-capacity substation connectors,” *IET Gener. Transm. Distrib.*, vol. 11, no. 9, pp. 2283–2291, 2017, doi: 10.1049/iet-gtd.2016.1717.

[42] International Electrotechnical Commission, “IEC TS 61586:2017 Estimation of the reliability of electrical connectors.” IEC, pp. 1–55, 2017.

[43] J. R. Riba, Á. Gómez-Pau, J. Martínez, and M. Moreno-Eguilaz, “On-line remaining useful life estimation of power connectors focused on predictive maintenance,” *Sensors*, vol. 21, no. 11, 2021, doi: 10.3390/s21113739.

[44] J. Martínez, A. Gómez-Pau, J. R. Riba, and M. Moreno-Eguilaz, “On-Line Health Condition Monitoring of Power Connectors Focused on Predictive Maintenance,” *IEEE Trans. Power Deliv.*, vol. 36, no. 6, pp. 3611–3618, 2021, doi: 10.3390/s21113739.

[45] J. Martínez, J. R. Riba, and M. Moreno-Eguilaz, “State of health prediction of power connectors by analyzing the degradation trajectory of the electrical resistance,” *Electron.*, vol. 10, no. 12, 2021, doi: 10.3390/electronics10121409.

[46] Á. Gómez-pau, J. R. Riba, and M. Moreno-eguilaz, “Time series rul estimation of medium voltage connectors to ease predictive maintenance plans,” *Appl. Sci.*, vol. 10, no. 24, pp. 1–14, 2020, doi: 10.3390/app10249041.

[47] D. Gonzalez, F. Berger, M. Hopfeld, and P. Schaaf, “Model switch experiments for determining the evolution of contact resistance of electrical contacts in contactors,” *Electr.*

Contacts, Proc. Annu. Holm Conf. Electr. Contacts, vol. 2016-December, pp. 129–134, Dec. 2016, doi: 10.1109/HOLM.2016.7780020.

[48] F. Capelli, J. R. Riba, and D. Gonzalez, "Thermal behavior of energy-efficient substation connectors," *Proc. - 2016 10th Int. Conf. Compat. Power Electron. Power Eng. CPE-POWERENG 2016*, pp. 104–109, 2016, doi: 10.1109/CPE.2016.7544167.

[49] A. Kadechkar, J. R. Riba, M. Moreno-Eguilaz, F. Capelli, and D. Gonzalez, "On-line Resistance Measurement of Substation Connectors Focused on Predictive Maintenance," *Proc. - 2018 IEEE 18th Int. Conf. Power Electron. Motion Control. PEMC 2018*, no. 1, pp. 846–851, 2018, doi: 10.1109/EPEPEMC.2018.8521913.

[50] M. Yamaguchi, K. H. Kim, T. Kuribara, and K. I. Arai, "Thin-film RF noise suppressor integrated in a transmission line," *IEEE Trans. Magn.*, vol. 38, no. 5 I, pp. 3183–3185, 2002, doi: 10.1109/TMAG.2002.802408.

[51] S. Jinno, S. Kitora, H. Toki, and M. Abe, "Mechanism of Common-mode Noise Generation in Multi-conductor Transmission Lines," *Sci. Rep.*, vol. 9, no. 1, pp. 1–8, 2019, doi: 10.1038/s41598-019-51259-w.

[52] J. Gong, D. Li, T. Wang, W. Pan, and X. Ding, "A comprehensive review of improving power quality using active power filters," *Electr. Power Syst. Res.*, vol. 199, p. 107389, Oct. 2021, doi: 10.1016/J.EPSR.2021.107389.

[53] C. Morales-Perez, J. Rangel-Magdaleno, H. Peregrina-Barreto, J. Cerezo-Sanchez, and A. Leon-Bonilla, "Selective Signal Extraction based on OMP algorithm and DCT and DST Dictionaries," *2022 IEEE Int. Autumn Meet. Power, Electron. Comput. ROPEC 2022*, 2022, doi: 10.1109/ROPEC55836.2022.10018725.

[54] S. L. Yu and J. C. Gu, "Removal of decaying DC in current and voltage signals using a modified fourier filter algorithm," *IEEE Trans. Power Deliv.*, vol. 16, no. 3, pp. 372–379, 2001, doi: 10.1109/61.924813.

[55] P. Gangsar and R. Tiwari, "Signal based condition monitoring techniques for fault detection and diagnosis of induction motors: A state-of-the-art review," *Mech. Syst. Signal Process.*, vol. 144, p. 106908, 2020, doi: 10.1016/j.ymssp.2020.106908.

[56] F. Khan, A. Ghaffar, N. Khan, and S. H. Cho, "An Overview of Signal Processing Techniques for Remote Health Monitoring Using Impulse Radio UWB Transceiver," *Sensors 2020, Vol. 20, Page 2479*, vol. 20, no. 9, p. 2479, Apr. 2020, doi: 10.3390/S20092479.

[57] D. M. Kipping *et al.*, "THE HUNT for EXOMOONS with KEPLER (HEK). V. A SURVEY of 41 PLANETARY CANDIDATES for EXOMOONS," *Astrophys. J.*, vol. 813, no. 1, Nov. 2015, doi: 10.1088/0004-637X/813/1/14.

[58] A. B. Abdusalomov, F. Safarov, M. Rakhimov, B. Turaev, and T. K. Whangbo, "Improved Feature Parameter Extraction from Speech Signals Using Machine Learning Algorithm," *Sensors 2022, Vol. 22, Page 8122*, vol. 22, no. 21, p. 8122, Oct. 2022, doi: 10.3390/S22218122.

[59] C. Zhang, A. A. Mousavi, S. F. Masri, G. Gholipour, K. Yan, and X. Li, "Vibration feature extraction using signal processing techniques for structural health monitoring: A review," *Mech. Syst. Signal Process.*, vol. 177, p. 109175, Sep. 2022, doi: 10.1016/J.YMSSP.2022.109175.

[60] A. Kheirati Roonizi and I. W. Selesnick, "A Kalman Filter Framework for Simultaneous LTI Filtering and Total Variation Denoising," *IEEE Trans. Signal Process.*, vol. 70, no. 1, pp. 4543–4554, 2022, doi: 10.1109/TSP.2022.3203852.

[61] G. Revach, N. Shlezinger, X. Ni, A. L. Escoriza, R. J. G. Van Sloun, and Y. C. Eldar, "KalmanNet: Neural Network Aided Kalman Filtering for Partially Known Dynamics," *IEEE Trans. Signal Process.*, vol. 70, pp. 1532–1547, 2022, doi: 10.1109/TSP.2022.3158588.

[62] M. Khodarahmi and V. Maihami, "A Review on Kalman Filter Models," *Arch. Comput. Methods Eng.*, vol. 30, no. 1, pp. 727–747, 2023, doi: 10.1007/s11831-022-09815-7.

[63] M. Hossain, M. E. Haque, and M. T. Arif, "Kalman filtering techniques for the online model parameters and state of charge estimation of the Li-ion batteries: A comparative analysis," *J. Energy Storage*, vol. 51, no. March, p. 104174, 2022, doi: 10.1016/j.est.2022.104174.

[64] P. Shrivastava, T. K. Soon, M. Y. I. Bin Idris, and S. Mekhilef, "Overview of model-based online state-of-charge estimation using Kalman filter family for lithium-ion batteries," *Renew. Sustain. Energy Rev.*, vol. 113, p. 109233, Oct. 2019, doi: 10.1016/J.RSER.2019.06.040.

[65] Z. Cui, J. Dai, J. Sun, D. Li, L. Wang, and K. Wang, "Hybrid Methods Using Neural Network and Kalman Filter for the State of Charge Estimation of Lithium-Ion Battery," *Math. Probl. Eng.*, vol. 2022, 2022, doi: 10.1155/2022/9616124.

[66] H. Li *et al.*, "A cubature Kalman filter for online state-of-charge estimation of lithium-ion battery using a gas-liquid dynamic model," *J. Energy Storage*, vol. 53, p. 105141, Sep. 2022, doi: 10.1016/J.EST.2022.105141.

[67] P. S. Madhukar and S. Madhukar, "Kalman Filters in different biomedical signals-An Overview," *Proc. - Int. Conf. Smart Electron. Commun. ICOSEC 2020*, pp. 1268–1272, Sep. 2020, doi: 10.1109/ICOSEC49089.2020.9215335.

[68] M. M. Rana, N. Halim, M. M. Rahamna, and A. Abdelhadi, "Position and Velocity Estimations of 2D-Moving Object Using Kalman Filter: Literature Review," *Int. Conf. Adv. Commun. Technol. ICACT*, vol. 2020, pp. 541–544, Feb. 2020, doi: 10.23919/ICACT48636.2020.9061241.

[69] X. Lai, Y. Huang, X. Han, H. Gu, and Y. Zheng, "A novel method for state of energy estimation of lithium-ion batteries using particle filter and extended Kalman filter," *J. Energy Storage*, vol. 43, p. 103269, Nov. 2021, doi: 10.1016/J.EST.2021.103269.

[70] C. Jiang, S. Wang, B. Wu, C. Fernandez, X. Xiong, and J. Coffie-Ken, "A state-of-charge estimation method of the power lithium-ion battery in complex conditions based on adaptive square root extended Kalman filter," *Energy*, vol. 219, p. 119603, Mar. 2021, doi: 10.1016/J.ENERGY.2020.119603.

[71] H. Zhu, G. Zhang, Y. Li, and H. Leung, "A novel robust Kalman filter with unknown non-stationary heavy-tailed noise," *Automatica*, vol. 127, p. 109511, May 2021, doi: 10.1016/J.AUTOMATICA.2021.109511.

[72] M. Bai, Y. Huang, Y. Zhang, and F. Chen, "A Novel Heavy-Tailed Mixture Distribution Based Robust Kalman Filter for Cooperative Localization," *IEEE Trans. Ind. Informatics*, vol. 17, no. 5, pp. 3671–3681, May 2021, doi: 10.1109/TII.2020.3015001.

[73] P. S. Madhukar and L. B. Prasad, "State Estimation using Extended Kalman Filter and Unscented Kalman Filter," *Proc. - 2020 Int. Conf. Emerg. Trends Commun. Control Comput. ICONC3 2020*, Feb. 2020, doi: 10.1109/ICONC345789.2020.9117536.

[74] I. Ullah, Y. Shen, X. Su, C. Esposito, and C. Choi, "A Localization Based on Unscented Kalman Filter and Particle Filter Localization Algorithms," *IEEE Access*, vol. 8, pp. 2233–2246, 2020, doi: 10.1109/ACCESS.2019.2961740.

[75] L. Ling, D. Sun, X. Yu, and R. Huang, "State of charge estimation of Lithium-ion batteries based on the probabilistic fusion of two kinds of cubature Kalman filters," *J. Energy Storage*, vol. 43, p. 103070, Nov. 2021, doi: 10.1016/J.EST.2021.103070.

[76] W. Dyason, T. I. Van Niekerk, R. Phillips, and R. Stopforth, "Performance evaluation and comparison of filters for real time embedded system applications," *2017 Pattern Recognit. Assoc. South Africa Robot. Mechatronics Int. Conf. PRASA-RobMech 2017*, vol. 2018-Janua, pp. 242–248, 2017, doi: 10.1109/RoboMech.2017.8261155.

[77] N. A. T. N. K. R. Rao, "Discrete Cosine Transfonn," *IEEE Trans. Comput.*, vol. C–23, no. 1, pp. 90–93, 1974.

[78] T. Mazeh and S. Faigler, "Detection of the ellipsoidal and the relativistic beaming effects in the CoRoT-3 lightcurve," *Astron. Astrophys.*, vol. 521, no. 6, pp. 1–4, 2010, doi: 10.1051/0004-6361/201015550.

[79] S. Faigler and T. Mazeh, "Photometric detection of non-transiting short-period low-mass companions through the beaming, ellipsoidal and reflection effects in Kepler and CoRoT light curves," *Mon. Not. R. Astron. Soc.*, vol. 415, no. 4, pp. 3921–3928, 2011, doi: 10.1111/j.1365-2966.2011.19011.x.

[80] D. M. Kipping, J. Hartman, L. A. Buchhave, A. R. Schmitt, G. Á. Bakos, and D. Nesvorný, "The hunt for exomoons with Kepler (HEK). II. Analysis of seven viable satellite-hosting planet candidates," *Astrophys. J.*, vol. 770, no. 2, 2013, doi: 10.1088/0004-637X/770/2/101.

[81] F. Guo, B. Yang, W. Zheng, and S. Liu, "Power frequency estimation using sine filtering of optimal initial phase," *Measurement*, vol. 186, p. 110165, Dec. 2021, doi: 10.1016/J.MEASUREMENT.2021.110165.

[82] L. Tuta, M. Nicolaescu, G. Rosu, A. Grivei, and B. Barbulescu, "A Robust Adaptive Filtering Method based on Independent Component Analysis (ICA)," *2020 13th Int. Conf. Commun. COMM 2020 - Proc.*, no. 3, pp. 59–64, 2020, doi: 10.1109/COMM48946.2020.9141995.

[83] S. K. S. Fan, Y. J. Chang, and N. Aidara, "Nonlinear profile monitoring of reflow process data based on the sum of sine functions," *Qual. Reliab. Eng. Int.*, vol. 29, no. 5, pp. 743–758, 2013, doi: 10.1002/qre.1425.

[84] R. Kher, "Signal Processing Techniques for Removing Noise from ECG Signals," *Jber*, vol. 3, pp. 1–9, 2019, doi: 10.17303/jber.2019.3.101.

[85] R. Koswatta and N. C. Karmakar, "Moving average filtering technique for signal processing in digital section of UWB chipless RFID reader," *Asia-Pacific Microw. Conf. Proceedings, APMC*, pp. 1304–1307, 2010.

[86] Z. Shan, J. Yang, M. A. F. Sanjuán, C. Wu, and H. Liu, "A novel adaptive moving average method for signal denoising in strong noise background," *Eur. Phys. J. Plus*, vol. 137, no. 1, 2022, doi: 10.1140/epjp/s13360-021-02279-x.

[87] G. G. Redhyka, D. Setiawan, and D. Soetraprawata, "Embedded sensor fusion and moving-average filter for Inertial Measurement Unit (IMU) on the microcontroller-based stabilized platform," *Proc. 2015 Int. Conf. Autom. Cogn. Sci. Opt. Micro Electro-Mechanical Syst. Inf. Technol. ICACOMIT 2015*, pp. 72–77, 2016, doi: 10.1109/ICACOMIT.2015.7440178.

[88] M. B. Perry, "The Weighted Moving Average Technique," *Wiley Encycl. Oper. Res. Manag. Sci.*, no. June 2010, 2011, doi: 10.1002/9780470400531.eorms0964.

[89] D. Haynes, S. Corns, and G. K. Venayagamoorthy, "An exponential moving average

algorithm," *2012 IEEE Congr. Evol. Comput. CEC 2012*, pp. 10–15, 2012, doi: 10.1109/CEC.2012.6252962.

[90] IEEE Std 738-2012, "IEEE Standard for Calculating the Current-Temperature of Bare Overhead Conductors," New York, USA, 2012. doi: 10.1109/IEEESTD.2013.6692858.

[91] International Electrotechnical Commission and IEC, "IEC TR 61597:2021 Overhead electrical conductors - Calculation methods for stranded bare conductors," IEC, Geneva, Switzerland, 2021.

[92] S. Karimi, P. Musilek, and A. M. Knight, "Dynamic thermal rating of transmission lines: A review," *Renew. Sustain. Energy Rev.*, vol. 91, pp. 600–612, 2018, doi: 10.1016/j.rser.2018.04.001.

[93] Cigré Working Group 22.12, "Thermal behaviour of overhead conductors," Cigré, Paris (France), 2002.

[94] Hydro Tasmania Consulting, "Dynamic Transmission Line Rating Technology Review." Cambridge, Tasmania, Australia, pp. 1–39, 2009.

[95] K. J. Park, "A Novel Way to Select the Optimal Electrical Power Demand Management Provider for Robust Smart Grid," *Int. J. Circuits, Syst. Signal Process.*, vol. 14, pp. 511–519, 2020, doi: 10.46300/9106.2020.14.66.

[96] C. J. Wallnerstrom, Y. Huang, and L. Soder, "Impact from dynamic line rating on wind power integration," *IEEE Trans. Smart Grid*, vol. 6, no. 1, pp. 343–350, Jan. 2015, doi: 10.1109/TSG.2014.2341353.

[97] M. K. Hasan, M. M. Ahmed, and S. S. Musa, "Measurement and Modeling of DTCR Software Parameters Based on Intranet Wide Area Measurement System for Smart Grid Applications," *Adv. Intell. Syst. Comput.*, vol. 1166, pp. 1139–1150, 2021, doi: 10.1007/978-981-15-5148-2_96.

[98] M. Numan, D. Feng, F. Abbas, S. Habib, and S. Hao, "Coordinated operation of reconfigurable networks with dynamic line rating for optimal utilization of renewable generation," *Int. J. Electr. Power Energy Syst.*, vol. 125, p. 106473, Feb. 2021, doi: 10.1016/J.IJEPES.2020.106473.

[99] J. Teh and C.-M. Lai, "Reliability Impacts of the Dynamic Thermal Rating System on Smart Grids Considering Wireless Communications," *IEEE Access*, vol. 7, 2019, Accessed: Oct. 26, 2021. [Online]. Available: https://ieeexplore-ieee-org.recursos.biblioteca.upc.edu/document/8675908/.

[100] M. EL-Azab, W. A. Omran, S. F. Mekhamer, and H. E. A. Talaat, "Congestion management of power systems by optimizing grid topology and using dynamic thermal rating," *Electr. Power Syst. Res.*, vol. 199, p. 107433, Oct. 2021, doi: 10.1016/J.EPSR.2021.107433.

[101] K. Kopsidas, C. Cruzat, and M. Ni, "Cyber-physical reliability of dynamic line rating ICT failures in OHL networks," *IET Gener. Transm. Distrib.*, vol. 15, no. 2, pp. 371–382, Jan. 2021, doi: 10.1049/GTD2.12027.

[102] R. Pal, S. Chavhan, D. Gupta, … A. K.-I. R., and U. 2021, "A comprehensive review on IoT-based infrastructure for smart grid applications," *IET Renew. Power Gener.*, vol. 8, 2021, doi: 10.1049/rpg2.12272.

[103] B. Bera, S. Saha, A. Das, A. V.-I. I. of Things, and U. 2021, "Designing blockchain-based access control protocol in iot-enabled smart-grid system," *IEEE Internet Things J.*, 2021, Accessed: Oct. 26, 2021. [Online]. Available: https://www.diva-portal.org/smash/record.jsf?pid=diva2:1476911.

[104] M. Y. Mehmood *et al.*, "Edge Computing for IoT-Enabled Smart Grid," *Secur. Commun. Networks*, vol. 2021, 2021, doi: 10.1155/2021/5524025.

[105] Y. Z. Zhang, R. Xiong, H. W. He, and M. Pecht, "Validation and verification of a hybrid method for remaining useful life prediction of lithium-ion batteries," *J. Clean. Prod.*, vol. 212, pp. 240–249, Mar. 2019, doi: 10.1016/j.jclepro.2018.12.041.

[106] D. Dai, X. Zhang, and J. Wang, "Calculation of AC Resistance for Stranded Single-Core Power Cable Conductors," *IEEE Trans. Magn.*, vol. 50, no. 11, pp. 1–4, Nov. 2014, doi: 10.1109/TMAG.2014.2326040.

[107] I. Albizu, E. Fernandez, P. Eguia, E. Torres, and A. J. Mazon, "Tension and ampacity monitoring system for overhead lines," *IEEE Trans. Power Deliv.*, vol. 28, no. 1, pp. 3–10, 2013, doi: 10.1109/TPWRD.2012.2213308.

[108] B. S. Howington, "AC Resistance of ACSR—Magnetic and Temperature Effects: Prepared by a Task Force of the Working Group on Calculation of Bare Overhead Conductor Temperatures," *IEEE Power Eng. Rev.*, vol. PER-5, no. 6, pp. 67–68, 1985, doi: 10.1109/MPER.1985.5526666.

[109] V. T. Morgan, B. Zhang, and R. D. Findlay, "Effect of magnetic induction in a steel-cored conductor on current distribution, resistance and power loss," *IEEE Trans. Power Deliv.*, vol. 12, no. 3, pp. 1299–1306, 1997, doi: 10.1109/61.637007.

[110] V. T. Morgan, "The current distribution, resistance and internal inductance of linear power system conductors-a review of explicit equations," *IEEE Trans. Power Deliv.*, vol. 28, no. 3, pp. 1252–1262, 2013, doi: 10.1109/TPWRD.2012.2213617.

[111] R. A. Meyberg, F. M. Absi Salas, L. A. M. C. Domingues, M. A. Sens, M. T. Correia de Barros, and A. C. S. Lima, "Magnetic properties of an ACSR conductor steel core at temperatures up to 230 ∘C and their impact on the transformer effect," *IET Sci. Meas. Technol.*, vol. 15, no. 2, pp. 143–153, 2021, doi: 10.1049/smt2.12016.

[112] D. Zhang and P. Dang, "Study on AC Resistance of Overhead Conductors by Numerical Simulation," *7th IEEE Int. Conf. High Volt. Eng. Appl. ICHVE 2020 - Proc.*, Sep. 2020, doi: 10.1109/ICHVE49031.2020.9279899.

[113] Cigré 345, "Alternating current (AC) resistance of helically stranded conductors." Cigré, Paris, pp. 1–59, 2008.

[114] V. T. Morgan and R. D. Findlay, "The effect of frequency on the resistance and internal inductance of bare acsr conductors," *IEEE Trans. Power Deliv.*, vol. 6, no. 3, pp. 1319–1326, 1991, doi: 10.1109/61.85881.

[115] V. T. Morgan, "Electrical characteristics of steel-cored aluminium conductors," *Proc. Inst. Electr. Eng.*, vol. 112, no. 2, p. 325, 1965, doi: 10.1049/piee.1965.0051.

[116] IEC, "IEC 60287-1-1:2006. Electric cables - Calculation of the current rating - Part 1-1: Current rating equations (100 % load factor) and calculation of losses - General." IEC, Geneva, Switzerland, pp. 1–136, 2006.

[117] J. Fu, D. J. Morrow, S. Abdelkader, and B. Fox, "Impact of Dynamic Line Rating on Power Systems," in *46th International Universities' Power Engineering Conference (UPEC)*, 2011, pp. 1–5.

[118] D. Douglass *et al.*, "Real-Time Overhead Transmission-Line Monitoring for Dynamic Rating," *IEEE Trans. Power Deliv.*, vol. 31, no. 3, pp. 921–927, 2016, doi: 10.1109/TPWRD.2014.2383915.

[119] A. H. Wijethunga, J. V. Wijayakulasooriya, J. B. Ekanayake, and N. De Silva, "Conductor

temperature based low cost solution for dynamic line rating calculation of power distribution lines," *2015 IEEE 10th Int. Conf. Ind. Inf. Syst. ICIIS 2015 - Conf. Proc.*, pp. 128–133, 2016, doi: 10.1109/ICIINFS.2015.7398998.

[120] C. Singh, A. Singh, P. Pandey, and H. Singh, "Power Donuts in Overhead Lines for Dynamic Thermal Rating Measurement, Prediction and Electric Power Line Monitoring," *Int. J. Adv. Res. Electr. Electron. Instrum. Eng.*, vol. 3, no. 5, pp. 9394–9400, 2014.

[121] Y. Q. Ding *et al.*, "The effect of calculated wind speed on the capacity of dynamic line rating," *ICHVE 2016 - 2016 IEEE Int. Conf. High Volt. Eng. Appl.*, pp. 13–16, 2016, doi: 10.1109/ICHVE.2016.7800912.